Flow of yield-stress fluids through channels

Dissertation zur Erlangung des akademischen Grades eines Doktors der Naturwissenschaften an der Universität Konstanz
Mathematisch-Naturwissenschaftliche Sektion
Fachbereich Physik

Dissertation submitted for the degree of Doctor Natural Sciences at the University of Konstanz
Faculty of Sciences
Department of Physics

vorgelegt von | *submitted by*: Simon Papenkort

Tag der mündlichen Prüfung | *Date of Defense*: 2013-12-16

Referenten | *Referees*: Dr. Thomas Voigtmann, Prof. Dr. Peter Nielaba

Contents (short)

Contents

Acknowledgments

First, I thank my supervisor Dr. Thomas Voigtmann for the opportunity to study an intriguing topic, for the freedom to pursue different angles and approaches, and especially for his continuous support and infectious enthusiasm.

I am grateful to Prof. Dr. Peter Nielaba for agreeing to be the second referee.

I thank Prof. Dr. Matthias Fuchs for the discussions and his helpful insight. I also thank Prof. Dr. Joseph Brader, Prof. Dr. Mike Cates and Dr. Davide Marenduzzo for their ideas and for their readiness to share and discuss.

Special thanks to all my colleagues and to Marianne Griesser for meeting the administrative challenges.

Many thanks go to my family for their unwavering support, and to Thomas for proof-reading on tight schedules.

1 Introduction

The physics of fluid dynamics presents a rich and fascinating field of study. Although gas and fluid flows take place all around us at all times, its dynamics presents still many interesting and unsolved problems. A mathematical description is provided by the Navier-Stokes (NS) equation

$$\partial \rho \boldsymbol{v} + \boldsymbol{\nabla} \cdot (\rho \boldsymbol{v}\boldsymbol{v}) = \rho \boldsymbol{f}^{\text{ext}} - \boldsymbol{\nabla} p + \boldsymbol{\nabla} \cdot \boldsymbol{\sigma}, \tag{1.1}$$

which is easily derived by applying Newton's second law to fluid flows. The material derivative (left hand side) describes the acceleration of a fluid moving with a velocity $\boldsymbol{v}$ and is balanced by the sum of forces acting on the fluid, which may come in the form of external forces $\boldsymbol{f}^{\text{ext}}$, pressure gradients $\boldsymbol{\nabla} p$, and viscous forces $\boldsymbol{\nabla} \cdot \boldsymbol{\sigma}$. ρ is the density of the fluid, and the stress tensor has been split into an isotropic part $-p\mathbf{1}$ and the deviatoric stress tensor $\boldsymbol{\sigma}$. The NS equation is not closed and does not provide a relation between the velocity and stress. In constitutive equations, further assumptions on the material properties of the fluid are made. Isaac Newton assumed the stress to respond linearly to a velocity gradient $\boldsymbol{\kappa}$. For an incompressible flow $\operatorname{tr} \boldsymbol{\kappa} = 0$, the Newtonian constitutive equation reads

$$\boldsymbol{\sigma} = \eta(\boldsymbol{\kappa} + \boldsymbol{\kappa}^{\mathsf{T}}). \tag{1.2}$$

In this model, the viscosity η is a scalar constant. The dimensionless Reynolds number Re relates the inertial forces to viscous forces and characterizes the flow. For large Re, the non-linearity of the NS equation is dominant and we find turbulent flows. Even for a Newtonian fluid, it becomes very difficult to find numerical solution to the NS equation. For small Reynolds numbers, contributions of the non-linear term are small. The flow remains laminar and flow problems can often be solved analytically.

Although a fluid ultimately has a molecular structure, typical flow problems do not probe this length scale, and the dynamics is sufficiently resolved. For example, molecular oscillations in water take place at times about $\tau \approx 1\text{ps}$, which is always small compared to the time scale set by the shear rate of the flow $1/\dot{\gamma}$. The ratio between both time scales defines the Péclet number $\text{Pe} = \dot{\gamma}\tau \ll 1$. The situation is quite different for complex fluids, such as colloidal suspensions, polymer melts, foams, and gels. In these liquids, a second and much larger microscopic substructure exists, and the characteristic time scale easily reaches milliseconds to seconds. Flows with Péclet numbers much larger than one are commonly encountered, and the linear response approximation made by the Newtonian constitutive equation breaks down.

Complex fluids are ubiquitous in nature, industry, and everyday life [9, 66, 95]. Typical examples are ketchup, wall paint, shampoo, and blood. The properties of these liquids change dramatically under shear, and therefore depend sensitively on the flow. Complex

fluids give rise to some fascinating phenomena, such as bouncing jets [54], the tubeless siphon, elastic recoiling fluids, and the rod-climbing effect [9]. To understand the dynamics, we need to either take the microscopic structure into account or we have to develop more adequate constitutive equations. Both approaches have their merits and are followed in non-linear rheology. In a Molecular Dynamics (MD) simulations, the dynamics of each colloid [90, 103], polymer [42, 89] or even blood cell [61] is simulated. This provides a lot of control over the microscopic dynamics, but many particles are needed for hydrodynamic behavior to emerge, making simulations of large and complex flow geometries next to impossible. In these systems, the details about the microscopic dynamics is less important, but the flow is governed by the changes in the rheological properties it inflicts on the fluid. If we can capture the non-linear response of the fluid in a suitable constitutive equation, the Navier-Stokes equation remains a valid description of the flow. Finding such a constitutive equation is far from a trivial matter. A common and practical starting point is to identify the qualitative changes the fluid undergoes first and use them to develop a phenomenological model for the constitutive equation. One obvious non-linear response of the fluid is a dramatic change in the effective viscosity, $\eta(\dot{\gamma})$, under shear. With increasing shear rates, $\dot{\gamma}$, the viscosity decreases rapidly. Viscosity drops by several order of magnitudes are not uncommon, and the effect is especially noteworthy for glass-forming liquids, which can be molten under shear. The opposite effect, an increase in the viscosity called shear-thickening, is also observed [66], but is less common. In the Newtonian constitutive equation, only shear stresses arise. However, in complex fluids one find non-vanishing normal stress differences, $\sigma_{\alpha\alpha} - \sigma_{\beta\beta}$, which are for example responsible for the liquid to climb up a stirring rod [9]. To account for these additional stresses, the constitutive equations needs to be supply a tensorial structure. Already J. C. Maxwell noticed some materials to show the properties of an elastic solid on short times, but for long time to behave like a viscous fluid. Silly putty is a toy that bounces from walls when thrown, but flows like a liquid when given enough time. Maxwell developed a simple model of viscoelasticity by coupling a spring to a viscous damper. The model is a huge success, and we will come back to it later.

When a good quantitative agreement between a computed and the experimentally observed flow is paramount, e.g. in applied sciences or biorheology, one would measure the fluid properties and derive a model to match the results closely. Even for blood, which features some non-trivial microscopic dynamics of the blood cells [61, 82], the phenomenological constitutive equations in form of generalized Maxwell models work well [10]. Channel flow problems of shear-thinning fluids have been studied experimentally for laminar flows [32, 57, 88] and also in the turbulent regime [84]. Simple non-linear constitutive equations are sufficient to describe the steady state flow profiles, which develop a no-shear central plug in the center and a high shear region near the wall. Although the transient dynamics of the flow is even richer due to viscoelastic effects, these are usually only studied under steady shear [11],

Ultimately, one would like to start with the microscopic mechanism and derive a constitutive equation from first principles. Then the features of the model would emerge naturally and would not have to be inserted by hand. However, this is a formidable task, and in the case of polymer melts M. Doi and S. F. Edwards [30] managed to derive a constitutive equation. For dense colloidal suspensions undergoing a glass transition, mode-coupling theory (MCT) yields a way to a constitutive equation which is determined only by the

microscopic interactions of the particles [16, 36]. Yet it is so far not possible to treat this model even numerically, and it has been simplified to a schematically simplified version [17] which incorporate the important features of the original one.

Having found a constitutive equation is only half the task. We still need to solve the Navier-Stokes equation, which is now much more complicated than for a Newtonian fluid. The Lattice Boltzmann (LB) method presents an elegant way to solve flow problems [31, 87]. The model is inherently well-suited for parallel computation and for studying even the most complex flow problems.

Outline

In this thesis, we will demonstrate how mode-coupling theory can be combined with a Lattice Boltzmann simulation, and we will study the pressure-driven flow through a straight channel. In Chap. 2, we derive a modified LB algorithm capable of handling tensorial and non-Newtonian constitutive equations. In Sec. 2.1 and 2.2, an introduction to the LB method and appropriate boundary conditions are given. In Sec. 2.3, we show in a Chapman-Enskog expansion how the algorithm correctly reproduces the Navier-Stokes dynamics.

Chap. 3 introduces the constitutive equation for colloidal particle suspensions we will use. We recapitulate the main ideas and mode-coupling approximations going into the schematic MCT constitutive equation. We then develop a suitable algorithm to solve the MCT model, which can be implemented into a LB simulation. In Sec. 3.2, we make further approximations to the model and arrive at a non-linear Maxwell (nlM) constitutive equation, which is modeled to give the same qualitative features as the schematic MCT model.

In Chap. 4, we apply our modified LB solver to simulate the flow in a channel with a driving pressure. We start using the instantaneous non-linear Maxwell model (inlM), which allows the stress to adjust immediately to a change in the flow, Sec. 4.2. The model does not show a dependence on the flow history, but shares the same steady state results, which we present in Sec. 4.2.2. We then discuss the transient flows after the pressure has been switched on and off again in Sec. 4.2.3 (inlM model) and Sec. 4.3 (nlM model). Finally, we implement the full schematic MCT constitutive equation in a Lattice Boltzmann simulation in Sec. 4.4 and compare our findings with previous results.

Chap. 5 gives an outlook to open questions and possible future projects. A conclusion is provided in English, Chap. 6, and in German, Chap. 7.

2 Lattice Boltzmann

The Lattice Boltzmann (LB) model developed from Lattice Gas Cellular Automata (LGCA) [34] and became increasingly popular in the last decades. Because of its minimalist approach it is intrinsically well-suited for parallel computing, and is by now considered a mesoscopic fluid dynamics solver in its own right. Nevertheless, the history of improvements which ultimately resulted in the LB scheme is quite rich [87]. The main idea, to develop a highly simplified Molecular Dynamics simulation, which nonetheless reproduces the Navier-Stokes equation of a Newtonian fluid in the continuum limit, is the same for both concepts.

In the LGCA model, the fluid particles are encoded on a regular lattice with a set of discrete velocities pointing to the adjacent cells. On each lattice node, there may only be one particle for each direction at the same time. The zeroth and first moment of the particles with respect to the velocity set give the hydrodynamic density and velocity. The algorithm consists of two distinct parts, a collision step and a streaming step in which particles hop to the neighboring cell. The particles are only allowed to interact during the collision step and move otherwise unperturbed along the lattice nodes. Yet a collision may only occur if the particles can be rearranged in a way that conserves mass and momentum. There are some drawbacks with the LGCA model. The Reynolds number turns out to be proportional to the collision rate, and reaching a higher number of collisions in the LGCA model proves to be challenging. Second, due to the small number of particles and the stark simplification, the simulation results suffer from high statistical noise and require extensive averaging. A third problem comes up when going to going to 3 dimensions. Here, a 3 dimensional projection of a 24 speed 4 dimensional lattice is needed to ensure isotropy, whereas for a 2 dimensional flow, a 6 speed 2D hexagonal lattice proves sufficient. Yet, the complexity of the collision operator grows exponentially with the number of speeds, rendering a 3 dimensional simulation very difficult and costly [87].

LB managed to overcome all these challenges, cf. [6] and [47, 73], by introducing particle *densities* and by choosing an ensemble-averaged collision operator, in some cases at the price of losing the H-theorem as a stringent connection to statistical mechanics [87, 105]. Often the H-theorem remains valid for small velocities, but thermal LB models are found to suffer from instabilities [20]. Nevertheless, the LB scheme preserves the local structure of the LGCA model and benefits greatly from parallelized computing. The simplest collision operator, the Lattice Bhatnagar-Gross-Krook (LBGK) scheme, involves only one relaxation time [21, 58, 80]. If only a single relaxation time is provided, mass, momentum, and heat transfer will have to take place at the same rate [87], which is valid only for an ideal gas. Even more, due to the symmetry of the underlying lattice, spurious invariants, so-called ghost modes, may survive, which in a LB model with multiple relaxation times (MRT) can be suppressed individually. However, these concerns become relevant when the lattice resolution is low and only very few lattice points are provided. As we are for now interested in channel flows and the lattice resolution is high enough, we take advantage of the simplicity of the model.

The LB model proves to be a versatile tool since the algorithm is easily modified by introducing extra terms. These are usually dubbed body-forces and can be used to manipulate the continuum dynamics to one's heart's content as long as the update scheme yields the correct hydrodynamic limit in a Chapman-Enskog expansion. Even fundamental changes like implementing a temperature field [43] or simulating cylindrical polar coordinates on a rectangular lattice [45] can be achieved. We will rely on such a body-force term to modify the standard scalar Newtonian constitutive equation to a full tensorial shear-thinning one. A derivation of this term is presented below.

However, there is no unique way to extend the LB method to non-Newtonian fluids and the algorithm has been modified in various and very different manners. An overview is given in [78]. The simplest approach to account for changes in the viscosity was proposed by Aharanov and Rothman [1]. In an *ad hoc* extension, they allowed the relaxation time, which is directly connected to the viscosity of the fluid, to change locally. Although, due to its scalar nature, the model cannot provide the means to implement a tensorial non-Newtonian constitutive equation, it is very effective when simulating generalized Newtonian fluids with shear rate-dependent viscosities. The symmetric shear rate tensor is computed locally from the second moment [22] and is used to iteratively adjust the relaxation time [39, 55, 104], preserving the locality of the algorithm.

In [76,77,79] a different approach is pursued to ensure non-Newtonian behavior. Instead of modifying the collision step, the equilibrium distribution is supplemented by an extra term to incorporate visco-elasticity. This method is also used in so called lattice kinetic schemes, where instead of a collision step the particle densities are replaced by their equilibrium values [50,106]. Lattice kinetic schemes are closely related to the LB method and correspond to the LBGK model with the dimensionless relaxation time set to one.

In several hybrid LB models, a differential constitutive equation is solved in parallel and coupled back to the LB scheme to study complex fluids. For example, the algorithm can be made to simulate liquid crystals [18, 71, 72] by introducing an additional tensorial order parameter for each particle density [23]. A more microscopic oriented approach immerses colloids [31, 64, 65], polymers [2], and binary fluids [86] into a LB fluid with additional thermal fluctuations. In [24, 25] a thixotropic solvent is used. The viscosity of the fluid is derived using a finite difference scheme with the same discretization as the LB lattice, and the viscosity is again adjusted locally.

This chapter is structured as follows. We start by briefly presenting a standard Lattice Boltzmann model suitable for describing the flow of Newtonian fluids to familiarize ourselves with the basic concepts of this simulation scheme, Sec. 2.1. In Sec. 2.2 we then introduce suitable boundary conditions to describe pressure-driven channel flows and simple-shear geometries, which we will also rely on when simulating non-Newtonian fluids. During the remaining, major part of the chapter, we then introduce a new modification to the LB algorithm, which allows us to change the underlying dynamics of scalar Newtonian constitutive equation of the standard model to an arbitrary tensorial non-Newtonian one. In a multi-time scale Chapman-Enskog expansion, Sec. 2.3, we derive an extra term to the collision step similar to a body-force. This term can be used to locally adjust the pressure, momentum, and the stress of the fluid. Our model differs from similar approaches, where not the non-Newtonian stress is implemented but only the effects of the additional stresses on the momentum are accounted for [51]. For pressure-driven channel flows, we find the

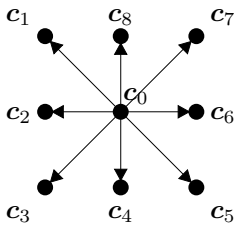

Figure 2.1: D2Q9 lattice. The speed of sound in this model is $c_\mathrm{s} = \sqrt{1/3}(\delta x/\delta t)$. The discrete velocities are numbered as depicted and have the lattice weights $a^0 = 4/9$, $a^1 = 1/9$ for the nearest neighbors $2, 4, 6, 8$, and $a^{\sqrt{2}} = 1/36$ for the next to nearest neighbors $1, 3, 5, 7$.

applied external pressure and the non-Newtonian pressure to cancel in parts. The algorithm can be made more lean and efficient; in Sec. 2.3.3 the final model is presented. In Sec. 2.3.4, we give an alternative approach to incorporate non-Newtonian pressure contributions. Last, the simulation setup and the conversion from lattice to physical units are described, Sec. 2.4.

2.1 The Lattice Boltzmann scheme

The standard Lattice Boltzmann model describes the incompressible, isothermal flow of a single Newtonian fluid. The charm and versatility of the scheme lie in its simplicity and makes it inherently well-suited for parallel computing. The actual algorithm can be described by only a single equation

$$n_i(\boldsymbol{r} + \delta t \boldsymbol{c}_i, t + \delta t) = n_i^*(\boldsymbol{r}, t) = n_i(\boldsymbol{r}, t) + \Delta_i[n_i(\boldsymbol{r}, t)]. \tag{2.1a}$$

Each lattice node $\boldsymbol{r}$ provides a discrete set of mass density distributions n_i with velocities $\boldsymbol{c}_i$. A LB update then consists of two steps. First the n_i are collided locally using a collision operator Δ_i, which is only a function of densities at the same lattice point $\boldsymbol{r}$. In the collision step, the densities are relaxed towards their equilibrium value n_i^eq. Using a Maxwell-Boltzmann distribution as the equilibrium form restores Galilean invariance and ensures that in the continuum limit the Navier-Stokes equation of a Newtonian fluid is recovered. The simplest collision operator, introduced by P. L. Bhatnagar, E. P. Gross, and M. Krook [8], employs only a single relaxation τ_LB,

$$\Delta_i = -\frac{1}{\tau_\mathrm{LB}} \left(n_i(\boldsymbol{r}, t) - n_i^\mathrm{eq}(\boldsymbol{r}, t) \right). \tag{2.1b}$$

Then the post-collision values n_i^* are streamed to the adjacent lattice cells. The discrete set of velocities is chosen in such a way that $\boldsymbol{r} + \delta t \boldsymbol{c}_i$ is the position of the i-th neighbor. The exact number and kind of velocities can be varied so far as they still conserve isotropy in the large-scale limit. This is often achieved by choosing a suitable set of weights and an appropriate collision operator. Qian *et al.* [80] introduced several such models and also standardized the naming. For example, the D2Q9 model later used is a 2-dimensional square lattice, in which each lattice node is shared by a set of 9 density distributions with velocities pointing to the cell itself, the 4 nearest neighbors, and the 4 diagonal next-to-nearest neighbors, cf. Fig. 2.1.

The streaming step takes place without any interactions between the particle densities and therefore the LB fluid obeys the equation of state of an ideal gas $p_0 = \rho_0 T$. The flow is isothermal, $T =$ constant, and to implement pressure gradients, we consider small

variations in the density

$$p = p_0 + (\rho - \rho_0)c_\mathrm{s}^2 = p_0 + \delta\rho\, c_\mathrm{s}^2 \tag{2.2}$$

where c_s is the speed of sound and ρ_0 is a reference density, which in lattice units is typically set to unity. As we are primarily interested in pressure differences, we can neglect the constant term and arrive at the equation of state

$$p = \delta\rho\, c_\mathrm{s}^2 \tag{2.3}$$

By working in the quasi-incompressible limit, the LB model introduces an error of order $\mathcal{O}(\mathrm{Ma}^2)$, $\mathrm{Ma} = u/c_\mathrm{s} \ll 1$, and restricts its application to sub-sonic flows, where the fluid velocity u remains small. The speed of sound c_s is a lattice constant and cannot be set to arbitrarily large values, which is common in conventional computational fluid dynamics. However, the speed of sound plays an important conceptual role in the Chapman-Enskog expansion since it separates the time scale of sound propagation and viscous momentum diffusion, cf. Sec. 2.3.

In the large scale limit, the algorithm Eq. (2.1) reproduces the Navier-Stokes equation of a Newtonian fluid with a constant kinematic viscosity

$$\nu = c_\mathrm{s}^2 \left(\tau_\mathrm{LB} - \tfrac{1}{2}\right) \tag{2.4}$$

as shown below, Sec. 2.3. Both the relaxation time τ_LB and the speed of sound c_s are constants for a given simulation and therefore yield a fixed kinematic viscosity in lattice units. The viscosity of the fluid is solely controlled by the chosen discretization in space and time, cf. Sec. 2.4. The collision operator is ensured to conserve mass and momentum, so that the mass and momentum densities, ρ and $\boldsymbol{j}$, are given by the first two moments of the density distributions with respect to the velocity set $\boldsymbol{c}_i$

$$\rho(\boldsymbol{r}, t) = \sum_i n_i(\boldsymbol{r}, t) \tag{2.5}$$

$$\boldsymbol{j}(\boldsymbol{r}, t) = \sum_i n_i(\boldsymbol{r}, t)\boldsymbol{c}_i \tag{2.6}$$

and are also needed to compute the equilibrium values of the density distribution

$$n_i^\mathrm{eq}(\rho, \boldsymbol{j}) = a^{c_i}\left[\rho + \frac{\boldsymbol{j}\cdot\boldsymbol{c}_i}{c_\mathrm{s}^2} + \frac{1}{\rho}\left(\frac{(\boldsymbol{j}\cdot\boldsymbol{c}_i)^2}{2c_\mathrm{s}^4} - \frac{j^2}{2c_\mathrm{s}^2}\right)\right]. \tag{2.7}$$

In principle, we have now everything at hand to simulate a Newtonian fluid, yet one key element is still missing. Up until now, we have exclusively discussed the dynamics of the bulk flow only and neglected the question of suitable boundary conditions, which we will discuss next.

2.2 Boundary Conditions

Concerning boundary nodes, the LB model profits once more massively from its local structure. Boundaries are easily implemented by replacing the dynamics of a lattice node, which makes the LB method is especially favorable for studying complex flow geometries. To implement boundaries which are not aligned to the lattice geometry a staircase approximation is usually applied.

Boundary conditions can be optimized to increase the precision of the simulation [48,68,91] and present a study in its own right [46, 52, 53]. Consequently there exists a huge variety of specialized methods serving different purposes, which we cannot discuss in total here. Instead, we briefly present three popular boundary conditions, which we will use to set up pressure-driven channel and simple shear flows. Please note that although all three boundary schemes work fine with the modified LB model we will later use, this is certainly not the general case.

2.2.1 Generalized periodic boundary condition

As the fluid dissipates energy due to its viscosity, we need a constant energy input to drive the system. For a channel flow, it is common practice to exploit the symmetry of the system by implementing periodic boundary conditions in flow direction. In a Poiseuille flow problem, the channel width is constant and a pressure gradient may be replaced with an effective body-force. A modified periodic boundary condition to incorporate a pressure difference was first introduced by Zhang and Kwok [108]. This paved the way to simulate more complex pressure-driven flow problems. Kim and Pitsch [56] proposed a refined method to conserve momentum rather than the velocity of the fluid, which they named generalized periodic boundary condition (GPBC). This can even be modified to study a periodic array of obstacles [41].

The main idea behind the GPBC is to set a target value for the average density of the inlet and outlet column of the simulation box. Since the equation of state $\rho = c_\mathrm{s}^{-2} p$ connects the pressure to the density, we can thereby keep the pressure fixed at both ends. The equilibrium function

$$n_i^{\mathrm{eq}}(\rho, \boldsymbol{j}) = a^{c_i} \left[\rho + \frac{\boldsymbol{j} \cdot \boldsymbol{c}_i}{c_\mathrm{s}^2} + \frac{1}{\rho} \left(\frac{(\boldsymbol{j} \cdot \boldsymbol{c}_i)^2}{2c_\mathrm{s}^4} - \frac{j^2}{2c_\mathrm{s}^2} \right) \right] \tag{2.8}$$

is only a function of the density and the momentum. We want the post-collision n_i^* leaving the system at the one end and being reinserted at the other end to have the correct target density. Therefore, we split the distribution in an equilibrium and a non-equilibrium part and compute the difference $\Delta\rho$ between the average density of the boundary column and the target value. This density difference is then used to match the density of only the equilibrium part with the target value, without changing the momentum:

$$n_i^*(\rho, \boldsymbol{j})|_{\mathrm{in}} = n_i^{\mathrm{eq}}(\rho + \Delta\rho, \boldsymbol{j}) + n_i^{*\,\mathrm{neq}}\big|_{\mathrm{out}} \,. \tag{2.9}$$

Although the authors only considered stationary flow profiles, we find the boundary condition to work fine for transient dynamics, too. Although we primarily use the b.c. to study

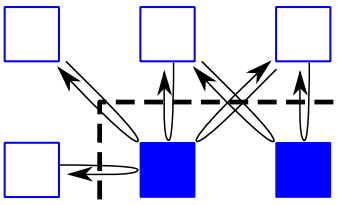

Figure 2.2: Solid squares are bounce-back nodes, non-solid squares fluid nodes. Instead of a collision step, the velocity distributions n_i at a bounce-back node are only reversed and remain otherwise unmodified. But only in the following streaming step, the n_i are sent back to the fluid node they originate from. The bounce-back rule results in a no-slip wall between the fluid and the solid node indicated by a dashed line.

Poiseuille flows, one great advantage of this method is that the channel width does not have to be kept constant.

2.2.2 Bounce-back rule

The bounce-back scheme is the most simple boundary condition to ensure a no-slip wall and widely used, see for example [87]. The name stems from the way such a node reacts to incoming density populations n_i. Instead of a collision step, all n_i are turned around and send back to the original node in the next streaming step, see Fig. 2.2. The physical boundary lies not on the lattice grid, but half-way to the last fluid node. Because the density distributions take a full time step to bounce back, this bounce-back scheme is only first order accurate in the lattice spacing. By correcting this, second order accuracy is recovered, but the implementation is more difficult as the wall orientation has to be taken into account. The bounce-back rule can even be generalized to incorporate boundaries on length scales smaller than the lattice spacing [91].

The bounce-back rule is especially useful concerning non-trivial flow problems. Even complex geometries that do not align to the lattice grid are easily set up by using staircase approximations. However, when non-local quantities are computed, for example a velocity gradient from a finite difference scheme, one has to bear in mind that the physical boundary lies in-between the lattice nodes.

2.2.3 Zou/He velocity boundary condition

In a simple shear geometry, instead of using a pressure gradient the system is driven by a plate moving with a constant velocity. The Zou/He method works quite similar to the generalized pressure b.c. Again, the non-equilibrium part n_i^{neq} is separated off the velocity distribution n_i. The equilibrium part is substituted to match the desired target value, whereas a simple bounce-back rule is applied to the n_i^{neq} [68, 109].

The Zou/He scheme can also be used to implement rigid walls. In this case, the target velocity is simply set to zero. If a high precision is needed, this is favorable to the bounce-back rule, which yields a small but nonzero slip velocity [46].

2.3 LB model for tensorial non-Newtonian constitutive equations

2.3.1 Chapman-Enskog expansion

A very helpful review about the Lattice Boltzmann model and the emergence of the Navier-Stokes equation through a Chapman-Enskog expansion is given by B. Dünweg and A. Ladd

in [31]. Concerning the basic LB dynamics, the following discussion relates closely to this report.

The standard LB algorithm, Eq. (2.1), assumes a Newtonian constitutive equation. However, adding to the collision step an extra term, comparable to an external body-force, provides a handhold to make the algorithm reproduce the dynamics of a tensorial non-Newtonian fluid. We describe a way to directly manipulate the underlying constitutive equation of the fluid, similar to methods by A. Vikhansky [92, 93] and J. Onishi *et al.* [76]. Introducing a body-force term is a powerful tool, but it affects the LB model quite profoundly and may lead to a redefinition of the hydrodynamic variables [44]. To understand all the implications and consequences, we will consider the body-force in its most general form and allow for changes in density, momentum, and stress. As it turns out, this proves necessary in case of non-Newtonian pressure contributions.

Again, we consider only a single-component, isothermal, and incompressible fluid and allow the LB model to approximate the Navier-Stokes equation in the quasi-incompressible limit, so that the pressure p is still connected linearly to density variation ρ via the equation of state

$$p = \delta\rho\, c_\mathrm{s}^2 \tag{2.10}$$

The speed of sound c_s is a pure lattice constant we need for the multi-time scale expansion below to distinguish between sound propagation and viscous momentum diffusion. Therefore, it may take unphysical values as long as the separation between both time scales is assured.

The modified LB algorithm reads

$$n_i(\boldsymbol{r} + \delta t \boldsymbol{c}_i, t + \delta t) = n_i^*(\boldsymbol{r}, t) = n_i(\boldsymbol{r}, t) + \Delta_i[n_i(\boldsymbol{r}, t)] + F_i[n_i(\boldsymbol{r}, t)], \tag{2.11}$$

and differs only by the additional body-force term F_i from the standard LB scheme. During the following Chapman-Enskog expansion, we will track the influence of the F_i on hydrodynamic properties. We will then use the term to adjust the stress, momentum, and pressure of the fluid locally, so that in the continuum limit the Navier-Stokes equation of an arbitrary non-Newtonian fluid is recovered.

Coarse-graining

The Navier-Stokes equation describes a fluid in the framework of a classical field theory, whereas the Lattice Boltzmann model acts on single particle densities. To determine the large-scale dynamics which will emerge from a LB scheme, we need to increase the coarse graining. In a multi-time scale approach, we introduce the dimensionless scaling parameter $\varepsilon \ll 1$ to define a convective time scale $\tilde{t}$ describing wave-like phenomena and a second one, $\hat{t}$, to account for moment diffusion,

$$\tilde{\boldsymbol{r}} = \varepsilon \boldsymbol{r}, \quad \tilde{t} = \varepsilon t, \quad \hat{t} = \varepsilon^2 t. \tag{2.12}$$

ε can be identified as the Knudsen number Kn, which gives the ratio between the mean free path length and the representative length scale of the physical system. The distribution function n_i, the collision operator Δ_i, and the body-force term F_i are subjected to the same

expansion:

$$n_i = n_i^{(0)} + \varepsilon n_i^{(1)} + \mathcal{O}(\varepsilon^2) \tag{2.13a}$$
$$\Delta_i = \Delta_i^{(0)} + \varepsilon \Delta_i^{(1)} + \varepsilon^2 \Delta_i^{(2)} + \mathcal{O}(\varepsilon^3) \tag{2.13b}$$
$$F_i = F_i^{(0)} + \varepsilon F_i^{(1)} + \varepsilon^2 F_i^{(2)} + \mathcal{O}(\varepsilon^3). \tag{2.13c}$$

Using the coarse-grained variables Eq. (2.12), the LB scheme takes the form

$$n_i(\tilde{\boldsymbol{r}} + \boldsymbol{c}_i \varepsilon \delta t, \tilde{t} + \varepsilon \delta t, \hat{t} + \varepsilon^2 \delta t) - n_i(\tilde{\boldsymbol{r}}, \tilde{t}, \hat{t}) = \Delta_i[\boldsymbol{n}(\tilde{\boldsymbol{r}}, \tilde{t}, \hat{t})] + F_i. \tag{2.14}$$

We expand this in a Taylor series to second order of ε and get

$$\begin{aligned} &\partial_{\tilde{\alpha}} n_i \varepsilon \delta t c_{i\alpha} + \partial_{\tilde{t}} n_i \varepsilon \delta t + \partial_{\hat{t}} n_i \varepsilon^2 \delta t \\ &+ \tfrac{1}{2} \partial_{\tilde{\alpha}} \partial_{\tilde{\beta}} n_i \varepsilon^2 \delta t^2 c_{i\alpha} c_{i\beta} + \partial_{\tilde{\alpha}} \partial_{\tilde{t}} n_i \varepsilon^2 \delta t^2 c_{i\alpha} + \tfrac{1}{2} \partial_{\tilde{t}}^2 n_i \varepsilon^2 \delta_{\tilde{t}}^2 + \mathcal{O}(\varepsilon^3) = \Delta_i + F_i, \end{aligned} \tag{2.15}$$

where $\partial_{\tilde{\alpha}}$ is the α-component of $\partial_{\tilde{\boldsymbol{r}}}$ and summation over repeated Greek indices is implied. The index i is reserved for the density velocity distribution $n_i = n_i(\tilde{\boldsymbol{r}}, \tilde{t}, \hat{t})$, where the argument has been omitted for brevity. In a second step, the series in ε of the remaining variables, Eq. (2.13), are inserted. For the expansion to work, the time scales between collision, sound propagation, and momentum diffusion have to be separated by a factor ε each. Then different orders of ε may be treated independently. For the first two orders, $\mathcal{O}(\varepsilon^0)$ and $\mathcal{O}(\varepsilon^1)$, we find

$$0 = \Delta_i^{(0)} + F_i^{(0)} \tag{2.16}$$
$$\left(c_{i\alpha} \partial_{\tilde{\alpha}} + \partial_{\tilde{t}}\right) n_i^{(0)} = \frac{1}{\delta t} \left(\Delta_i^{(1)} + F_i^{(1)}\right) = \frac{1}{\delta t} \left(n_i^{(1)*} - n_i^{(1)}\right). \tag{2.17}$$

The second order, $\mathcal{O}(\varepsilon^2)$, is given by

$$\left(c_{i\alpha} \partial_{\tilde{\alpha}} + \partial_{\tilde{t}}\right) n_i^{(1)} + \partial_{\hat{t}} n_i^{(0)} + \frac{\delta t}{2} \left(c_{i\alpha} \partial_{\tilde{\alpha}} + \partial_{\tilde{t}}\right)^2 n_i^{(0)} = \frac{1}{\delta t} \left(\Delta_i^{(2)} + F_i^{(2)}\right), \tag{2.18}$$

which, with the help of Eq. (2.17), can be put into the more practical form

$$\frac{1}{2} \left(c_{i\alpha} \partial_{\tilde{\alpha}} + \partial_{\tilde{t}}\right) \left(n_i^{(1)*} + n_i^{(1)}\right) + \partial_{\hat{t}} n_i^{(0)} = \frac{1}{\delta t} \left(\Delta_i^{(2)} + F_i^{(2)}\right). \tag{2.19}$$

The collision dynamics at order k are defined by distribution functions up to order $k-1$ and at $k = 0$ by $n_i^{(0)}$ only. From Eq. (2.16) we can then conclude $n_i^{(0)}$ to be a collisional invariant, which we identify with a equilibrium distribution n_i^{eq}. In order to avoid spurious invariants, n_i^{eq} can only be a function of the local values of the conserved hydrodynamic density ρ^{h} and momentum $\boldsymbol{j}^{\mathrm{h}}$. From

$$n_i^{\mathrm{eq}}(\rho^{\mathrm{h}}, \boldsymbol{j}^{\mathrm{h}}) = n_i^{(0)}(\rho^{\mathrm{h}}, \boldsymbol{j}^{\mathrm{h}}) \tag{2.20}$$

we can conclude that the density and momentum do not have contributions of ε or higher

$$\rho^{\mathrm{h}} = \rho^{(0)}, \qquad \boldsymbol{j}^{\mathrm{h}} = \boldsymbol{j}^{(0)}, \tag{2.21}$$

as these would be in contradiction to Eq. (2.16). For the same reason, any change in the dynamics of the LB model has to enter the Chapman-Enskog expansion at order ε.

Hydrodynamic invariants

In absence of the body-force term, the standard LB model is recovered. For this, one finds the density and momentum to be given by the zeroth and first moment of the density distribution with respect to the set of discrete velocities $\boldsymbol{c}_i$, cf. Eq. (2.5). By introducing the extra term F_i in the collision rule Eq. (2.11), we have modified the dynamics of the LB scheme in the continuum limit. We intend to make use of this change to implement a different, non-Newtonian constitutive equation, but we have to be aware that this may have an unintended effect on other parts of the LB model, too.

To determine the LB dynamics on large time and length scales and to see how the algorithm can be made to model the Navier-Stokes equation, we need to identify the conserved hydrodynamic density ρ^{h} and momentum $\boldsymbol{j}^{\mathrm{h}}$. We start by taking the first moments of Eq. (2.17) and (2.19). For the zeroth moment, we get

$$\partial_{\tilde{\alpha}} \sum_i c_{i\alpha} n_i^{(0)} + \partial_{\tilde{t}} \sum_i n_i^{(0)} = \frac{1}{\delta t} \sum_i \left(\Delta_i^{(1)} + F_i^{(1)} \right) \tag{2.22a}$$

$$\begin{aligned} &\frac{1}{2} \partial_{\tilde{\alpha}} \sum_i c_{i\alpha} \left(n_i^{(1)*} + n_i^{(1)} \right) + \frac{1}{2} \partial_{\tilde{t}} \sum_i \left(n_i^{(1)*} + n_i^{(1)} \right) + \partial_{\hat{t}} \sum_i n_i^{(0)} \\ &\qquad = \frac{1}{\delta t} \sum_i \left(\Delta_i^{(2)} + F_i^{(2)} \right). \end{aligned} \tag{2.22b}$$

The hydrodynamic fields depend on the lattice-scale variables parametrically, cf. Eq. (2.12),

$$\partial_\alpha = \varepsilon \partial_{\tilde{\alpha}}, \qquad \partial_t = \varepsilon \partial_{\tilde{t}} + \varepsilon^2 \partial_{\hat{t}}, \tag{2.23}$$

which we can use to put Eq. (2.22) back together. The sum of Eq. (2.22a) times ε and Eq. (2.22b) times ε^2

$$\begin{aligned} &\varepsilon \partial_{\tilde{\alpha}} \sum_i c_{i\alpha} \left(n_i^{(0)} + \varepsilon n_i^{(1)} + \frac{\varepsilon}{2} \left(\Delta_i^{(1)} + F_i^{(1)} \right) \right) \\ &+ \varepsilon \partial_{\tilde{t}} \sum_i \left(n_i^{(0)} + \varepsilon n_i^{(1)} + \frac{\varepsilon}{2} \left(\Delta_i^{(1)} + F_i^{(1)} \right) \right) + \varepsilon^2 \partial_{\hat{t}} \sum_i n_i^{(0)} \\ &\qquad = \frac{1}{\delta t} \sum_i \left(\varepsilon \left(\Delta_i^{(1)} + F_i^{(1)} \right) + \varepsilon^2 \left(\Delta_i^{(2)} + F_i^{(2)} \right) \right) \end{aligned} \tag{2.24}$$

is correct to second order in ε. Using Eq. (2.23), this becomes a continuity equation at

order $\mathcal{O}(\varepsilon^0)$

$$\partial_\alpha j_\alpha^{\mathrm{h}} + \partial_t \rho^{\mathrm{h}} = 0 + \frac{1}{\delta t} \sum_i \left(\varepsilon \left(\Delta_i^{(1)} + F_i^{(1)} \right) + \varepsilon^2 \left(\Delta_i^{(2)} + F_i^{(2)} \right) \right) \tag{2.25}$$

of the hydrodynamic density and moment

$$\rho^{\mathrm{h}} = \sum_i \left(n_i^{(0)} + \varepsilon n_i^{(1)} + \frac{\varepsilon}{2} \left(\Delta_i^{(1)} + F_i^{(1)} \right) \right), \tag{2.26a}$$

$$j_\alpha^{\mathrm{h}} = \sum_i c_{i\alpha} \left(n_i^{(0)} + \varepsilon n_i^{(1)} + \frac{\varepsilon}{2} \left(\Delta_i^{(1)} + F_i^{(1)} \right) \right). \tag{2.26b}$$

The hydrodynamic variables conserved by the modified algorithm differ from the ones of the standard LB model given by Eq. (2.5). Since nonetheless the moments in Eq. (2.26) have to be identified with the equilibrium values, cf. Eq. (2.21), higher order terms in ε have to cancel out

$$\sum_i \left(n_i^{(1)} + \tfrac{1}{2}(\Delta_i^{(1)} + F_i^{(1)}) \right) = 0, \qquad \sum_i \left(\Delta_i^{(2)} + F_i^{(2)} \right) = 0, \tag{2.27a}$$

$$\sum_i c_{i\alpha} \left(n_i^{(1)} + \tfrac{1}{2}(\Delta_i^{(1)} + F_i^{(1)} \right) = 0, \qquad \sum_i c_{i\alpha} \left(\Delta_i^{(2)} + F_i^{(2)} \right) = 0. \tag{2.27b}$$

Having identified the conserved quantities, let us take another, closer look at the zeroth moment, Eq. (2.22). On the time scale $\tilde{t}$, Eq. (2.22a), we find a continuity equation for the density ρ^{h} and momentum density j_α^{h}

$$\partial_{\tilde{\alpha}} j_\alpha^{\mathrm{h}} + \partial_{\tilde{t}} \rho^{\mathrm{h}} = \frac{1}{\delta t} \sum_i \left(\Delta_i^{(1)} + F_i^{(1)} \right). \tag{2.28}$$

The additional source term on the right side solely affects the density at the first order of ε, the same scale where small fluctuations are connected to the pressure by the equation of state (2.3). On the larger time scale $\hat{t}$, Eq. (2.22b) yields the incompressibility relation

$$\partial_{\hat{t}} \rho^{\mathrm{h}} = 0. \tag{2.29}$$

Putting both equations back together, we again arrive at the continuity equation

$$\partial_\alpha j_\alpha^{\mathrm{h}} + \partial_t \left(\rho^{\mathrm{h}} - \tilde{\rho} \right) = 0 \tag{2.30}$$

where we have defined

$$\partial_t \tilde{\rho} = \frac{1}{\delta t} \sum_i \varepsilon \left(\Delta_i^{(1)} + F_i^{(1)} \right). \tag{2.31}$$

The term $\partial_t \tilde{\rho}$ offers a way to modify the density fluctuations of the fluid locally. As mentioned before, the LB model works in the quasi-incompressible regime, where small density variations $\delta\rho$ around a reference value ρ_0 are connected to a change in pressure by the equation of state $p = \delta\rho\, c_{\mathrm{s}}^2$, cf. Eq. (2.2). We can therefore employ Eq. (2.31) to

account for extra pressure contributions by a non-Newtonian constitutive equation. The D-dimensional stress tensor $\sigma^{\mathrm{nN}}_{\alpha\beta}$ is split into the traceless deviatoric stress tensor $\bar{\sigma}^{\mathrm{nN}}_{\alpha\beta}$ and the pressure $-\frac{1}{D}\sigma^{\mathrm{nN}}_{\gamma\gamma}$. We approximate the change in density at time t by

$$\partial_t \tilde{\rho}(t) = -\frac{1}{Dc_{\mathrm{s}}^2 \delta t}\left(\sigma^{\mathrm{nN}}_{\gamma\gamma}(t) - \sigma^{\mathrm{nN}}_{\gamma\gamma}(t-\delta t)\right), \tag{2.32}$$

where $\sigma^{\mathrm{nN}}_{\gamma\gamma}(t-\delta t)$ is the trace of the non-Newtonian stress tensor of the previous time step $(t-\delta t)$. We thereby ensure that the accumulated change in density of all previous times $0 \leq t' \leq t$ translates to the right extra pressure at time t

$$\sum_{t'=0}^{t} \partial_t \tilde{\rho}(t') = -\frac{1}{Dc_{\mathrm{s}}^2}\sigma^{\mathrm{nN}}_{\gamma\gamma}. \tag{2.33}$$

Having dealt with the implementation of non-Newtonian pressure contributions, we turn our attention to the first moment of Eq. (2.17) and (2.19)

$$\partial_{\tilde{\beta}} \sum_i c_{i\alpha} c_{i\beta} n_i^{(0)} + \partial_{\tilde{t}} \sum_i c_{i\alpha} n_i^{(0)} = \frac{1}{\delta t} \sum_i c_{i\alpha} \left(\Delta_i^{(1)} + F_i^{(1)}\right), \tag{2.34a}$$

$$\frac{1}{2}\partial_{\tilde{\beta}} \sum_i c_{i\alpha} c_{i\beta} \left(n_i^{(1)*} + n_i^{(1)}\right) + \frac{1}{2}\partial_{\tilde{t}} \sum_i c_{i\alpha} \left(n_i^{(1)*} + n_i^{(1)}\right) + \partial_{\hat{t}} \sum_i c_{i\alpha} n_i^{(0)} = \frac{1}{\delta t} \sum_i c_{i\alpha} \left(\Delta_i^{(2)} + F_i^{(2)}\right). \tag{2.34b}$$

On the time scale $\tilde{t}$, we find a continuity equation for the momentum density

$$\partial_{\tilde{\beta}} \pi^{(0)}_{\alpha\beta} + \partial_{\tilde{t}} j^{\mathrm{h}}_{\alpha} = \frac{1}{\delta t} \sum c_{i\alpha} \left(\Delta_i^{(1)} + F_i^{(1)}\right) \tag{2.35a}$$

and momentum conservation on the $\hat{t}$ time scale

$$\frac{1}{2}\left(\pi^{(1)*}_{\alpha\beta} + \pi^{(1)}_{\alpha\beta}\right) + \partial_{\hat{t}} j_{\alpha} = 0, \tag{2.35b}$$

where we have defined the momentum-fluxes $\pi^{(0)}_{\alpha\beta} = \sum_i c_{i\alpha} c_{i\beta} n_i^{(0)}$ and $\pi^{(1)}_{\alpha\beta} = \sum_i c_{i\alpha} c_{i\beta} n_i^{(1)}$. Using Eq. (2.23) once more, we reassemble Eq. (2.35) to a single equation in lattice units

$$\partial_\beta \pi^{(0)}_{\alpha\beta} + \frac{1}{2}\partial_\beta \left(\pi^{\mathrm{neq}*}_{\alpha\beta} + \pi^{\mathrm{neq}}_{\alpha\beta}\right) + \partial_t j^{\mathrm{h}}_{\alpha} = f_{\alpha}, \tag{2.36a}$$

with

$$f_{\alpha} = \frac{1}{\delta t} \sum_i c_{i\alpha} \varepsilon \left(\Delta_i^{(1)} + F_i^{(1)}\right). \tag{2.36b}$$

The first moment f_α of the body-force term is often used to implement an effective pressure gradient or a gravitational force. Z. Guo *et al.* [44] first pointed out the necessity to correct the definition of the hydrodynamic current. As we have seen, the same is true for the density,

cf. Eq. (2.26). However, it is common practice to sidestep this problem by constructing the body-force term with a vanishing zeroth moment. In absence of the source term Eq. (2.31), mass conservation is ensured by the LB algorithm locally at every order of ε. It is even possible to keep the definition of both density and momentum unaffected if the body-force is designed to only supply a second moment. However, losing the ability to adjust the pressure would either restrict the applicability to certain flow problems or the pressure advection would have to be implemented separately. We will give these problems some more thoughts later. To keep this discussion as general as possible, we for now carry both terms along.

Let us return to our original objective to recover from Eq. (2.36) the Navier-Stokes equation

$$\begin{aligned}\partial_t \rho u_\alpha + \partial_\beta(\rho u_\alpha u_\beta) &= \partial_\beta \Pi_{\alpha\beta} + f_\alpha^{\mathrm{ex}} \\ &= -\partial_\alpha p + \partial_\beta \sigma_{\alpha\beta} + f_\alpha^{\mathrm{ex}},\end{aligned} \tag{2.37}$$

where the pressure $p = -\frac{1}{D}\operatorname{tr}\boldsymbol{\Pi}$ has been removed from momentum-flux tensor $\boldsymbol{\Pi}$ to give the traceless deviatoric stress tensor $\boldsymbol{\sigma}$ in D dimensions. The convective derivative on the left hand side and the pressure are determined by the density ρ and velocity $\boldsymbol{u} = \boldsymbol{j}/\rho$ alone. These are conserved quantities and therefore have to be identified with the equilibrium variables in Eq. (2.36a). The equilibrium part of the second moment tensor is responsible for providing the Euler stress

$$\pi_{\alpha\beta}^{\mathrm{eq}} = \pi_{\alpha\beta}^{(0)} = p\delta_{\alpha\beta} + \rho^{\mathrm{h}} u_\alpha^{\mathrm{h}} u_\beta^{\mathrm{h}}. \tag{2.38}$$

We will depend on the non-equilibrium part to give the right deviatoric stress

$$\sigma_{\alpha\beta} = \frac{1}{2}\left(\pi_{\alpha\beta}^{\mathrm{neq}\,*} + \pi_{\alpha\beta}^{\mathrm{neq}}\right). \tag{2.39}$$

The right hand side of Eq. (2.36a) paves a way for an external body-force f_α^{ex} to enter.

Matching the viscous stresses

The equilibrium distribution is constructed from a series expansion of the Maxwell-Boltzmann equilibrium distribution, thereby curing the lack of Galilean invariance stemming from the finite number of speeds, cf. [31, 87]. The expansion is truncated at second order in the velocity and is valid only for small Mach numbers. The symmetry of the chosen lattice dictates additional constraints. For a square lattice, we need to introduce lattice weights a^{c_i} to restore isotropy, see Fig. 2.1. The first moments of the equilibrium distribution

$$n_i^{\mathrm{eq}}(\rho, \boldsymbol{u}) = a^{c_i}\rho\left(1 + \frac{\boldsymbol{u}\cdot\boldsymbol{c}_i}{c_{\mathrm{s}}^2} + \frac{(\boldsymbol{u}\cdot\boldsymbol{c}_i)^2}{2c_{\mathrm{s}}^4} - \frac{u^2}{2c_{\mathrm{s}}^2}\right) \tag{2.40}$$

then give the density $\sum_i n_i^{\mathrm{eq}} = \rho$, momentum $\sum_i c_{i\alpha} n_i^{\mathrm{eq}} = j_\alpha = \rho u_\alpha$ and Euler stress $\sum_i c_{i\alpha} c_{i\beta} n_i^{\mathrm{eq}} = \rho c_{\mathrm{s}}^2 \delta_{\alpha\beta} + \rho u_\alpha u_\beta$.

To match the non-equilibrium second moment tensors $\pi_{\alpha\beta}^{\mathrm{neq}}$ in Eq. (2.36) to the viscous

stresses, we need to determine them first. We start with the second moment of Eq. (2.17)

$$\partial_{\tilde{\gamma}}\phi^{(0)}_{\alpha\beta\gamma} + \partial_{\tilde{t}}\pi^{(0)}_{\alpha\beta} = \frac{1}{\delta t}\left(\pi^{(1)\,*}_{\alpha\beta} - \pi^{(1)}_{\alpha\beta}\right), \tag{2.41}$$

where

$$\phi^{(k)}_{\alpha\beta\gamma} = \sum_i n_i^{(k)} c_{i\alpha} c_{i\beta} c_{i\gamma}. \tag{2.42}$$

Eq. (2.41) provides only the difference, whereas it is the sum appearing in Eq. (2.36). The third moment $\phi^{(0)}_{\alpha\beta\gamma} = \phi^{\mathrm{eq}}_{\alpha\beta\gamma}$ is directly accessible from the equilibrium distribution $n_i^{\mathrm{eq}}(\rho^{\mathrm{h}}, \boldsymbol{j}^{\mathrm{h}})$. The only surviving term not vanishing due to lattice symmetry constraints

$$\phi^{(0)}_{\alpha\beta\gamma} = \rho^{\mathrm{h}} c_{\mathrm{s}}^2 \left(u^{\mathrm{h}}_\alpha \delta_{\beta\gamma} + u^{\mathrm{h}}_\beta \delta_{\alpha\gamma} + u^{\mathrm{h}}_\gamma \delta_{\alpha\beta}\right) \tag{2.43}$$

then determines the derivative

$$\partial_{\tilde{\gamma}}\phi^{(0)}_{\alpha\beta\gamma} = c_{\mathrm{s}}^2 \left(\partial_{\tilde{\alpha}}\rho^{\mathrm{h}} u^{\mathrm{h}}_\beta + \partial_{\tilde{\beta}}\rho^{\mathrm{h}} u^{\mathrm{h}}_\alpha + \delta_{\alpha\beta}\partial_{\tilde{\gamma}}\rho^{\mathrm{h}} u^{\mathrm{h}}_\gamma\right). \tag{2.44}$$

Putting the equation of state $p = \rho c_{\mathrm{s}}^2$ into the Euler stress Eq. (2.38) and differentiating with respect to $\tilde{t}$ will give us the second term in Eq. (2.41):

$$\partial_{\tilde{t}}\pi^{(0)}_{\alpha\beta} = c_{\mathrm{s}}^2 \partial_{\tilde{t}}\rho^{\mathrm{h}}\delta_{\alpha\beta} + \partial_{\tilde{t}}\left(\rho^{\mathrm{h}} u^{\mathrm{h}}_\alpha u^{\mathrm{h}}_\beta\right).$$

We use the mass continuity equation (2.28) twice and get

$$\begin{aligned}\partial_{\tilde{t}}\pi^{(0)}_{\alpha\beta} = &\left(-c_{\mathrm{s}}^2\delta_{\alpha\beta} + u^{\mathrm{h}}_\alpha u^{\mathrm{h}}_\beta\right)\partial_{\tilde{\gamma}}\left(\rho^{\mathrm{h}} u^{\mathrm{h}}_\gamma\right) + \frac{1}{\delta t}\left(c_{\mathrm{s}}^2\delta_{\alpha\beta} - u^{\mathrm{h}}_\alpha u^{\mathrm{h}}_\beta\right)\sum_i\left(\Delta_i^{(1)} + F_i^{(1)}\right)\\ &+ u^{\mathrm{h}}_\beta \partial_{\tilde{t}} j^{\mathrm{h}}_\alpha + u^{\mathrm{h}}_\alpha \partial_{\tilde{t}} j^{\mathrm{h}}_\beta.\end{aligned}$$

Next, we insert the momentum continuity equation Eq. (2.35a) and arrive at

$$\begin{aligned}\partial_{\tilde{t}}\pi^{(0)}_{\alpha\beta} = &\left(-c_{\mathrm{s}}^2\delta_{\alpha\beta} + u^{\mathrm{h}}_\alpha u^{\mathrm{h}}_\beta\right)\partial_{\tilde{\gamma}}\rho^{\mathrm{h}} u^{\mathrm{h}}_\gamma + \frac{1}{\delta t}\left(c_{\mathrm{s}}^2\delta_{\alpha\beta} - u^{\mathrm{h}}_\alpha u^{\mathrm{h}}_\beta\right)\sum_i\left(\Delta_i^{(1)} + F_i^{(1)}\right)\\ &- u^{\mathrm{h}}_\beta \partial_{\tilde{\gamma}}\pi^{(0)}_{\alpha\gamma} - u^{\mathrm{h}}_\alpha \partial_{\tilde{\gamma}}\pi^{(0)}_{\beta\gamma}\\ &+ u^{\mathrm{h}}_\beta \frac{1}{\delta t}\sum_i c_{i\alpha}\left(\Delta_i^{(1)} + F_i^{(1)}\right) + u^{\mathrm{h}}_\alpha \frac{1}{\delta t}\sum_i c_{i\beta}\left(\Delta_i^{(1)} + F_i^{(1)}\right).\end{aligned} \tag{2.45}$$

Now, the derivative of the Euler stress is known

$$\partial_{\tilde{\gamma}}\pi^{(0)}_{\alpha\gamma} = c_{\mathrm{s}}^2\partial_{\tilde{\alpha}}\rho^{\mathrm{h}} + \partial_{\tilde{\gamma}}\left(\rho^{\mathrm{h}} u^{\mathrm{h}}_\alpha u^{\mathrm{h}}_\gamma\right), \tag{2.46}$$

which we can use to write Eq. (2.45) as

$$\begin{aligned}\partial_{\tilde{t}}\pi^{(0)}_{\alpha\beta} =& -c_{\mathrm{s}}^2\delta_{\alpha\beta}\partial_{\tilde{\gamma}}\rho^{\mathrm{h}}u^{\mathrm{h}}_{\gamma} - c_{\mathrm{s}}^2u^{\mathrm{h}}_{\alpha}\partial_{\tilde{\beta}}\rho^{\mathrm{h}} - c_{\mathrm{s}}^2u^{\mathrm{h}}_{\beta}\partial_{\tilde{\alpha}}\rho^{\mathrm{h}}\\ &-u^{\mathrm{h}}_{\beta}\partial_{\tilde{\gamma}}\rho^{\mathrm{h}}u^{\mathrm{h}}_{\alpha}u^{\mathrm{h}}_{\gamma} + u^{\mathrm{h}}_{\alpha}u^{\mathrm{h}}_{\beta}\partial_{\tilde{\gamma}}\rho^{\mathrm{h}}u^{\mathrm{h}}_{\gamma} - u^{\mathrm{h}}_{\alpha}\partial_{\tilde{\gamma}}\rho^{\mathrm{h}}u^{\mathrm{h}}_{\beta}u^{\mathrm{h}}_{\gamma}\\ &+\frac{u^{\mathrm{h}}_{\beta}}{\delta t}\sum_i c_{i\alpha}\left(\Delta_i^{(1)}+F_i^{(1)}\right)+\frac{u^{\mathrm{h}}_{\alpha}}{\delta t}\sum_i c_{i\beta}\left(\Delta_i^{(1)}+F_i^{(1)}\right)\\ &+\frac{1}{\delta t}\left(c_{\mathrm{s}}^2\delta_{\alpha\beta}-u^{\mathrm{h}}_{\alpha}u^{\mathrm{h}}_{\beta}\right)\sum_i\left(\Delta_i^{(1)}+F_i^{(1)}\right).\end{aligned} \tag{2.47}$$

In compliance with the small Ma-number expansion, we cross out the second line, which is proportional to u^3. Together, Eq. (2.44) and Eq. (2.47) give

$$\begin{aligned}\partial_{\tilde{t}}\pi^{(0)}_{\alpha\beta}+\partial_{\tilde{\gamma}}\phi^{(0)}_{\alpha\beta\gamma} =& c_{\mathrm{s}}^2\rho^{\mathrm{h}}\left(\partial_{\tilde{\alpha}}u^{\mathrm{h}}_{\beta}+\partial_{\tilde{\beta}}u^{\mathrm{h}}_{\alpha}\right)+\frac{1}{\delta t}\left(c_{\mathrm{s}}^2\delta_{\alpha\beta}-u^{\mathrm{h}}_{\alpha}u^{\mathrm{h}}_{\beta}\right)\sum_i\left(\Delta_i^{(1)}+F_i^{(1)}\right)\\ &+u^{\mathrm{h}}_{\beta}\frac{1}{\delta t}\sum_i c_{i\alpha}\left(\Delta_i^{(1)}+F_i^{(1)}\right)+u^{\mathrm{h}}_{\alpha}\frac{1}{\delta t}\sum_i c_{i\beta}\left(\Delta_i^{(1)}+F_i^{(1)}\right)\\ \overset{\text{Eq. (2.41)}}{=}&\frac{1}{\delta t}\left(\pi^{(1)\,*}_{\alpha\beta}-\pi^{(1)}_{\alpha\beta}\right).\end{aligned} \tag{2.48}$$

We multiply with ε and write in the unscaled variables

$$\begin{aligned}\pi^{\mathrm{neq}\,*}_{\alpha\beta}-\pi^{\mathrm{neq}}_{\alpha\beta} =& \delta t\rho^{\mathrm{h}}c_{\mathrm{s}}^2\left(\partial_{\alpha}u^{\mathrm{h}}_{\beta}+\partial_{\beta}u^{\mathrm{h}}_{\alpha}\right)\\ &+\left(c_{\mathrm{s}}^2\delta_{\alpha\beta}-u^{\mathrm{h}}_{\alpha}u^{\mathrm{h}}_{\beta}\right)\partial_t\tilde{\rho}+\left(u^{\mathrm{h}}_{\beta}f_{\alpha}+u^{\mathrm{h}}_{\alpha}f_{\beta}\right).\end{aligned} \tag{2.49}$$

Constructing the body-force term

This is as far as one can get without specifying the collision operator Δ_i. A sensible choice is the single-time Lattice Bhatnagar-Gross-Krook (LBGK) collision operator

$$\Delta_i = -\frac{n_i^{\mathrm{neq}}}{\tau_{\mathrm{LB}}}. \tag{2.50}$$

The collision step will then affect the non-equilibrium part of the second moment by

$$\pi^{\mathrm{neq}\,*}_{\alpha\beta}-\pi^{\mathrm{neq}}_{\alpha\beta} = -\frac{1}{\tau_{\mathrm{LB}}}\pi^{\mathrm{neq}}_{\alpha\beta}+\mathcal{F}_{\alpha\beta}, \tag{2.51}$$

where

$$\mathcal{F}_{\alpha\beta} = \sum_i c_{i\alpha}c_{i\beta}F_i \tag{2.52}$$

is the second moment of the body force term. We use Eq. (2.49) and Eq. (2.51) to finally determine the non-equilibrium part of the second moment before and after the collision

$$\begin{aligned}\pi^{\mathrm{neq}}_{\alpha\beta} =& -\tau_{\mathrm{LB}}\delta t\rho^{\mathrm{h}}c_{\mathrm{s}}^2\left(\partial_\alpha u^{\mathrm{h}}_\beta + \partial_\beta u^{\mathrm{h}}_\alpha\right) + \tau_{\mathrm{LB}}\mathcal{F}_{\alpha\beta},\\ &-\tau_{\mathrm{LB}}\left(c_{\mathrm{s}}^2\delta_{\alpha\beta} - u^{\mathrm{h}}_\alpha u^{\mathrm{h}}_\beta\right)\partial_t\tilde{\rho} - \tau_{\mathrm{LB}}\left(u^{\mathrm{h}}_\beta f_\beta + u^{\mathrm{h}}_\alpha f_\beta\right).\end{aligned} \tag{2.53a}$$

$$\begin{aligned}\pi^{\mathrm{neq}\,*}_{\alpha\beta} =& (1-\tau_{\mathrm{LB}})\,\delta t\rho^{\mathrm{h}}c_{\mathrm{s}}^2\left(\partial_\alpha u^{\mathrm{h}}_\beta + \partial_\beta u^{\mathrm{h}}_\alpha\right) + \tau_{\mathrm{LB}}\mathcal{F}_{\alpha\beta}\\ &+(1-\tau_{\mathrm{LB}})\left(c_{\mathrm{s}}^2\delta_{\alpha\beta} - u^{\mathrm{h}}_\alpha u^{\mathrm{h}}_\beta\right)\partial_t\tilde{\rho} + (1-\tau_{\mathrm{LB}})\left(u^{\mathrm{h}}_\beta f_\alpha + u^{\mathrm{h}}_\alpha f_\beta\right)\end{aligned} \tag{2.53b}$$

In presence of an external force field, we find spurious terms, which we have to cancel by a careful choice of $\mathcal{F}_{\alpha\beta}$. As a start, we split the body-force in two parts

$$\mathcal{F}_{\alpha\beta} = \mathcal{F}^{\mathrm{corr}}_{\alpha\beta} + \mathcal{F}^{\mathrm{visc}}_{\alpha\beta}, \tag{2.54}$$

where the second part is used to match the constitutive equation and

$$\mathcal{F}^{\mathrm{corr}}_{\alpha\beta} = \left(1-\frac{1}{2\tau_{\mathrm{LB}}}\right)\left[\left(c_{\mathrm{s}}^2\delta_{\alpha\beta} - u^{\mathrm{h}}_\alpha u^{\mathrm{h}}_\beta\right)\partial_t\tilde{\rho} + \left(u^{\mathrm{h}}_\beta f_\alpha + u^{\mathrm{h}}_\alpha f_\beta\right)\right] \tag{2.55}$$

takes care of the extra terms in Eq. (2.53). Comparing of Eq. (2.36) and (2.53) with the Navier-Stokes equation (2.37) yields

$$p = \frac{1-2\tau_{\mathrm{LB}}}{D}\delta t\rho^{\mathrm{h}}c_{\mathrm{s}}^2\partial_\gamma u^{\mathrm{h}}_\gamma + \frac{\tau_{\mathrm{LB}}}{D}\mathcal{F}^{\mathrm{visc}}_{\gamma\gamma} \tag{2.56a}$$

$$\sigma_{\alpha\beta} = \frac{2\tau_{\mathrm{LB}}-1}{2}\delta t\rho^{\mathrm{h}}c_{\mathrm{s}}^2\left(\overline{\partial_\alpha u^{\mathrm{h}}_\beta} + \overline{\partial_\beta u^{\mathrm{h}}_\alpha}\right) - \tau_{\mathrm{LB}}\bar{\mathcal{F}}^{\mathrm{visc}}_{\alpha\beta}, \tag{2.56b}$$

where we have split the traceless part, denoted by an overbar, off the tensor. We recover the Newtonian constitutive equations if we identify the shear viscosity η and volume viscosity η_{v}

$$\eta = \delta t\rho^{\mathrm{h}}c_{\mathrm{s}}^2\left(\tau_{\mathrm{LB}} - \tfrac{1}{2}\right), \qquad \eta_{\mathrm{v}} = \delta t\rho^{\mathrm{h}}c_{\mathrm{s}}^2\left(2\tau_{\mathrm{LB}}-1\right)/D \tag{2.57}$$

and if we demand the second moment of the body-force to be traceless, $\mathcal{F}_{\gamma\gamma} = 0$. The traceless part of the non-Newtonian stress contributions then will enter via

$$\bar{\sigma}^{\mathrm{nN}}_{\alpha\beta} = -\tau_{\mathrm{LB}}\bar{\mathcal{F}}^{\mathrm{visc}}_{\alpha\beta}. \tag{2.58}$$

When constructing the body forces, we have to keep in mind that the actual hydrodynamic density and momentum are modified due to the presence of the same body force. However, the LBGK collision operator is still the one correct for the original variables. Therefore, the body-force term itself should provide the necessary correction terms. Recall that the hydrodynamic variables differ in the first order of ε only

$$n_i^{\mathrm{h\,neq}} - n_i^{\mathrm{neq}} = \varepsilon\left(n_i^{\mathrm{h}\,(1)} - n_i^{(1)}\right) = \frac{1}{2}\varepsilon\left(\Delta_i^{(1)} + F_i^{(1)}\right). \tag{2.59}$$

The collision rule in the original variables reads

$$j_\alpha^* = j_\alpha + \varepsilon \sum_i c_{i\alpha} \left(\Delta_i^{(1)} + F_i^{(1)} \right) \tag{2.60}$$

and is missing an additional term to be sufficient for the hydrodynamic current

$$\begin{aligned} j_\alpha^{\mathrm{h}\,*} =& j_\alpha^{\mathrm{h}} - \frac{1}{2\tau_{\mathrm{LB}}} \sum_i c_{i\alpha} \varepsilon \left(\Delta_i^{(1)} + F_i^{(1)} \right) + \sum_i c_{i\alpha} \varepsilon \left(\Delta_i^{(1)} + F_i^{(1)} \right) \\ =& j_\alpha^{\mathrm{h}} + \left(1 - \frac{1}{2\tau_{\mathrm{LB}}} \right) \delta t f_\alpha. \end{aligned} \tag{2.61}$$

A comparison of the density yields the same result and the difference can be elevated by a correction factor $(1 - \frac{1}{2\tau_{\mathrm{LB}}})$. Having the first three moments together, we construct the force term

$$F_i = a^{c_i} \left\{ \left(1 - \frac{1}{2\tau_{\mathrm{LB}}} \right) \left[\partial_t \tilde{\rho} + \frac{f_\alpha c_{i\alpha}}{c_{\mathrm{s}}^2} \right] + \frac{\mathcal{F}_{\alpha\beta}^{\mathrm{ex}} + \mathcal{F}_{\alpha\beta}^{\mathrm{visc}}}{2c_{\mathrm{s}}^4} \left(c_{i\alpha} c_{i\beta} - c_{\mathrm{s}}^2 \delta_{\alpha\beta} \right) \right\} \tag{2.62}$$

and in presence of an external body-force f_α and a non-Newtonian stress contribution $\sigma_{\alpha\beta}^{\mathrm{nN}}$, we arrive at

$$\begin{aligned} F_i = a^{c_i} \Bigg\{ & \left(1 - \frac{1}{2\tau_{\mathrm{LB}}} \right) \left[\partial_t \tilde{\rho} + \frac{f_\alpha c_{i\alpha}}{c_{\mathrm{s}}^2} \right] \\ & + \left(1 - \frac{1}{2\tau_{\mathrm{LB}}} \right) \frac{c_{i\alpha} c_{i\beta} - c_{\mathrm{s}}^2 \delta_{\alpha\beta}}{2c_{\mathrm{s}}^4} \left[\partial_t \tilde{\rho} \left(c_{\mathrm{s}}^2 \delta_{\alpha\beta} - u_\alpha^{\mathrm{h}} u_\beta^{\mathrm{h}} \right) + \left(u_\beta^{\mathrm{h}} f_\alpha + u_\alpha^{\mathrm{h}} f_\beta \right) \right] \\ & - \frac{\bar{\sigma}_{\alpha\beta}^{\mathrm{nN}}}{2c_{\mathrm{s}}^4 \tau_{\mathrm{LB}}} \left(c_{i\alpha} c_{i\beta} - c_{\mathrm{s}}^2 \delta_{\alpha\beta} \right) \Bigg\}, \end{aligned} \tag{2.63}$$

with

$$\partial_t \tilde{\rho} = -\frac{1}{D c_{\mathrm{s}}^2 \delta t} \left(\sigma_{\gamma\gamma}^{\mathrm{nN}}(t) - \sigma_{\gamma\gamma}^{\mathrm{nN}}(t - \delta t) \right). \tag{2.64}$$

We are finally in the position to change the dynamics to match a non-Newtonian constitutive equation. The first line of Eq. (2.63) changes the density by $\partial_t \tilde{\rho}$ to take extra pressure contributions into account and implements an external body-force f_α. This leads to a redefinition of the hydrodynamic variables and a correction term is needed, which is given by the second line. Only in the last line the stress of the fluid is adjusted by $\bar{\sigma}_{\alpha\beta}^{\mathrm{nN}}$. Please note that although the non-Newtonian stress tensor is traceless, since we have treated $-\operatorname{tr} \boldsymbol{\sigma}^{\mathrm{nN}}/D$ as an additional pressure, nevertheless the diagonal elements may very well take finite values. In fact, this is the whole point, as it allows us to change the scalar Newtonian constitutive equation to a full tensorial non-Newtonian one.

Using Eq. (2.39) and Eq. (2.51), we find the total stress to be given by

$$\begin{aligned}\sigma_{\alpha\beta} &= -\frac{1}{2}\left(\pi_{\alpha\beta}^{\mathrm{neq}\,*} + \pi_{\alpha\beta}^{\mathrm{neq}}\right) = -\frac{1}{2}\left(2\pi_{\alpha\beta}^{\mathrm{neq}} - \frac{1}{\tau_{\mathrm{LB}}}\pi_{\alpha\beta}^{\mathrm{neq}} + \mathcal{F}_{\alpha\beta}\right) \\ &= \left(1 - \frac{1}{2\tau_{\mathrm{LB}}}\right)\left(-\pi_{\alpha\beta}^{\mathrm{neq}}\right) - \frac{1}{2}\mathcal{F}_{\alpha\beta},\end{aligned} \tag{2.65}$$

which yields with the definition of $\mathcal{F}_{\alpha\beta}$, cf. Eq. (2.54), Eq. (2.55), and Eq. (2.58),

$$\sigma_{\alpha\beta} = \left(1 - \frac{1}{2\tau_{\mathrm{LB}}}\right)\left[-\pi_{\alpha\beta}^{\mathrm{neq}} - \frac{1}{2}\left(u_\alpha^{\mathrm{h}} f_\beta + u_\beta^{\mathrm{h}} f_\alpha\right) - \frac{1}{2}\left(c_{\mathrm{s}}^2\delta_{\alpha\beta} - u_\alpha^{\mathrm{h}} u_\beta^{\mathrm{h}}\right)\partial_t\tilde{\rho}\right] + \frac{1}{2\tau_{\mathrm{LB}}}\bar{\sigma}_{\alpha\beta}^{\mathrm{nN}}. \tag{2.66}$$

In absence of a body-force term, the Newtonian stress $(1 - \frac{1}{2\tau_{\mathrm{LB}}})\boldsymbol{\pi}^{\mathrm{neq}}$ of the standard LB model is recovered. If the body-force has non-vanishing first moments, the redefinition of the hydrodynamic variables leads to correction terms.

2.3.2 Simulating a non-Newtonian fluid

Let us briefly recapitulate the changes we have applied to the standard LB model. The algorithm is not modified much, only a body-force term F_i has been added to the collision step

$$n_i(\boldsymbol{r} + \delta t\boldsymbol{c}_i, t + \delta t) = n_i^*(\boldsymbol{r}, t) = n_i(\boldsymbol{r}, t) - \frac{1}{\tau_{\mathrm{LB}}}n_i^{\mathrm{neq}}(\boldsymbol{r}, t) + F_i, \tag{2.67}$$

where $n_i^{\mathrm{neq}} = n_i - n_i^{\mathrm{eq}}$ is the non-equilibrium part of the velocity distribution and τ_{LB} the LBGK relaxation time. The F_i are devised to locally modify the pressure, momentum and stress of the fluid if need be. The dynamics of the fluid are thereby matched to an arbitrary tensorial constitutive equation, which may depend on the local flow. In presence of an external force f_α and a non-Newtonian stress contribution $\sigma_{\alpha\beta}^{\mathrm{nN}}$ the body-force takes the form

$$\begin{aligned}F_i = a^{c_i}\Bigg\{ &\left(1 - \frac{1}{2\tau_{\mathrm{LB}}}\right)\left[\partial_t\tilde{\rho} + \frac{f_\alpha c_{i\alpha}}{c_{\mathrm{s}}^2}\right] \\ &+ \left(1 - \frac{1}{2\tau_{\mathrm{LB}}}\right)\frac{c_{i\alpha}c_{i\beta} - c_{\mathrm{s}}^2\delta_{\alpha\beta}}{2c_{\mathrm{s}}^4}\left[\partial_t\tilde{\rho}\left(c_{\mathrm{s}}^2\delta_{\alpha\beta} - u_\alpha^{\mathrm{h}}u_\beta^{\mathrm{h}}\right) + \left(u_\beta^{\mathrm{h}}f_\alpha + u_\alpha^{\mathrm{h}}f_\beta\right)\right] \\ &- \frac{\bar{\sigma}_{\alpha\beta}^{\mathrm{nN}}}{2c_{\mathrm{s}}^4\tau_{\mathrm{LB}}}\left(c_{i\alpha}c_{i\beta} - c_{\mathrm{s}}^2\delta_{\alpha\beta}\right)\Bigg\}.\end{aligned} \tag{2.68a}$$

Here, a^{c_i} and c_{s} are the lattice weights and the speed of sound of the chosen lattice. $\boldsymbol{c}_i$ is the velocity pointing to the ith neighbor. We identify the isotropic part of the normal stresses, given by the trace of the stress tensor, with a non-Newtonian pressure contribution $-\frac{1}{D}\sigma_{\gamma\gamma}^{\mathrm{nN}}$. The equation of state $p = \rho c_{\mathrm{s}}^2$ connects this extra pressure to a small density

variation we implement by

$$\partial_t \tilde{\rho} = -\frac{1}{Dc_s^2 \delta t} \left(\sigma_{\gamma\gamma}^{\mathrm{nN}}(t) - \sigma_{\gamma\gamma}^{\mathrm{nN}}(t - \delta t) \right) \tag{2.68b}$$

where $\sigma_{\gamma\gamma}^{\mathrm{nN}}$ denotes the trace of the non-Newtonian stress tensor at the present time t and the previous time step $(t - \delta t)$, respectively. The remaining traceless part of the stress tensor is denoted by $\bar{\sigma}_{\alpha\beta}^{\mathrm{nN}}$. The presence of a body-force term also affects the definition of the hydrodynamic quantities. The density and momentum of the fluid are now given by

$$\rho^{\mathrm{h}} = \sum_i n_i + \frac{\delta t}{2} \partial_t \tilde{\rho}, \tag{2.69a}$$

$$j_\alpha^{\mathrm{h}} = \rho^{\mathrm{h}} u_\alpha^{\mathrm{h}} = \sum_i c_{i\alpha} n_i + \frac{\delta t}{2} f_\alpha, \tag{2.69b}$$

whereas the total stress has to be computed by

$$\sigma_{\alpha\beta} = \left(1 - \frac{1}{2\tau_{\mathrm{LB}}}\right) \left[-\pi_{\alpha\beta}^{\mathrm{neq}} - \frac{1}{2} \left(u_\alpha^{\mathrm{h}} f_\beta + u_\beta^{\mathrm{h}} f_\alpha \right) - \frac{1}{2} \left(c_s^2 \delta_{\alpha\beta} - u_\alpha^{\mathrm{h}} u_\beta^{\mathrm{h}} \right) \partial_t \tilde{\rho} \right] + \frac{1}{2\tau_{\mathrm{LB}}} \bar{\sigma}_{\alpha\beta}^{\mathrm{nN}}. \tag{2.69c}$$

Having derived a body-force term to modify the density, and thereby the pressure, the momentum, and the stress of the fluid, we can change the LB dynamics to model an arbitrary non-Newtonian fluid. The non-Newtonian stress is evaluated from a constitutive equation taking the present flow field as an input parameter. The stress may also depend on the flow history as demonstrated for the integrally formulated models, cf. Chap. 4.3. The second moment of the body-force term is then used to adjust the shear stress and the normal stress difference locally. The non-Newtonian pressure contribution enters the LB dynamics separately in form of a small variation in the density. Each moment of the body-force term leads to a redefinition of the corresponding hydrodynamic variable. Eq. (2.69) assumes a single relaxation time τ_{LB}. In multi-relaxation times algorithms, only one time is connected to the shear viscosity and the generalization is straight-forward.

In summary, the LB scheme consists of the following steps:

1. evaluate the non-Newtonian stress and pressure contributions,

2. LB collision step including the

3. application of the body-force term F_i and GPBC,

4. streaming step.

Please note that the definitions of all hydrodynamic variables are modified in presence of a body-force term. When measuring the flow field or when computing the equilibrium distributions for the collision step, the correct quantities are given by Eq. (2.69).

2.3.3 Simplification for pressure-driven channel flows

The scheme derived above provides a general algorithm, which works fine for all kind of flow geometries and always is a safe choice. However, due to the high symmetry of the pressure-driven channel flow we want to study, it proves worthwhile to take a closer look. By adapting the algorithm specifically to our problem, we can simplify the body-force term considerably.

Instead of using an effective body-force to implement a linear pressure gradient, we apply generalized periodic boundary conditions, cf. Sec. 2.2.1, and keep the pressure at both ends fixed. Obviously, the first moment f_α of the body-force term becomes obsolete, but so does the zeroth moment. To understand this, consider the steady state limit. After the flow has fully developed, the stress remains constant and $\partial_t \tilde{\rho}$ vanishes. So, as the 'dynamics' of the flowing steady state is fully accounted for by the second moment alone, the only way $\partial_t \tilde{\rho}$ can affect the steady state lies in a constant pressure offset accumulated during the transient dynamics. Yet the GPBC ensures the pressure at both ends of the simulation box to remain constant and thereby cancels out any influence of $\partial_t \tilde{\rho}$. We can therefore construct the body-force term to solely provide a second moment

$$F_i = -\frac{a^{c_i}}{2c_\mathrm{s}^4 \tau_\mathrm{LB}} \bar{\sigma}^\mathrm{nN}_{\alpha\beta} \left(c_{i\alpha} c_{i\beta} - c_\mathrm{s}^2 \delta_{\alpha\beta} \right). \tag{2.70}$$

Then the stress is simply given by

$$\sigma_{\alpha\beta} = \left(1 - \frac{1}{2\tau_\mathrm{LB}} \right) \left(-\pi^\mathrm{neq}_{\alpha\beta} \right) + \frac{1}{2\tau_\mathrm{LB}} \bar{\sigma}^\mathrm{nN}_{\alpha\beta}. \tag{2.71}$$

The density $\rho^\mathrm{h} = \rho$ and momentum density $j^\mathrm{h}_\alpha = j_\alpha$ remain completely unaffected and are the same as for the unmodified LB model. For comparison, in Sec. 4.2.2 a simulation using an effective body-force to implement the pressure gradient is carried out. In this case it is necessary for the body-force term to include all three moments and the whole algorithm is put to use.

2.3.4 Separate pressure advection

There is a second way to implement the pressure advection. Again, we construct a body-force term with only a second moment. But instead of removing the trace of the non-Newtonian stress, we actually use the full tensor

$$F_i = -\frac{a^{c_i}}{2c_\mathrm{s}^4 \tau_\mathrm{LB}} \sigma^\mathrm{nN}_{\alpha\beta} \left(c_{i\alpha} c_{i\beta} - c_\mathrm{s}^2 \delta_{\alpha\beta} \right). \tag{2.72}$$

The problem with this approach is that the LB model has no way to know about the additional non-Newtonian pressure $-\operatorname{tr} \boldsymbol{\sigma}^\mathrm{nN}/D$. Instead, the force exerted by the normal stresses is absorbed into the bulk viscosity, cf. Eq. (2.56a). We can, however, fix this shortcoming with a separate method similar to the GPBC, which takes care of the extra pressure advection.

The pressure difference between a node at position $\boldsymbol{r}$ and its neighbor at $\boldsymbol{r} + \delta t \boldsymbol{c}_i$ is

$$\Delta p_i = \left(- \operatorname{tr} \boldsymbol{\sigma}^{\mathrm{nN}}(\boldsymbol{r} + \delta t \boldsymbol{c}_i, t) - \operatorname{tr} \boldsymbol{\sigma}^{\mathrm{nN}}(\boldsymbol{r}, t) \right) / D. \tag{2.73}$$

We treat this pressure in the same way as the pressure step in the GPBC, cf. Sec. 2.2.1:

$$n_i^*(\rho, \boldsymbol{j}) = n_i^{\mathrm{eq}}(\rho + c_{\mathrm{s}}^{-2} \Delta p_i, \boldsymbol{j}) + n_i^{*\,\mathrm{neq}}. \tag{2.74}$$

Again, only the density of the equilibrium part of the post collision n_i^* is modified to account for the non-Newtonian pressure difference between the neighboring nodes, leaving the non-equilibrium part and the momentum untouched.

Since we only modify the density *variations* at order ε and we do not change the momentum $\boldsymbol{j}$, it is save to neglect the second order term of the equilibrium distribution Eq. (2.8), and we arrive at the computationally much more efficient update rule

$$n_i^*(\rho, \boldsymbol{j}) \to n_i^*(\rho, \boldsymbol{j}) + a^{c_i} c_{\mathrm{s}}^{-2} \Delta p_i. \tag{2.75}$$

At the neighboring node, the n_i^* pointing back will be modified by $-\Delta p_i$. Therefore, the overall mass is still conserved, but the simulation allows now small local variations in the density to account for a change in pressure.

2.4 Unit conversion and choice of LB units

As we have seen in the previous section, the Lattice Boltzmann algorithm is sufficient to model a system evolving in the way described by the Navier-Stokes equation. However, to map the simulation onto an actual physical problem, we have to find adequate simulation parameters and a way to translate the results we obtain within our LB model to real world physics.

Since we are interested in the solution of the incompressible Navier-Stokes equation, the flow is characterized by only a single dimensionless, and therefore system independent, parameter: the Reynolds number Re. Instead of choosing the direct route from the physical to the discrete LB system, we take an intermediate step by introducing a dimensionless system[1] [67]. To make the physical variables dimensionless, we express all quantities in units of a characteristic length l and time t_0. The transition to the discrete system is done the same way by choosing a discrete lattice spacing δ_x and time step δ_t, cf. Fig. 2.3. Finding the space step δ_x is straightforward, the number of lattice nodes in one dimension gives us $\delta_x = 1/N$.[2] However, the choice of δ_t is more sophisticated, and we have to give it some more thought.

In principle, the accuracy of the model is limited by two different kinds of errors, lattice effects and compressibility errors. The LB scheme features second-order accuracy, meaning the error scales with the square of the lattice resolution $\mathcal{E} \sim \delta_x^2$. However, the algorithm has

[1] N.b.: The here defined dimensionless variables are not necessarily the same as the ones used when discussing flow problems.

[2] The actual number of nodes used in a simulation may differ, since $N + 1$ nodes are needed for a lattice of length 1 and a lattice spacing of $1/N$. The boundary conditions and periodicity affect this further. For clarity reasons and generality, we will neglect these effects in this discussion.

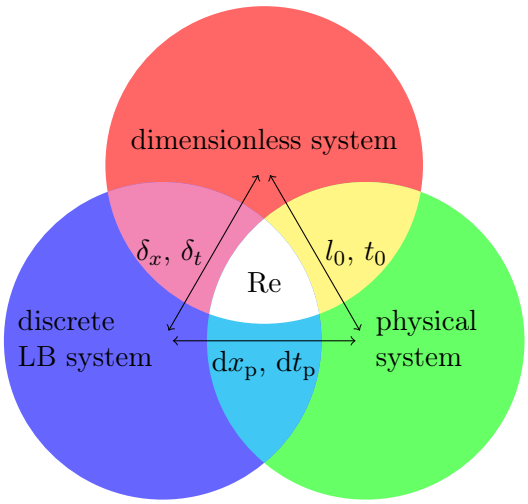

Figure 2.3: The diagram depicts the parameters translating between the different systems. The Reynolds number is system-independent.

no means to account for velocities larger than the speed of sound c_s and is restricted to subsonic lattice velocities $\frac{\delta_t}{\delta_x} < c_\mathrm{s}$. Even more, the simulation works in the quasi-incompressible limit and allows small variations in the density. This is fine for small Ma numbers, typically smaller than 0.4Ma, as compressibility effects scale with Ma^2. But nonetheless an error $\mathcal{E}_\mathrm{Ma} \sim \frac{\delta_x^2}{\delta_t^2}$ is introduced. It is eligible to keep both errors at the same magnitude, and we arrive at

$$\delta_t \sim \delta_x^2, \tag{2.76}$$

which gives us a valid choice for the time step.

To put some flesh on the bones, let us walk through the simulation setup of a shear-thinning fluid in a Poiseuille flow geometry. For the Reynolds number $\mathrm{Re} = \frac{u_0 l_0}{\nu}$, we need the characteristic velocity u_0, length l_0, and kinematic viscosity $\nu = \eta/\rho$ of the flow problem. η is the shear viscosity and ρ the density of the fluid. The characteristic length is found easily enough, and we define l_0 as the channel diameter. However, as the viscosity decreases under shear, we neither have a unique viscosity nor velocity. The fluid forms two high-shear, low viscosity regions near the walls and a no-shear, high viscosity center. The flow velocity is decided in the low viscosity regime, and we introduce a shear modulus $G = \eta_\mathrm{min}/t_0$ to define the characteristic velocity

$$u_0 = \frac{l_0}{t_0} = \frac{l_0 G}{\eta_\mathrm{min}}. \tag{2.77}$$

The dynamics in the center is much slower. We use the high viscosity η_max to make sure that the time resolution is high enough to resolve the plug. Together, this yields a valid definition of the Reynolds number

$$\mathrm{Re} = \frac{u_0 l_0}{\nu} = \frac{l_0^2/t_0 \rho}{\eta_\mathrm{max}}. \tag{2.78}$$

In the dimensionless system, getting the Reynolds number is a trivial task. Since the characteristic length and time scale equal one by definition, Re is just the inverse kinematic viscosity ν_{D}.

In the discrete Lattice Boltzmann system, the kinematic viscosity is a constant, $\nu_{\mathrm{LB}} = \frac{\tau_{\mathrm{LB}}-0.5}{3}$, and we use the Reynolds number $\mathrm{Re} = \frac{\delta_t/\delta_x^2}{\nu_{\mathrm{LB}}}$ to choose the time step

$$\delta_t = \mathrm{Re}\,\nu_{\mathrm{LB}}\,\delta_x^2. \tag{2.79}$$

With the help of dimensional analysis, the unit conversion is easily achieved. For example, the lattice velocity u_{LB} relates to a velocity u_{p} in the physical system by

$$u_{\mathrm{p}} = u_{\mathrm{LB}}\mathrm{d}u_{\mathrm{p}} = u_{\mathrm{LB}}\frac{\mathrm{d}x_{\mathrm{p}}}{\mathrm{d}t_{\mathrm{p}}} = u_{\mathrm{LB}}\frac{\delta_x}{\delta_t}\frac{l_0}{\tau_0}. \tag{2.80}$$

δ_x and δ_t translate u_{LB} to the dimensionless system, and multiplication with the characteristic length l_0 and time t_0 yields u_{p}.

3 Constitutive equations

The Navier-Stokes (NS) equation is the central equation in fluid dynamics and provides a mathematical framework for the description of fluid flows. The non-linear differential equation is derived by applying mass and momentum conversation laws to an arbitrary portion of the fluid. Although the NS equation is used to model all kind of problems, a mathematical proof that there always exists a global and smooth solution in 3 dimensions is still not found, cf. Millennium Prize.

For a fluid with a density ρ and velocity $\boldsymbol{v}$, the Navier-Stokes equation reads

$$\partial_t \rho \boldsymbol{v} + \boldsymbol{\nabla} \cdot (\rho \boldsymbol{v}\boldsymbol{v}) = \rho \boldsymbol{f}^{\text{ext}} - \boldsymbol{\nabla} p + \boldsymbol{\nabla} \cdot \boldsymbol{\sigma} \tag{3.1}$$

and is very much a statement of Newton's second law. The material derivative (left hand side) describes the acceleration of the fluid and is balanced by the sum of forces acting on the fluid. These may come in the from of external forces $\boldsymbol{f}^{\text{ext}}$, pressure gradients $\boldsymbol{\nabla} p$, and viscous forces by the deviatoric stress tensor $\boldsymbol{\sigma}$. We have followed the convention to split the stress tensor into an isotropic part $-p\mathbf{1}$ and an anisotropic part $\boldsymbol{\sigma}$.

The dynamics of the flow is not fully described by Eq. (3.1) alone. Constitutive equations make further assumptions on the material properties of the fluid to close the NS equation. For a non-viscous gas, the term $\boldsymbol{\nabla} \cdot \boldsymbol{\sigma}$ vanishes, and we get the Euler equation. In a viscous liquid, stresses arise from its flow, and the Newtonian constitutive equation simply states a linear dependence between the stress and the symmetric velocity gradient tensor. For an incompressible flow $\operatorname{tr} \kappa = 0$, we can write

$$\boldsymbol{\sigma} = \eta \boldsymbol{D} = \eta(\boldsymbol{\kappa} + \boldsymbol{\kappa}^{\mathsf{T}}). \tag{3.2}$$

η is the viscosity and a scalar constant for a Newtonian fluids. This model is only valid for simple liquids. The microscopic structure of complex fluids, e.g. gels, polymer melts or colloid solutions, makes the viscosity depend sensitively on the flow and even the flow history. In dense suspension, polymers are entangled and colloid particles are trapped in cages by their neighbors. Because the dynamics is very slow, correlations survive and affect the fluid properties for a long time. Under shear the polymers can align with the flow and the cages are broken. The accelerated dynamics not only yields a drop in the viscosity of the fluid, but also reduces the influence of the flow history.

There are two principle ways to approach these fluids. From an engineer's point of view, it is best to develop phenomenological models, which can be adjusted to quantitatively match the viscosity. There exists a wide range of specialized models, which are used to set up and solve flow problems. These are easily implemented in the Navier-Stokes equation and useful to specifically compute the flow in a certain geometry. But the relation between the shear stress and the shear rate has to be determined beforehand, and they cannot provide any new insight into the physics.

Starting from the opposite end provides its own struggles. Most commonly it is not possible to derive a constutive equation from first principles. One rare exception is Doi and Edwards's model of polymer melts [26–30]. For glass-forming fluids, the details of the microscopic interactions become less important, and the relaxation of density fluctuations is governed by a non-linear feedback mechanism. For a colloidal suspension at the glass transition, the fluctuations become arrested and cannot relax. Each colloid is surrounded by a cage of other particles it cannot leave unless the cage is broken by an externally imposed flow. The mode-coupling theory (MCT) and the integration-through-transients (ITT) formalism [13, 16, 36] successfully describes such a system and yields in principle a constitutive equation. However, the model is too complex to be used except for very simple flows. Even simplified schematic models are troublesome to solve beyond the steady state [97].

In the following chapter, we introduce the basic ideas behind the MCT-ITT approach and how they lead to the schematic MCT (sMCT) model. Further approximations yield a non-linear generalization of the viscoelastic Maxwell model (nlM), Sec. 3.2. These models provide a closure to the Navier-Stokes equation, but instead of solving the boundary value problem numerically, we follow a different approach. Lattice-Boltzmann simulations are intrinsically well-suited for complex flow geometries, and the modified algorithm derived in Chap. 2 is able to handle constitutive equations like the sMCT model and non-linear Maxwell model. In the sMCT model, the evolution of the correlation function is described by an integro-differential equation. In Sec. 3.1.1 ff., we present a scheme which keeps track of the flow history and is able to solve the sMCT constitutive equation in a way that is compatible with the LB simulation.

3.1 Schematic mode-coupling theory

A complete discussion of mode-coupling theory (MCT) [13, 36, 40], its application [16, 94, 97] on colloid rheology [4, 33, 85, 98], and the derivation of the schematic model [17] we implement as a constitutive equation is beyond the scope of this chapter. However, because the uniqueness of the model lies in its first-principle approach, a brief outline of the main features and ideas going into schematic model is well in place. For a more detailed discussion, see for example [12, 14].

The Smoluchowski equation presents a suitable starting-point to describe a system of colloidal particles dispersed in a Newtonian solvent. For high volume fractions near the glass transition, hydrodynamic interactions are negligible, and we can describe the system by a probability distribution function Ψ for the position of the particles. The evolution is dictated by the Smoluchowski operator $\Omega(t)$:

$$\frac{\partial \Psi(t)}{\partial t} = \Omega(t)\Psi(t). \tag{3.3}$$

Assuming an equilibrium distribution Ψ_{eq} exists and the system has been in equilibrium

for $t \to -\infty$, Eq. (3.3) is solved by

$$\Psi(t) = \Psi_{\mathrm{eq}} + \int_{-\infty}^{t} \mathrm{d}t_1 \; \Psi_{\mathrm{eq}} \, \boldsymbol{\kappa}(t_1) : \hat{\boldsymbol{\sigma}} \; \mathrm{e}_{-}^{\int_{t_1}^{t} \mathrm{d}s \; \Omega^{\dagger}(s)} \tag{3.4}$$

with the microscopic stress $\hat{\sigma}_{\alpha\beta} = -\sum_i F_i^{\alpha} r_i^{\beta}$ and the adjoint Smoluchowski operator

$$\Omega^{\dagger}(t) = \sum_i \left[D_0 \left(\boldsymbol{\partial}_i + \frac{1}{k_{\mathrm{B}} T} \boldsymbol{F}_i \right) + \boldsymbol{r}_i \cdot \boldsymbol{\kappa}^{\mathsf{T}}(t) \right] \cdot \boldsymbol{\partial}_i. \tag{3.5}$$

The sum runs over all particles i, and D_0 is the single particle diffusion coefficient. The non-equilibrium average of an arbitrary (not necessarily scalar) function of the particle coordinates f is given by

$$\langle f \rangle^{\mathrm{neq}} = \langle f \rangle + \int_{-\infty}^{t} \mathrm{d}t_1 \left\langle \boldsymbol{\kappa}(t_1) : \hat{\boldsymbol{\sigma}} \; \mathrm{e}_{-}^{\int_{t_1}^{t} \mathrm{d}s \; \Omega^{\dagger}(s)} f \right\rangle. \tag{3.6}$$

Here $\langle \cdot \rangle$ denotes an equilibrium Boltzmann-Gibbs average. In a homogeneous system, correlation functions obviously have to satisfy translational invariance. However, due to the affine flow of the solvent, a fluctuation at a certain wave vector $\boldsymbol{k}$ at time t' is correlated to the advected wave vector $\boldsymbol{k} \, \mathrm{e}_{-}^{-\int_{t'}^{t} \mathrm{d}s \; \boldsymbol{\kappa}(s)}$ at time t. Thereby, we can identify the deformation gradient tensor describing the affine motion of the fluid as

$$\boldsymbol{E}^{-1}(t, t') = \mathrm{e}_{-}^{-\int_{t'}^{t} \mathrm{d}s \; \boldsymbol{\kappa}(s)} \quad \text{and} \quad \boldsymbol{E}(t, t') = \mathrm{e}_{+}^{\int_{t'}^{t} \mathrm{d}s \; \boldsymbol{\kappa}(s)}, \tag{3.7}$$

respectively. Because the infinitesimal deformations do not commute, the exponentials are time-ordered indicated by the signs. The deformation tensor is the unique solution of the initial value problem $\frac{\partial}{\partial t} \boldsymbol{E}(t, t') = \boldsymbol{\kappa}(t) \boldsymbol{E}(t, t')$, $\boldsymbol{E}(t, t) = 1$. Since we are interested in a constitutive equation, we use Eq. (3.6) to get an expression for the stress tensor. We assume the system to start from an equilibrated state in the infinite past. Then all stress contributions are considered by an exact non-equilibrium Green-Kubo relation

$$\boldsymbol{\sigma}(t) = \frac{1}{V} \int_{-\infty}^{t} \mathrm{d}t_1 \left\langle \boldsymbol{\kappa}(t_1) : \hat{\boldsymbol{\sigma}} \; \mathrm{e}_{-}^{\int_{t_1}^{t} \mathrm{d}s \; \Omega^{\dagger}(s)} \hat{\boldsymbol{\sigma}} \right\rangle. \tag{3.8}$$

Stress fluctuations decay priorly via slow structural relaxations. In the MCT and integration through transient (ITT) approach, the average of Eq. (3.8) is factorized by projecting the dynamics onto density fluctuations before being subjected to further approximations [13]. We arrive at a constitutive equation which relates the stress to a time integral over the strain history:

$$\boldsymbol{\sigma}(t) = -\int_{-\infty}^{t} \mathrm{d}t' \int \mathrm{d}k^3 \left[\frac{\partial}{\partial t'} \left(\boldsymbol{e}_{\boldsymbol{k}}{}^{\mathsf{T}} \cdot \boldsymbol{B}(t, t') \cdot \boldsymbol{e}_{\boldsymbol{k}} \right) \boldsymbol{e}_{\boldsymbol{k}} \boldsymbol{e}_{\boldsymbol{k}}{}^{\mathsf{T}} \right] \mathcal{G}_{\boldsymbol{k}}(t, t'). \tag{3.9}$$

The Finger or left Cauchy-Green deformation tensor

$$\boldsymbol{B}(t, t') = \boldsymbol{E}(t, t') \cdot \boldsymbol{E}^{\mathsf{T}}(t, t'), \tag{3.10}$$

describes the deformation while respecting the principle of material frame-indifference, i.e. a pure rotation does not induce any stresses. However, the appearance of $\boldsymbol{B}$ is not self-evident, and it is a feature of the model to favor the Finger tensor. In phenomenological constitutive equations, other rotation-independent deformation tensors are frequently used, for example the Cauchy deformation tensor $\left(\boldsymbol{E}^{-1}\right)^{\intercal}\boldsymbol{E}^{-1}$. $\boldsymbol{e}_{\boldsymbol{k}} = \boldsymbol{k}/|\boldsymbol{k}|$ denote the unit vectors of fluctuations $\boldsymbol{k}$ the Finger tensor is projected on. The wave vector-dependent kernel

$$\mathcal{G}_{\boldsymbol{k}}(t,t') = \frac{k^3}{32\pi^3}\frac{S_k' S_{k(t,t')}'}{k(t,t')S_k^2}\,\Phi^2_{\boldsymbol{k}(t,t')}(t,t') \tag{3.11}$$

is a function of only the equilibrium static structure factor S_k, its derivative and the correlator Φ. Here, the strain enters a second time as the decay of the correlator is accelerated by shear, cf. Fig. 3.6a. The fluctuations are affected by the flow field, resulting in a change of the wave vector. The correlator $\Phi_{\boldsymbol{k}(t,t')}$ measures the overlap of fluctuations at a wave vector $\boldsymbol{k}$ and time t with previous fluctuations stemming from time t' which wave vectors have been advected and now coincident with $\boldsymbol{k}$.

Further Zwanzig-Mori like approximations yield an integro-differential equation for the time evolution of the correlator:

$$\frac{\partial}{\partial t}\Phi_{\boldsymbol{k}}(t,t_0) + \Gamma_{\boldsymbol{k}}(t,t_0)\left(\Phi_{\boldsymbol{k}}(t,t_0) + \int_{t_0}^{t}\mathrm{d}t'\; m_{\boldsymbol{k}}(t,t',t_0)\,\frac{\partial}{\partial t'}\Phi_{\boldsymbol{k}}(t',t_0)\right) = 0, \tag{3.12}$$

where $\Gamma_{\boldsymbol{k}}(t,t_0)$ is the initial decay rate. The approximated memory kernel $m_{\boldsymbol{k}}(t,t',t_0)$ is a non-trivial function of three time arguments, the equilibrium static structure factor and the correlator. The exact form is not relevant to us, however, one finds the memory kernel to depend quadratically on the correlator and on the accumulated strain between the three time arguments. Together with Eq. (3.9) and Eq. (3.11), this gives us a microscopically derived, closed constitutive equation for Brownian particles near the glass transition.

The complexity of this model restricts its application to simple flows [38, 97]. Brader *et al.* [17] proposed a much simplified schematic model, which nonetheless stays true to the central aspects of the full microscopic model. Assuming isotropy and disregarding all angular dependences Eq. (3.9) and Eq. (3.11) become

$$\boldsymbol{\sigma}(t) = \int_{-\infty}^{t}\mathrm{d}t'\;\left[-\frac{\partial}{\partial t'}\boldsymbol{B}(t,t')\right]G(t,t'), \tag{3.13}$$

$$G(t,t') = \frac{1}{60\pi^2}\int \mathrm{d}k\; k^5\left(\frac{S_k' S_{k(t,t')}'}{k(t,t')S_k^2}\right)\Phi^2_{k(t,t')}(t,t'). \tag{3.14}$$

Next, the dependence on the wave vector is disregarded altogether, and we approximate Eq. (3.14) with the generalized modulus

$$G(t,t') = \nu_\sigma \Phi^2(t,t'). \tag{3.15}$$

$\nu_\sigma = G(t,t)$ measures the strength of the stress fluctuations and determines the initial height of the shear modulus. The time evolution of the single remaining correlator is then

described by the equation of motion

$$\frac{\partial}{\partial t}\Phi(t,t') + \Gamma\left(\Phi(t,t') + \int_{t'}^{t} \mathrm{d}s\; m(t,s,t')\,\frac{\partial}{\partial s}\Phi(s,t')\right) = 0. \tag{3.16a}$$

For the memory kernel, the following ansatz is chosen:

$$m(t,s,t') = h(t,t')h(t,s)\left[\nu_1\Phi(t,s) + \nu_2\Phi^2(t,s)\right], \tag{3.16b}$$

where the h-factors

$$h(t,\tau) = \frac{\gamma_\mathrm{c}^2}{\gamma_\mathrm{c}^2 + [\nu I_1(t,\tau) + (1-\nu)I_2(t,\tau) - D]} \tag{3.16c}$$

are responsible for the shear-induced decay of the memory. Eq. (3.16c) is modeled to give under steady shear the value $1/(1+(\gamma/\gamma_\mathrm{c})^2)$, which is known to be a good approximation to full MCT-ITT results. $I_1 = \operatorname{tr}\boldsymbol{B}$ and $I_2 = \operatorname{tr}\boldsymbol{B}^{-1}$ are the first two invariants of the Finger tensor and give a scalar measure for the accumulated strain γ. By using the invariants of $\boldsymbol{B}$ material objectivity is ensured. A mixing parameter ν between I_1 and I_2 is chosen and set to 0.5. The cross-over strain parameter γ_c is known to be 0.1, and the parameters $\nu_{1,2}$ are conventionally set to $\nu_2 = 2$ and $\nu_1 = 2(\sqrt{2}-1) + \epsilon/(\sqrt{2}-1)$. The schematic model then provides the same asymptotic behavior as the full microscopic model and the critical exponents also match those found for typical colloidal suspensions [40]. The separation parameter ϵ measures the proximity to the glass transition: in the fluid phase ϵ has negative values and in the glass ϵ is positive.

The schematic MCT model gives a constitutive equation in three parts. Thanks to the integral formulation of Eq. (3.13), the stress tensor is not only a function of the present shear rate but of the complete flow history, and the model features a memory. The Finger tensor preserves the tensorial character of the model. Its derivative can be written as

$$-\partial_{t'}\boldsymbol{B}(t,t') = \boldsymbol{E}(t,t')\boldsymbol{\kappa}(t')\boldsymbol{E}^\mathsf{T}(t,t') + (\boldsymbol{E}(t,t')\boldsymbol{\kappa}(t')\boldsymbol{E}^\mathsf{T}(t,t'))^\mathsf{T}, \tag{3.17}$$

and illustrates the dependence on past shear rates $\boldsymbol{\kappa}(t')$ and the accumulated strain. The shear modulus is a quadratic function of the correlator and given by Eq. (3.15). All wave-vector dependences have been integrated out and are absorbed in a single scalar value ν_σ. The time-evolution of the single remaining correlator is described by Eq. (3.16). As the decay of the correlator is accelerated by shear, the generalized modulus exhibits shear-thinning behavior.

3.1.1 Adaptation to Lattice Boltzmann

On first thought, implementing the schematic model in a Lattice Boltzmann simulation seems quite straightforward. The schematic MCT model takes the strain rate as an input value and computes the accumulated strain, correlation, and memory functions to determine the stress. The modified LB algorithm then uses the non-Newtonian stress to advance one time step, and we can measure the new strain-rate, cf. Fig. 3.1. Putting both parts together, we should be able to simulate the time-dependent flow of glass-forming liquids –

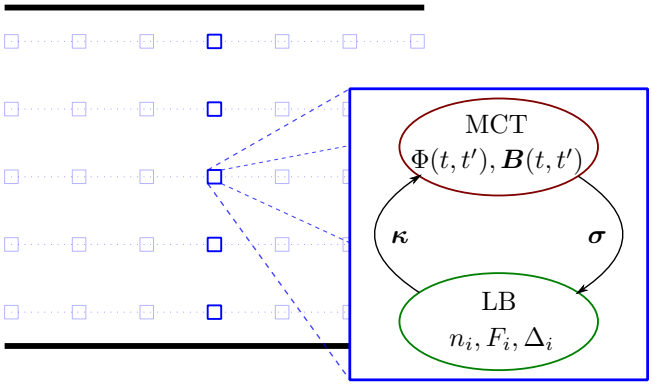

Figure 3.1: Schematic representation of the schematic mode-coupling model implementation in a Lattice Boltzmann simulation. A lattice node consists of two parts working together. The computed strain rate $\boldsymbol{\kappa}$ is measured in the LB frame work and handed to the MCT solver. There, $\boldsymbol{\kappa}$ is added to the memory and the stress $\boldsymbol{\sigma}$ is computed. The stress is handed to the modified LB model, which performs a local collision step and streams the density distributions n_i to the neighbor cells.
As each cell keeps track of the flow history and correlator, the demand for CPU time and RAM is high. Therefore, only in a single column in the center of the simulation box the schematic MCT model is solved for simple channel flows. The stresses are then relayed along the symmetry axis to the other nodes.

problem solved.

However, life proves to never be quite as simple as that and the devil is in the details. By coupling the MCT code to the LB simulation, the flow history is fixed to the lattice instead to a comoving reference system. The difference amounts to a term of the kind $(\boldsymbol{u}\cdot\boldsymbol{\partial})\boldsymbol{\sigma}$ [75]. In general, the stress would have to be advected with the fluid, but how this can be achieved is still open to some discussion, cf. Chap. 5. Luckily, in a straight channel flow and simple shear geometry, the advection term cancels out due to the symmetry of the system. In the derivation of the schematic MCT model, all angular and wave-vector dependences are neglected, yet a laminar channel flow is by no means isotropic. By combining the sMCT model with a Lattice Boltzmann simulation we implicitly assume that we may make a local approximation of the flow. A full MCT model should take spacial variations of the flow into account.

The second difficulty is a more practical but nonetheless serious one. The MCT works near the glass transition, where the short time dynamics is separated from a second, divergent time scale. Correlations can survive for very long times if not destroyed by shear. This relates to the caging effect, and we clearly do not want to give up this essential slowing down of the dynamics. In previous works [35,60,107], a constant strain rate was considered. Under steady shear, the correlator $\Phi(t,t')$ becomes a function of only the time difference $t-t'$, which simplifies the model very much. The strain and even the invariants are analytically accessible for all times, and one would successively increase the time step to adequately sample both, the short time regime and the long time limit. Since the Lattice Boltzmann model has to progress linearly in time, and we explicitely want to consider time-dependent flows, this is not a viable option here. This causes a vast demand of memory increasing linearly in time and renders a long time simulation effectively impossible. Luckily, there is a way out. In the next section, we will discuss a purpose-built memory layout on a

quasi-logarithmic grid to face this matter.

Prior to this, let us consider adequate variables the algorithm needs to keep track of. In principle, only the correlator $\Phi(t, t')$ and the Finger tensor $\boldsymbol{B}(t, t')$ enter the schematic MCT model. However, it turns out to be advantageous to treat the memory function independently from the correlator. Furthermore, from a technical point of view, the Finger tensor is not the best point to start from, as numerical differentiation might become problematic. Using Eq. (3.17) and inserting the shear modulus Eq. (3.15), the stress integral Eq. (3.13) becomes

$$\boldsymbol{\sigma}(t) = \nu_\sigma \int_{-\infty}^{t} \mathrm{d}t' \boldsymbol{E}(t, t') \boldsymbol{D}(t') \boldsymbol{E}^{\intercal}(t, t') \Phi^2(t, t') \tag{3.18}$$

and is now a function of the strain rate and the deformation tensor, instead. For a discrete time step δt_{LB}, the time-ordered exponential is approximated by the product

$$\boldsymbol{E}(t, t') = \exp_+ \left[\int_{t'}^{t} \mathrm{d}s\, \boldsymbol{\kappa}(s) \right] = \prod_{s=t'}^{t} \exp(\boldsymbol{\kappa}_s \delta t_{\mathrm{LB}}). \tag{3.19}$$

The strain rate and the strain are the first values we need to track in time. It is, however, favorable not to save the deformation tensor $\boldsymbol{E}$ but the factors $\exp(\boldsymbol{\kappa}_s \delta t_{\mathrm{LB}})$, which will become clear in the next section.

Eq. (3.16) describes the time evolution of the correlator and needs only slight modifications

$$\frac{\partial}{\partial t} \Phi(t, t') + \Gamma \left(\Phi(t, t') + h(t, t') \int_{t'}^{t} \mathrm{d}s\; M(t, s) \frac{\partial}{\partial s} \Phi(s, t') \right) = 0, \tag{3.20a}$$

where

$$M(t, s) = h(t, s) \left[\nu_1 \Phi(t, s) + \nu_2 \Phi^2(t, s) \right]. \tag{3.20b}$$

The first h-factor is independent of the integration variable s and has been separated from the original memory kernel $m(t, s, t')$. Therefore, we need to record the correlator Φ and the memory M. Please note that due to the way the correlator enters Eq. (3.20a), Φ actually depends on two times. Whereas in the other variables the time dependence is restricted to the second argument, the integration runs over the first time variable of the correlator derivative.

3.1.2 Memory handling

During the simulation, the next time step is set by the LB model. In fact, *only* the next time step is fixed, yet there is no need to use a constant discretization to sample all past times. By successively increasing the discretization of the memory back in time, we can utilize the advantages offered by a non-constant time step in a linearly processing algorithm. To do so, we divide our memory in B blocks with C cells each. The discretization step δt doubles with each block and the top block is chosen to have the smallest time step set by

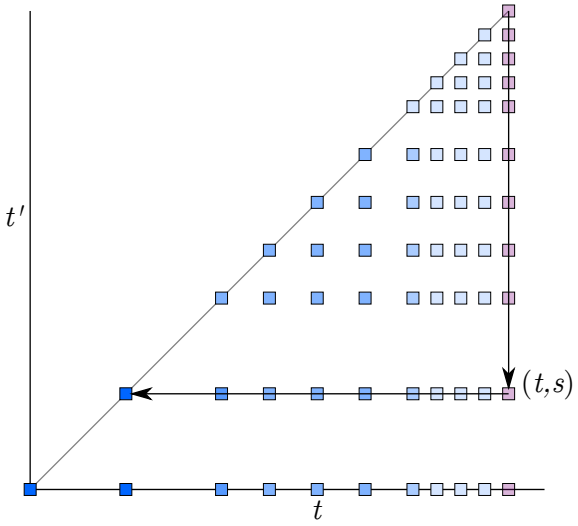

Figure 3.2: Two dimensional, quasi-logarithmic memory grid used for the correlator Φ. For each entry (t, s), the time is discretized in t and t' direction with the spacing. With each LB step a new correlator (purple) has to be added by successively moving from $(t, t' = t)$ downwards to $(t, t' = 0)$. The layout of the memory grid ensures that the most recent flow history is sampled with the highest precision. For a better visibility, the maximum number of cells per block is set to only $C = 4$. The color saturation indicates the grid spacing and is taken up again in Fig. 3.3.

the LB model

$$\delta t_{\mathrm{LB}} = \delta t_B = \tfrac{1}{2}\, \delta t_{B-1}. \tag{3.21}$$

This works fine for the strain rate, the memory and especially well for the deformation tensor. While the simulation is running, the memory will continuously be filled. When a block is fully occupied, the two oldest entries will be merged and moved to the next block with a larger time step. The strain rate and memory will be averaged, and we have to give up some precision. However, since we do not to save $\boldsymbol{E}(t, t')$ itself but its discrete contributions $\exp(\boldsymbol{\kappa}\delta t)$, we just have to carry out the multiplication and lose no information whatsoever:

$$\boldsymbol{E}(t, t') = \mathrm{e}^{\boldsymbol{\kappa}(t-\delta t_B)\delta t_B} \ldots \underbrace{\mathrm{e}^{\boldsymbol{\kappa}(t-(C-1)\delta t_B)\delta t_B} \mathrm{e}^{\boldsymbol{\kappa}(t-C\delta t_B)\delta t_B}}_{=\mathrm{e}^{\boldsymbol{\kappa}\delta t_{B-1}}} \ldots \mathrm{e}^{\boldsymbol{\kappa}(t')\delta t_{B-X}}. \tag{3.22}$$

2D memory layout and decimation scheme

Considering the correlation function, the situation is slightly more complicated due to the way Φ enters the integral (3.20), and the full two-times dependence of the problem comes into light. We have to construct a two dimensional version of the blocked quasi-logarithmic grid. To avoid nasty interpolation issues, we need to ensure that for each point (t, s) the discretization is the same, both in $-t$ and in $-t'$ direction, cf. Fig. 3.2. As the number of cells in a block are limited, the necessity of a decimation process to free space again becomes immediately obvious.

Fig. 3.3 illustrates the main principle of the scheme we apply. Every time the top block with the smallest time step is completely filled, we check the next blocks for free space. Moving downwards, the decimation scheme will start at the last filled block in a row. Later blocks may still be completely filled as long as the next one has some space left. In both time directions, the last two entries in each block are then mapped onto a single one in the next block. One can think of many ways how this mapping can be achieved. Yet in most cases, the outcome depends only slightly on the actual choice of implementation.

We achieve the best results when simply keeping the higher value of smaller times and discarding the other one. The reasoning is that the influence of a too large correlator is relatively small, but a slightly smaller value may result in a much too fast decay. This is especially true in the glass, where the correlator will take a constant plateau value for all times. However, once the correlator drops below this value, it will always decay to zero. Therefore, it is essential not to choose a too small estimate for Φ and we like being save more than being sorry.

There is one exception to the rule. In theory all diagonal elements $t = t'$ equal one. For blocks with large time steps, the next element may be much smaller. This does affect the computation of the time derivative $\partial_s \Phi(s, t')$ quite heavily and it proves advantageous to average over the neighboring Φ, thereby allowing the diagonal elements to take smaller values.

3.1.3 Discrete schematic model

Having found a suitable memory we now derive an appropriate discrete formulation of the constitutive equation. Considering the layout of our memory the integral has to become a sum running over all entries j in each block b

$$j = (b-1)C + c_b, \tag{3.23}$$

with $0 < b \leq B$ and $0 \leq c_b < C(b)$, where $C(b)$ is the number of occupied cells in block b. May i be the last occupied column of the correlator Φ corresponding to the time t, then (3.18) becomes

$$\boldsymbol{\sigma}_i = \nu_\sigma \sum_j \delta t_b \left[\boldsymbol{E}_j \boldsymbol{\kappa}_j \boldsymbol{E}_j^\intercal + (\boldsymbol{E}_j \boldsymbol{\kappa}_j \boldsymbol{E}_j^\intercal)^\intercal \right] \Phi_{i,j}^2, \quad \text{with} \tag{3.24}$$

$$\boldsymbol{E}_j = \prod_{j'=i,\ldots,j} \exp(\boldsymbol{\kappa}_{j'} \delta t_b). \tag{3.25}$$

Let us take a look at the correlator (3.20) next. For each time step, we have to successively solve the integro-differential equation starting at the diagonal $(t, t' = t)$. Fig. 3.2 shows the memory layout of the correlator. The purple column represents the new correlator which is added at time t. We start at the diagonal $(t, t' = t)$, and the next value one is easily computed

$$\Phi_{i,i-1} = 1 - \Gamma \delta t_{\mathrm{LB}}. \tag{3.26}$$

When going on the algorithm moves down the purple column, subsequently computing the correlator from the previous Φ values in horizontal t' and M values in vertical t direction as indicated by the arrows. Special care has to be taken of the time derivative of Φ. We apply 3-stencil Lagrange polymers to approximate $\partial_s \Phi$. If the abscissae are equally spaced, this is identical to a second order finite difference scheme. However, at $t = t'$ or $i = j$, respectively, only backward differentiation is possible, and the discretization is nonuniform at the last

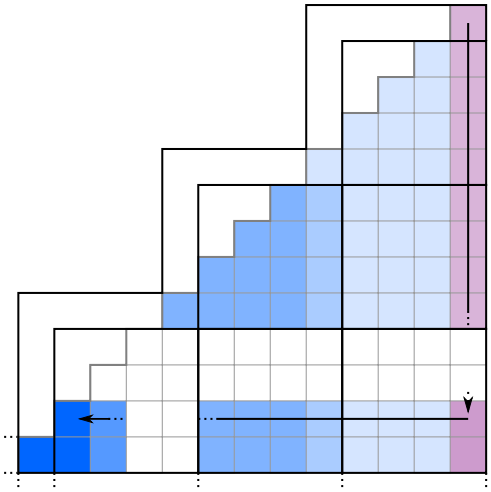

(a) The same correlator as in Fig. 3.2 is depicted as it appears in the 2d memory layout. The color coding is the same as before, a higher saturation indicates a more coarse grid. White boxes are not in use. N.b., when computing the derivative of the correlator along the arrow in horizontal direction, the stencils are not equally spaced at the rightmost entry.

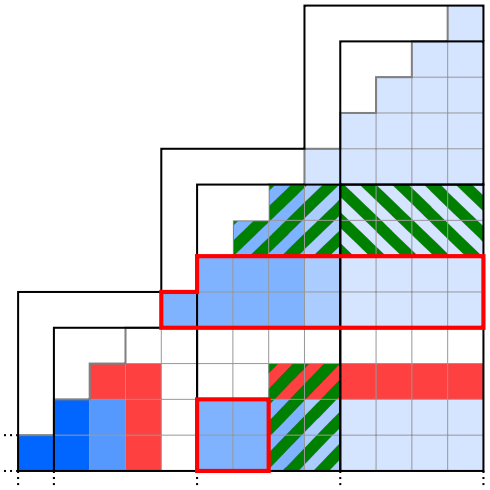

(b) Second to last decimation step. The decimation had to start with the last consecutive filled block so that new columns may be added. The red lined cells will be mapped onto the red colored boxes in the adjoined blocks. Afterwards, the freed space will be used to move the purple striped boxes down to the lower left end of the block.

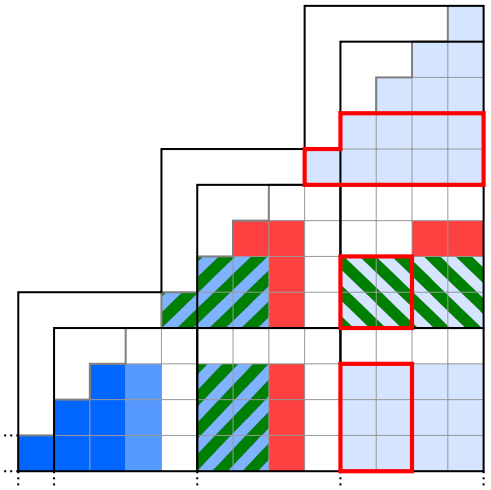

(c) Last decimation step. The green striped boxes in (3.3b) have been moved. Again, the cells to be decimated are marked in red.

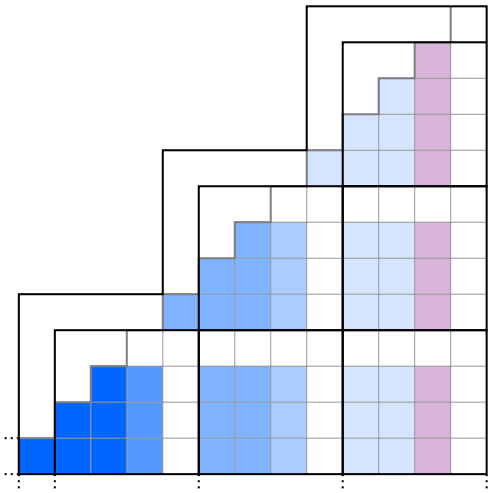

(d) The decimation is complete and a new (purple) column is computed. Decimation to some degree will have to be performed every second time step.

Figure 3.3: 2d memory of the correlator and the decimation scheme in action. In Fig. (3.3a) the last free column has been filled. Before the correlator of the next time step can be computed, some memory has to be freed. Fig. (3.3b) and (3.3c) show a cartoon of the last two steps of the decimation progress.
The coarse-grained staircase-like outer structure depicts the memory which is actually allocated by the simulation, and is the result of a compromise between computation speed and memory demand. This way, whole columns can be swapped in each block, which proves useful since every other step the memory will have to be rearranged during a decimation step.

entry of a block. Eq. (3.20a) becomes

$$
\begin{aligned}
0 = &\underbrace{\frac{1}{\Gamma \delta t_{\mathrm{LB}}}\left(\frac{3}{2}\Phi_{i,j} - 2\Phi_{i-1,j} + \frac{1}{2}\Phi_{i-2,j}\right)}_{\text{backwards Lagrange}} + \Phi_{i,j} + \underbrace{h_{i,j} M_{i,j}\left(1 - \Phi_{j,j}\right)}_{k=j} \\
&+ \frac{1}{2} h_{i,j} \sum_{k=j+1}^{i-2} M_{i,k} \begin{cases} \left(\Phi_{k+1,j} - \Phi_{k-1,j}\right) & \text{if no block change} \\ \left(\frac{8}{3}\Phi_{k+1,j} - 2\Phi_{k,j} - \frac{2}{3}\Phi_{k-1,j}\right) & \Phi_{k-1,j} \in \text{next block} \end{cases} \\
&+ \underbrace{h_{i,j} M_{i,i-1} \frac{1}{2}\left(\Phi_{i,j} - \Phi_{i-2,j}\right)}_{k=i-1,\text{ central Lagrange}} + \underbrace{h_{i,j} M_{i,i}\left(\frac{3}{2}\Phi_{i,j} - 2\Phi_{i-1,j} + \frac{1}{2}\Phi_{i-2,j}\right)}_{k=i,\text{ backwards Lagrange}}.
\end{aligned}
\tag{3.27}
$$

This gives us an expression for the next $\Phi_{i,j}$, which is only just a function of known values:

$$
\begin{aligned}
\Phi_{i,j} = \Big[&4\Phi_{i-1,j}\left(\Gamma^{-1} + \delta t_{\mathrm{LB}} h_{i,j} M_{i,i}\right) - \Phi_{i-2,j}\left(\Gamma^{-1} + \delta t_{\mathrm{LB}} h_{i,j}\left(M_{i,i} - M_{i,i-1}\right)\right) \\
&- \delta t_{\mathrm{LB}} h_{i,j} \sum_{k=j+1}^{i-2} M_{i,k} \begin{cases} \left(\Phi_{k+1,j} - \Phi_{k-1,j}\right) & \text{if no block change} \\ \left(\frac{8}{3}\Phi_{k+1,j} - 2\Phi_{k,j} - \frac{2}{3}\Phi_{k-1,j}\right) & \Phi_{k-1,j} \in \text{next block} \end{cases} \\
&- 2\delta t_{\mathrm{LB}} h_{i,j} M_{i,j}\left(1 - \Phi_{j,j}\right)\Big] \frac{1}{N},
\end{aligned}
\tag{3.28}
$$

with

$$
N = 3\Gamma^{-1} + 2\delta t_{\mathrm{LB}} + \delta t_{\mathrm{LB}} h_{i,j}\left(3M_{i,i} + M_{i,i-1}\right).
$$

There is one hidden dependence on $\Phi_{i,j}$ left in the memory function, cf. Eq. (3.20b). For $\nu_2 \neq 0$, Eq. (3.28) is a quadratic function in $\Phi_{i,j}$ we could in principle solve analytically. However, numerical errors in the computation of the square root may accidentally cause the correlator to decay. Therefore, we choose a starting value for $\Phi_{i,j}$ and solve the equation iteratively. But again, the small time step δt_{LB} plays in our hands: We can start with a good estimator, $\Phi_{i,j} = \frac{1}{2}(\Phi_{i-1,j} + \Phi_{i,j+1})$, and it takes the iteration only a few steps to converge.

Fine-tuning and comparison

The steady state profile of a Poiseuille channel flow is symmetric in flow direction and the strain rate tensor is zero in all but one component. To test the linear two-time MCT solver, we consider a constant shear rate $\kappa_{xy} = \dot{\gamma}$ and zero, else. Since the shear rate has no time dependence, the correlator and memory become functions of the time difference $(t - t')$ only. The time evolution of the correlator, cf. Eq. (3.16a), is then described by the much simpler equation

$$
\dot{\Phi}(t - t') + \Gamma\left(\Phi(t - t') + \int_0^{t-t'} \mathrm{d}s\; M(t - s)\dot{\Phi}(s)\right) = 0. \tag{3.29}
$$

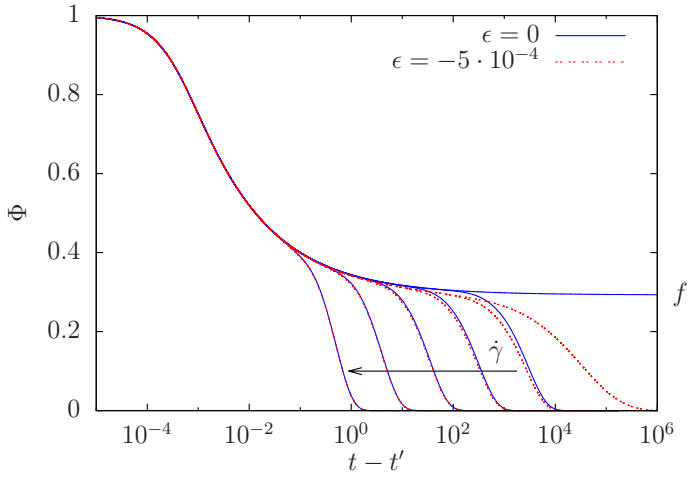

Figure 3.4: Correlator Φ in the glass, $\epsilon = 0$ (blue), and close to the glass transition in the fluid phase, $\epsilon = -5 \cdot 10^{-4}$ (red), under steady shear rate $\kappa_{xy} = \dot{\gamma} = \{0, 10^{-5}, 10^{-4}, ..., 10^{-1}\}$. We set the initial decay rate $\Gamma = 500\text{s}^{-1}$ and the critical strain $\gamma_c = 0.1$. For $\epsilon = 0$ and $\dot{\gamma} = 0$, the correlator decays to a plateau value f and remains there for all times.

The constant shear rate allows the use of an exponentially increasing time step which has been employed before [17]. Fig. 3.4 illustrates the typical features of the glass-forming fluids and shows the effect of shear on the correlator. We consider correlators in the glass limit $\epsilon = 0$ (blue) and in the fluid phase $\epsilon = -5 \cdot 10^{-4}$ (red). The density correlation functions always share the same initial decay set by Γ. For the second decay, there are two different mechanisms at work. In the fluid phase $\epsilon < 0$, the correlator will always decay to zero with a stretched exponential (right-most red line) but the time diverges as the fluid approaches the glass limit $\epsilon = 0$. The blue curve only decays to the plateau value f and remains there for all times. Since the stress is proportional to the integral over Φ, the glass can sustain stresses even in absence of shear. If an external shear flow is applied, correlations are destroyed and Φ decays on a time scale set by the shear rate. The curves fall on top of each other as the glass is molten by the shear.

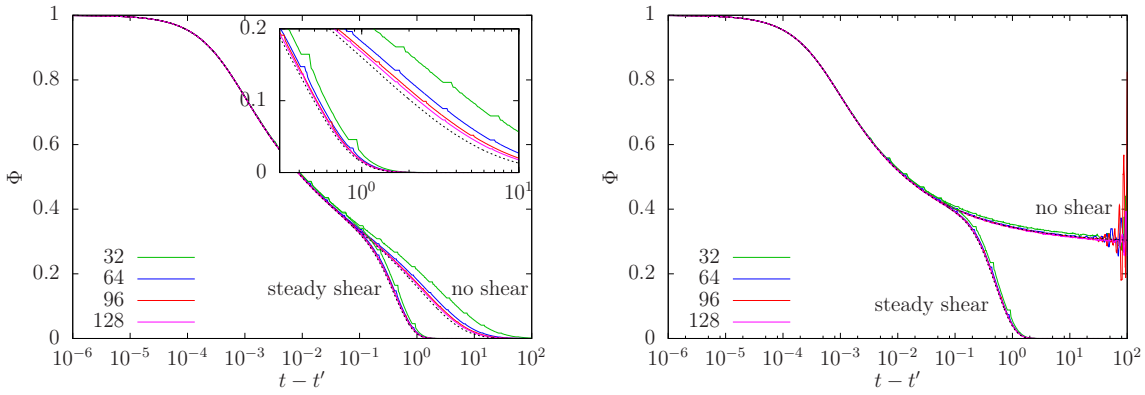

Figure 3.5: Correlator under steady shear $\kappa_{xy} = 0.1\text{s}^{-1}$ and no shear for a fluid (left), $\epsilon = -3.5 \cdot 10^{-2}$, and in the glass limit (right), $\epsilon = 0$. The colored lines show the results of the two-time algorithm for different block sizes B, $\Gamma = 500\text{s}^{-1}$, $\gamma_c = 0.1$. The dashed line is computed using the 1-time algorithm.

Obviously, in this special scenario, the linear two-time algorithm is not the best-adopted algorithm by a long shot making this a hard test to pass. The problems we will run into give an impression of what artifacts and shortcomings we may encounter and have to keep

in mind when interpreting the LB results. As it turns out, the algorithm experiences some heavy oscillations at the beginning of a new block. These are a result of the Lagrange interpolation employed to approximate the derivate, cf. Runge's phenomenon, and seriously affect the stability of the algorithm.

We counter this effect with two means. First, choosing a sufficient large block size gives the oscillations time to decay. Second, as we expect the correlator to decrease, we will discard a value at the beginning of a block if it is larger than the previous one, and keep the first four entries constant. This, of course, requires the block to be large enough. Fig. 3.5 compares the results of the two-time algorithm using a constant time step with the reference correlator obtained with a one-time algorithm and an increasing time step. We consider steady shear and no-shear scenarios for $\epsilon = 0$ and $\epsilon = -3.5 \cdot 10^{-2}$, which we later use for the LB simulations. A block size of $B = 32$ is sufficient for stable results if the correlator decays to zero fast enough. For a better quantitative agreement, at least $B = 64$ cells are needed, cf. Fig. 3.5. In the glass limit $\epsilon = 0$, the correlator decays only to a plateau value and for long times the two-time algorithm becomes unstable. However, this does not present a problem as the maximum change in stress the LB simulation can handle sets a much earlier limit.

3.2 Non-linear Maxwell model

The derivation from first principles makes the schematic MCT model a unique and fascinating constitutive equation. However, it is not what one would call a sleek model, and the computational demand is high, both in the number of challenges to overcome before it can be fitted into a LB code and also in the raw computational power needed. The by far biggest effort stems from the correlator $\Phi(t, t')$ which has to be computed successively each time step and is a function of two time arguments.

In continuum mechanics, the Maxwell model is well established for describing viscoelasticity [9]. A purely viscous damper and an ideal elastic spring are connected in series. Under strain, the stress response of the system is elastic on short times and will exponentially relax on a long time scale. We capitalize on this result and discard any dependences on the correlator to approximate the shear modulus Eq. (3.15) with a simple exponential

$$G(t, t') = G_\infty \mathrm{e}^{-(t-t')/\tau_\mathrm{M}}. \tag{3.30}$$

For a constant relaxation time τ_M this is just the Maxwell model and describes the slow relaxation from the plateau modulus G_∞ as an exponential decay approximating the stretched exponential seen in Fig. 3.4. There is a second, fast relaxation to this plateau on a time scale $\tau_0 = \Gamma^{-1}$ which amounts to a Newtonian background viscosity $\eta_\infty = G_\infty \tau_0$ we will handle separately. The ratio between the initial modulus and the plateau modulus is proportional to the square of the plateau value $f^2 \approx 1/10$, which agrees well with findings for hard sphere-like systems [37]. The correlator decays faster in presence of shear, see Fig. 3.4. To mimic the shear induced acceleration of the dynamics, we set

$$\tau_\mathrm{M}^{-1} = \tau^{-1} + \frac{\sqrt{II_{\boldsymbol{D}}}}{\gamma_\mathrm{c}}, \tag{3.31}$$

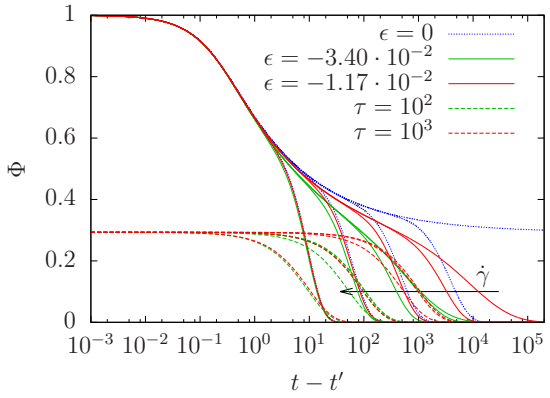

(a) The correlator and the non-linear Maxwell exponential under steady shear $\dot\gamma = 0, 10^{-5}, 10^{-4}, 10^{-3}, 10^{-2}$.

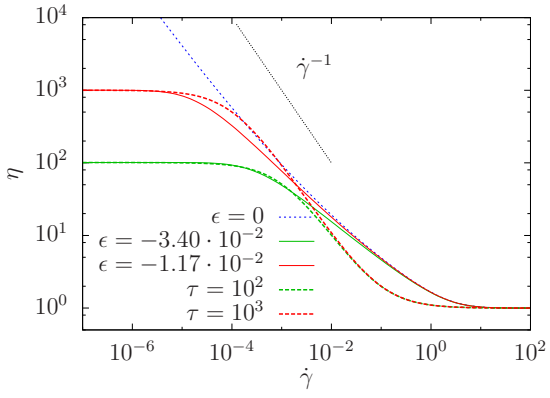

(b) Flow curve of the schem. MCT model and the non-linear Maxwell model.

Figure 3.6: Comparison of the non-linear Maxwell and the schematic MCT model with $\Gamma = \tau_0^{-1} = 1\mathrm{s}^{-1}$ and $\nu_\sigma = 2G_\infty = 2\mathrm{Pa}$. The distance to the glass transition ϵ has been chosen to give the same change in viscosity. The results of the schem. MCT model are obtained using the single-time algorithm.

where $II_{\boldsymbol{D}} = \frac{1}{2}\boldsymbol{D} : \boldsymbol{D} = \frac{1}{2}\operatorname{tr}\boldsymbol{D}^2$ is the second invariant of the symmetric velocity gradient tensor $\boldsymbol{D} = \boldsymbol{\kappa} + \boldsymbol{\kappa}^\intercal$ and a typical choice for a generalized strain rate in fluid mechanics. This yields the constitutive equation for the tensorial non-linear Maxwell model (nlM) [96]

$$\boldsymbol{\sigma}(t) = \eta_\infty \boldsymbol{D}(t) + \int_{-\infty}^{t} \mathrm{d}t' \left[\frac{\partial}{\partial t'}\boldsymbol{B}(t,t')\right] G_\infty \mathrm{e}^{-(t-t')/\tau_\mathrm{M}(t')}. \tag{3.32}$$

Although the model is radically simplified, the first part of the integrand remains unchanged and it still features the dependence on the accumulated strain and the tensorial structure of the full model. As we have stayed true to the integral formulation, the model accounts for memory effects contrary to simple differential constitutive equations commonly used. Please note, the time argument of τ_M is t' rather than t, and both parts of the integrand are in fact subject to the strain history. The model stays true to the (t, t')-dependence of the full MCT model as the generalized Maxwell time is a function of $\dot\gamma(t')$, which is sufficient to capture MCT effects, for example in creep flow and large amplitude oscillatory shear [85, 96].

To illustrate the effect of replacing the correlator with an exponential, we consider a steady shear flow $\kappa_{xy} = \dot\gamma$. The derivative of the Finger tensor simplifies to $\dot\gamma$, and we can use the single-time MCT algorithm. Fig. 3.6a shows the evolution of one correlator in the glass ($\varepsilon = 0$) and two in the fluid phase ($\varepsilon < 0$) for different shear rates. The distance to the glass transition determines a time scale on which correlations have to decay. In the glass, correlations may survive for all times and the correlator decays to constant plateau value, but for a fluid correlations will always vanish for long times. If shear is applied, the correlator can decay on time scale set by the shear rate, even for $\varepsilon = 0$. In the non-linear Maxwell model, the decay from the plateau is replaced with an exponential. There is a principle difference in the way both models are implemented. For the schem. MCT model, the initial decay $\exp(-(t-t')\Gamma)$ introduces a lower bound. The correlations

cannot decay faster, which gives rise to a minimum viscosity. In the non-linear Maxwell model, this viscosity minimum is captured by a constant term outside the integral. We, therefore, can only compare the shape of the decay from the plateau, but not the position in time. For both models, we find similar shear-induced decays of the correlator. In the fluid phase and under no shear, the decay of the non-linear Maxwell model is again an exponential, $\exp(-(t-t')/\tau)$, while in the schematic MCT model, the correlator relaxes more slowly. The lack of an initial decay makes the non-linear Maxwell model appear cruder than it actually is. Fig. 3.6b shows the viscosity as a function of the strain rate for both models, and both flow curves are quite similar. The agreement is even better closer to the glass transition. Both models show a viscosity drop proportional to $\dot{\gamma}^{-1}$ in the glass limit. This shear thinning coefficient does not change for the non-linear Maxwell model, yet for the schem. MCT model the slope is less steep in absence of a pronounced plateau in the correlator. For the dynamics of a fluid, the flow curve is most important. The good agreement of both models in this quantity, vindicates the approximation and is promising for the non-linear Maxwell model.

On a side-note: If necessary one can easily lose the tensorial structure of the model and derive a scalar version of the non-linear Maxwell model,

$$\sigma_{xy}(t) = \eta_\infty D_{xy}(t) + \int_{-\infty}^{t} \mathrm{d}t' \ \mathrm{sgn}(D_{xy}(t))\sqrt{II_{\boldsymbol{D}}(t')}\, G_\infty \mathrm{e}^{(t-t')/\tau_\mathrm{M}(t')}. \tag{3.33}$$

Last, we simplify the non-linear Maxwell model even more and derive a constitutive equation which only depends on the instantaneous shear rate at time t. Taking the time derivative of Eq. (3.32) yields

$$\dot{\boldsymbol{\sigma}}(t) - \boldsymbol{\kappa}(t)\boldsymbol{\sigma}(t) - \boldsymbol{\sigma}(t)\boldsymbol{\kappa}^\intercal(t) + (\boldsymbol{u}\cdot\boldsymbol{\partial})\boldsymbol{\sigma}(t) = \boldsymbol{D}(t)G_\infty - \boldsymbol{\sigma}(t)/\tau_\mathrm{M}(t) \tag{3.34}$$

The left side of the equation is the upper convected derivative. In symmetric geometries like a straight channel the advected stress term does not contribute, $(\boldsymbol{u}\cdot\boldsymbol{\partial})\boldsymbol{\sigma}(t) = 0$. Eq. (3.34) then has the formal steady state $\dot{\boldsymbol{\sigma}} = 0$ solution

$$\boldsymbol{\sigma}(t) = \eta_\infty \boldsymbol{D}(t) + \sum_{n\geq 1} G_\infty \tau_\mathrm{M}(t)^n \boldsymbol{d}(t)^n \tag{3.35a}$$

with

$$\boldsymbol{d}^n(t) = \sum_{m=0}^{n} \binom{n}{m} \boldsymbol{\kappa}(t)^m \boldsymbol{\kappa}^\intercal(t)^{n-m}. \tag{3.35b}$$

For general flow geometries the infinite sum in Eq. (3.35a) is not guaranteed to converge. Yet for a simple shear flow, $\kappa_{xy}(t) = \dot{\gamma}$ and zero else, we find $\boldsymbol{\kappa}^2 = 0$ and all terms for $n > 2$ to vanish. For an incompressible fluid in an infinite channel, the symmetry of the geometry prevents the appearance of secondary flows at low Reynolds numbers. In $D = 2$ dimensions, the strain rate tensor varies only in one transversal flow direction, and we only need to carry the first two terms of the sum. The instantaneous non-linear Maxwell (inlM) model used in later simulations refers to Eq. (3.35) with $n = 1, 2$ only. Two non-zero stress

elements remain, a shear stress

$$\sigma_{xy}(t) = \eta_\infty \dot{\gamma}(t) + G_\infty \tau_\mathrm{M}(t) \dot{\gamma}(t) \tag{3.36a}$$

and a normal stress

$$\sigma_{xx}(t) = 2 G_\infty \tau_\mathrm{M}(t)^2 \dot{\gamma}(t)^2. \tag{3.36b}$$

We then expect from the model a first normal stress difference

$$\mathcal{N}_1(t) = \sigma_{xx}(t) - \sigma_{yy}(t) = \sigma_{xx}(t) = 2 G_\infty \tau_\mathrm{M}(t)^2 \dot{\gamma}(t)^2 \tag{3.36c}$$

and a change in pressure by

$$\delta p(t) = -\frac{1}{D} \operatorname{tr} \boldsymbol{\sigma}(t) = -\frac{1}{D} \sigma_{xx}(t) = -\frac{2}{D} G_\infty \tau_\mathrm{M}(t)^2 \dot{\gamma}(t)^2. \tag{3.36d}$$

The dependence on a time t is meant in the way that at each LB step the non-linear Maxwell time τ_M as a function of the current strain rate $\boldsymbol{\kappa}(t)$ will be calculated anew. Obviously, the transient flow will differ from the full nlM model as the stress in Eq. (3.35) adjust instantly to a change in flow. Memory effects are lost, but both models give the same steady state flow.

The normal stresses first enter the model at second order in compliance with MCT predictions. If we restrict the model to its first summand, we arrive at the scalar version of the instantaneous non-linear Maxwell model already proposed in [37]. This model provides an interesting playground and an important cross-check for the proposed LB algorithm in Chap. 2 as we can find an analytic solution of the velocity profile for a pressure driven channel flow, cf. Chap. 4.2.1.

Certainly, due to the long way of ever-accumulating approximations in this chapter, arriving at this model may give a misleading impression of triviality. However, this model is much more refined than commonly chosen constitutive equations, such as the power-law model. The non-linear Maxwell model does provide a physical motivation and reproduces the most central aspects of MCT. Even from a pure end-user's point of view, this model is advantageous to several ad-hoc equations, as it already provides all the necessary time scales, and presents an upper and lower bound for the viscosity, thereby increasing the stability of a simulation.

Conclusion

The schematic MCT model is derived from first principles and much more refined than the Maxwell model. However, because it still incorporates much of the microscopic details, it is restricted in its range of application. The non-linear Maxwell model presents a good compromise between usefulness and amount of detail. By approximating the decay of the correlator with an exponential, the dynamics is freed of an integro-differential equation at the expense of leaving behind the two-time dependence of the correlator and of loosing the connection to the microscopic world. Having said that, some calculations are only made possible by having simplified the model. The price we pay is less steep than it appears at

first as the non-linear Maxwell model is build to mimic the physics of a glassy fluid and incorporates the most important features of the sMCT qualitatively. Because approximating the correlator decay with an exponential works best if the correlator has a broad plateau, the nlM model tends to overstate the glass limit. This is not categorically a bad thing and even serves our purpose at some points since already moderate relaxation times τ make the fluid behave very glass-like.

There exists a multitude of Maxwell-type models and different spring-damper constitutive equations are commonly applied in biophysics [3, 81]. We could consider using distributions of τ, cf. Maxwell-Wiechert or generalized Maxwell model, but this does not change the qualitative behavior of the model. As these models have more adjustable parameters, they provide a better quantitative agreement to experiments, but it is the non-linear Maxwell model that arises naturally out of mode coupling theory.

The instantaneous non-linear Maxwell (inlM) model is certainly a very interesting constitutive equation as it gives the same steady state results as the non-linear model. The stress can adjust instantly to a change in flow and the model is similar to other frequently used non-Newtonian constitutive equations such as the power-law model [10, 100, 104]. But different to these models, inlM model inherits the tensorial structure of the schematic MCT model and normal stresses arise. We will compare the transient and steady state profiles of all three models in a pressure-driven channel flow. It will be very interesting to see how much of the information about the microscopic structure of the fluid is actually relevant for the macroscopic flow.

4 Channel flow of non-Newtonian fluids: Lattice Boltzmann simulations

Having derived both various non-Newtonian constitutive equations and a Lattice Boltzmann algorithm to handle those, we now complete the puzzle and combine the parts to study pressure-driven channel flow problems. For the simulation, some basic code of the open-source Palabos[1] project was used. In Chap. 3 we have started from first principles and successively devised more and more simplified constitutive equations. Here, in Sec. 4.2, we start from the opposite end and begin with the most simple constitutive equation, the scalar instantaneous non-linear Maxwell model (scalar inlM). The steady state Poiseuille flow profile is analytically accessible, cf. Sec. 4.2.1, and presents us a powerful tool to check the accuracy of the simulation. When moving on to the tensorial instantaneous non-linear Maxwell model (inlM), we find it to reproduce the previous results. This is fine as the scalar model can be understood as the limiting case of the tensorial one with an additional, reasonable constraint of an incompressible flow, $\mathrm{tr}\,\boldsymbol{\kappa} = 0$. The tensorial model is the first to give rise to non-Newtonian normal stresses, which we find intimately connected to the problem of pressure advection. We use this opportunity to illustrate the aforementioned strategies to implement pressure gradients, Sec. 2.3.3, and point out the differences.

Next, we implement in Sec. 4.3 the integral formulated non-linear Maxwell model (nlM), which depends on the full flow history instead of only the instantaneous shear rate. As presumed, the steady state profile remains unchanged, yet the transient behavior is very much affected by new memory effects. The velocity profile now sports over- and undershoots as the stress evolves on a separate time scale from the flow.

Last, we demonstrate in Sec. 4.4 how to embed the full schematic MCT model in a Lattice Boltzmann simulation. This paves a way to apply mode coupling theory, if in a simplified version, to arbitrary time-dependent flow problems for the first time. Using the mesoscopic LB model as a link between the microscopic, first-principle MCT and a macroscopic flow geometry opens new fields of application and promises a better understanding of non-Newtonian effects.

4.1 Simulation setup

We consider a 2-dimensional straight channel in x-direction with a constant width $2H$, cf. Fig. 4.1. The origin is coincidents with the symmetry axis and we choose no-slip boundary conditions for the walls $u(\pm H) = 0$, where u is the velocity component in flow direction. In the LB simulation, the walls are implemented as bounce-back nodes. We do not want to study in- and outlet effects of the flow for now, but assume the channel to be infinitely long and only define a pressure gradient $(-\Delta p/L, 0)^\intercal$ to drive the fluid. At the start, $t = 0$,

[1] Palabos V1.1r0, www.palabos.org

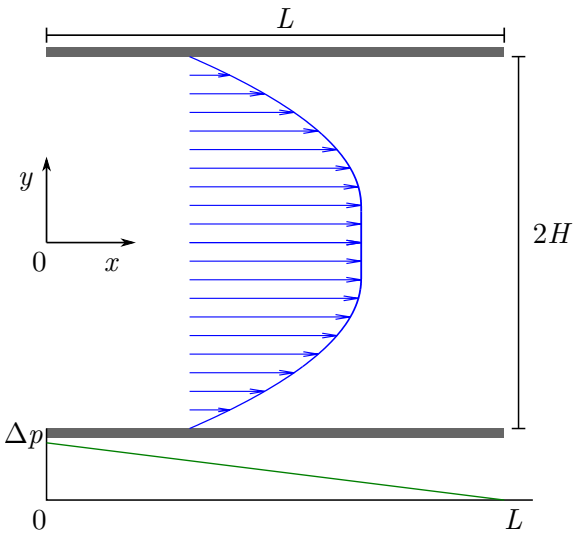

Figure 4.1: Schematic plot of the flow geometry. We consider a 2-dimensional straight channel with a constant diameter $2H$. The fluid is driven by a pressure drop Δp on a length L in x-direction, resulting in a constant pressure gradient $(-\Delta p/L, 0)^\intercal$. Due to the channel symmetry, the flow velocity $\boldsymbol{v} = (u(y), 0)^\intercal$ is only a function of the distance from the symmetry axis, which we choose as the x-axis. The walls of the channel are modeled with no-slip boundary conditions $u(\pm H) = 0$. In x-direction periodic boundaries are applied. The pressure step is either implemented via generalized periodic b.c., cf. Sec. 2.2.1, or a constant effective body-force is used.

the fluid is at rest and the pressure is instantly switched on. The simulation uses a periodic lattice and either an effective body-force to account for the pressure drop, or generalized periodic boundary conditions (gpbc), cf. Sec. 2.2.1 and citations there. In the latter case, the simulations are initialized with a pressure gradient. Doing otherwise would cause shock waves which the LB model describing incompressible fluids at small Ma numbers is unable to handle. This does not render the simulation unstable, but for very small times the fluid velocity would show small oscillations.

The LB time step is directly linked to the unmodified Newtonian (reference) viscosity. The time step becomes smaller for larger viscosities. For all simulations the single non-dimensional relaxation time $\tau_{\mathrm{LB}} = 0.9$ is used, which for a Newtonian fluid is found to be close to the optimum reducing the error in the shear stress [62, 63]. The non-Newtonian stresses given by the constitutive equations depend sensitively on the strain-rate. To ensure a sufficient precision, we always take the maximum viscosity of the model as the reference value. The additional body-force term in the LB algorithm then is used to *reduce* the shear stress, but takes care of the full normal stress components on its own.

4.2 Instantaneous non-linear Maxwell model without memory

4.2.1 Analytic steady state profile of the scalar model

We consider the scalar non-linear Maxwell model (cf. Eq. (3.35) with $n = 1$ only) first. For small Reynolds numbers, the channel flow remains laminar and the fluid velocity $\boldsymbol{v} = (u(y), 0)^\intercal$ is only a function of the distance to the symmetry axis y. The Navier-Stokes equation is simplified significantly and the flow is described by a single partial differential equation

$$\partial_t \left(\rho u(y,t)\right) = \frac{\Delta p}{L} + \partial_y \left(G_\infty \left(\tau_0 + \frac{\tau}{1 + \tau \left| \frac{\partial}{\partial_y} u(y,t) \right| / \dot{\gamma}_c} \right) \partial_y u(y,t) \right). \tag{4.1}$$

Introducing the ratio $h = H/L$ and the dimensionless units for length $d = y/H$, time $s = t/\tau_0$, and pressure $p = \Delta p/G_\infty$, Eq. (4.1) becomes

$$\partial_s \left(\frac{\mathrm{Re}}{4} w(d,s) \right) = \frac{hp}{2} + \partial_d \left(\left(1 + \frac{\theta}{1 + 2\theta \left| \partial_d w(d,s) \right| / \gamma_\mathrm{c}} \right) \partial_d w(d,s) \right), \tag{4.2}$$

where we have defined the Reynolds number $\mathrm{Re} = \frac{LL/\tau_0}{\eta/\rho}$ and the dimensionless velocity $w(d,s) = u(y,t)\frac{\tau_0}{2H}$. Eq. (4.2) has no analytic solution, but can be solved numerically [83].

In the long time limit, the fluid reaches a steady state $\lim_{s\to\infty} w(d,s) = w_\mathrm{s}(d)$ and the time derivative on the left hand side vanishes. We then find the shear stress

$$\sigma_{xy} = -\frac{hp}{2} d \tag{4.3}$$

to decrease linearly along the channel diameter. After integrating once with respect to d, the remaining terms are just a simple quadratic equation in the shear rate, for which an analytical solution exists. For $d \geq 0$, the strain rate is negative and we get

$$\frac{\partial}{\partial d} w_\mathrm{s}(d) = \frac{hp}{4} \left[-\left(d - \frac{\gamma_\mathrm{c}}{hp} \frac{\theta+1}{\theta} \right) - \sqrt{\left(d - \frac{\gamma_\mathrm{c}}{hp} \frac{\theta-1}{\theta} \right)^2 + 4 \left(\frac{\gamma_\mathrm{c}}{hp} \right)^2 \frac{1}{\theta}} \right] \tag{4.4}$$

where we have defined the dimensionless shear-thinning parameter $\theta = \tau/\tau_0$. Assuming no-slip boundary conditions at the wall, $w_\mathrm{s}(\pm 1) = 0$, a second integration in d yields the steady state flow profile[2]

$$w_\mathrm{s}(d) = \widetilde{w}_\mathrm{s}(1) - \widetilde{w}_\mathrm{s}(|d|), \tag{4.5}$$

with

$$\begin{aligned} \widetilde{w}_\mathrm{s}(d) = \frac{hp}{8} \Bigg\{ & \left(d - \frac{\gamma_\mathrm{c}}{hp} \frac{\theta+1}{\theta} \right)^2 + \left(d - \frac{\gamma_\mathrm{c}}{hp} \frac{\theta-1}{\theta} \right) \sqrt{\left(d - \frac{\gamma_\mathrm{c}}{hp} \frac{\theta-1}{\theta} \right)^2 + 4 \left(\frac{\gamma_\mathrm{c}}{hp} \right)^2 \frac{1}{\theta}} \\ & + 4 \left(\frac{\gamma_\mathrm{c}}{hp} \right)^2 \frac{1}{\theta} \ln \left[\left(d - \frac{\gamma_\mathrm{c}}{hp} \frac{\theta-1}{\theta} \right) + \sqrt{\left(d - \frac{\gamma_\mathrm{c}}{hp} \frac{\theta-1}{\theta} \right)^2 + 4 \left(\frac{\gamma_\mathrm{c}}{hp} \right)^2 \frac{1}{\theta}} \right] \Bigg\}. \end{aligned}$$

The solution knows two limiting cases. In the Newtonian limit, $\theta \to 0$, the viscosity $\eta = \sigma_{xy}/\dot{\gamma} = \text{const}$ is once again independent of the shear rate $\dot{\gamma}$ and the well-known parabolic velocity profile of a Poiseuille flow is recovered. Increasing the shear-thinning parameter θ allows larger changes in the viscosity, see Fig. 4.2. In the glass limit, $\theta \to \infty$, a finite yield stress remains even for vanishing shear.

The flow profile, cf. Fig. 4.3, is very much affected by the shear-thinning constitutive equation. Since the viscosity decreases under shear, it is advantageous for the fluid to form high-shear regions close to the walls and a no-shear region in the center of the channel. The formation of a plug flow is a characteristic feature of shear-thinning and yield stress

[2] obtained using Mathematica V9.0 from Wolfram Research, Inc.

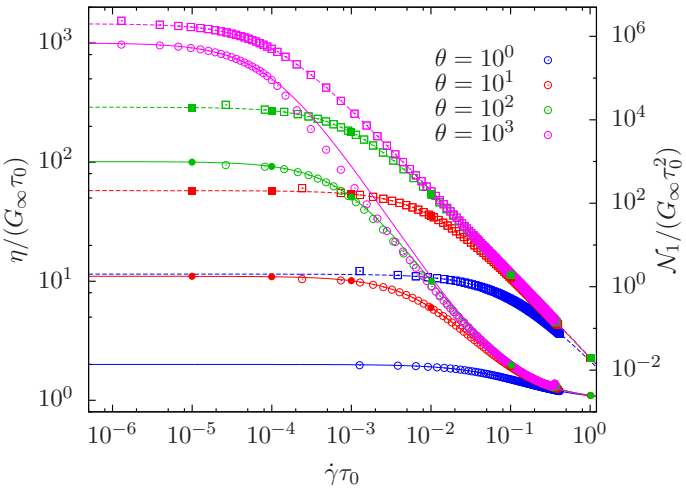

Figure 4.2: Circles give the shear viscosity $\eta = \sigma_{xy}/\dot{\gamma}$ (left axis), squares the first normal stress coefficient $(\sigma_{xx} - \sigma_{yy})/\dot{\gamma}^2$ (right axis) as a function of the local shear rate $\dot{\gamma}$ for different θ. Open symbols are LB results from a pressure-driven channel flows. The filled symbols are obtained in separate simple shear simulations each. Lines are analytic predictions for the instantaneous nonlinear Maxwell model, cf. Eq. (3.36)

fluids [9, 90].

The analytic flow profile gives some valuable insight into the model. If the shear-thinning parameter becomes large, $\theta \gg 1$, a new, critical length $\frac{\gamma_c}{hp}$ emerges. For large θ, the strain rate takes the asymptotic form

$$\frac{\partial}{\partial d} w(d) = \begin{cases} -\frac{hp}{2} \frac{1}{\frac{1}{d} - \frac{hp}{\gamma_c}} \frac{1}{\theta} & d \gtrsim 0 \\ -\frac{hp}{2} \left(d - \frac{\gamma_c}{hp} \right) & d \lesssim 1. \end{cases} \tag{4.6}$$

In the channel center, any shear is suppressed by a factor θ^{-1}, while the strain rate decreases linearly with d near the walls. In the actual glass limit, the steady state profile then becomes

$$w(d) = \begin{cases} \frac{hp}{4} \left(1 - \frac{\gamma_c}{hp} \right)^2 & |d| \leq \frac{\gamma_c}{hp} \\ \frac{hp}{4} \left[\left(1 - \frac{\gamma_c}{hp} \right)^2 - \left(|d| - \frac{\gamma_c}{hp} \right)^2 \right] & 1 \geq |d| \geq \frac{\gamma_c}{hp}. \end{cases} \tag{4.7}$$

This is quite an interesting special case as we find a sharp definition for the plug width. The velocity profile takes the form of two shifted parabolic half-profiles and is constant in the center of the channel up to the critical distance. The glass behaves like a comoving, perfectly solid plug of width $2\frac{\gamma_c}{hp}$ which separates two channels of shear-molten glass. As the actual width is still a function of the dimensionless pressure p, we arrive at another interesting consequence: If the applied pressure is below a threshold $p_{\text{yield}} = \frac{\gamma_c}{h}$, the plug fills the complete width of the channel and no flow is found at all. This emergence of a yield stress has important consequences for the temporal evolution of the flow profile after the driving pressure is removed.

4.2.2 Stationary profiles of the inlM model

For our simulation, we choose a 2-dimensional channel with a constant width $L = 2H = 0.01\text{m}$. The fluid is described by the tensorial instantaneous non-linear Maxwell model (3.35), where we set the elastic modulus $G_\infty = 1\text{Pa}$ and the lower viscosity $\eta_\infty = G_\infty \tau_0 = 1\text{Pa}$. The density $\rho = 1360\text{kg/m}^3$ of the fluid is comparable to honey. The pressure gradient

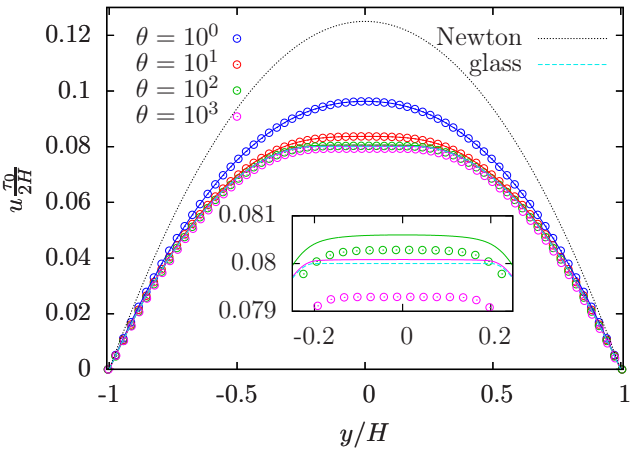

Figure 4.3: Steady state velocity profile for the tensorial non-linear Maxwell model driven by a pressure gradient $\Delta p/(2H) = G_\infty$. The circles are LB results, the lines show the analytic solution obtained from Eq. (4.5). For reference, the analytic flow profile in the glass limit $\theta \to \infty$, Eq. (4.7), and Newtonian limit $\theta \to 0$ are given.

$\Delta p/L = 1\text{Pa}/L$ is of the same order as the elastic modulus, where we expect to find interesting flow behavior. For $\theta \leq 10^2$, a vertical lattice resolution of $N = 200$ nodes is used, respectively $N = 400$ for $\theta = 10^3$.

Since the fluid is incompressible and the flow laminar, the shear rate $\boldsymbol{\kappa}$ has only one non-zero component κ_{xy} and the flow profile of the tensorial inlM fluid does not deviate from the scalar model we solved analytically. Fig. 4.2 shows the rate-dependent shear viscosity $\eta = \sigma_{xy}/\dot\gamma$ and the first normal stress coefficient $(\sigma_{xx} - \sigma_{yy})/\dot\gamma^2$ as a function of the local shear rate $\dot\gamma = \kappa_{xy}$. In the Maxwell model, the slow structural relaxation is captured by the (large) relaxation time τ and yields an increase in the viscosity linear in τ and in the first normal stress coefficient proportional to τ^2 in the limit $\dot\gamma \to 0$. Under shear, a second, shear induced relaxation mechanism opens up. As $\dot\gamma\tau$ approaches the critical strain γ_c, the time scale $1/\dot\gamma$ assumes control of the non-linear Maxwell time $\tau_\text{M} = \left(\tau^{-1} + \dot\gamma/\gamma_\text{c}\right)^{-1}$. The viscosity $\eta(\dot\gamma)$ drops with $\dot\gamma^{-1}$ and provides a trivial shear-thinning exponent -1. For large shear rates, the influence of τ becomes negligible and the viscosity approaches the minimal value $\eta_\infty = G_\infty\tau_0$ we set. In both limits, for large and no shear, the viscosity of the non-linear Maxwell model takes constant but different values. Although in both cases the fluid acts like Newtonian, i.e. independent of the shear rate, large normal stresses appear in the limit $\dot\gamma \to 0$. The channel flow simulations shown in Fig. 4.2 do not cover the full shear rate spectrum, but by increasing the pressure the low viscosity regime becomes accessible, too. We find the steady state LB results to trace the theoretical predictions Eq. (3.36) very well over six orders of magnitude in the shear rate. The quantitative agreement depends on the structural relaxation time τ. For large values, the viscosity depends very sensitively on the shear rate and a higher lattice resolution is needed, cf. Fig. 4.2, $\theta = 10^3$.

Fig. 4.3 compares the velocity profiles to the analytic solution of the strictly incompressible case, Eq. (4.5). For reference, the parabolic Poiseuille flow profile of a Newtonian fluid $\theta \to 0$, $\eta(\dot\gamma) \to \eta_\infty = G_\infty\tau_0$ is added (dotted line). As already discussed, for increasing $\theta = \tau/\tau_0$ the velocity profile forms a plug, trading a wider central low-shear and high-viscosity region for narrower large-shear and low-viscosity flanks. Already for $\theta = 10^2$, the velocity profile and the plug width are close to the glass limit $\theta \to \infty$ (dashed line), see inset and the plug $[-0.2 : 0.2]$ there. Again, we find the LB results to agree very well with the analytical solution. Even for $\theta = 10^3$ the error is less than 1% and can be reduced further by choosing

a higher lattice resolution.

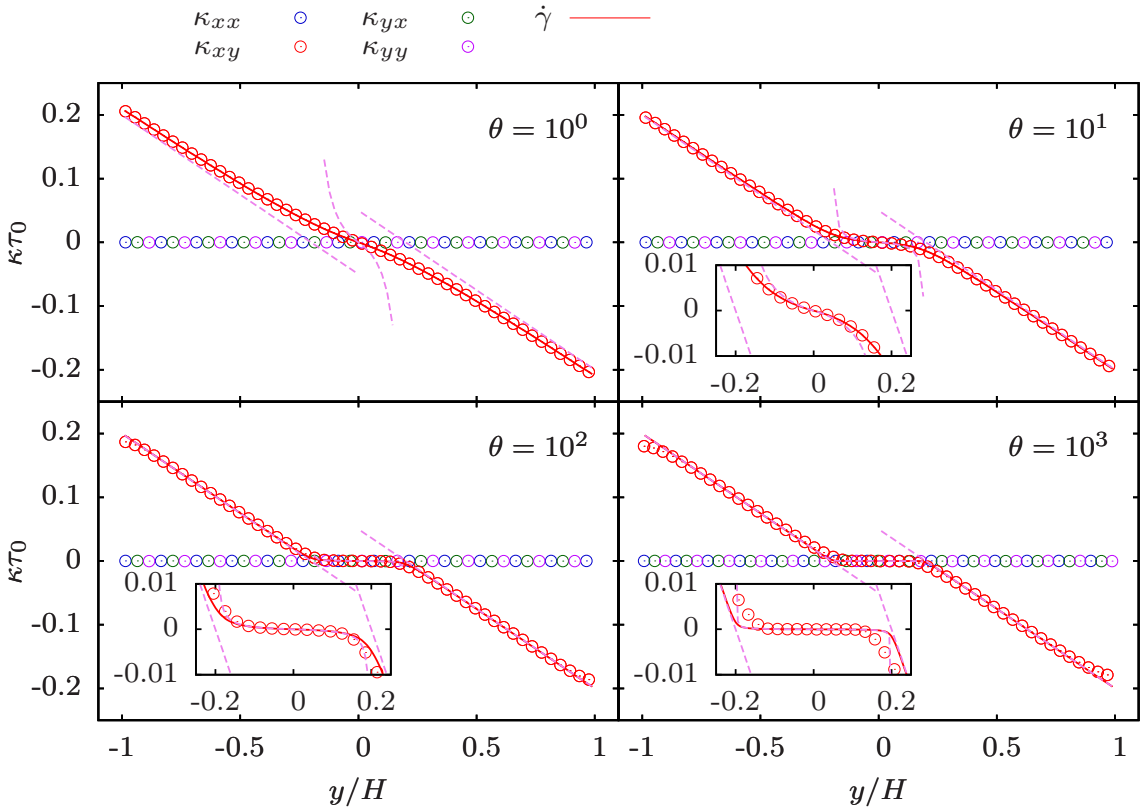

Figure 4.4: Steady state velocity gradient tensor $\boldsymbol{\kappa}$ for different values of θ. The circles are values obtained from LB simulations using the tensorial non-linear Maxwell model. For comparison, the red line shows the analytic solution, Eq. (4.4). The violet dashed lines give the asymptotes, Eq. (4.6), valid for large θ.

The plug is even better visible in the velocity gradient tensor $\boldsymbol{\kappa}$, cf. Fig. 4.4. The strain rate κ_{xy} is the only non-zero component, as we expected from the incompressible solution. The violet dashed lines show the asymptotic behavior Eq. (4.6) for large θ. The asymptotes are close to the exact solution Eq. (4.4) (red line) for $\theta = 10^2, 10^3$ and still in surprisingly good agreement for $\theta = 10^1$. For $\theta = 1$ the strain rate does not deviate much from a linear Newtonian profile. The LB results reproduce the exact solutions very well, larger θ values demand a higher lattice resolution. For $\theta = 10^3$, we find the largest errors near the walls causing the offset in the velocity profile Fig. 4.3

We turn to the components of the stress tensor $\boldsymbol{\sigma}$ next, see top panels of Fig. 4.5. The inset shows the expected linear behavior of the shear stress σ_{xy} in perfect agreement with Eq. (4.3). The body-force takes only the traceless part of the non-Newtonian stress, and indeed we find $\sigma_{xx} + \sigma_{yy} = 0$. As the non-linear Maxwell model is completely local in space and time, we can use the incompressible solution of the strain rate, Eq. (4.4), to get an expression for the normal stress difference $\mathcal{N}_1 = \sigma_{xx} - \sigma_{yy}$, Eq. (3.36c), in a channel flow. In the glass limit $\theta \to \infty$, the normal stress difference takes a constant value at the borders

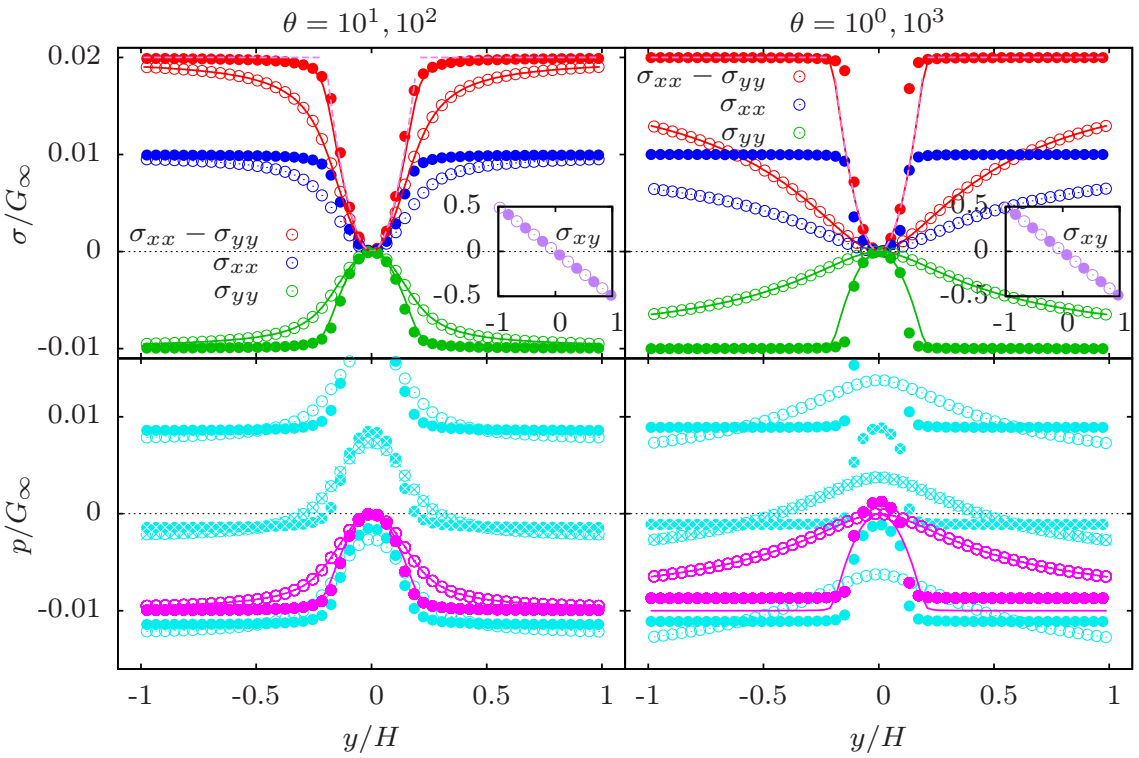

Figure 4.5: Stress tensor elements $\sigma_{\alpha\beta}$ for a pressure-driven channel flow of an inlM fluid. Open symbols show LB results for $\theta = 1, 10$, filled symbols for $\theta = 10^2, 10^3$. The inset shows the expected linear behavior of the shear stress. The lines are the analytic calculations from the Maxwell model, assuming incompressibility, Eq. (4.4) and Eq. (3.36c). The dashed line gives the asymptotic behavior, Eq. (4.8). The lower panel shows a projection of the pressure gradient and visualizes the difference between both ways of implementing a pressure gradient. For the magenta circles an effective body-force was applied, whereas for the cyan symbols generalized periodic b.c. was used. The central column is marked with crosses.

and forms a parabola in the channel center

$$\sigma_{xx} - \sigma_{yy} \sim \begin{cases} 2G_\infty \gamma_c^2 & |d| > \gamma_c/(hp) \\ 2G_\infty (phd)^2 & |d| < \gamma_c/(hp). \end{cases} \tag{4.8}$$

The LB results trace the theoretical normal stress profile (red lines) for the first three values of θ very well. Only for $\theta = 10^3$ some small deviations become visible due to the lattice discretization as seen before. For $\theta = 10^2$ and $\theta = 10^3$ we find the asymptotes from Eq. (4.8) to work very well. Even for $\theta = 10$ the central parabolic profile (dashed lines) and the constant flanks are still recognizable.

For small Reynolds numbers the flow remains laminar and only the velocity gradient component $\kappa_{xy} \neq 0$. By removing the trace, the normal stress difference has been distributed on both diagonal elements σ_{xx} and σ_{yy}. We identify the trace as a negative pressure and find an non-Newtonian change in the pressure $p = -\frac{1}{2}\mathcal{N}_1 = \sigma_{yy}$ (magenta line). The lower part of Fig. 4.5 shows the pressure profile using two different approaches. In both cases, we use our proposed LB scheme, cf. Chap. 2, to construct a body-force term $\boldsymbol{\mathcal{F}}$ which modifies

the LB algorithm to model a non-Newtonian constitutive equation. The body-force term is chosen in such a way that the second moment of $\boldsymbol{\mathcal{F}}$ with respect to the lattice velocities gives the non-Newtonian stress contribution, cf. Eq. (2.63).

In a channel of constant diameter, a pressure step between the inlet and outlet results in a uniform linear pressure gradient. On the level of the Navier-Stokes equation, this pressure gradient is mathematically identical to an effective external force density $\boldsymbol{f}$. For the magenta points, the first moment of $\boldsymbol{\mathcal{F}}$ is modeled to give $\boldsymbol{f}$. As the LB model works in the nearly-incompressible limit, the non-Newtonian pressure is connected by the equation of state to a small change in the density. The zeroth moment of $\boldsymbol{\mathcal{F}}$ is used to adjust the density. The LB results are again in very good agreement to the expected pressure profile. For $\theta = 10^3$ the shape of the curve is still good, but slightly shifted to positive values. This implementation of the pressure gradient seems to be more sensitive to an insufficient lattice resolution. The pressure increase in the channel center balances the normal stresses pointing inwards and meets our expectations. However it is remarkable, that the non-linear Maxwell model does achieve this change not by a higher pressure in the channel center, but by a pressure drop in the high-shear regions, which is especially evident for this LB scheme.

In the second case, generalized periodic boundary condition (gpbc) are applied to account for a pressure jump between the inlet and the outlet of the channel. This implementation is the method of choice when studying more complex pressure-driven flows where a uniform pressure gradient is not guaranteed. In the lower panel of Fig. 4.5 the pressure profile is projected in flow direction. The symmetry of the channel is still conserved in all but the pressure. As there is now an overall pressure gradient, different positions along the channel are now offset by a constant value. The central column of the lattice is marked with crosses and needs to be compared to the magenta one. The relative pressure gradient in y-direction is the same, but the absolute values are shifted. The gpbc keeps the average pressure at both channel ends fixed, which ensures that the pressure averaged over each column is also conserved. The pressure drop is canceled by the boundary condition.

For a Poiseuille flow, both methods give exactly the same simulation results, besides the aforementioned offset in the pressure profile. All plots displayed here use the generalized periodic boundary conditions if not stated otherwise. As the effect of the zeroth moment of the body-force is undone by the b.c. and no first moment is needed, the body-force term is constructed to only modify the stress to meet the chosen non-Newtonian constitutive equation.

4.2.3 Transient dynamics of the inIM model

We consider the time evolution of the velocity profiles next. A sudden pressure difference is applied to a quiescent fluid and switched off again after the flowing steady state profile has developed. For a Newtonian fluid, the time-dependent Navier-Stokes equation can be solved analytically [5]. The starting and stopping flow are symmetric and can be mapped onto each other by a simple variable transformation

$$\begin{aligned} w(d,s)_{\text{stop}} &= \sum_{n=0} D_n \cos\left(\pi\left(n+\tfrac{1}{2}\right)d\right) \exp\left(-\frac{4}{\text{Re}}\pi^2\left(n+\tfrac{1}{2}\right)^2 s\right), \\ w(d,s)_{\text{start}} &= w_{\text{s}}(d) - w(d,s)_{\text{stop}} \end{aligned} \tag{4.9a}$$

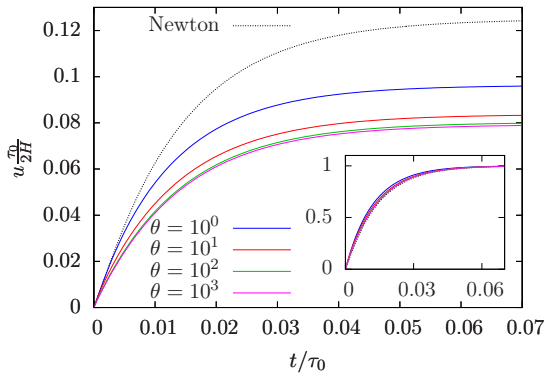

(a) Evolution of the mid-channel velocity after application of a pressure gradient (startup). In the inset, the velocities are scaled by the steady state values.

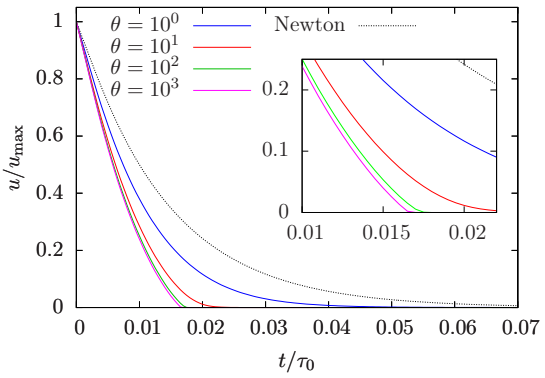

(b) Evolution of the mid-channel velocity after removal of a constant pressure gradient (cessation). The velocities are scaled by the flowing steady state values.

Figure 4.6: Time evolution of the tensorial non-linear Maxwell model after switching the pressure gradient on (left) and off again (right). The lines are LB results for different θ and give the fluid velocity in the channel center. For comparison, the dotted lines show a Newtonian fluid.

with the Fourier coefficients

$$D_n = \int_{-1}^{1} \frac{ph}{4}(1-d^2)\cos\left(\pi\left(n+\tfrac{1}{2}\right)d\right)\mathrm{d}d. \tag{4.9b}$$

Higher order terms only give small corrections, and the solution essentially amounts to an exponential approach to the flowing steady state value $w_\mathrm{s}(d) = \frac{ph}{4}\left(1-d^2\right)$. We use the zeroth order contribution, $n = 0$, to define a characteristic time t_on on which the flow evolves:

$$\frac{t_\mathrm{on}}{\tau_0} = \frac{\mathrm{Re}}{\pi^2} = \frac{L^2\rho}{\pi^2\tau_0\eta}. \tag{4.10}$$

The variables are the same as defined when deriving the steady state solution of the non-linear Maxwell model in Sec. 4.2.1. The Reynolds number is again given by $\mathrm{Re} = \frac{L^2\rho}{\tau_0\eta}$.

For a non-Newtonian fluid, the situation is more complicated. An analytical solution is not available, and the transients are known to be qualitatively different for yield stress fluids [49, 74]. In Fig. 4.6a the fluid is initially at rest when at $t = 0\tau_0$ the pressure is switched on. The lines give the mid-channel velocity for different values of θ, the full profile is shown in the left panels of Fig. 4.7. Besides the difference in the steady state profile, the transients do not change qualitatively from a Newtonian fluid (dotted line). For the solution of the time-dependent Navier-Stokes equation (4.2), nonlinear stress contributions are small compared to the constant pressure gradient term, and in this model, the stress can adjust instantaneously to a change in flow. The startup velocities very nearly scale on top of each other when divided by their steady state value, see inset. One interesting detail remains: In the inset, the transient of the Newtonian fluid has changed its relative position to the other curves and is now just below the one of $\theta = 10^3$. The reason behind this lies in the dimensionless velocity we have chosen. For a channel flow, the time τ_0 associated with

the low viscosity limit influences the maximum velocity most. In the glass limit $\theta \to \infty$, the fluid behaves like a Newtonian fluid phase in two narrow channels at the walls, separated by a comoving solid phase in the center. The effect of the reduced channel width scales out when dividing by the steady-state value. So, interestingly, the startup profile for $\theta = 10^3$ is actually closer to a Newtonian fluid than for $\theta = 1$.

The situation is very different considering the cessation profiles. The non-linearity of the stress tensor becomes important as the pressure gradient is removed and the time derivative of the velocity has to be balanced by the derivative of the stress tensor only. Fig. 4.6b shows the mid-channel velocity after the pressure step has been removed. The velocities are divided by their flowing steady state values. Although the cessation profile for $\theta = 1$ is not symmetric to the startup flow, we find it to decay asymptotically to zero just like the Newtonian fluid. By increasing θ the dynamics undergo a qualitative change. Although the ultimate flow decay is again Newtonian, the cessation profiles for large θ hint at a finite stopping time characteristic for yield stress fluids. A minimum pressure drop needs to be applied to overcome the yield stress of a fluids before a flow can develop. For cessation flows, the same mechanism makes a flow stop abruptly at finite times instead of vanishing asymptotically like a Newtonian fluid. R. Huilgol [49] relates this pressure and the least eigenvalue of the Laplace operator in the channel cross section to derive an upper bound for the stopping time, which gives a good approximation of the one found numerically [74]. The inlM only provides a yield stress in the glass limit $\theta = \infty$. However, as seen in the steady-state profiles before, $\theta = 100$ essentially reproduces the properties of the glass phase.

Fig. 4.7 gives the full profile at various times for $\theta = 1, 10, 100$. The startup flows (left panels) look the same in all three cases and can only be distinguished by the difference in the plateau. The right panels show the cessation profiles. Whereas for $\theta = 1$ the switch-off profiles resemble the starting flow, already for $\theta = 10$ the finite stopping time becomes obvious. As mentioned above, the time-dependent Navier-Stokes equation does not provide an analytical solution. However, we have compared the temporal evolution of the profile with results from numerical partial differential solvers [83] and found them to reproduce the LB results.

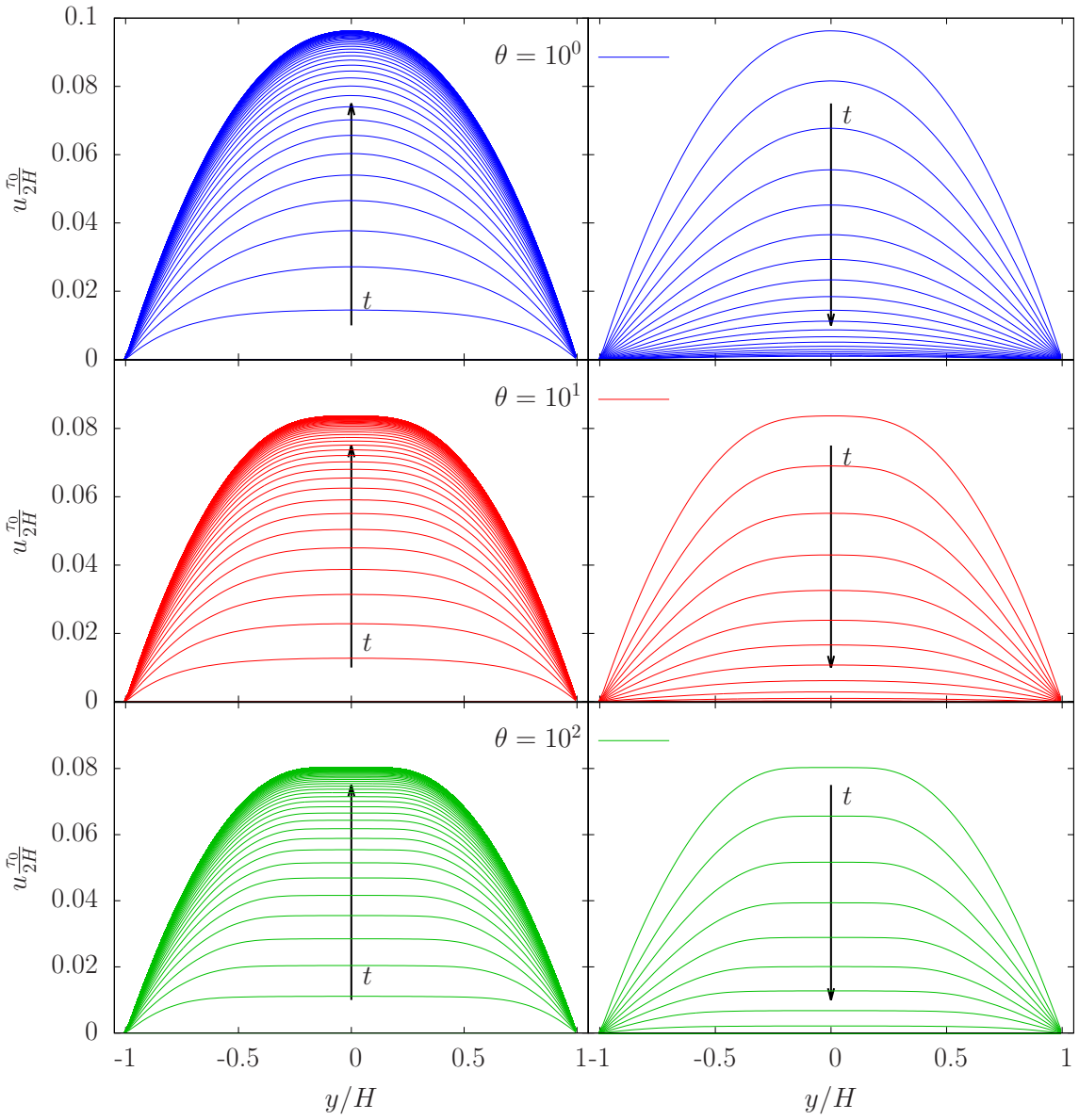

Figure 4.7: Startup (left) and cessation (right) velocity profiles of a pressure-driven 2D channel flow, for $\theta = 1, \theta = 10, \theta = 100$ (top to bottom). The lines are LB results and separated by a constant time $2 \cdot 10^{-3}\tau_0$ each.

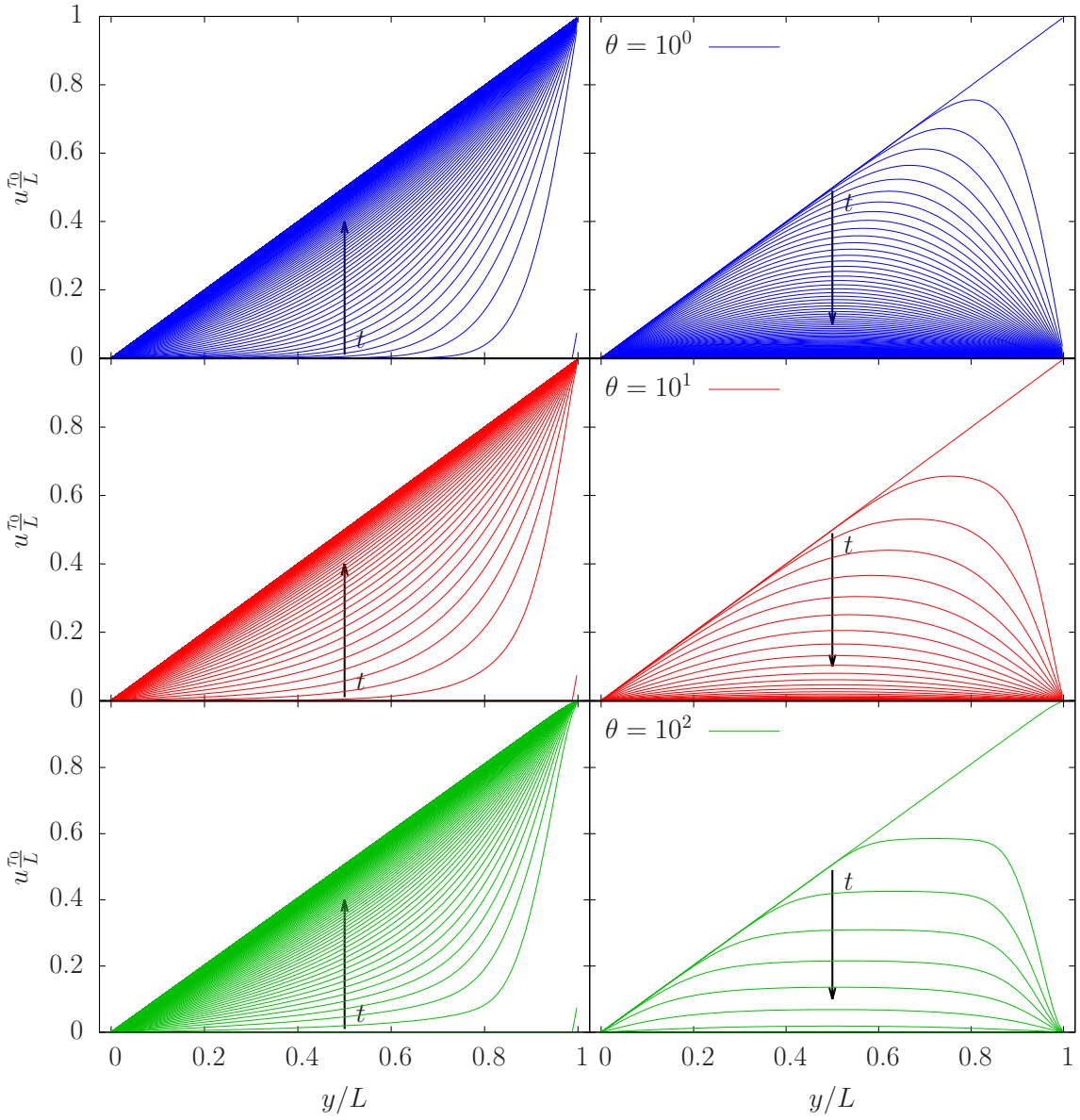

Figure 4.8: Startup (left) and cessation (right) velocity profiles between two plates, for $\theta = 10^0, 10^1, 10^2$ (top to bottom). The upper plane ($y = 1$) moves with the velocity $10^{-2}L/\tau_0$ in the left panels. The lines are LB results and separated by a constant time $4 \cdot 10^{-4}\tau_0$ each.

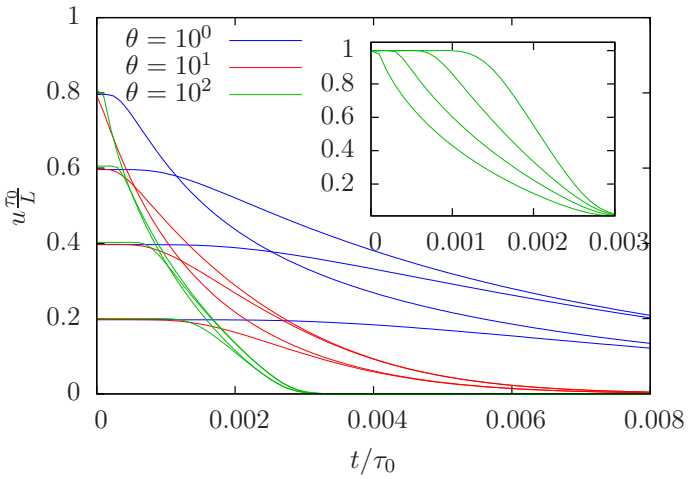

Figure 4.9: Lines are LB results for the non-linear Maxwell model and show four cessation velocity profiles equally spaced throughout the channel for $\theta = 10^0, \theta = 10^1, \theta = 10^2$ in simple shear geometry. In the inset, the steady state velocities are scaled to unity for $\theta = 10^2$.

Simple shear flows

Instead of using a pressure gradient, we now drive the system by moving the upper plate of the channel with a constant velocity u. Having modified the LB algorithm, we have to be cautious to choose a suitable boundary condition to account for the moving plate. We found the velocity boundary condition by Q. Zou and X. He [109] to work well. The Zou/He method is quite similar to the generalized pressure b.c. and the pressure advection we know to fit well, cf. Sec. 2.2. Again, the non-equilibrium part f_i^{neq} is separated off the velocity distribution f_i. The equilibrium part is substituted to match the desired target value, whereas a simple bounce-back rule is applied to the f_i^{neq} [68]. The periodic boundary condition in x-direction and the bounce-back condition for the lower plate remain unmodified.

Fig. 4.8 shows the startup (left) and cessation (right) velocity profiles after stopping the plate for $u = 10^{-2}L/\tau_0$ and $\theta = 1, 10, 100$. The parameters $\tau_0 = 1\text{s}$, $\gamma_c = 0.1$, $G_\infty = 1\text{Pa}$, $L = 10^{-2}\text{m}$ and $\rho = 1360\text{kg/m}^3$ are the same as before. Since the flowing steady state has the identical linear profile for all θ, it is hard to see a difference in the startup case at all. The opposite is true for the stopping flow. After stopping the upper plate $y = 1$, for large θ a pronounced plug is found again. The plug forms near the stopped plate. As the overall velocity decreases the velocity profile peels off the linear steady state. The plug becomes wider and moves slightly moves towards the center.

In the time evolution we find the same finite stopping time already seen in the results of the pressure-driven channel flow simulations. Instead of an asymptotic decay to zero, the flow comes to a near-stop at $t \approx 0.003\tau_0$ for $\theta = 100$. This can be seen even better in Fig. 4.9 where the time evolution of the velocity at different position in the channel is shown. At the far end of the stopped wall, the velocity initially stays constant, until the decaying velocity profile catches on. To illustrate this, in the inset the velocity curves for $\theta = 100$ are scaled to unity. Since the outer and inner velocity curves are taken at the same distance to a wall, it is nice to observe how the symmetry of the profile is restored as the curves meet.

4.3 Integral non-linear Maxwell model with memory

We now turn our attention to the full integral non-linear Maxwell model (nlM). In the long time limit, the constitutive equation (3.32)

$$\boldsymbol{\sigma}(t) = \eta_\infty \boldsymbol{D} + \int_{-\infty}^{t} \mathrm{d}t' \left[\frac{\partial}{\partial t'}\boldsymbol{B}(t,t')\right] G_\infty \mathrm{e}^{-(t-t')/\tau_\mathrm{M}(t')} \tag{4.11}$$

shares the steady state solution with the instantaneous model considered in the previous section. So the discussion of the steady state profiles in Sec. 4.2.2 is also valid for this model, although the transient dynamics is very much different. We have checked the scalar version of the integral model, cf. Eq. (3.33), to give the same results for the shear stress and velocity profile, and we will not discuss it here separately. The new constitutive equation increases the computational demand quite a lot. Since we know the flow to be translational invariant in flow direction for small Reynolds-numbers, we only keep track of the flow history at the channel center to compute the non-Newtonian part of the stress tensor. However, to minimize boundary effects, the LB steps and the computation of hydrodynamic variables are still carried out for each lattice node individually.

In the instantaneous non-linear Maxwell model the stress tensor $\boldsymbol{\sigma}(t)$ is only a function of the current velocity gradient tensor $\boldsymbol{\kappa}(t)$ at the same time step t. The flow variables do not affect the dynamics beyond this point. In Eq. (4.11), now the full history ($-\infty < t' < t$) enters via the derivative of the Finger tensor $\partial_{t'}\boldsymbol{B}(t,t')$. The time derivative can be expressed by the deformation between its time arguments and the rate of strain tensor at time t', cf. Eq. (3.17). An exponential decay on the time-scale set by τ_M is used to account for the memory loss. The generalized Maxwell time $\tau_\mathrm{M}(t')$ again is a function of the shear rate at previous times t' and used to mimic the accelerated decay of memory by shear, cf. Eq. (3.31).

The transient dynamics are profoundly affected by the new dependence of the stress on the flow history. Using the same simulation parameters as before, Fig. 4.10 shows the transient dynamics of the integral non-linear Maxwell model. Two things immediately stand out: First, the velocity profile is no longer monotone, but shows over- and undershoots, and second, it takes the fluid much longer to reach the steady state for both, start- and stopping flows. Indeed, for $t/\tau_0 < 0.04$, a time in which for the inlM model the flow has nearly reached the steady state, the fluid behaves like a Newtonian. Only then the starting flow deviates from a Newtonian starting flow and decreases slowly to the steady state flow profile known from the inlM model, cf. Fig. 4.10a. For the stopping flow, we observe quite a similar behavior, Fig. 4.10b. The fluid velocity decreases even faster than before (dashed lines in the inset are inlM results). But instead of stopping, the fluid velocity goes on to negative values before slowly coming to a rest.

The only difference between the integral formulation Eq. (4.11) of the full non-linear Maxwell model and the previously used simplified inlM model is the short-time reaction to a change in the flow profile. For long times, both models yield just the same steady state results. In the inlM model, the stress immediately adjusts to any change in the flow. The sole purpose of the generalized Maxwell time τ_M is to allow shear-thinning behavior. In the full model, $\tau_\mathrm{M}[\dot\gamma]$ sets a time scale on which the stress develops. Not only is the response to

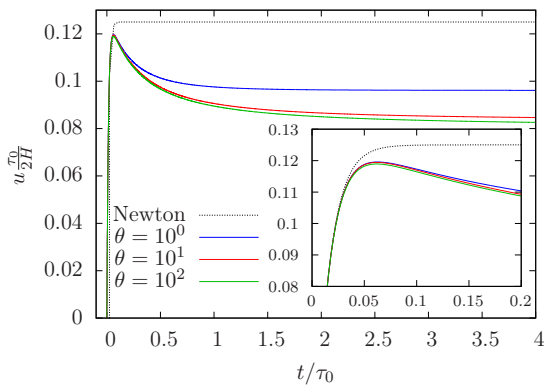

(a) Evolution of the mid-channel velocity after application of a constant pressure gradient (startup).

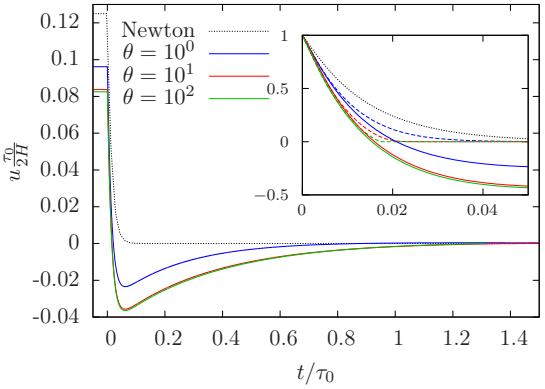

(b) Evolution of the mid-channel velocity after removal of a constant pressure gradient (cessation). In the inset, the velocities are scaled by the velocity at $t = 0\tau_0$.

Figure 4.10: Time evolution of the integral non-linear Maxwell model after switching the pressure gradient on and off again. The lines are LB results for different θ and give the fluid velocity in the channel center. For comparison, the dotted line shows a Newtonian fluid, dashed lines (inset right) are results for the instantaneous non-linear Maxwell model. The parameters are the same as before, cf. Sec. 4.2.2.

a change in the flow no longer instantaneous, but also the time scale is modified by the local shear rate.

It is reasonable to assume that exactly this new transient stress is responsible for the effects we observe. Both times, for the starting and the stopping flow, the initial response of the fluid differs distinctively from the instantaneous model. The effect is especially astonishing for the cessation profile when the fluid starts moving in the opposite direction of the previous flow. Because the fluid has already stopped before the stress has had time to relax, the system is left in a peculiar situation. Despite the obvious absence of motion, the fluid is not at rest in the meaning of a steady state, but the system exhibits true viscoelastic behavior. The only way the fluid can release the resident stresses is to start flowing again. Yet since the shear stress works in opposite flow direction, the fluid starts moving backwards. The velocity and stress transients at quarter channel position in Fig. 4.13 support this hypothesis. The interplay between the shear stress and the velocity plays an important role for the transient dynamics, and we will resume the discussion in more detail in Sec. 4.3.3.

In polymer melts, it is common for the stress to take a finite time to build up [69, 99] and still an on-going research subject [11, 59]. This effect clearly has a strong influence on the startup and cessation dynamics of the channel flow. However, we cannot study the transient stress by changing the time scale set by the generalized Maxwell time τ_M directly. The high-shear regions are most important for the dynamics of the flow, but there τ_M is dominated by the shear rate $\dot{\gamma}$. The shear-thinning parameter θ has only a minor influence on the transient flow and primarily affects the steady state results. Luckily, there is a way around. Rather than changing the dynamics of the stress, we can vary the time it takes the flow to develop. Recall, that the flow of a Newtonian fluid evolves on a time-scale set by

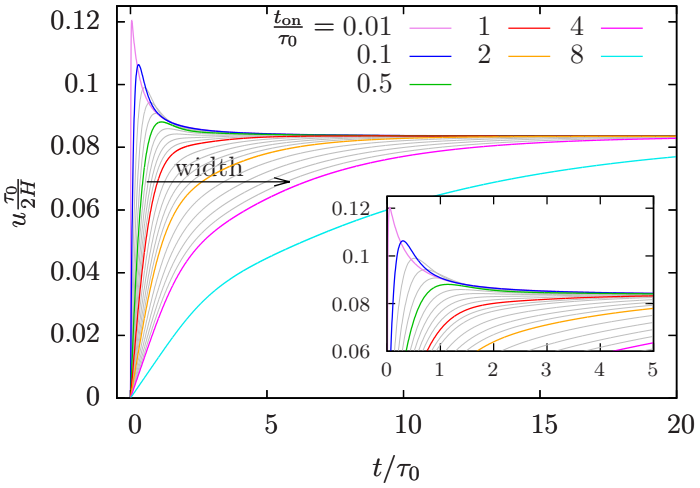

Figure 4.11: Lines are LB results for the integral non-linear Maxwell model and show the evolution of the mid-channel velocity after switching on the pressure. The lines correspond to different channel diameters chosen to give characteristic times $t_{on}/\tau_0 = \mathrm{Re}/\pi^2 = 0.01, ..., 8$, cf. Eq. (4.13). Grey lines in between colored lines are equally spaced in t_{on}.

the channel diameter and the fluid parameters, cf. Eq. (4.9),

$$\frac{t_{on}}{\tau_0} = \frac{\mathrm{Re}}{\pi^2} = \frac{L^2\rho}{\pi^2\tau_0\eta}. \tag{4.12}$$

In fluid mechanics, the time scale for transverse momentum diffusion is typically set by the inverse viscosity η^{-1}. Information about boundaries and geometric constraints cannot pass instantly throughout the fluid, and t_{on} is a measure for the time it takes the channel walls to affect the flow. Quite differently, in glassy systems, the dynamics is governed by density fluctuations. The longitudinal momentum is dominant, and the typical time scale is proportional to η instead.

Using the channel diameter L as a parameter, we can tweak the time a Newtonian flow takes to develop and thereby vary the influence the startup stress can exert on the transient flow, which is exactly what we will do in the next section. Throughout the following discussion, we will keep a constant $\tau = 10\tau_0 = 10\mathrm{s}$, which is large enough to give a distinct non-Newtonian plug flow profile. The density $\rho = 1360\mathrm{kg/m}^3$, the shear modulus $G_\infty = 1\mathrm{Pa}$ and the applied pressure step $\Delta p = 1G_\infty$ are the same parameters as used in the previous simulations. $N = 100$ lattice nodes in transversal flow direction prove to be sufficient.

4.3.1 Effect of the channel diameter on the transient dynamics

Fig. 4.11 shows the velocity u in the channel center $d = y/H = -0.01$ after the pressure is switched on at time $t/\tau_0 = 0$. The channel diameter $L = 2H$ is chosen to give a characteristic time t_{on} we would associate with a Newtonian fluid and a viscosity $\eta = G_\infty\tau_0$:

$$\frac{t_{on}}{\tau_0} = \frac{L^2\rho}{\pi^2 G_\infty \tau_0^2}. \tag{4.13}$$

We choose the minimal viscosity of the non-linear Maxwell model because τ_0 is the relevant time scale for both, the steady state velocity and the startup flow. Starting with $t_{on} = 0.01\tau_0$,

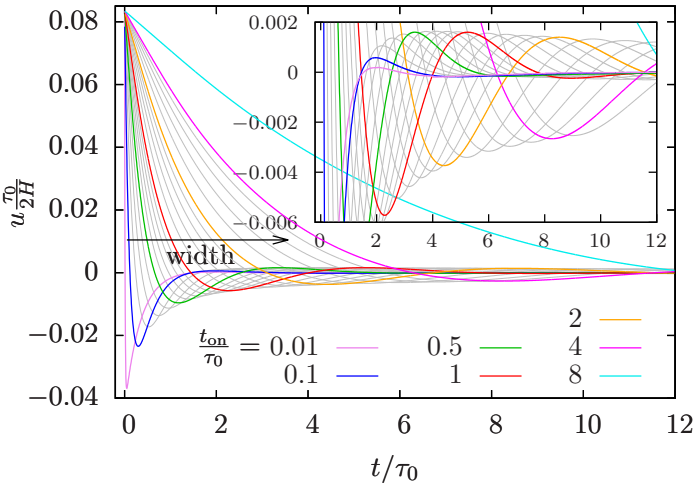

Figure 4.12: Lines are LB results for the integral non-linear Maxwell model and show the evolution of the mid-channel velocity after switching off the pressure. The lines correspond to different channel diameters chosen to give characteristic times $t_{on}/\tau_0 = \mathrm{Re}/\pi^2 = 0.01, ..., 8$, cf. Eq. (4.10). Grey lines in between colored lines are equally spaced in t_{on}.

we find a similar velocity overshoot as previously ($t_{on} = 0.0138$s for $L = 1$cm). Since the height of the overshoot is limited by the maximum velocity $ph/4 = 0.125$, cf. Eq. (4.9), and the transient velocity already comes close to this limit, reducing the channel diameter even further does not yield qualitative different results. However, by increasing the channel width and thereby t_{on} it takes the fluid longer to develop a flow. This gives the extra stress, which distinguishes the non-linear Maxwell model from a Newtonian fluid, more time to develop, and it inhibits the flow at an earlier stage, before the fluid has reached such an high overshoot. For larger channel diameter, the overshoot vanishes continuously. At about $t_{on} = 1\tau_0$, we cannot find an overshoot in the velocity altogether. The velocity profile still exhibits a sharp kink and is clearly different from a Newtonian profile, but otherwise monotonically rising. By increasing t_{on} further, the kink becomes less pronounced and happens at an earlier time of the startup flow.

In Fig. 4.12, after reaching the flowing steady state, the driving pressure is suddenly switched off at $t/\tau_0 = 0$. Again, we find the fluid in the interesting situation that the velocity and the shear stress decrease at different rates. The fluid velocity drops to zero before the shear stress can be relieved. This situation is quite similar to the starting flow, but the undershoot happens every time, no matter what channel diameter we choose. Taking a closer look, we find the fluid not to relax monotonously to the steady state value as before, but in fact it experiences oscillations around zero. In the inset of Fig. 4.12 another interesting fact becomes obvious. Both, the undershoot and the overshoot are subject to an enveloping curve which sets a limit to the height of the oscillation. But whereas the largest undershoot occurs for the narrowest channel, the following overshoot is largest for $t_{on} \approx 0.5\tau_0$. One last remark regarding the symmetry between startup and cessation flow. For very narrow channels, the velocity profile seems to conserve some of the symmetry typical for Newtonian fluids. Although the startup profile does only show a single overshoot and no oscillations, the overshoot does happen at the same time and has the same height as when the pressure is switched off. So for narrow channels, we find distinct Newtonian aspects in the transient behavior. Increasing the channel diameter reduces the influence of the Newtonian solution to a point where the asymmetry becomes glaring. We find oscillations in the cessation profiles of channels which do not show any overshoots in the

starting flow.

So far, we have only speculated about the interplay between the shear stress and velocity transients. During the next few chapters, we will go into a much more detailed discussion to check our hypotheses. First, to get the whole picture, we will take a look at all the relevant quantities of the flow: the velocity and the shear stress, the normal stress difference and the pressure, Sec. 4.3.2. As the previous discussion already suggests, we can identify two different regimes for different channel widths. To focus on the dynamics we select one channel, $t_{\mathrm{on}} = 0.1\tau_0$ and $t_{\mathrm{on}} = 4\tau_0$, for each regime and a third, critical with $t_{\mathrm{on}} = 1\tau_0$, which lies in-between and shows features from both ends. In Sec. 4.3.3 we look at the interplay between the evolution of the shear stress and the velocity profiles. We make a short side-trip to the unmodified viscoelastic Maxwell model. This gives us a comparison case, so we can relate our findings to viscoelasticity, shear-thinning behavior known from the instantaneous Maxwell model, or an interplay between both. The dynamics of the normal stress difference and pressure are subject to the other flow transients, but do not couple back. This allows us to discuss them separately in Sec. 4.3.4.

4.3.2 Transient dynamics of the nlM model

In the previous section, we only looked at the evolution of velocity in the channel center. To get the whole picture, we have to take the dynamics of the stress tensor $\boldsymbol{\sigma}$ into account. However, the situation is complicated by the fact that the symmetry of the channel requires the shear stress σ_{xy} and the normal stress difference $\sigma_{xx} - \sigma_{yy}$ to vanish in the center. In fact, both take their maximum values at the wall, where no-slip boundary conditions ensure the velocity to be zero. As a compromise, Fig. 4.13 shows the velocity and the stress components at quarter channel position. To improve comparability, all values are scaled by the flowing steady state value. However, the results have to be taken with a grain of salt because the transient dynamics are not truly independent of the channel position. Since the stress and velocity values are fixed to zero at specific positions, the height of an overshoot varies with the position in the channel. Furthermore, the overshoots do not happen at the same time throughout the channel. This variation in time is small for the velocity and shear stress, but not so for the normal stresses. This section allows us to get a first impression of the dynamics, so we can develop an intuition for the startup and stopping flow. Looking at a wide range of channel diameters helps us to identify qualitative changes in the transients for varying channel diameters. In the following section, we then discuss the dynamics for exemplary channels in detail.

The velocity $u(t)$ at $d = y/H = -0.51$ does not differ much from the velocity in the channel center, $d = -0.01$, we have already seen. However, it is noteworthy that the distinctive features are far less pronounced than previously. This was to be expected since the boundary condition inhibits any shenanigans in the velocity profile close to the wall. The kinks are smoothed out and the height of the velocity peak has decreased. For $t_{\mathrm{on}} = 0.5\tau_0$, the overshoot is gone altogether.

The biggest difference to the instantaneous non-linear Maxwell model is to be found in the shear stress σ_{xy}. Previously, the shear stress immediately adjusted to any changes in the shear rate, now it takes a finite time to react. We cannot help but observe how the stress starts to build up with the onset of the flow, yet after an initial delay, the shear

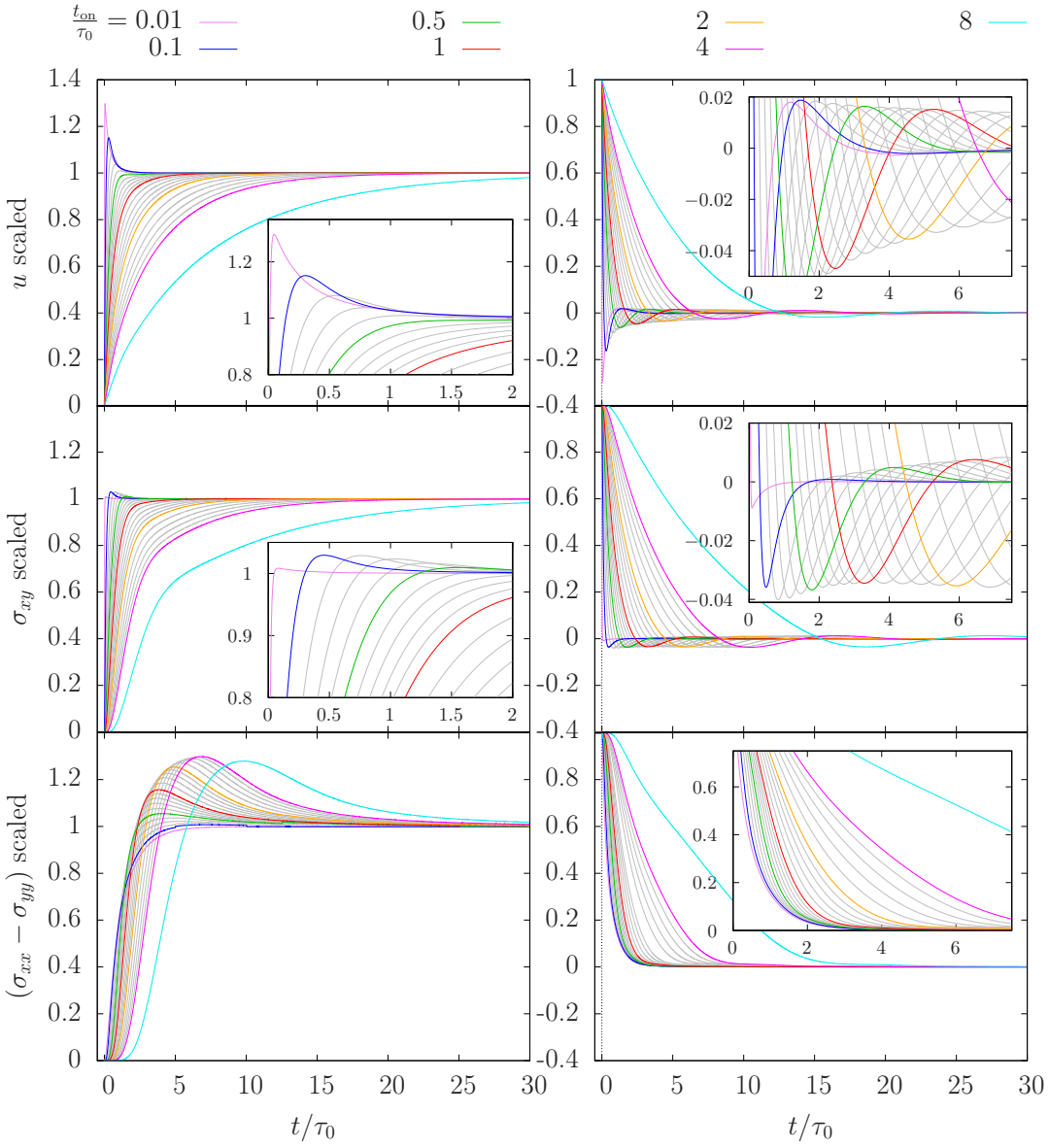

Figure 4.13: Lines are LB results for the integral generalized Maxwell model and show the evolution of the velocity (top), shear stress (middle) and normal stress difference (bottom) at $d = -0.51$ in time for startup (left) and cessation flow (right). For better comparison, all curves are scaled to the flowing steady state value. The channel diameter is varied to give different characteristic times $t_{on}/\tau_0 = \mathrm{Re}/\pi^2 = 0.01, ..., 8$, cf. Eq. (4.10). Grey lines in between colored lines are equally spaced in t_{on}.

stress evolves quite similarly to the velocity. We even find corresponding non-monotonous transients, though on a smaller scale. The overshoots vanish if t_{on}/τ_0 exceeds 1 and are replaced by kinks even more pronounced than in the velocity profile. Turning our attention to the stopping profile, we find the shear stress again to behave similarly to the velocity. Regardless of the channel diameters, the stress takes negative values, too. The amplitude of the undershoot is nearly constant, whereas the next overshoot vanishes for small channel diameters. Indeed, comparing the velocity and shear stress in time, the curves suggest an intricate relationship between both variables. Crossing the abscissa, the stress changes the direction of action and the velocity should take a local maximum. After the removal of the pressure gradient, the resident stress is the only quantity driving the system. For channels $t_{\mathrm{on}} > 0.1\tau_0$, the stress even develops an overshoot and causes the velocity to start oscillating. We will take up this point again, when we discuss the dynamics of the full channel. One question remains, why does $t_{\mathrm{on}} = 0.01\tau_0$ behave so differently? Note that for both, the shear stress and the velocity, the curves are more or less equally spaced with increasing t_{on}. But not so for $t_{\mathrm{on}} < 0.1\tau_0$. The inset seems to suggest, that the stress undershoot tries to move to smaller times but has run into a lower bound. By choosing a minimum viscosity for the Maxwell model we have also imposed an effective minimal time scale for any dynamics.

The normal stress difference $\sigma_{xx} - \sigma_{yy}$ is given in the two bottom panels of Fig. 4.13. Just as much as the velocity and shear stress share a common ground, the normal stress deviates from their dynamics and shows a strikingly different behavior. Although at first glance overshoots do appear, and even fairly large ones, these are not restricted to narrow channels. Quite the opposite, the overshoots become larger with increasing channel diameters and take their maximum at about $t_{\mathrm{on}} = 4\tau_0$. For extremely wide channels, $t_{\mathrm{on}} = 8\tau_0$, the overshoot is smaller again, but only slightly so. In the stopping flow, the normal stress difference does not seem to differ so much from the other flow variables. As the normal stresses are quadratic in the shear rate, we do not find any undershoots, but nevertheless the decay happens on similar time scales as for the shear stress and velocity. Only for narrow channels, $t_{\mathrm{on}} < 0.5\tau_0$, the normal stress seems to hit a lower bound, again.

At this point, we can only state that the velocity and shear are closely related, yet how deep this connection runs we will have to find out. The evolution of the normal stress difference is also strongly affected by the transient flow, but this exchange goes only one way. For the low Reynolds numbers considered here no secondary flow emerges, and the normal stresses do not couple back to the flow.

Rescaling with t_{on}

Obviously, the steady state profile develops much faster in a narrow channel than in a wide one. However, much of the qualitative change in physics is obscured because choosing a larger channel diameter will always cause the dynamics to slow down. Before we can use the channel diameter as a parameter to vary the influence the transient stress exerts on the flow, we have to reduce the purely quantitative effect of the channel diameter on the transient dynamics. Fig. 4.14a again shows the velocity and stress at $d = -0.51$ for various channel diameter, but now the time is given in units of t_{on}. In this scaling, the transient profiles of the instantaneous non-linear Maxwell model become independent of the channel

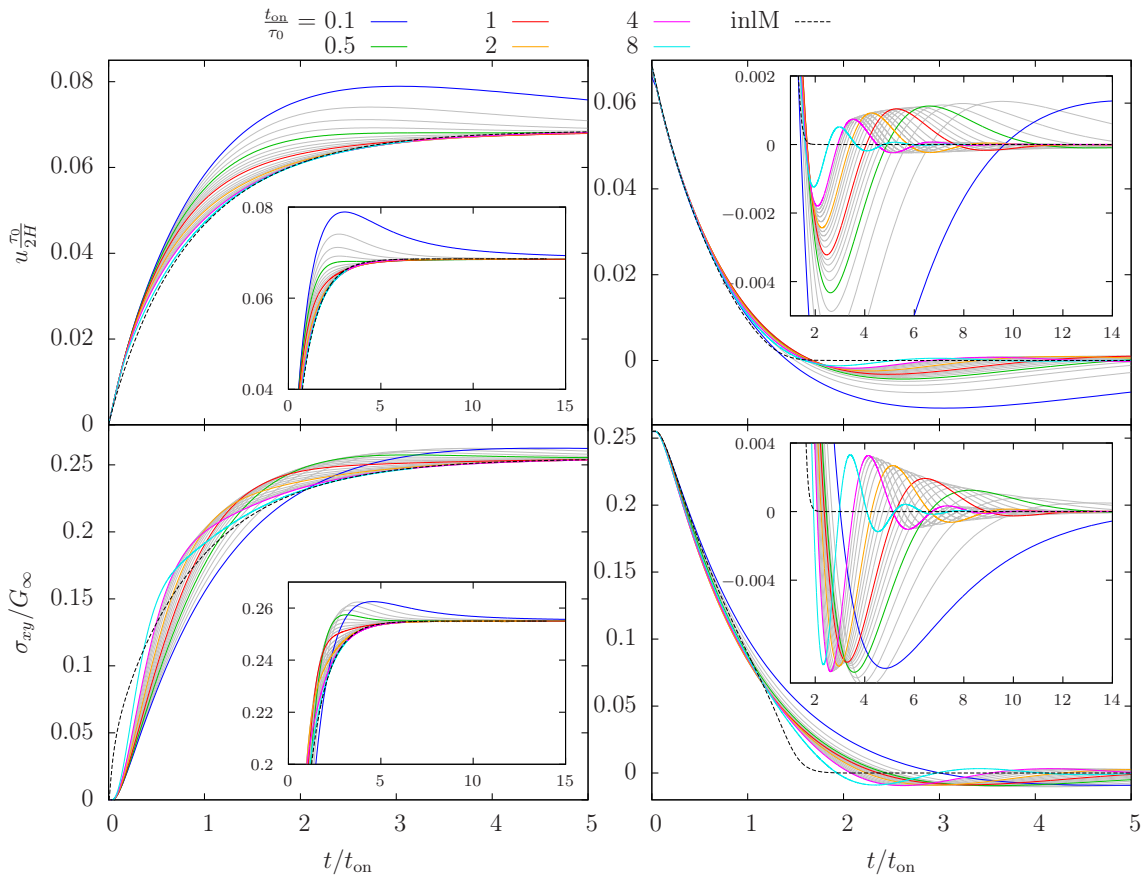

(a) Evolution of the velocity (top) and shear stress (bottom). The time is scaled by t_{on}.

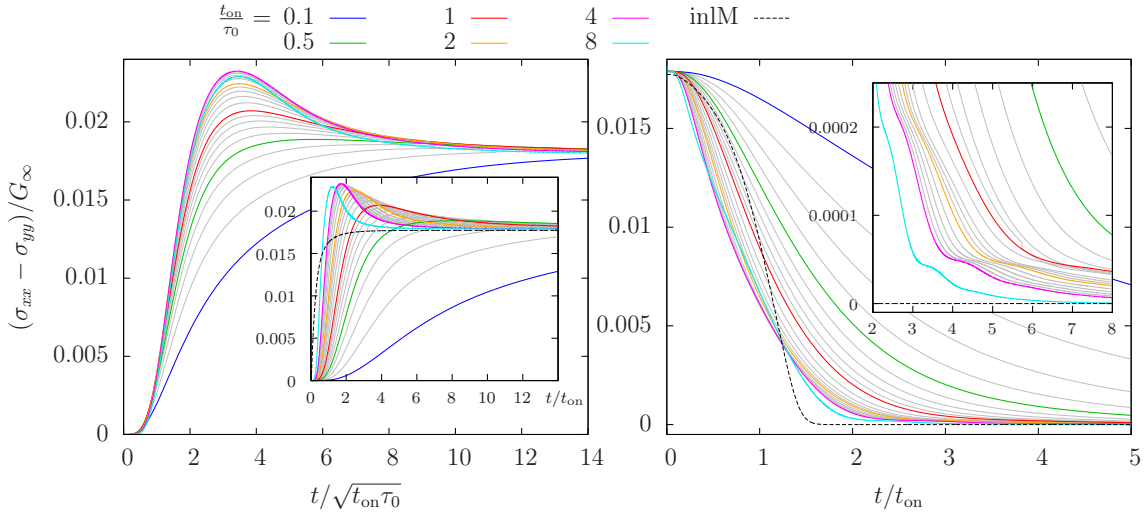

(b) Evolution of the normal stress difference. The time is measured in units of $\sqrt{t_{on}\tau_0}$ (left) and t_{on} (right and inset left).

Figure 4.14: Lines are the non-normalized LB results from Fig. 4.13 for startup (left) and cessation flow (right) at $d = -0.51$. The time is scaled by t_{on} or $\sqrt{t_{on}\tau_0}$, respectively. For comparison the instantaneous non-linear Maxwell model (inlM) is shown (dashed lines). If the time is measured in units of t_{on}, the inlM profiles are independent of the channel diameter.

diameter and form a single master curve (dashed lines). Variations from this curve by the integral non-linear Maxwell model are a sure sign of memory effects.

Let us consider the starting flow first (left panels). For the velocity, the scaling does work well if the channel is wide enough, $t_{\mathrm{on}} \gtrsim 2\tau_0$. Deviations become larger for about $t_{\mathrm{on}} = 1\tau_0$, but the scaling certainly breaks down when overshoots form. Having removed the net influence of the channel diameter on the startup time, we find that it takes the fluid in fact several times longer to reach the flowing steady state in the narrow channel, $t_{\mathrm{on}} = 0.1\tau_0$, than in a wide one. The stress induced slowing down of the fluid clearly happens on a different time scale.

So it is no surprise that the scaling works less well for the shear stress in a model where the stress does not adjust instantaneously to a change in the flow. The scaling with t_{on} ignores the separate time scale of the shear stress and the interplay between the transient stress and the starting flow, which is too complex to be condensed into a single number. Actually, the real surprise is how well the scaling still works. Although the shear stress does not form a single master curve, the transient stress now develops on similar time scales. Taking a few steps back (inset), we can clearly distinguish between narrow channels giving rise to pronounced overshoots and wide channels falling onto a single curve after the initial startup.

The normal stress grows quadratically with the shear rate. If we scale the time with $\sqrt{t_{\mathrm{on}}\tau_0}$ for the startup profile in Fig. 4.14b, the overshoots happen at the same time for wide channels. The overshoot decreases and is slightly delayed when going to intermediate channel diameters. However, decreasing t_{on} to $0.1\tau_0$, the time scale changes qualitatively. An overshoot still occurs, see Fig. 4.28, but so much later that it is not resolved in this plot.

Let us regard the stopping profiles next (right panels). For the velocity profile, the scaling works extremely well. During the initial decay after switching off the pressure, all curves fall onto each other. In the magnified inset, we can make out some more details. Whereas for channels with $t_{\mathrm{on}} > 0.5\tau_0$ it appears to be the same decay only stopped at different times, $t_{\mathrm{on}} = 0.1\tau_0$ seems to follow its own agenda again. Note how much the differences between the curves suddenly increase, although the channel diameters are equally spaced between $0.1\tau_0$ and $1\tau_0$. The air of generality continues, by doubling t_{on} the frequency increases by a factor of 1.5. This logarithmic relation explains in a way, why $t_{\mathrm{on}} = 0.1\tau_0$ seems to follow its own agenda.

Now that the stress is already fully developed, the initial decay of the shear stress is the same for all channels, although, unsurprisingly by now, the narrow channel is slightly off. The agreement to the instantaneous model is striking and even more so the point where the dynamics become different. Because the instantaneous model cannot go to negative values, we can see a clear kink in the transient at $t_{\mathrm{on}} \approx 1\tau_0$. Meanwhile the integral model remains on the same dacay channel all the way to the first undershoot. It is remarkable, that this initial undershoot is nearly constant for all channel diameters and marks a difference between the first and later oscillations. In the picture of a serial damper-spring Maxwell model, the spring is loaded by the kinetic energy of the fluid. At this stage, the damper has only a small influence, which allows a nearly constant amplitude. The spring then releases the tension in a damped oscillation, and we can clearly observe the exponential decrease of the amplitude.

For the normal stress difference, the restriction to positive values again imposes an

asymmetry on the startup and stopping profile. Although undershoots are impossible, the stopping flow is nevertheless affected by the oscillations. In the inset of Fig. 4.14b we can clearly observe how the decay is delayed with each oscillation.

Let us recap what we have learned so far. The velocity and the shear stress are closely related and affect each others dynamics profoundly. It is exactly this coupling that makes the dynamics exciting and complicated at the same time. For the startup flow, the transient dynamics of the velocity are strongly influenced by the lower viscosity bound of the Maxwell fluid giving rise to overshoots and breaking down the scaling with t_{on}. The shear stress benefits from higher initial shear rates and can build up a lot faster. However, for the same reason, it overshoots the target value (dashed line of the instantaneous nonlinear Maxwell model in Fig. 4.14a), and for $t_{\mathrm{on}} < 1\tau_0$ it will even increase beyond the flowing steady state value, just like the velocity. For very large channel diameters, $t_{\mathrm{on}} > 4\tau_0$, the flow develops slowly enough for the shear stress to follow, and the deviation to the starting flow of the instantaneous Maxwell model are small.

In the stopping flow profiles, the scaling with t_{on} works best as the shear stress is already fully developed and the transient stress affects the dynamics less. For narrow channels, the stopping time is small and the fluid will stop abruptly giving rise to large undershoots in the velocity. In wide channels, viscous damping at the walls is small and the fluid remains in motion for a long time, even allowing oscillations. The normal stress is affected by the transient flow, but does not couple back since the symmetry of the channel prevents secondary flows for low Reynolds numbers. Overshoots are found in the normal stress difference for all channel diameters, and the largest for wide channels. The stopping flow is much slower. Because of the quadratic dependence on the shear rate, the oscillations delay the decay of the normal stress.

We have shown that by varying the channel diameter, we can change the time scale t_{on} on which the flow develops. The evolution of the transient stress is complex and complicated further by its close relation to the velocity profile. The scaling of the transient profiles with t_{on} is not without flaws, but works rather well for both, the velocity and the shear stress. The transient velocity profile becomes time-independent, and only the second time scale set by the viscoelastic shear stress remains. This allows us to clearly identify two different limiting cases. For wide channels, $t_{\mathrm{on}} \gtrsim 2\tau_0$, the startup velocity profiles can be scaled on a single master curve identical to the one of the instantaneous non-linear Maxwell model. The oscillations of the stopping flow change their amplitude and frequency for different channel widths, but do not differ on a qualitative level. The time flow evolves slowly and gives the shear stress enough time to adjust to any changes in the flow. For very narrow channels, $t_{\mathrm{on}} < 0.5\tau_0$, the small startup time allows the fluid to behave initially like a low-viscosity Newtonian fluid. This gives rise to overshoots in the velocity and shear stress during startup. The dynamics of the starting flow is profoundly different from the instantaneous model, and also the stopping flow distinguishes itself substantially from the dynamics in wide channels.

When scaling the time with t_{on}, we can in parts eliminate the purely quantitative influence of the channel diameter on the transient profiles and highlight the qualitative changes. In the following chapters, we therefore continue plotting the time in units of t_{on}. For consistency and comparability, we will also apply the scaling to the normal stress difference, although it should be noted that t_{on} is not the natural time the normal stresses develop

on. So that we can discuss the dynamics throughout the whole channel in time, we choose three exemplary channel diameters. $t_{\text{on}} = 0.1\tau_0$ is a narrow channel in which we find clear overshoots in the velocity and stress. $t_{\text{on}} = 4\tau_0$ is at the far end of wide channels, where the influence of the transient stress is comparably small. $t_{\text{on}} = 1\tau_0$ is just at the brink of developing overshoots. The startup profiles are already quite different to the ones shared by wide channels, but the dynamics are not yet affected by a slow decay to the steady state as for narrow channels.

4.3.3 Transient dynamics of the velocity and shear stress

We will now discuss the full channel dynamics. The fluid properties depend on space and time, so visualizing the results is a 3-dimensional problem. We will resort to two different kind of plots which cut the flow profile along the time axis and transversal to the flow. We will consider the fluid velocity in flow direction u, the shear stress σ_{xy}, the normal stress difference $\sigma_{xx} - \sigma_{yy}$ and the pressure p. The velocity in transversal flow direction is always zero. In the plots showing the transient dynamics in time, e.g. Fig. 4.15, each line gives the fluid property at a different lattice node of the upper channel half, $-1 \leq d \leq 0$. The dynamics of the second channel half is symmetric in d and antisymmetric in case of the shear stress. For convenience, the central, $d = -0.01$, and half-to-center, $d = -0.51$, lines used in previous sections are colored in red and green. As a guide to the eye, every fifth line is colored blue. Each simulation was set up with a $N = 100$ lattice, so in each plot there are 50 lines in total. The time is always given in units of t_{on}. To visualize the changes in the flow profiles in time, the second type of plots consists of two parts, e.g. Fig. 4.16. On the left hand side, the same time-dependent profiles are shown as before. Vertical colored lines are used to mark particular times. The right hand side gives the flow profiles of the fluid at these times using bold lines of the same color. Thin lines are used for profiles at intermediate times. These are equally spaced in the time interval indicated by a horizontal line at the top of the left side. Whenever helpful, a 3D plot is also provided.

In Fig. 4.15 and 4.19 the transient dynamics of the velocity and shear stress are given for three channels with $t_{\text{on}} = 0.1\tau_0$ and $t_{\text{on}} = 1\tau_0$, $t_{\text{on}} = 4\tau_0$, respectively. The first thing to observe is that the dynamics is not independent of the position in the channels. The velocity overshoot is largest in the channel center and has to decrease the closer the fluid is to the wall. Just the other way round, the symmetry of the shear stress requires overshoots to vanish in the channel center, and we find the largest values next to the wall. Nevertheless, the time of the overshoot varies for both values only very slightly. In this section, we will focus on the connection between the velocity and shear stress profiles develop in time and how they interact with each other. For small Reynolds numbers, no secondary flow develops and the normal stresses do not couple back. We can therefore discuss the normal stress difference and the pressure separately in the Sec. 4.3.4.

We have already seen that the transient shear stress has as much influence on the startup velocity profile as the velocity on the shear stress. To understand the interaction, the best place to start looking is in the transient dynamics of the narrow channel, $t_{\text{on}} = 0.1\tau_0$, Fig. 4.15. The small diameter allows the velocity profile to evolve much faster than the shear stress. Recall that in the steady state limit, the shear-thinning non-linear Maxwell model forms two high-shear, low-viscosity regions at the walls and a no-shear, solid-like

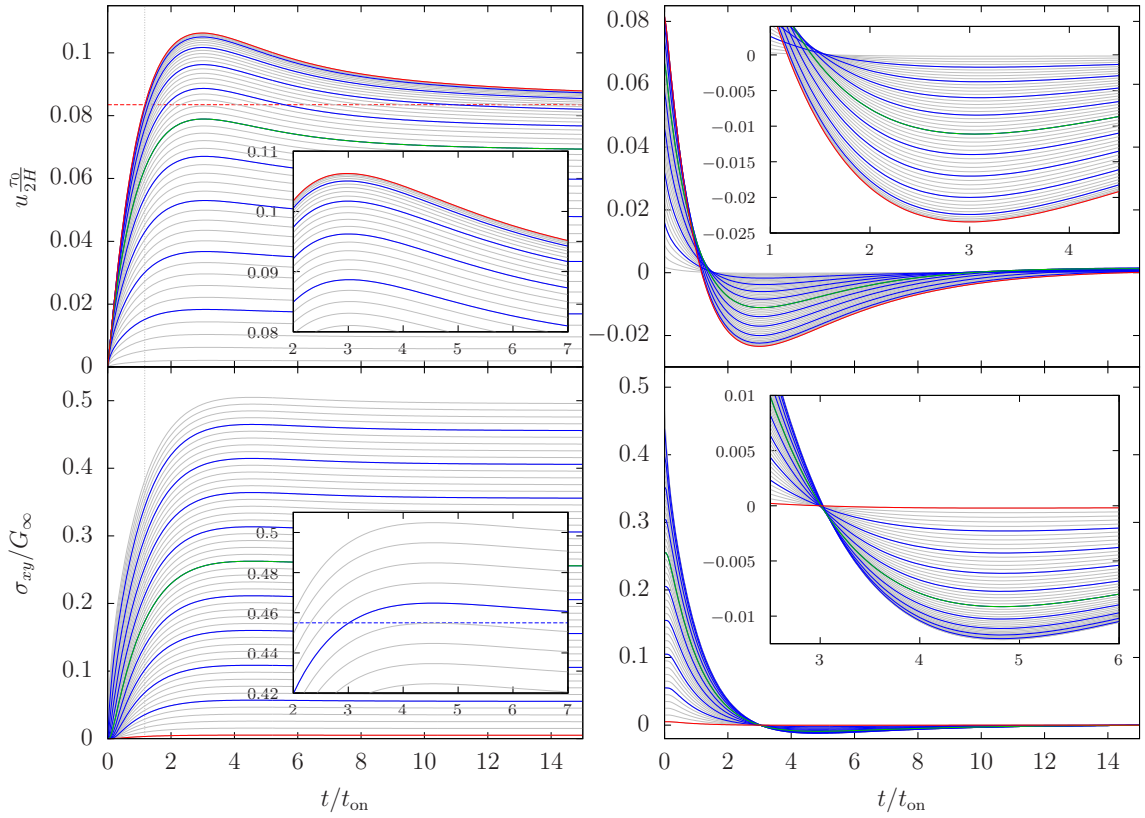

Figure 4.15: Startup (left) and cessation (right) profile for $t_{on} = 0.1\tau_0$ of the velocity (top) and shear stress (bottom). The time is scaled by t_{on}. Lines are LB results at different positions in the channel. The red ($d = -0.01$) and green ($d = -0.51$) lines are the central and half-to-center lines shown before. Every fifth line is colored blue. The dashed lines give the steady state value of the red velocity (top left) and the blue shear stress profile (inset bottom left).

center, which we call a plug flow. At startup, the whole channel is at rest and there is no shear stress. When the pressure is applied, the starting flow of the fluid is the same as for a Newtonian fluid with a viscosity $G_\infty\tau_0$ defined by the lower bound of the non-linear Maxwell model. Until the extra non-Newtonian stress contributions have had enough time to develop and can flatten the parabolic velocity profile to a plug flow profile, we cannot observe any differences to a Newtonian flow. Already at $t = 1.2t_{on}$, the center velocity (red solid line) exceeds the steady state value of a fully developed flow (dashed line). At this point, the shear stress is still well below its own steady state value, which allows the fluid to flow even faster. Because the velocity profile goes to even higher values, the shear stress is forced to exceed the steady state profile, too. The extra stress forces the velocity to now decrease to the true steady state and the plug starts to form. In the insets, we can nicely observe how the stress crossing the steady state value coincides with the maximum velocity. Interestingly, this happens at exactly $t = 3t_{on}$ within the numerical resolution.

Let us take a look at the velocity, Fig. 4.16a, and shear stress profiles, Fig. 4.17a, during the startup flow. For $t < 3t_{on}$, the velocity profile maintains a parabolic shape, and the shear stress has not yet developed the required linear profile (blue curves). At $t = 3t_{on}$ (green), the shear stress is fully developed, but is forced by the high velocity to increase

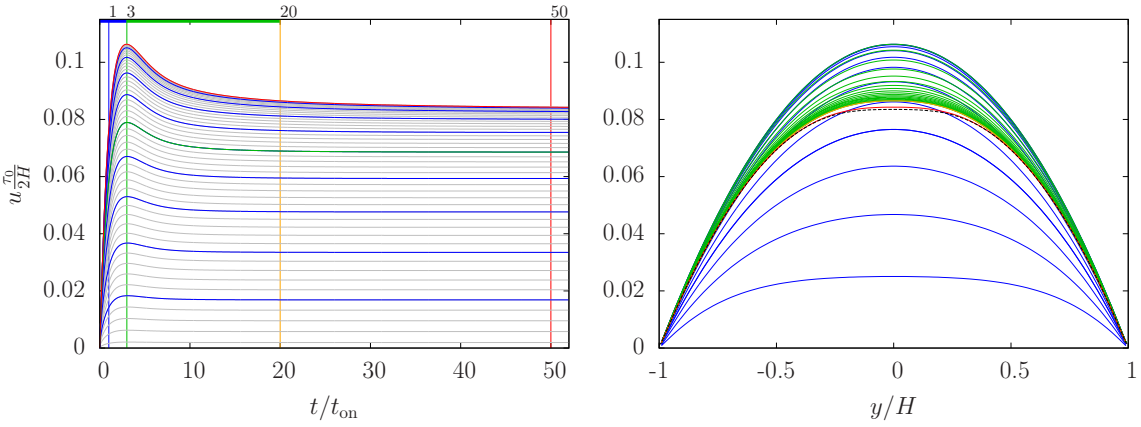

(a) $t_{\mathrm{on}} = 0.1\tau_0$. $\Delta t^{\mathrm{blue}} = 0.25\, t_{\mathrm{on}}$, $\Delta t^{\mathrm{green}} = 1\, t_{\mathrm{on}}$

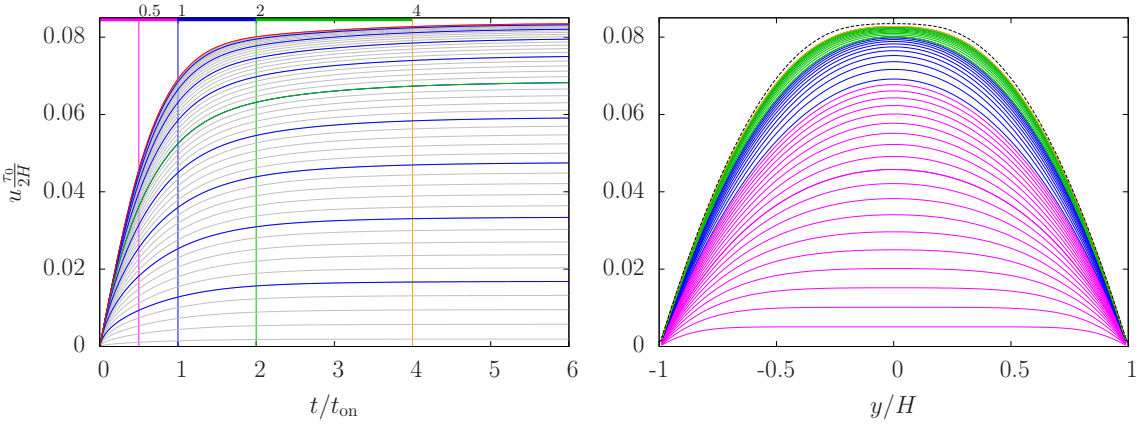

(b) $t_{\mathrm{on}} = 1\tau_0$. $\Delta t^{\mathrm{magenta}} = 0.05\, t_{\mathrm{on}}$, doubling with each new color.

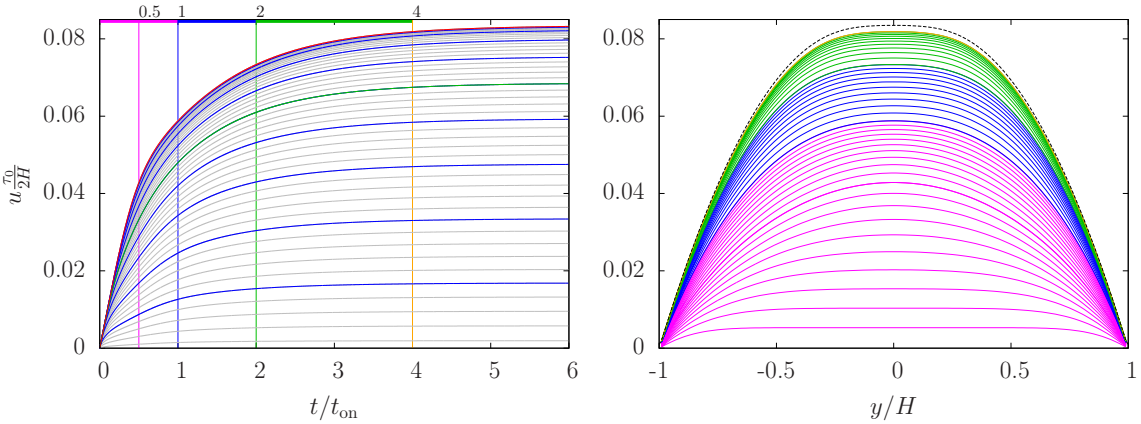

(c) $t_{\mathrm{on}} = 4\tau_0$. $\Delta t^{\mathrm{magenta}} = 0.05\, t_{\mathrm{on}}$, doubling with each new color.

Figure 4.16: Startup flow of the velocity u for three channel diameters, (a)–(c). The intermediate profiles (right) are plotted for different times indicated by a horizontal line of the same color at the top (left). Each line of the same color is separated by Δt. Profiles plotted with bold lines are taken at times marked by vertical lines.

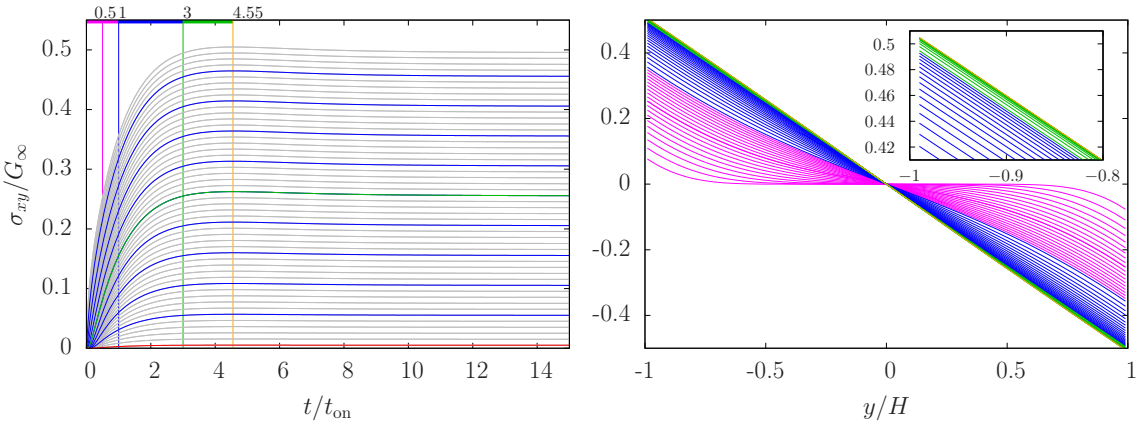

(a) $t_{on} = 0.1\tau_0$. $\Delta t^{magenta} = 0.05\, t_{on}$, doubling with each new color. First steady state crossing (green) again at $t_{on}/\tau_0 = 3$

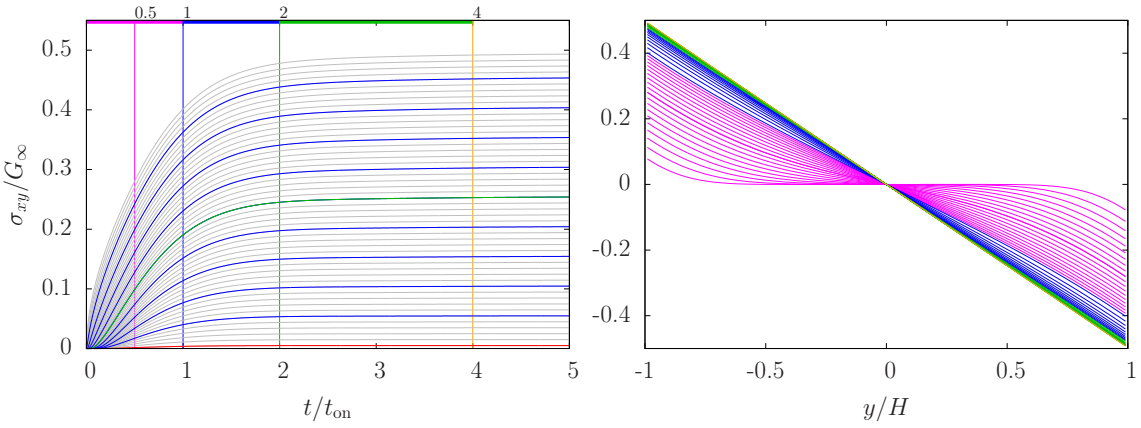

(b) $t_{on} = 1\tau_0$. $\Delta t^{magenta} = 0.05\, t_{on}$, doubling with each new color.

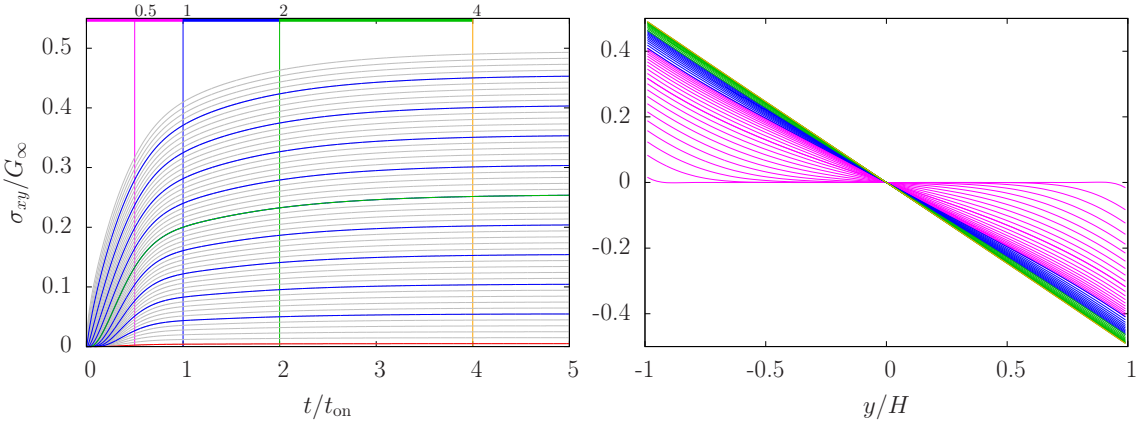

(c) $t_{on} = 4\tau_0$. $\Delta t^{magenta} = 0.05\, t_{on}$, doubling with each new color.

Figure 4.17: Startup flow of the shear stress σ_{xy} for three channel diameters, (a)–(c). The intermediate profiles (right) are plotted for different times indicated by a horizontal line of the same color at the top (left). Each line of the same color is separated by Δt. Profiles plotted with bold lines are taken at times marked by vertical lines.

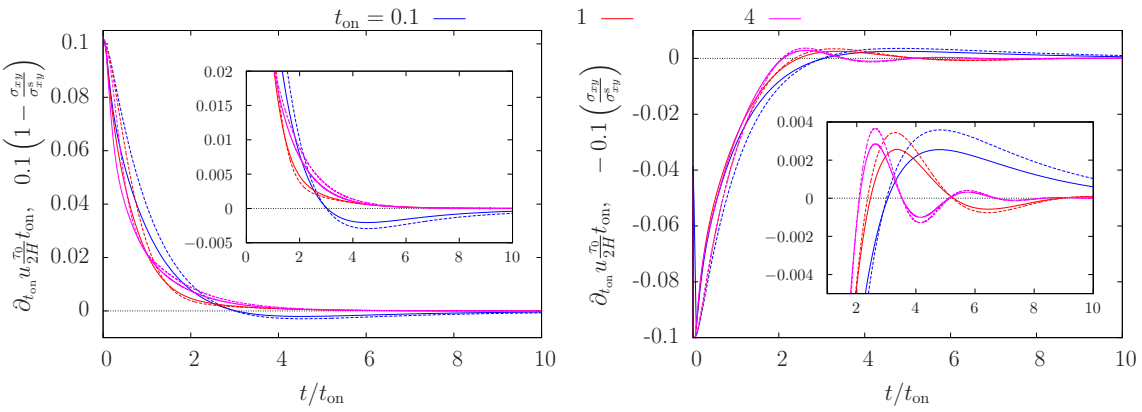

Figure 4.18: Time-derivative of the velocity u (solid lines) and scaled shear stress σ_{xy} (dashed lines) at half-to-center position $d = -0.51$ for three channels with $t_{on}/\tau_0 = \{0.1, 1, 4\}$ during startup (left) and cessation flow(right).

further. The overshoot happening in the shear stress is quite different to the one we observe in the velocity. The flow profile still has a Newtonian parabolic shape when the overshoot is happening. The shear stress, however, has already taken the correct profile the first time it crosses the steady state value, and actually stays true to this linear profile throughout the overshoot. The maximum value is reached at $t = 4.55t_{on}$ (orange), and the difference to the steady state profile appears quite small. The slope does not deviate so much, but it has a huge influence on the flow profile. It is the increased gradient of the shear stress that gives an additional body force, which makes the fluid slow down and form a plug flow, cf. the profiles after the overshoot (green) in Fig. 4.16a.

It takes the velocity much longer to decrease to the steady state value than for the initial startup. In fact, if we measure the time in units of t_{on}, the overshoot makes the fluid need much more time to reach the steady state than it would take otherwise. The reason for this lies in the two separate time scales of the velocity and shear stress. While t_{on} as a funtion of τ_0 is the natural time scale for the evolution of a velocity profile, the time scale for the shear stress is set by τ in the Maxwell model. During the initial low-viscosity flow, the shear rates are significantly larger than they would otherwise be, and the shear stress can develop much faster. Only when the fluid has to slow down as a direct response to the now too large stress, the different time scales become obvious.

Now, we have seen that the velocity takes a maximum value when the shear stresses crosses its steady state value. To see how close the relation between the shear stress and the time derivative of the velocity profile is, we compare both quantities in Fig. 4.18. The shear stress is scaled to give the same starting and steady state values. For very small times, the dynamics of the shear stress is slightly delayed, which was to be expected. Soon however, both curves show an excellent agreement, especially regarding the times of roots and extrema after switching off the pressure (inset right). Even the inflection points of the velocity are given by the extremes of the shear stress. Small deviations stem from the fact that we had to pick a single channel position again.

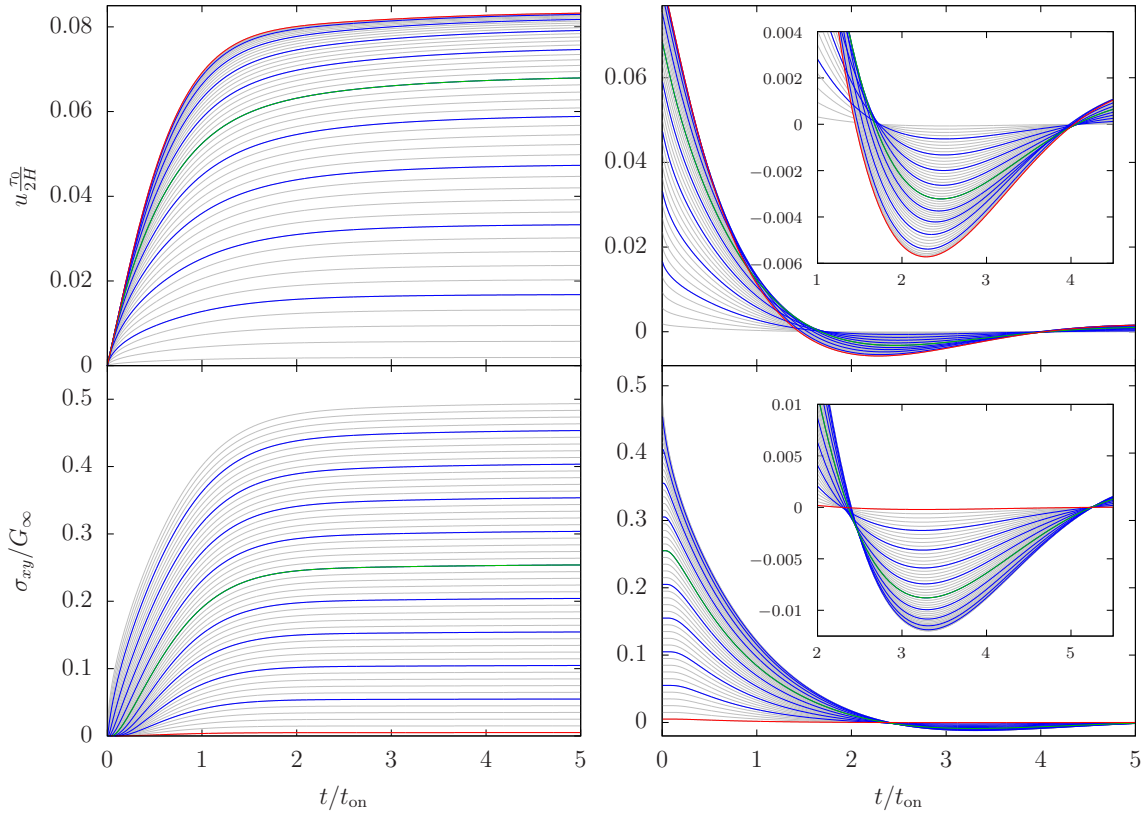

(a) Velocity (top) and shear stress (bottom) for $t_{\text{on}} = 1\tau_0$.

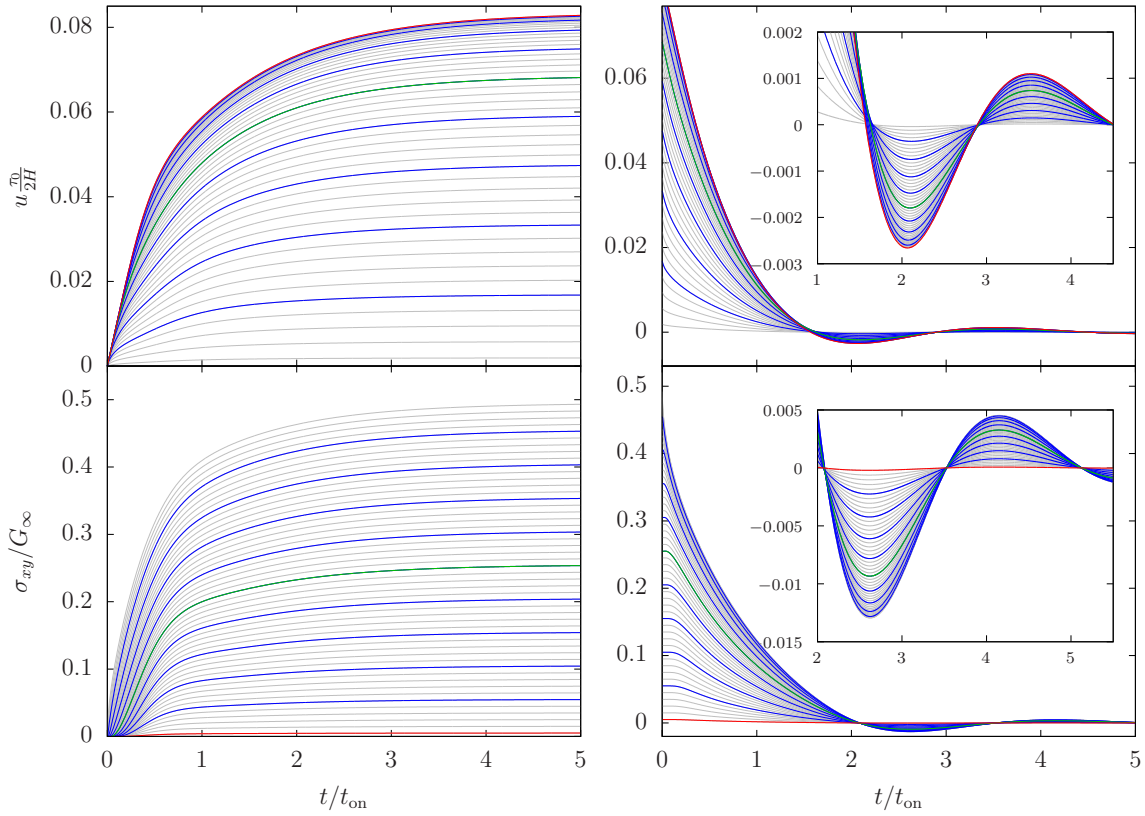

(b) Velocity (top) and shear stress (bottom) for $t_{\text{on}} = 4\tau_0$.

Figure 4.19: Startup (left) and cessation (right) profile of the velocity and shear stress for $t_{\text{on}}/\tau_0 = \{1, 4\}$. The time is scaled by t_{on}. Lines are LB results at different positions in the channel. The red ($d = -0.01$) and green ($d = -0.51$) lines are the central and half-to-center lines shown before. Every fifth line is colored blue.

The startup velocity profiles in the intermediate, $t_{\mathrm{on}} = 1\tau_0$, and wide channel, $t_{\mathrm{on}} = 4\tau_0$, do not show any overshoots, but approach the steady state monotonously from below. For these two channels, the shear stress has significantly more time to develop and reaches the steady state value at about the same time, Fig. 4.19a, or earlier than the velocity, Fig. 4.19b. For $t_{\mathrm{on}} = 1\tau_0$, the velocity forms the plug very late, see Fig. 4.16b, and a non-Newtonian flow profile emerges not until $t \approx 2t_{\mathrm{on}}$. The full plug completes with the velocity approaching the steady state. In a wide channel, $t_{\mathrm{on}} = 4\tau_0$ Fig. 4.16c, the plug forms at a much earlier time, and it is the full non-Newtonian plug flow profile that builds up. In the shear stress profiles, Fig. 4.17, this difference is far less pronounced, yet we can still observe that the shear stress of the wide channel builds up in the channel center faster than outside the plug.

Excursion: Linear Maxwell model

Before we go into any further discussions, let us briefly consider another limiting case of the non-linear Maxwell model. We can identify shear-thinning effects by comparing the results to the instantaneous non-linear Maxwell model, which conveniently shares the same steady state limit. We have seen that the transients of both model are very different, but we cannot tell without doubt which effects we have found are of a purely viscoelastic origin and which are a unique feature of our model. We will therefore consider the linear Maxwell model with a constant Maxwell time τ. The upper convected Maxwell model is well known in the literature and will take a Newtonian flow profile in the steady state limit, but at the same time provides the desired viscoelasticity

$$\boldsymbol{\sigma}(t) = \eta_\infty \boldsymbol{D} + \int_{-\infty}^{t} \mathrm{d}t' \left[\frac{\partial}{\partial t'}\boldsymbol{B}(t,t')\right] G_\infty \mathrm{e}^{(t-t')/\tau}. \tag{4.14}$$

By eliminating the dependence of the Maxwell time on the shear rate we essentially consider the limit of $\gamma_{\mathrm{c}} \to \infty$, and the normal stress difference in a channel flow takes a parabolic shape, cf. Eq. (4.8). For the transient velocity profile, there even exists an analytical solution by Waters and King [101, 102]. Instead of defining a lower bound for the viscosity, the authors introduced an additional retardation time S_2, which plays the same role. Their model is identical to the scalar version of Eq. (4.14) for $S_2 = 1/t_{\mathrm{on}}$ and $S_1 = S_2\,(\tau + \tau_0)$.

We use the same three channel diameters with $t_{\mathrm{on}} = \{0.1, 1, 4\}\tau_0$ as before, the results are given in Fig. 4.20, 4.21, and 4.22. Since the steady state flow is no longer accelerated by shear thinning, the velocity overshoot is much larger than previously. Nevertheless, we find two different starting profiles. In the narrow channel, the startup flow is qualitatively similar to the one of the non-linear Maxwell model. Although the small steady state velocity makes the overshoot appear large, the initial startup has not changed at all. When the shear stress has build up, the flow slows down monotonously down to the steady state profile. In the startup profiles for the intermediate, Fig. 4.21, and the wide channel, Fig. 4.22, we find something new. Unlike the non-linear Maxwell model, the starting flow is no longer monotonously approaching the steady state, but overshoots appear, and unlike the narrow channel, the fluid shows oscillation when slowing down to a steady flow. For $t_{\mathrm{on}} = 4\tau_0$, the velocity even dips briefly into negative values. From the analytical solution, we know the velocity profile to be symmetric for the starting and stopping flow, which the LB

simulations confirm. The symmetry does not survive for the normal stresses, which depend quadratically on the shear rate. Oscillations around the steady state contribute differently during starting and stopping flow.

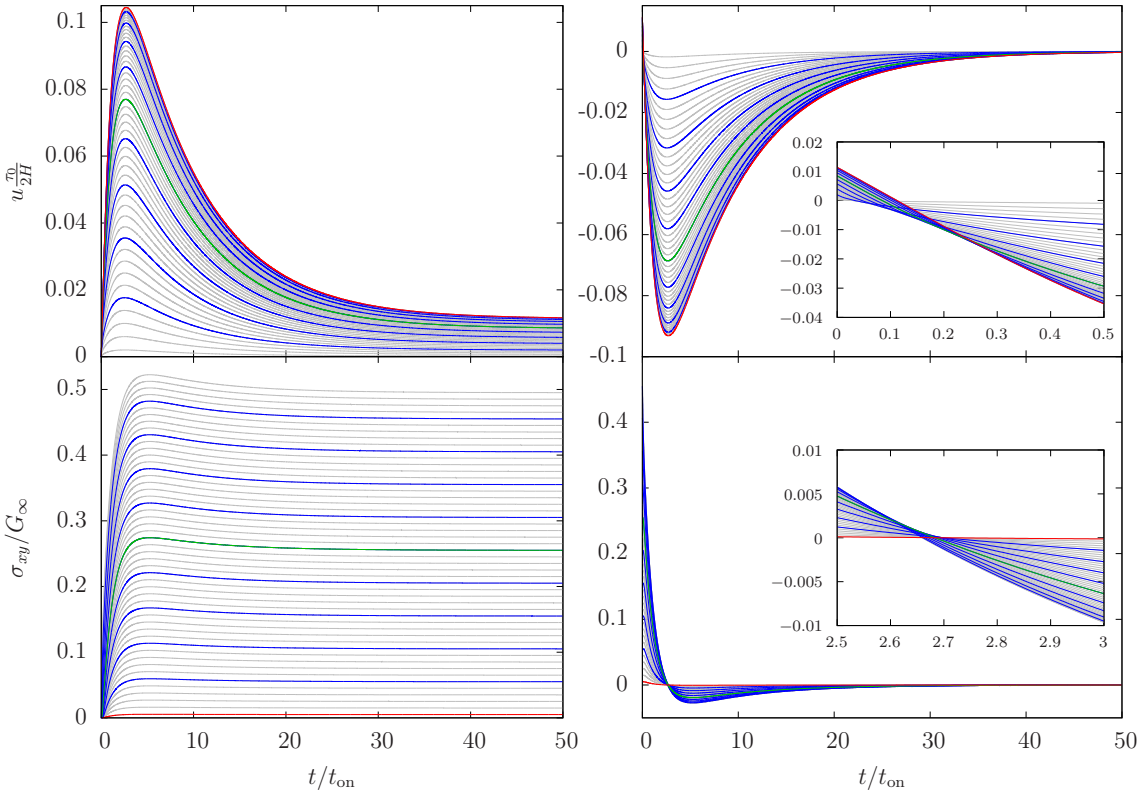

(a) Velocity (top) and shear stress (bottom).

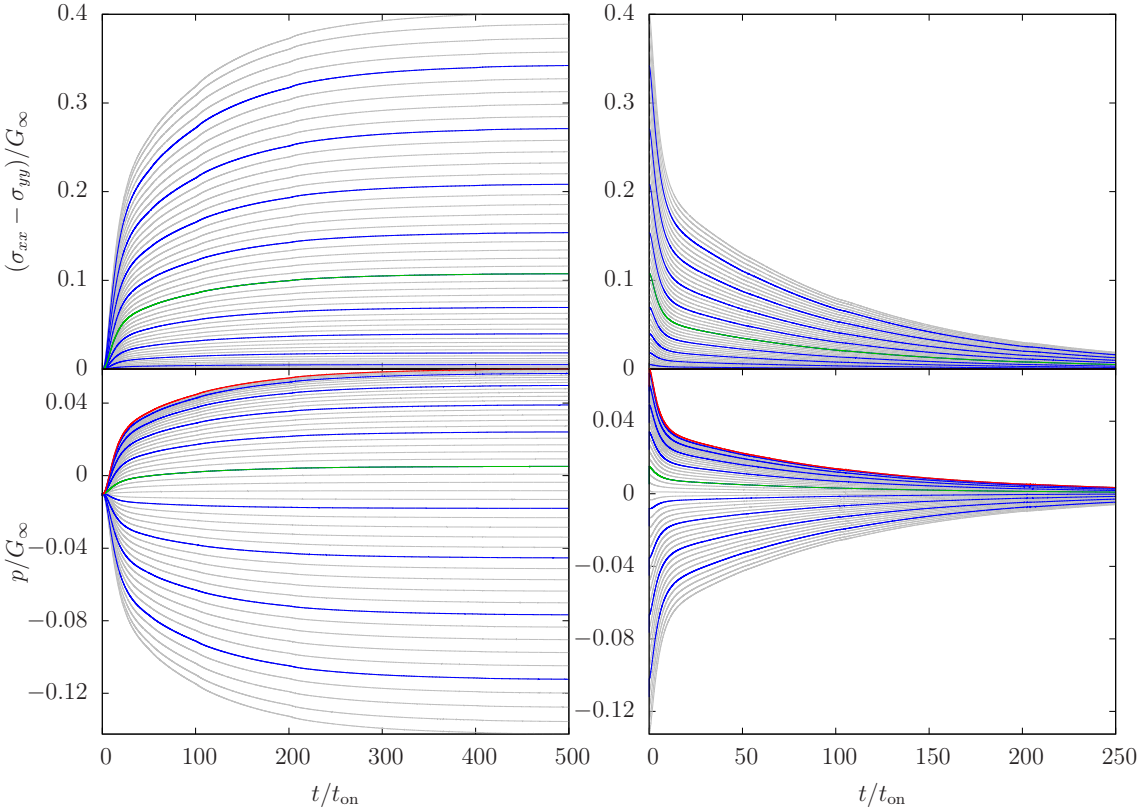

(b) Normal stress difference (top) and pressure (bottom).

Figure 4.20: Maxwell model. Startup (left) and cessation (right) profile for $t_{\text{on}} = 0.1\tau_0$. The time is scaled by t_{on}. Lines are LB results at different positions in the channel. The red ($d = -0.01$) and green ($d = -0.51$) lines are the central and half-to-center lines shown before. Every fifth line is colored blue.

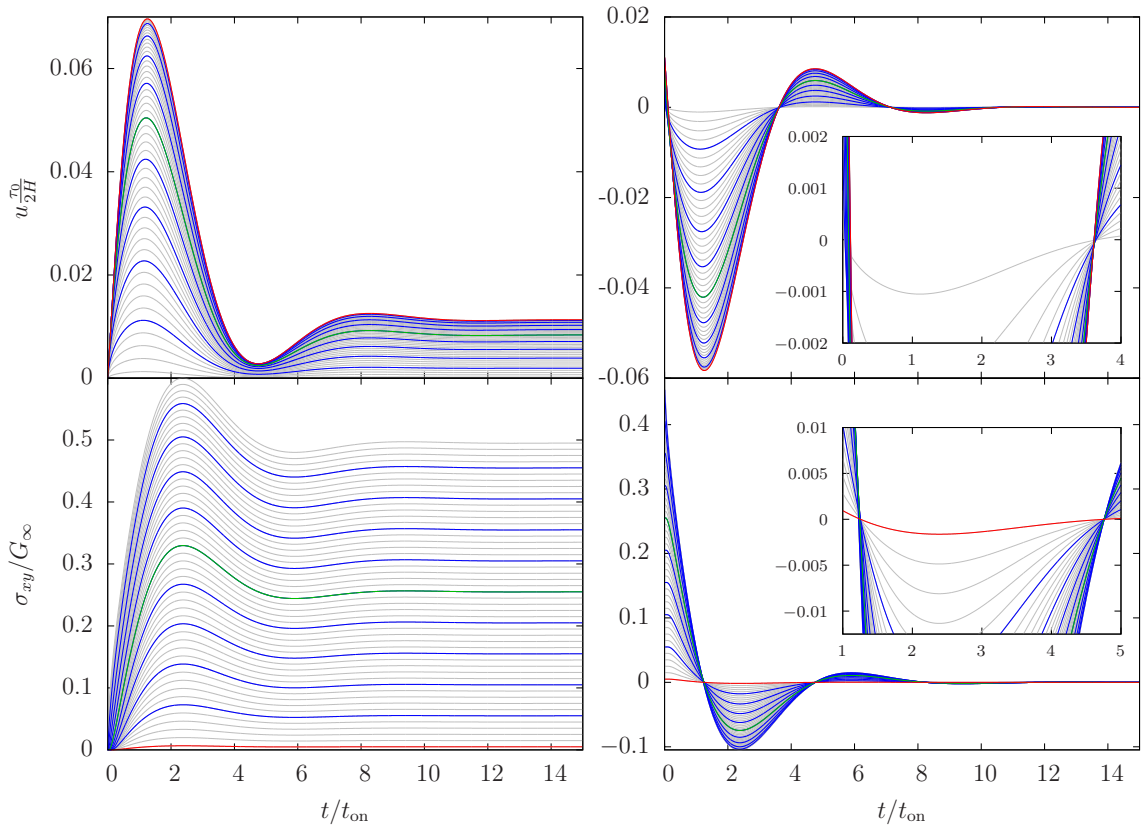

(a) Velocity (top) and shear stress (bottom).

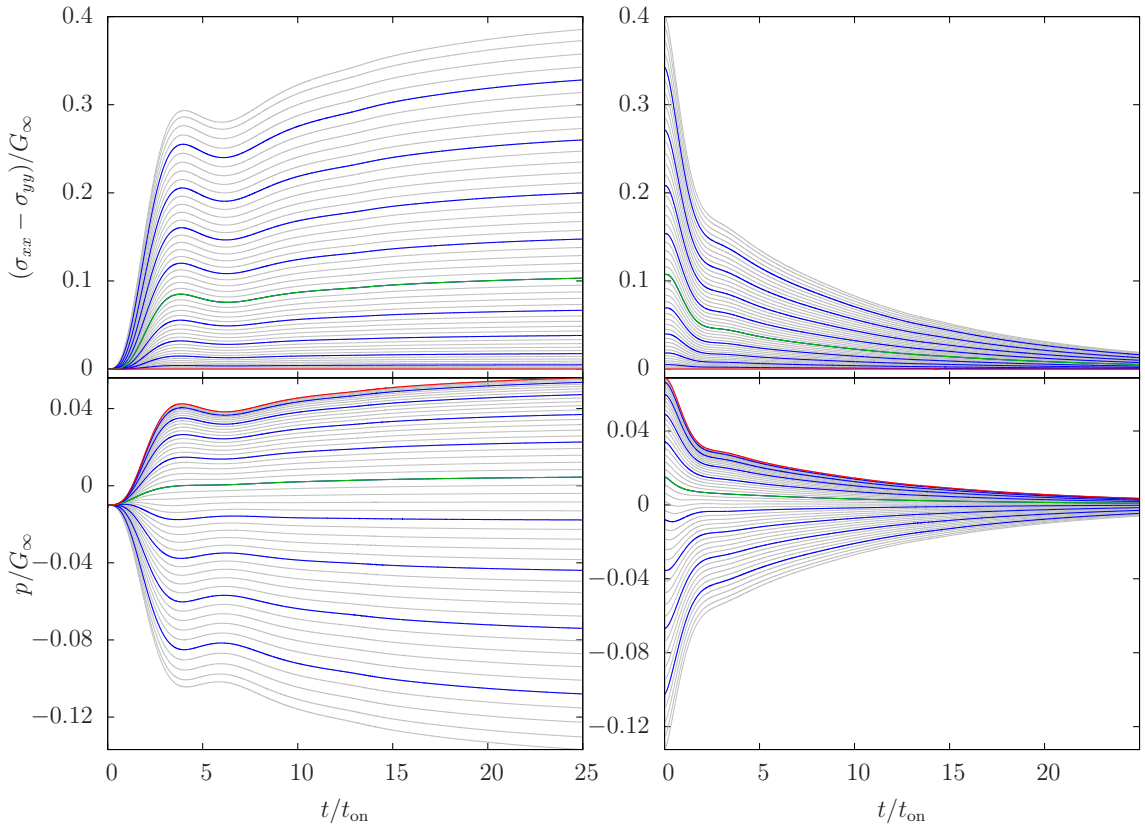

(b) Normal stress difference (top) and pressure (bottom).

Figure 4.21: Maxwell model. Startup (left) and cessation (right) profile for $t_{\text{on}} = 1\tau_0$. The time is scaled by t_{on}. Lines are LB results at different positions in the channel. The red ($d = -0.01$) and green ($d = -0.51$) lines are the central and half-to-center lines shown before. Every fifth line is colored blue.

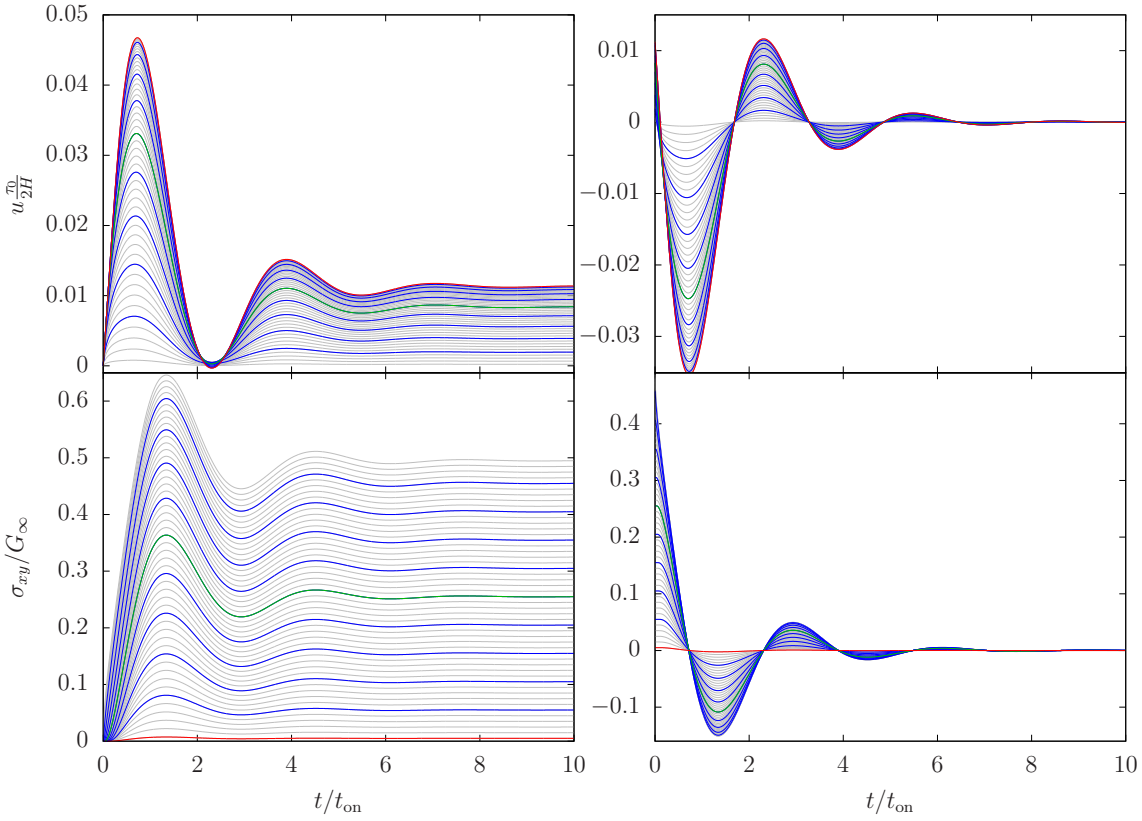

(a) Velocity (top) and shear stress (bottom).

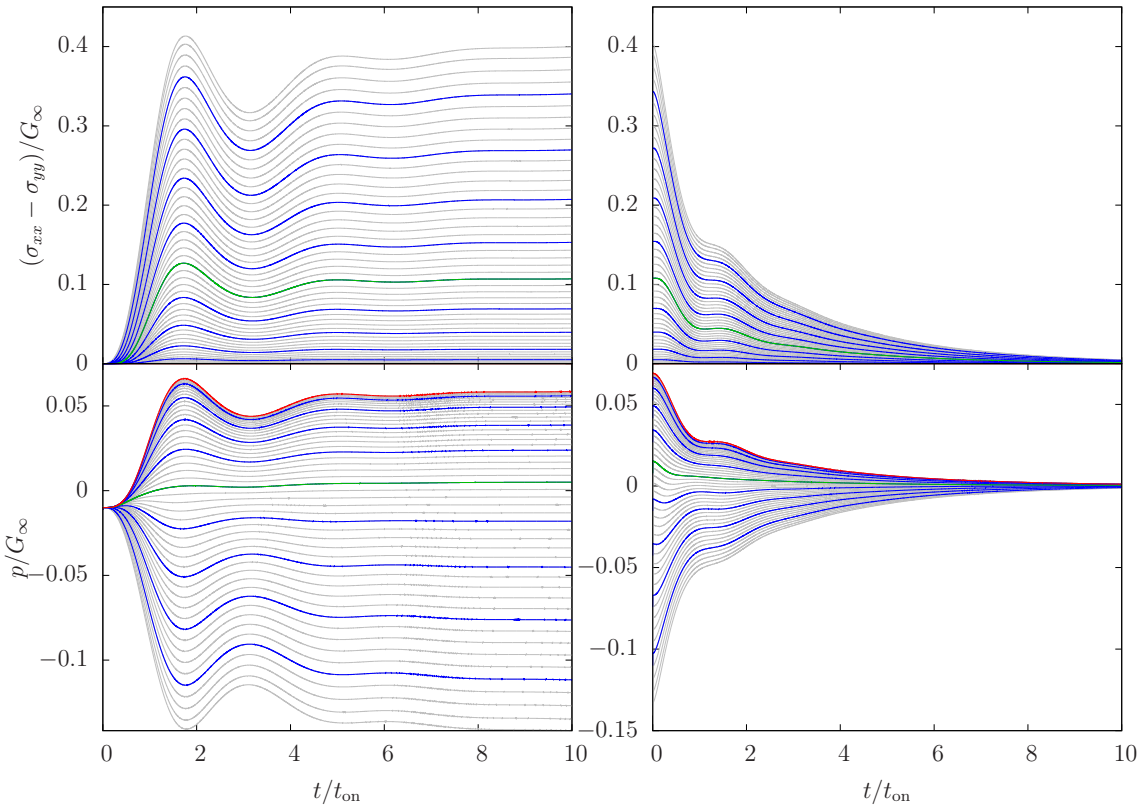

(b) Normal stress difference (top) and pressure (bottom).

Figure 4.22: Maxwell model. Startup (left) and cessation (right) profile for $t_{\text{on}} = 4\tau_0$. The time is scaled by t_{on}. Lines are LB results at different positions in the channel. The red ($d = -0.01$) and green ($d = -0.51$) lines are the central and half-to-center lines shown before. Every fifth line is colored blue.

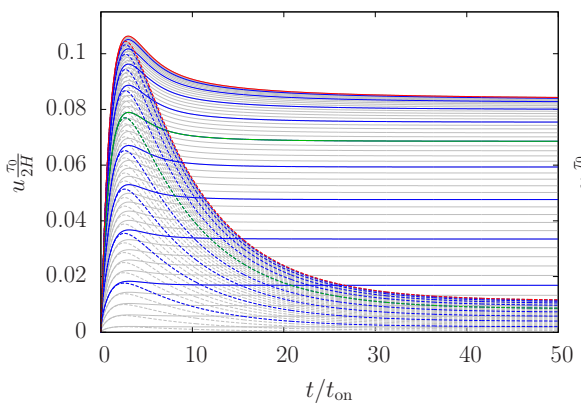

(a) $t_{\text{on}} = 0.1\tau_0$

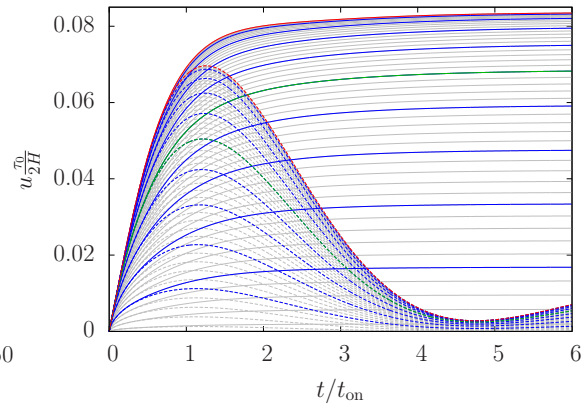

(b) $t_{\text{on}} = 1\tau_0$

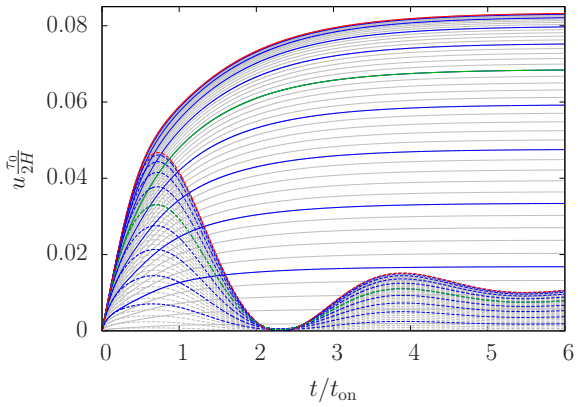

(c) $t_{\text{on}} = 4\tau_0$

Figure 4.23: Startup profiles for the non-linear (solid lines) and linear (dashed lines) Maxwell model profile for three channel diameters (a)–(c).

Back to topic

We have seen that for the narrow channel the transient dynamics of the linear and the full non-linear Maxwell model only deviate after the overshoot. In case of the intermediate and wide channel, the overshoots are lost in the shear-thinning model. However, they are not gone without leaving a trace. The kinks in the velocity profile where the starting flow suddenly slows down are nothing else but a resident of the viscoelastic overshoot, see Fig. 4.23. Because shear-thinning can only affect the flow once the transient stress is developed far enough, the initial starting flow is the same for both Maxwell models. The shear-thinning fluid takes advantage of the fast startup and only then takes charge of the dynamics. The velocity is still well below the steady state value and continues to increase, but the viscoelastic part is no longer helping.

Let us come back to the non-linear Maxwell model and take a look at the cessation profiles next, Fig. 4.15 and Fig. 4.19. For all channel diameters, we find undershoots in both, the velocity and shear stress transients. The velocity decays indeed faster than the stress, and the resident stress causes a flow reversal. The switch-off profiles for $t_{\text{on}} = 0.1\tau_0$ shows a different behavior than the ones in wider channels. The undershoot happens again at $t = 3t_{\text{on}}$, just like the overshoot during startup. In fact, the transients behave very

similar in both cases. Because t_{on} is very small, much of the symmetry of a non-shear thinning fluid is conserved in the narrow channel. After the undershoot, the velocity and shear stress decay slowly to zero and exhibit no further oscillations, quite differently to the other two channels.

For $t_{\mathrm{on}} = 1\tau_0$ and $t_{\mathrm{on}} = 4\tau_0$, the fluid shows a completely new transient behavior when the driving pressure is removed. During startup any viscoelastic oscillations are fairly well concealed by the overall flow buildup because the steady state flow profile of a shear-thinning fluid is so much larger. Yet for the stopping flow, the steady state is the same for any fluid, and viscoelastic effects can resurface. Indeed, the velocity and stress profiles not only show a single undershoot, but the same kind of damped oscillations we found earlier for the linear Maxwell model. In wide channels the viscous damping by the walls is small enough to allow several oscillations before the residual stress is decayed.

These are actually the same limiting cases known from a damped harmonic oscillator. Whereas the narrow channel, $t_{\mathrm{on}} = 0.1\tau_0$, shows the characteristics of an overdamped oscillator, the channels $t_{\mathrm{on}} = \{1, 4\}\tau_0$ are in the underdamped regime. This fits very nicely with the Maxwell model since the model is motivated by a coupled spring-damper system. The mechanism of the oscillations is the same as before, which we can see in the close relation between the slope of the velocity and the shear stress, Fig. 4.18. The velocity decays faster than the stress and the remaining stress makes the fluid move in the opposite direction. Only now, this happens fast enough to be repeated several times.

If we compare the cessation profile of both Maxwell models, we find the non-linear Maxwell model to give much smaller undershoots and oscillations. The shear-thinning property of the fluid affects the flow in two crucial points. First, the initial conditions upon removing the pressure are very different. The amplitude of the velocity profile is much larger than for the linear model, and it takes the fluid longer to stop giving the stress more time to adjust. Second, the overall stress in the fluid is smaller, again thanks to shear-thinning. Since it is the stress driving the system after the pressure is switched off, the amplitude of the oscillations is smaller than for the linear Maxwell model. However, the influence of the different initial conditions wears out fast. After the first undershoot, the frequency of the flow is about the same for both models. Because the flowing steady state is different for a shear-thinning fluid, the symmetry between the starting and stopping flow is lost.

So far we have discussed the flow reversal as if it was a single event in time. However, if we take a closer look, we find that the flow does not decay as one profile to zero. The fluid changes direction at different times throughout the channel, starting with the center. The effect is largest for the narrow channel and considerably smaller for the wide one, see insets in Fig. 4.15 and Fig. 4.19. For $t_{\mathrm{on}} = 1\tau_0$, it does not stop there. The shear stress shows a similar behavior, and the undershoots are distinctively tilted in time favoring the channel center at early times. Different to the other two channels, the nonuniform evolution of the velocity continues past the first undershoot and is still visible when the flow changes direction a second time.

Fig. 4.24 shows the full velocity profiles during the stopping flow. We can clearly observe how the plug flow profile breaks down and the channel center runs ahead. For $t_{\mathrm{on}} = 1\tau_0$, the effect is most pronounced and gives the impression of two profiles decaying side by side. After the flow has reversed, we find the fluid to behave very differently for each channel.

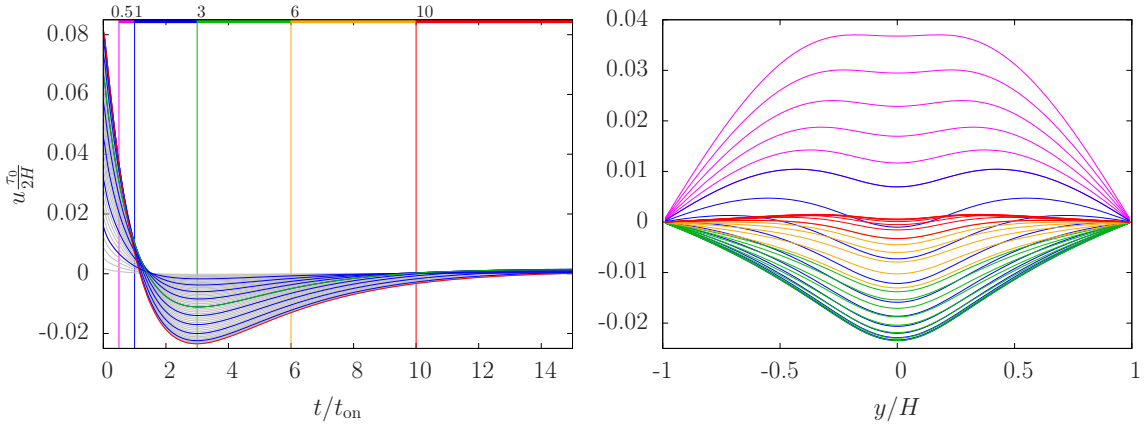

(a) $t_{\text{on}} = 0.1\tau_0$. $\Delta t^{\text{magenta}} = 0.1\, t_{\text{on}}$, doubling with each new color.

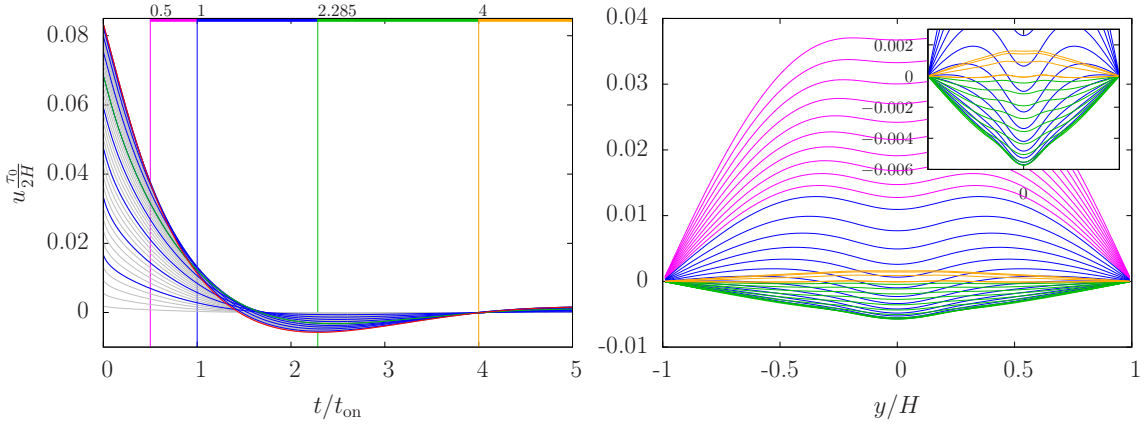

(b) $t_{\text{on}} = 1\tau_0$. $\Delta t^{\text{magenta}} = 0.05\, t_{\text{on}}$, doubling with each new color.

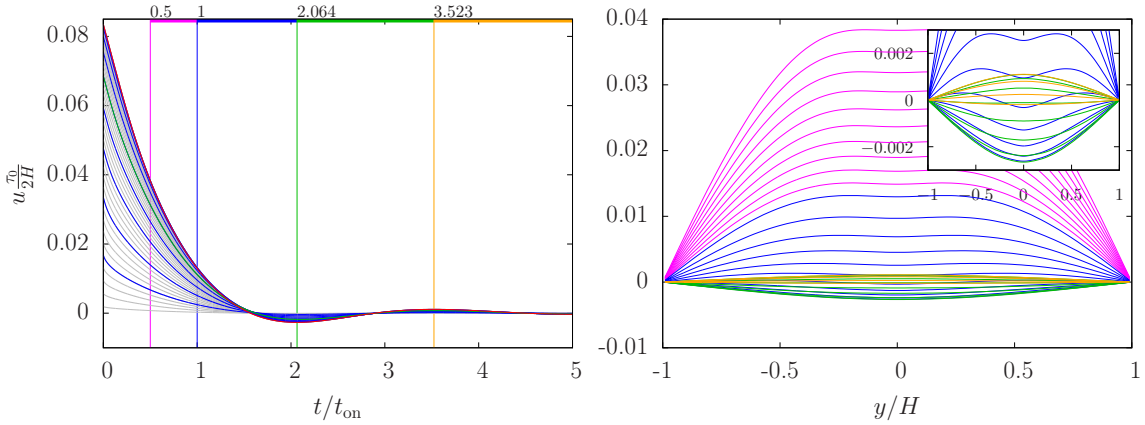

(c) $t_{\text{on}} = 4\tau_0$. $\Delta t^{\text{magenta}} = 0.05\, t_{\text{on}}$, doubling with each new color.

Figure 4.24: Stopping flow of the velocity u for three channel diameters, (a)–(c). The intermediate profiles (right) are plotted for different times indicated by a horizontal line of the same color at the top (left). Each line of the same color is separated by Δt. Profiles plotted with bold lines are taken at times marked by vertical lines.

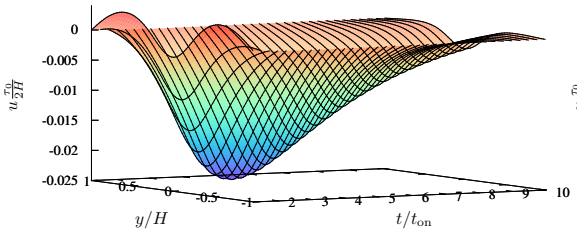

(a) $t_{\mathrm{on}} = 0.1\tau_0$

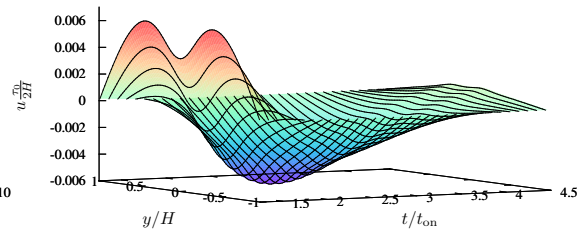

(b) $t_{\mathrm{on}} = 1\tau_0$

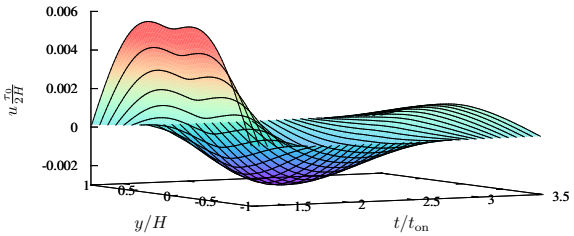

(c) $t_{\mathrm{on}} = 4\tau_0$

Figure 4.25: Stopping flow of the velocity profile for three channel diameters (a)–(c).

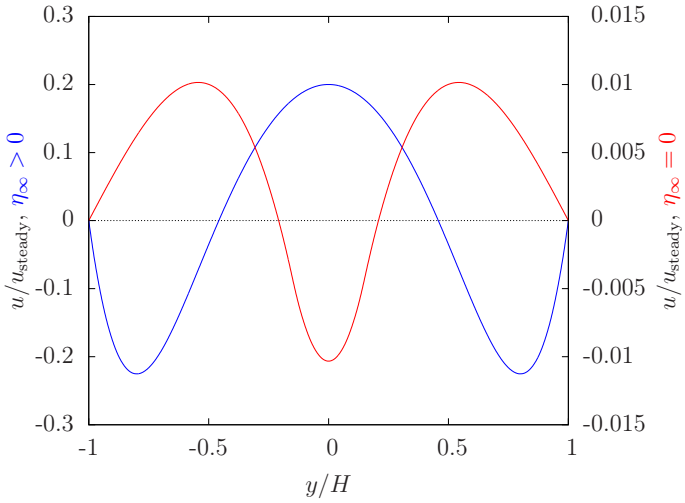

Figure 4.26: Velocity profile of the linear Maxwell model when changing the flow direction for the first time after the pressure is switched off. The parameters are set $t_{\mathrm{on}} = 1\tau_0$, $\tau_0 = 1$s, and $\tau = 10$s. For the blue profile (left y-axis) a minimal viscosity $\eta_\infty = G_\infty\tau_0$ is defined, but not for the red profile (right y-axis). Both profiles are analytical results and scaled by the flowing steady state value.

Let us start with the easiest one. In the wide channel the profile soon loses much of its distinct form and is not so much different from an ordinary parabolic flow profile. This is especially true for the following oscillations and explains why the cessation profile is quite similar to the one of the linear Maxwell model after the initial undershoot.

The intermediate channel is the most interesting one. The flow decays much faster in the channel center than at the walls, and the region seems to coincide roughly with previous plug. This reinforces the impression of two only slightly coupled stopping flows next to each other. This thought is not so far off as it might seem since in the glass limit the fluid does form two perfectly Newtonian half-channels separated by a comoving plug. After reaching the minimal velocity, the profile does not smooth out, but forms an additional pair of wiggles. The oscillations inside the profile survive for a long time and well beyond the flow changes directions the second time, see also the $3D$ plot Fig. 4.25.

The narrow channel is different to the both underdamped cases of the wider channels.

Again the center slows down fastest, but after the first undershoot, the fluid slows down very slowly. If we take a very close look, we find that the flow is not perfectly overdamped, but the velocity profile dips very slightly into positive values again. However, the overall shape of the profile, one local minimum flanked by two maxima, does not change at all during the stopping flow.

The shear stress profiles, Fig. 4.27, behave just like one would expect from the velocity profiles. Thanks to the channel geometry, the point symmetry is conserved. At the edge of the plug, the shear stress decays slightly faster than in the rest of the channel. It is this non-monotonic shear profile that causes the flow to form its distinct profile.

If we look back to the linear Maxwell model, we also find a nonuniform decay of the velocity, but the models differ in one important point. The profile is more or less inverted, and the fluid in the center of the channel does not run ahead, but actually lags behind. However, if we remove the retardation time, that is the lower viscosity bound, the velocity profile changes again and looks very much like the one of the non-linear Maxwell model. Fig. 4.26 shows the profiles for the intermediate channel, $t_{\mathrm{on}} = 1\tau_0$. Notice not only how similar the red velocity profile is to the ones we found in Fig. 4.24b, but the amplitude is also substantially smaller once the lower viscosity bound is removed. These results compare extremely well to the non-linear Maxwell model. The pressure is switched off after the flowing steady state is fully developed. Because the generalized Maxwell time $\tau_{\mathrm{M}}[\dot{\gamma}]$ allows the fluid to decay on a faster, shear-induced time scale, in the stopping flow the fluid is more closely related to the linear Maxwell model without a retardation time.

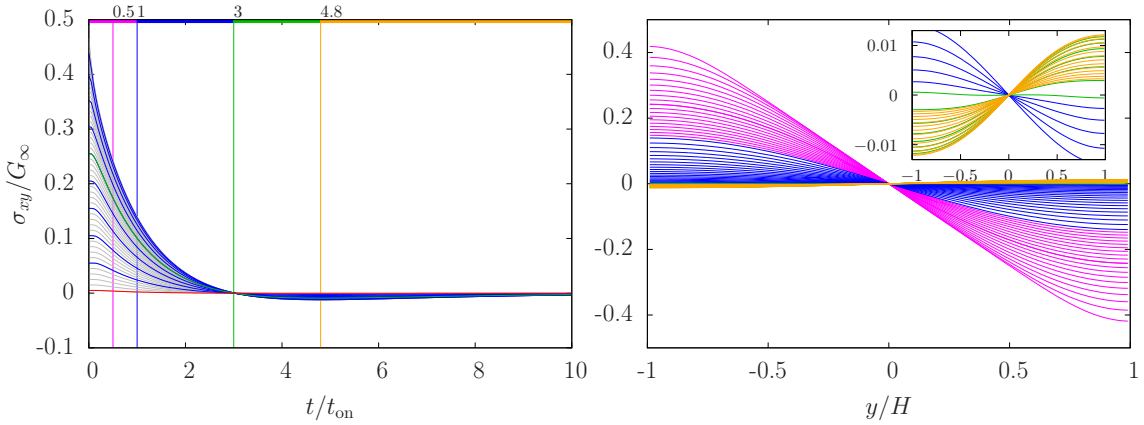

(a) $t_{\mathrm{on}} = 0.1\tau_0$. $\Delta t^{\mathrm{magenta}} = 0.05\, t_{\mathrm{on}}$, doubling with each new color. First zero-crossing (green) again at $t_{\mathrm{on}}/\tau_0 = 3$

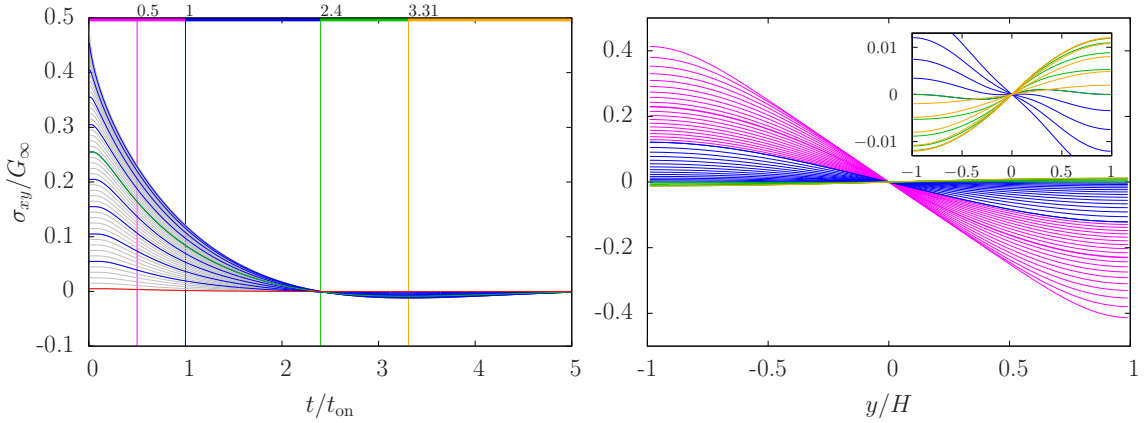

(b) $t_{\mathrm{on}} = 1\tau_0$. $\Delta t^{\mathrm{magenta}} = 0.05\, t_{\mathrm{on}}$, doubling with each new color.

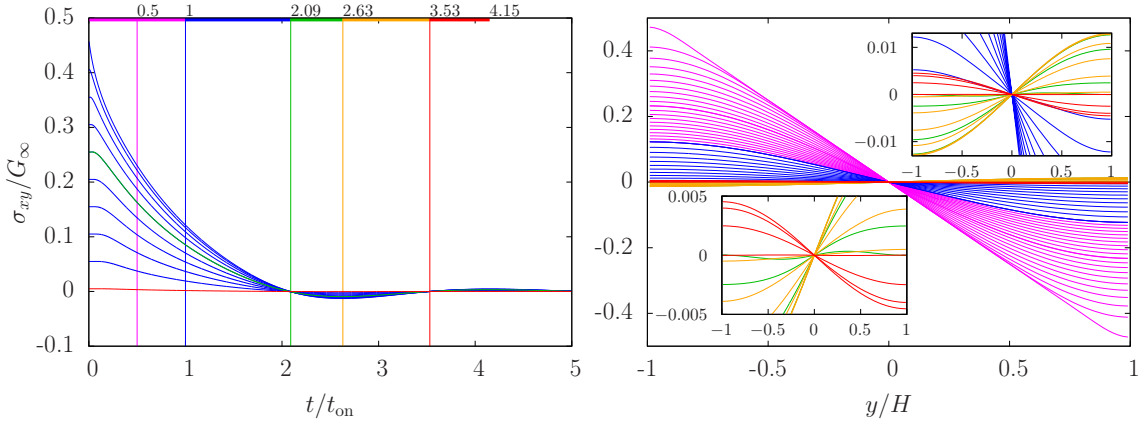

(c) $t_{\mathrm{on}} = 4\tau_0$. $\Delta t^{\mathrm{magenta}} = 0.05\, t_{\mathrm{on}}$, $\Delta t^{\mathrm{blue}} = 0.1\, t_{\mathrm{on}}$, $\Delta t^{\mathrm{green}} = \Delta t^{\mathrm{orange}} = \Delta t^{\mathrm{red}} = 0.2\, t_{\mathrm{on}}$

Figure 4.27: Stopping flow of the shear stress σ_{xy} for three channel diameters, (a)–(c). The intermediate profiles (right) are plotted for different times indicated by a horizontal line of the same color at the top (left). Each line of the same color is separated by Δt. Profiles plotted with bold lines are taken at times marked by vertical lines.

4.3.4 Transient dynamics of the normal stress difference and pressure

The physics behind the normal stress and pressure transients is much more simple than for the shear stress and velocity. We consider non-turbulent flows at low Reynolds numbers. Because the fluid only moves in channel direction and does not form any secondary flows, the normal stress transients are certainly affected by the way the flow evolves, but the coupling does not work both ways. Instead the normal stresses pointing to the channel center are balanced out by a pressure gradient, which decreases towards both walls.

Having said that, let us take a brief look at the linear Maxwell model first, see Fig. 4.20b, 4.21b, and 4.22b. Sure enough, we find the normal stress difference to be affected by the transient flow profile. Except for the narrow channel, the transients show oscillations, which are on par with the shear stress. The overshoots vary in their amplitudes, but take place at almost the same time throughout the channel. The velocity and shear stress are closely coupled and need to reach their steady states at the same time. There is no such constraint for the normal stresses, which are free to evolve on their own time scale. This is especially notable for the narrow channel, which small diameter makes the flow develop about 10 times faster than the normal stress difference. Actually, the normal stress difference reaches the steady state at about the same time in all three channels, which is obscured by the scaling with t_{on}. This also explains, why we do not find any oscillations in the transient profile of the narrow channel. From the point of view of the normal stresses, the flow has more or less always been fully developed. For very small times, the startup is accelerated by the overshoot in the velocity, but beside that the normal stress difference evolves as if under steady shear.

The normal stress difference does not share the symmetry the linear Maxwell model shows in the transient dynamics under startup and cessation flow. Because of the quadratic dependence on the strain rate, the normal stresses distinguishes between a flowing and a no-flow steady state. Velocity oscillations inhibit the evolution during startup, but delay the decay in the stopping flow. The dynamics of the pressure gradient mirrors the normal stress difference. The boundary condition ensures the average pressure in transverse flow direction to remain constant and provides an overall pressure gradient. Because the lattice has no node in the perfect center of the channel, the pressure starts with a small but negative value. The offset between the startup and cessation pressure profiles comes from switching of the driving pressure and thereby removing this constraint. Shock waves cannot be described by the LB model, yet the jump happens too fast to show up in the plot and does not affect the pressure transients beyond this offset.

The transient normal stress profile of the non-linear Maxwell model is much more complicated, see Fig. 4.28 and Fig. 4.29. We find overshoots, but no oscillations in the transients of the three channel. The overshoots are relatively small in the narrow channel, but already well pronounced for $t_{\mathrm{on}} = 1\tau_0$ and even larger in the wide channel. The real difference to the linear Maxwell model, however, is in the transients of each channel. Before, the overshoots occurred at about the same time throughout the channel, only the amplitude decreased towards the center. For the non-linear Maxwell model, however, the first and largest overshoots appear near the walls. Not only become the overshoots more delayed and smaller the more central the transients are, but at some point they are gone altogether. In the channel center, about the area of the plug, the normal stress difference approaches

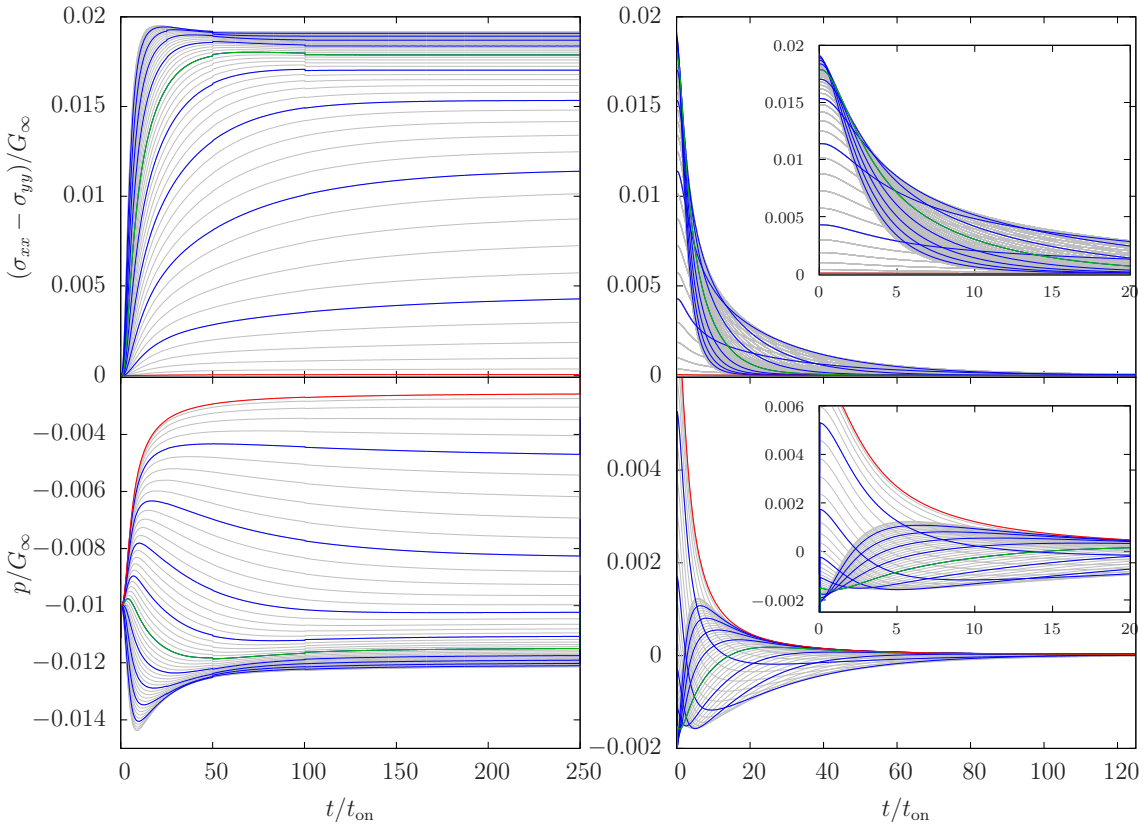

Figure 4.28: Startup (left) and cessation (right) profile for $t_{\text{on}} = 0.1\tau_0$ of the normal stress difference (top) and pressure (bottom). The time is scaled by t_{on}. Lines are LB results at different positions in the channel. The red ($d = -0.01$) and green ($d = -0.51$) lines are the central and half-to-center lines shown before. Every fifth line is colored blue.

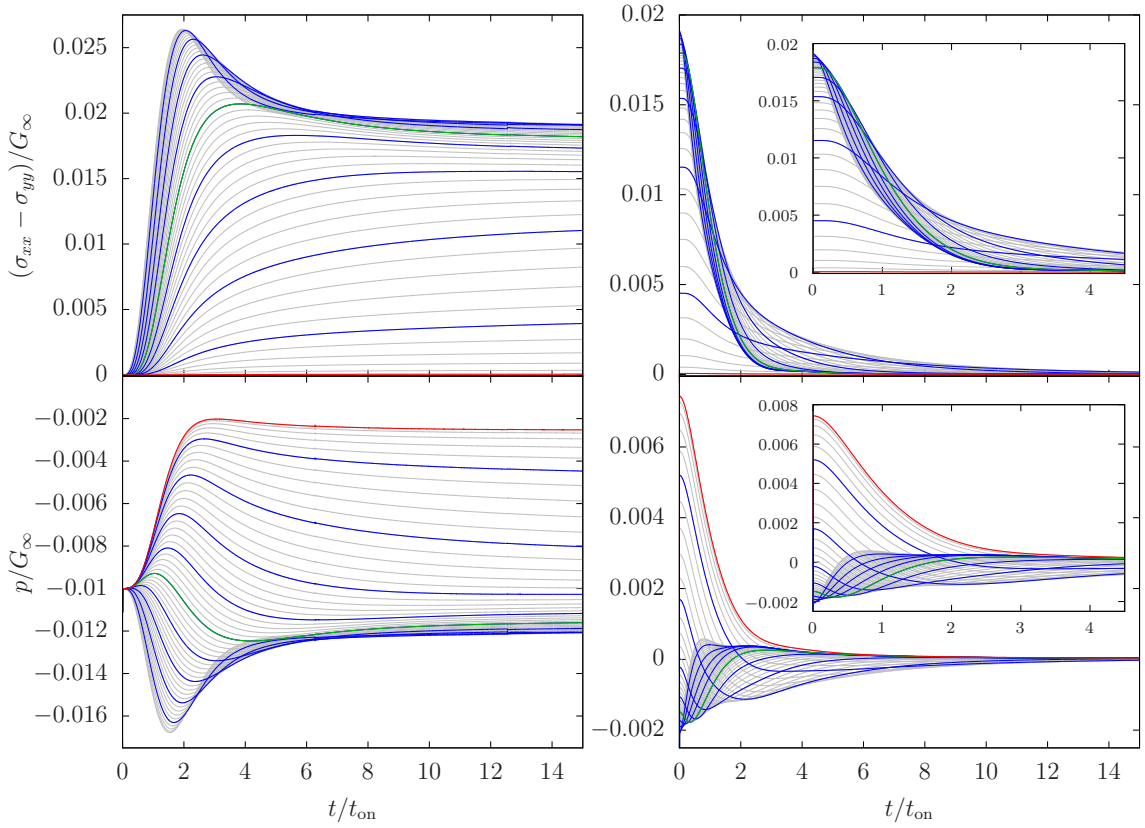

(a) Normal stress difference (top) and pressure (bottom) for $t_{\text{on}} = 1\tau_0$.

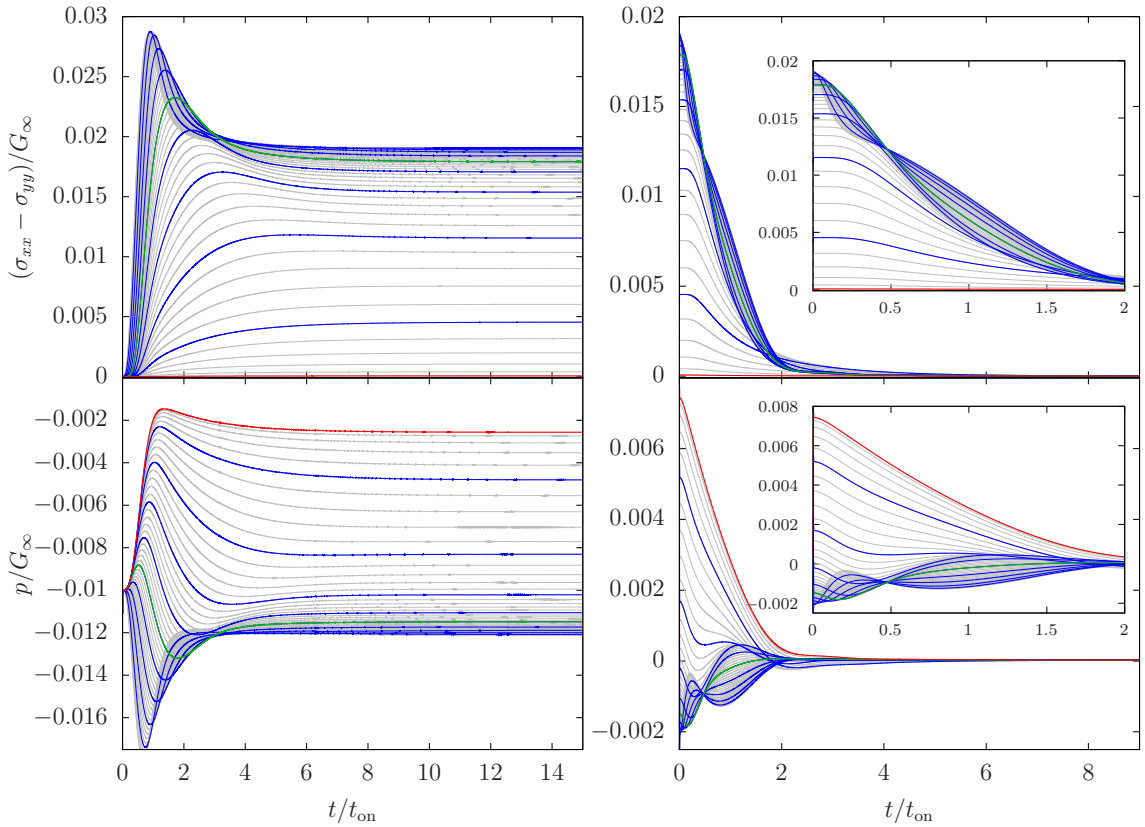

(b) Normal stress difference (top) and pressure (bottom) for $t_{\text{on}} = 4\tau_0$.

Figure 4.29: Startup (left) and cessation (right) profile for $t_{\text{on}} = \{1, 4\}\tau_0$. The time is scaled by t_{on}. Lines are LB results at different positions in the channel. The red ($d = -0.01$) and green ($d = -0.51$) lines are the central and half-to-center lines shown before. Every fifth line is colored blue. Dashed black lines give the steady state profile.

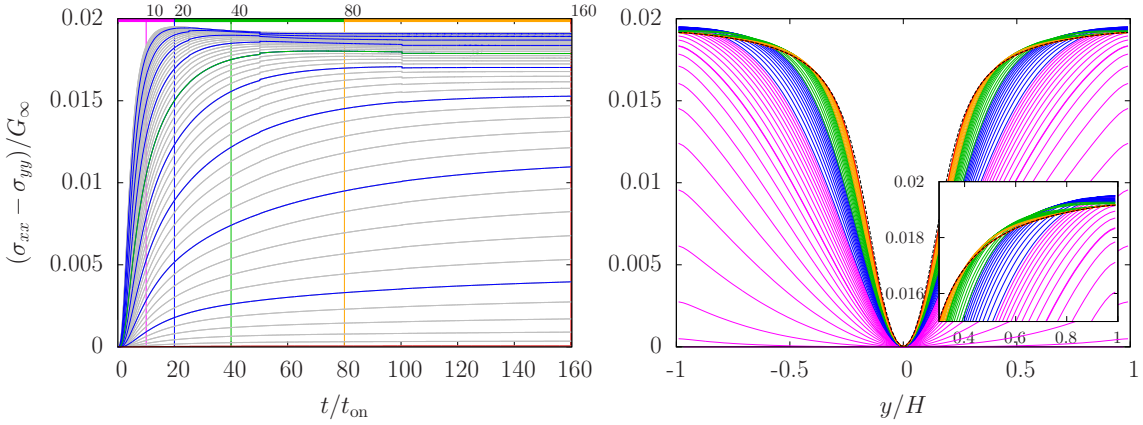

(a) $t_{on} = 0.1\tau_0$. $\Delta t^{magenta}/t_{on} = 0.1\, t_{on}$, doubling with each new color.

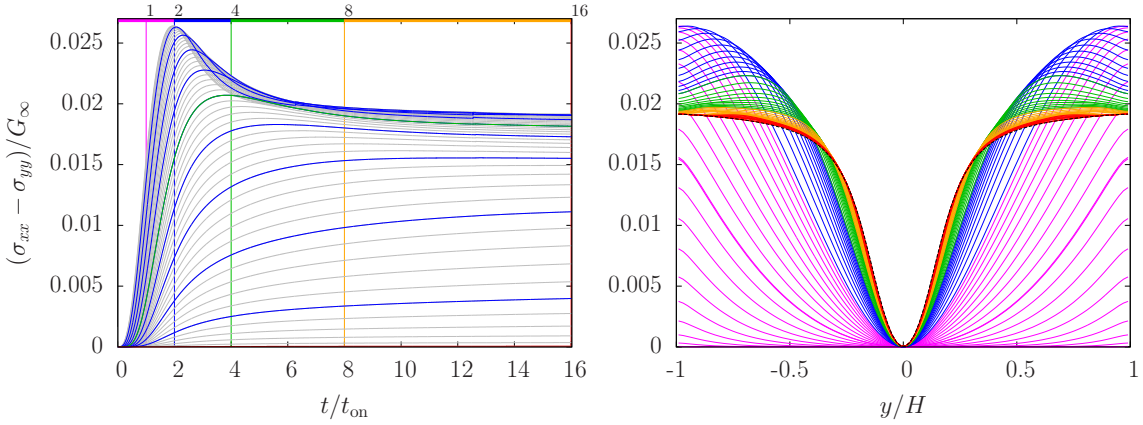

(b) $t_{on} = 1\tau_0$. $\Delta t^{magenta}/t_{on} = 0.1\, t_{on}$, doubling with each new color.

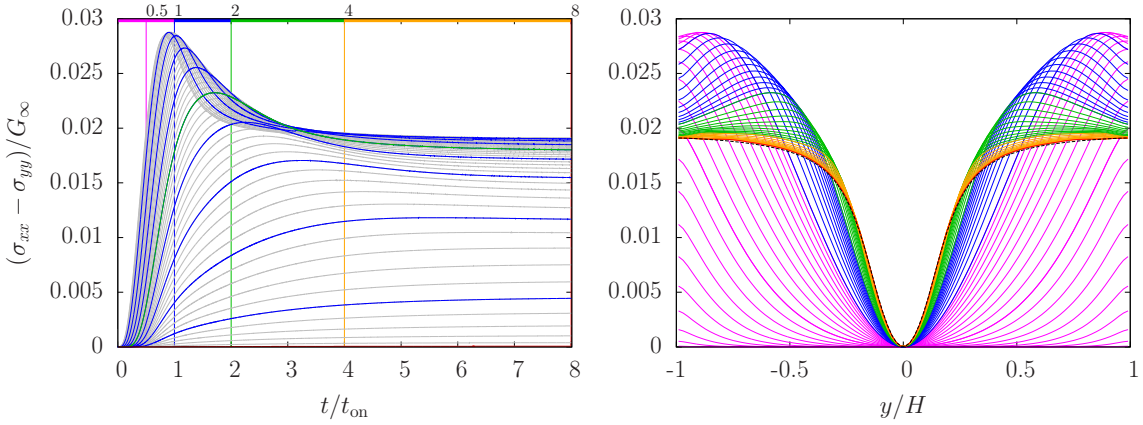

(c) $t_{on} = 4\tau_0$. $\Delta t^{magenta}/t_{on} = 0.05\, t_{on}$, doubling with each new color.

Figure 4.30: Starting flow of the normal stress difference $(\sigma_{xx} - \sigma_{yy})$ for three channel diameters, (a)–(c). The intermediate profiles (right) are plotted for different times indicated by a horizontal line of the same color at the top (left). Each line of the same color is separated by Δt. Profiles plotted with bold lines are taken at times marked by vertical lines.

the steady state from below, cf. Fig. 4.30. And this is exactly the point. Before the stresses have developed, the fluid has no way to find out about the shear-thinning properties of the non-linear Maxwell model. The normal stress is therefore heading for the quadratic profile of the linear Maxwell model. When shear-thinning sets in, the normal stress is forced to decrease to the correct steady state profile. However inside the plug, the non-linear Maxwell model shares the same parabolic shape, which is why no overshoots occur there. We can even observe, how the decay near the walls is accelerated by shear.

In Fig. 4.32, the evolution of the normal stress difference is shown in 3D. The floor color indicates the pressure, which balances the normal stresses working on the fluid. Again, the pressure gradient only mirrors the normal stress transients. Because the boundary condition keeps the average pressure fixed at $p = -0.01 G_\infty$, the profiles are fanned out and more colorful, but give no additional insight, cf. Fig. 4.33.

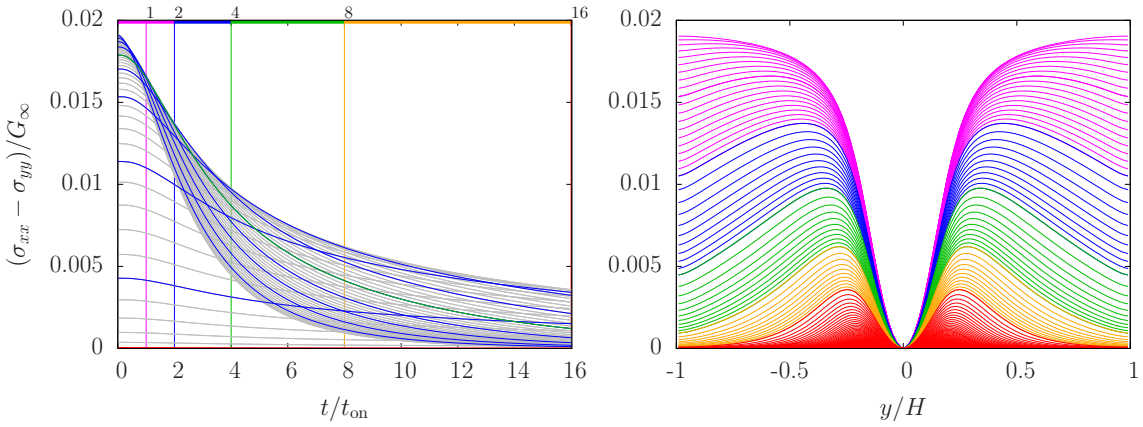

(a) $t_{\mathrm{on}} = 0.1\tau_0$. $\Delta t^{\mathrm{magenta}} = 0.1\, t_{\mathrm{on}}$, doubling with each new color.

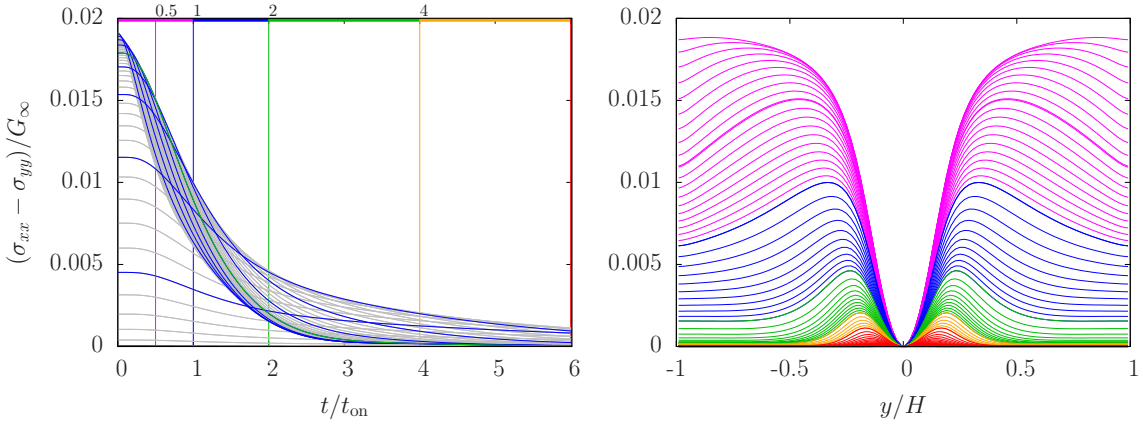

(b) $t_{\mathrm{on}} = 1\tau_0$. $\Delta t^{\mathrm{magenta}} = 0.05\, t_{\mathrm{on}}$, doubling with each new color.

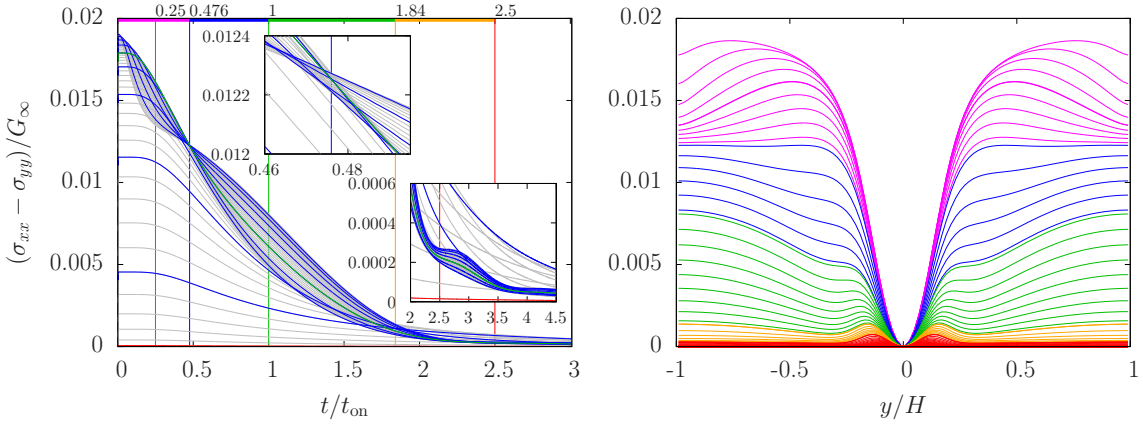

(c) $t_{\mathrm{on}} = 4\tau_0$. $\Delta t^{\mathrm{magenta}} = 0.05\, t_{\mathrm{on}}$, $\Delta t^{\mathrm{blue}} = \Delta t^{\mathrm{green}} = \Delta t^{\mathrm{orange}} = 0.1\, t_{\mathrm{on}}$, $\Delta t^{\mathrm{red}} = 0.2\, t_{\mathrm{on}}$

Figure 4.31: Stopping flow of the normal stress difference $(\sigma_{xx} - \sigma_{yy})$ for three channel diameters, (a)–(c). The intermediate profiles (right) are plotted for different times indicated by a horizontal line of the same color at the top (left). Each line of the same color is separated by Δt. Profiles plotted with bold lines are taken at times marked by vertical lines.

The switch-off normal stress transients need to differ from starting flow due to the quadratic dependence on the shear rate. This already applied for the linear Maxwell model, but non-linearities make the dynamics much richer. The cessation profiles of the normal stress differences are truly astounding and show some unique features, see Fig. 4.28 and Fig. 4.29. All three channels show nonuniform transient dynamics, and the decay time is very different throughout the channel. Near the wall, the relaxation is a lot faster than close to the channel center, where some few transients last exceptionally long. Fig. 4.31 gives the normal stress profiles during cessation. The profiles of the narrow channel, $t_{\text{on}} = 0.1\tau_0$ demonstrate nicely the different dynamics in the channel. Close to the walls, the shear rate is high and accelerates the stress relaxation. The normal stress peals off the central steady state profile, and forms two symmetric maxima near the center. At this point, the fluid has come to a proximate stand-still, but there are still quite large normal stresses remaining. With the flow gone, the normal stresses relax slowly via an exponential decay.

The initial reaction after the pressure is switched off is the same for the wide channels. The normal stresses in the plug relax more slowly than in the high-shear flanks. However, then the dynamics changes, and the normal stress decay at the very wall slows down. In the intermediate channel, $t_{\text{on}} = 1\tau_0$, at $t = 2t_{\text{on}}$ (bold green line), the normal stress has taken a profile which is constant in a large part of the channel except for the two maxima in the center. The normal stress difference then relaxes quite uniformly to a smaller version of the two-maxima profile we have already seen in the narrow channel and will decay eventually. Of course, the oscillations in the stopping flow have to be taken responsible for this change in the dynamics. Where the overdamped cessation profiles allowed a smooth decay of the normal stress difference, the dynamics in the wide channels reflects the oscillations the fluid encounters when the pressure is removed.

The wide channel, $t_{\text{on}} = 4\tau_0$, displays the most curious behavior. Already at $t = 0.25t_{\text{on}}$ (bold magenta line), the stress decay at the wall slows significantly down and the normal stress relaxes nearly linearly in time. At the same time the dynamics closer to the center speed up and give rise to an interesting ramification: At $t \approx 0.5t_{\text{on}}$ (bold blue line), the steady state profile makes an reappearance. In the transient plot, this manifests as a node where most transients aggregate. Afterwards, the central normal stresses actually stay ahead until about $t = 1.84t_{\text{on}}$ when the transients cross again. At this point the relaxation is very far progressed, but in the inset of Fig. 4.31c we can still observe how the decay is stalled by the oscillations. We find the same two-maxima resident normal stress profile as in the other two channels. The amplitude is much smaller which makes sense as the oscillations work both ways. New normal stress is build up, but the decay is also accelerated by shear.

For the sake of completeness, the pressure profiles are given in Fig. 4.33 and Fid. 4.34. Since the pressure gradient has to balance the normal stress differences, there is nothing new to learn, but the dynamics is beautiful nonetheless.

Conclusion

We have discussed the pressure-driven laminar channel flow of the tensorial non-linear Maxwell model. The new Lattice Boltzmann algorithm allows us to implement tensorial, non-Newtonian constitutive equation in differential (inlM model, Sec. 4.2) and integral

form (nlM model, Sec. 4.3). The shear-thinning properties of the model make the fluid form a stationary plug flow profile. Emerging normal stresses are balanced out by a relative increase in the pressure in the channel center. We checked the steady state results against theoretical predictions and found the LB results to be in good agreement. The properties of the non-linear Maxwell fluid are close to the glass limit already for moderate shear-thinning parameters. We considered the startup and cessation dynamics of the instantaneous non-linear Maxwell model next. Because shear-thinning affects the flowing but not the no-flow steady state, the symmetry between starting and stopping flow known from Newtonian fluids is lost. The finite stopping-time singularity is reproduced by the LB algorithm.

In its integral formulation, the non-linear Maxwell model opens up for viscoelastic effects. The stress no longer adjusts to a change in the flow instantaneously, but evolves on its own shear-dependent time scale. The dynamics of the shear stress and velocity are extensively affected by each other and give rise to over-shoots and oscillations. We identified a characteristic time scale t_{on} of the flow and used the channel diameter to vary the influence of the transient shear stress. In a narrow channel, $t_{\mathrm{on}} = 0.1\tau_0$, the dynamics is fast and the shear-thinning fluid gains more from the initial viscoelastic response upon applying a pressure gradient. Increasing the channel diameter slows down the development of a flow and allows the stress to adjust more readily. Differences to the instantaneous non-linear Maxwell model are restricted to short times and the time-dependent flow scales with t_{on} to form a single master curve for $t_{\mathrm{on}} \gtrsim 2\tau_0$. We identified a critical channel diameter, $t_{\mathrm{on}} \approx 1\tau_0$, where the crossover between both regimes takes place. The stopping flow makes visible what a capital influence the channel width has on the transient dynamics. For a narrow channel, the primary dynamics is that of an overdamped oscillator, and the flow decays asymptotically. In a wide channel, the viscous damping of the walls is small, and the fluid comes to an oscillatory stop.

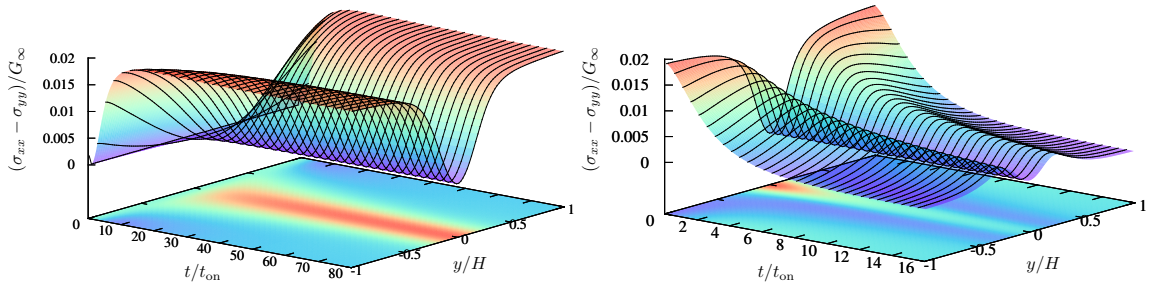

(a) $t_{on} = 0.1\tau_0$

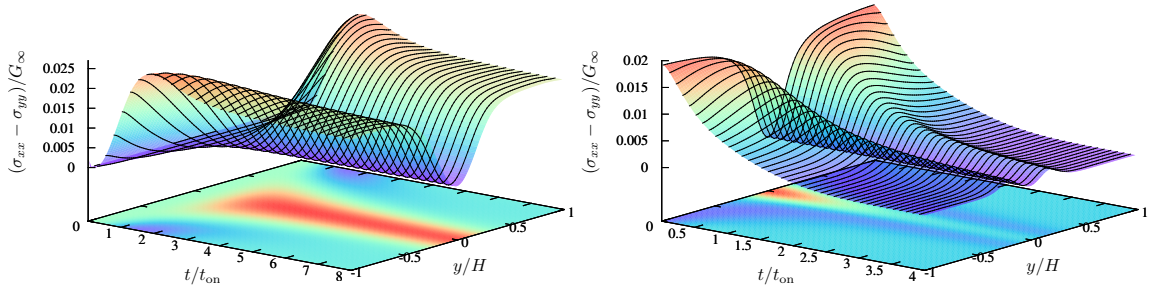

(b) $t_{on} = 1\tau_0$

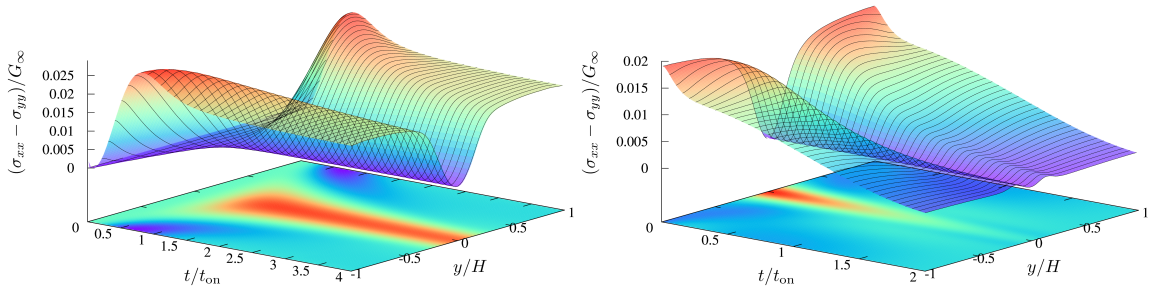

(c) $t_{on} = 4\tau_0$

Figure 4.32: Startup (left) and cessation (right) transient profile of the normal stress difference. The floor color indicates high (red) and low (violet) pressure.

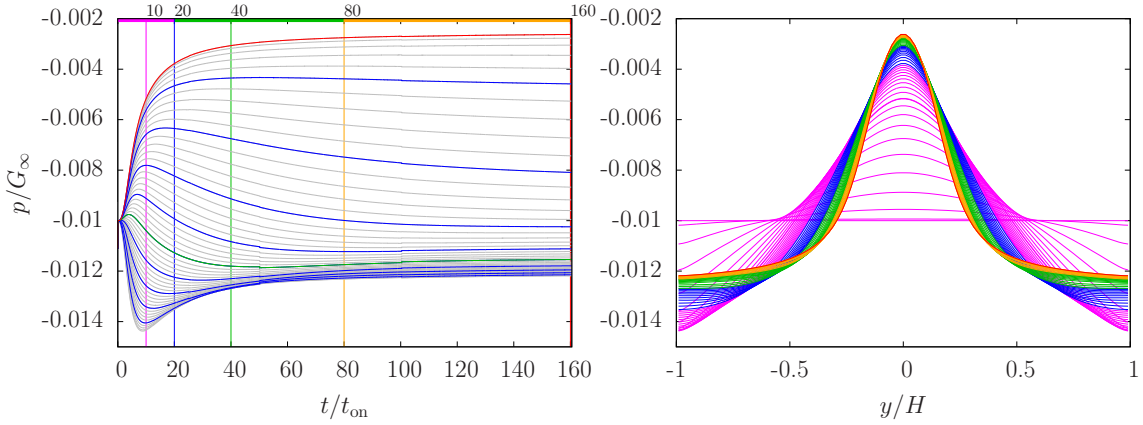

(a) $\Delta t^{\mathrm{magenta}}/t_{\mathrm{on}} = 1$, doubling with each new color.

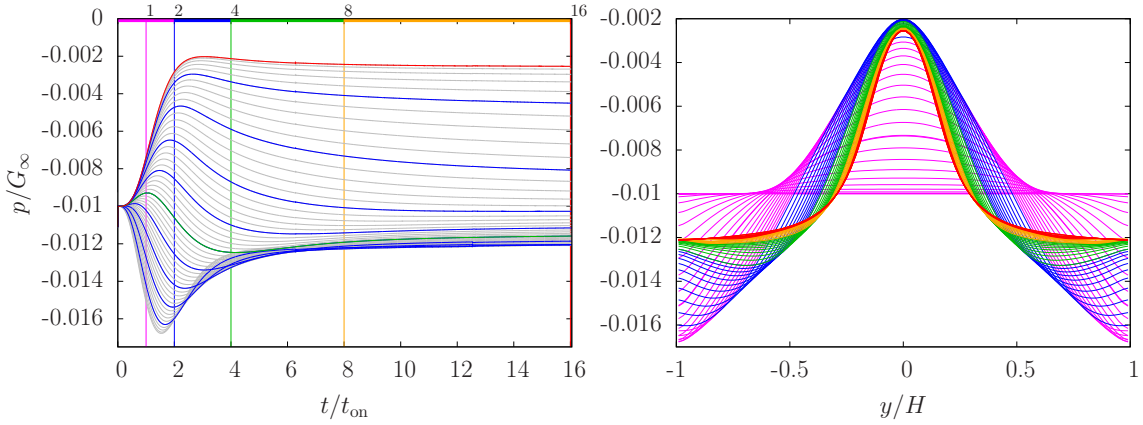

(b) $t_{\mathrm{on}} = 1\tau_0$. $\Delta t^{\mathrm{magenta}} = 0.1\, t_{\mathrm{on}}$, doubling with each new color.

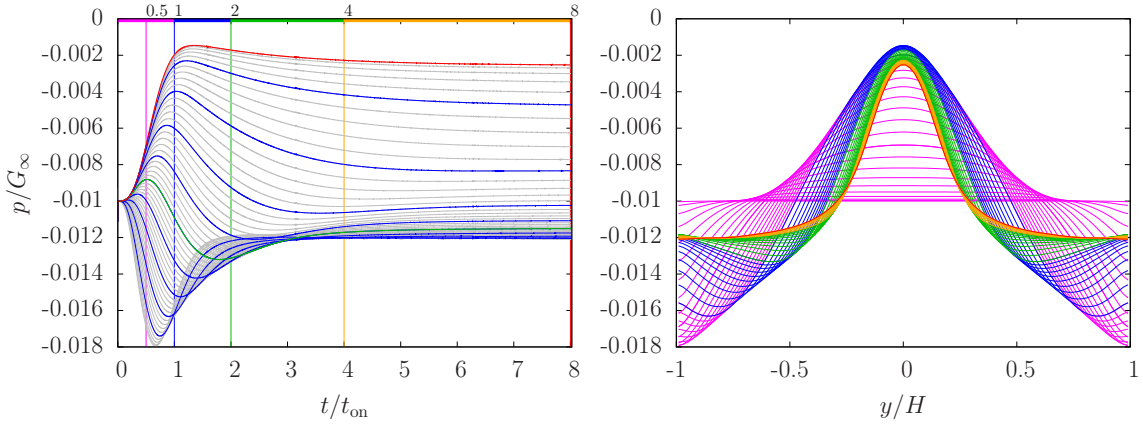

(c) $t_{\mathrm{on}} = 4\tau_0$. $\Delta t^{\mathrm{magenta}}/t_{\mathrm{on}} = 0.05\, t_{\mathrm{on}}$, doubling with each new color.

Figure 4.33: Starting flow of the pressure p for three channel diameters, (a)–(c). The intermediate profiles (right) are plotted for different times indicated by a horizontal line of the same color at the top (left). Each line of the same color is separated by Δt. Profiles plotted with bold lines are taken at times marked by vertical lines.

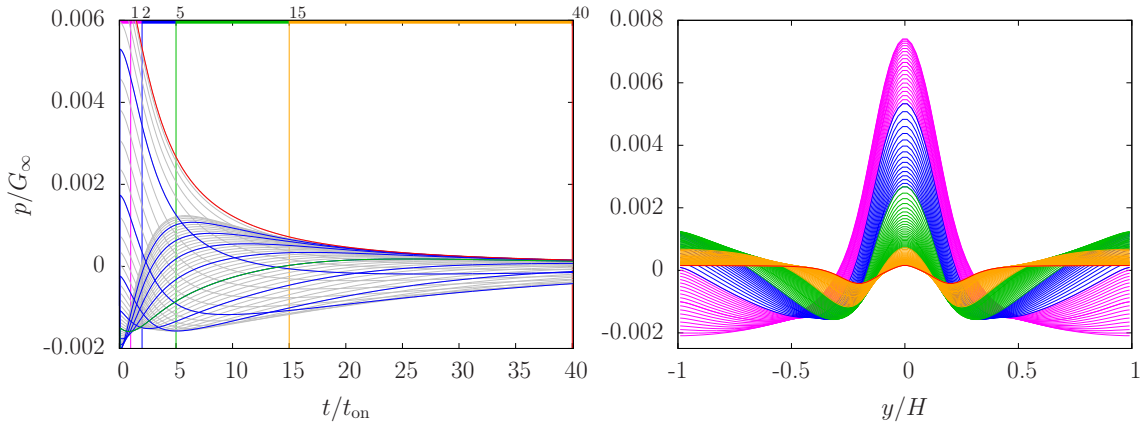

(a) $\Delta t^{\mathrm{magenta}}/t_{\mathrm{on}} = 0.1$, doubling with each new color.

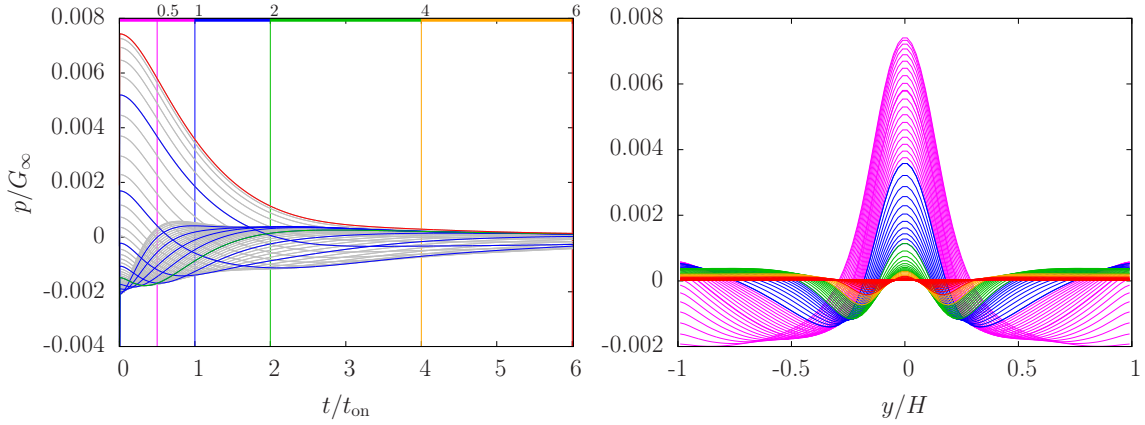

(b) $t_{\mathrm{on}} = 1\tau_0$. $\Delta t^{\mathrm{magenta}} = 0.05\, t_{\mathrm{on}}$, doubling with each new color.

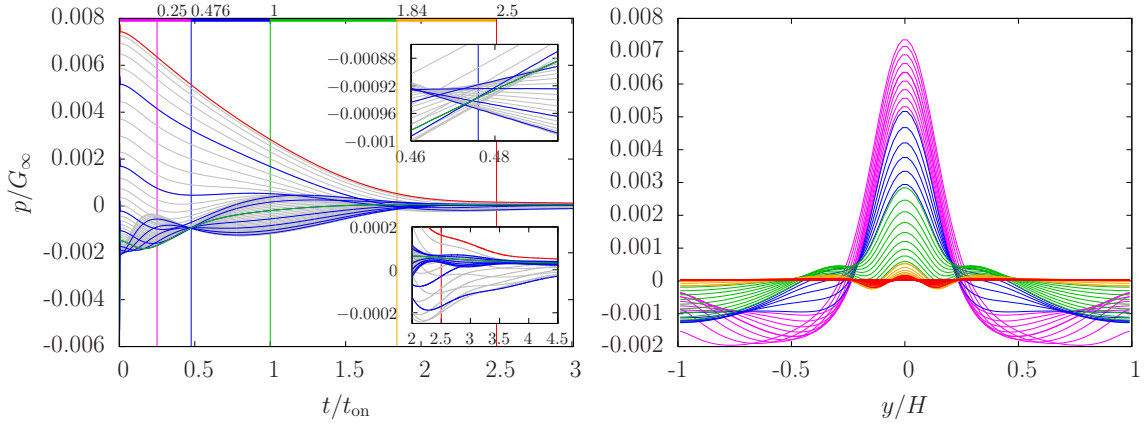

(c) $t_{\mathrm{on}} = 4\tau_0$. $\Delta t^{\mathrm{magenta}} = 0.05\, t_{\mathrm{on}}$, $\Delta t^{\mathrm{blue}} = \Delta t^{\mathrm{green}} = \Delta t^{\mathrm{orange}} = 0.1\, t_{\mathrm{on}}$, $\Delta t^{\mathrm{red}} = 0.2\, t_{\mathrm{on}}$

Figure 4.34: Stopping flow of the pressure p for three channel diameters, (a)–(c). The intermediate profiles (right) are plotted for different times indicated by a horizontal line of the same color at the top (left). Each line of the same color is separated by Δt. Profiles plotted with bold lines are taken at times marked by vertical lines.

4.4 Schematic MCT model

In the previous section, we have discussed the transient dynamics of the non-linear Maxwell model. The constitutive equation is motivated from microscopic theory and modeled to qualitatively reproduce the findings of mode coupling theory (MCT). Although it is a highly simplified model, we found rich and astounding dynamics we could explain and trace back to the two main features of the model, viscoelasticity and shear-thinning.

All this is well and good, but ultimately the non-linear Maxwell model is still a phenomenological model, and we set out to combine the mesoscopic Lattice Boltzmann simulation with a microscopic schematic MCT model. In Sec. 3.1.3, we have derived a discrete version of the constitutive equation, which is compatible with our Lattice Boltzmann algorithm. The implementation of the full schematic MCT (sMCT) model yields a large increase in computation time and puts a heavy constraint on the number of simulations we can run. But we can make use of our findings about the non-linear Maxwell model, and we already know the channel diameter to have an important influence on the fluid dynamics. The following section is not only a proof of an elegant concept to compute the flow of a colloidal suspension in a macroscopic system without explicitly touching either the colloidal dynamics or the Navier-Stokes equation, but we can also find out how good an approximation the non-linear Maxwell model is and how much of the physics is captured. After all, the model simplifies the correlator decay rather much and leaves out the dependence on the second time.

We conduct two simulations with different channel diameters 1.5mm and 4mm but otherwise identical parameters. We set $\nu_\sigma = 20\text{Pa}$, which translates to a colloidal particle radius of 58.7nm at room temperature. The density $\rho = 1000\text{kg/m}^3$ is the one of water, and we apply a pressure step $p = 0.15\nu_\sigma$. We choose the initial decay rate $\Gamma = 500\text{s}^{-1}$ and the distance to the glass transition $\epsilon = (\varphi - \varphi_\text{c})/\varphi_\text{c} = -3.5 \cdot 10^{-2}$, where φ denotes the (critical) volume fraction of the colloidal suspension. In the fluid phase, ϵ takes negative values and ϵ is positive in the glass. The critical strain is $\gamma_\text{c} = 0.1$ and the mixing parameter $\nu = 0.5$. This gives a minimal viscosity $\eta_\text{min} = 20\text{mPa s}$ and an increase by about a factor 10. The parameters are different to the ones we used for the non-linear Maxwell model. They are specifically chosen to give values that are typical for colloidal solutions and easily experimentally accessible, but also to have a smaller viscosity, which reduces the simulation runtime.

This brings us to the parameters of the Lattice Boltzmann algorithm. The lattice has $N = 128$ fluid nodes in transversal flow direction, and the LB relaxation time is set to $\tau_\text{LB} = 0.9$. The memory of the MCT solver is provided with $C = 96$ entries per block. We again make use of the symmetry of the flow and only use the central column of the lattice to compute the non-Newtonian stress contributions. The LB time step is much smaller than needed to compute the correlator. For this reason, the stress is computed anew only every 100 LB steps for the narrow channel (every 10 for the wide channel) and kept constant in-between. The correlator is still sampled by a time step $\delta t \approx 9.64 \cdot 10^{-7}\text{s}$ ($\delta t \approx 6.85 \cdot 10^{-7}\text{s}$), and we have checked the simulation to give identical results when the correlator is computed each LB step.

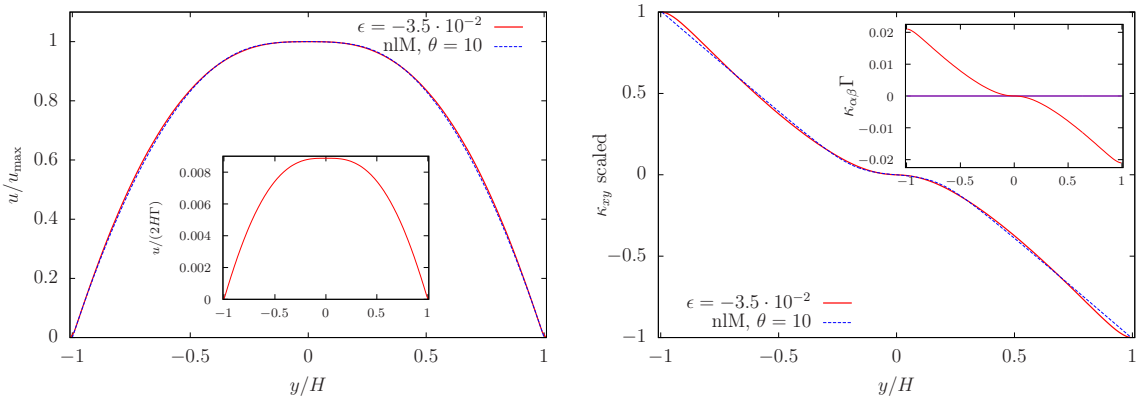

Figure 4.35: Steady state velocity (left) and strain rate (right) profile of the schematic MCT model. For comparison a non-linear Maxwell (nlM) fluid is shown. The velocity is scaled by the maximum value, the strain rate to match at $d = \pm 1$. The insets give the absolute values. All strain rate components are shown in the inset, but only $\kappa_{xy} \neq 0$.

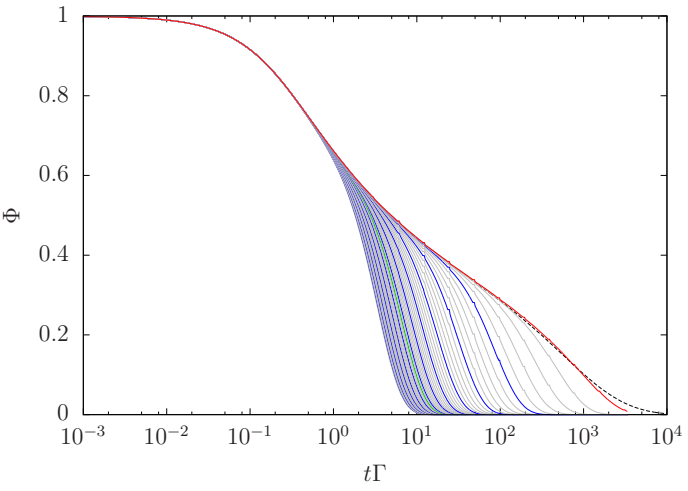

Figure 4.36: Correlator at different channel positions. The red ($d = y/H = -0.008$) and green ($d = -0.508$) lines are the central and half-to-center lines. Every fifth line is colored blue. The dashed line gives the correlator under no shear computed with the single-time algorithm.

4.4.1 Stationary profile

Let us take a look at the flowing steady state profiles first. The results are scaled by the channel diameter and are identical for both simulation. In Fig. 4.35 (left) the velocity profiles of a sMCT fluid (red solid line) are shown and compared to a non-linear Maxwell fluid (dashed blue line) with the same shear-thinning factor, $\theta = 10$. Because the fluids differ in the viscosity and the applied pressure, the absolute velocities are very different. However, if we scale the velocity profile by its maximum value, we find a truly astonishing agreement. Both models are very nearly identical and show the same plug flow profile. Only in the velocity gradient κ_{xy} we can make out some small differences. For the sMCT model, the shear rate is not exactly linear in the high-shear regions but shows some small wiggles resulting in imperfect parabolic half-profiles in the velocity profile. However, the deviation is small and quite similar to numerical errors the non-linear Maxwell model experiences for large shear-thinning parameters $\theta \geq 10^2$, see Fig. 4.4. In absence of a secondary flow, all other components of the velocity gradient tensor vanish.

In the sMCT model, the stress is proportional to the integral over the correlator squared,

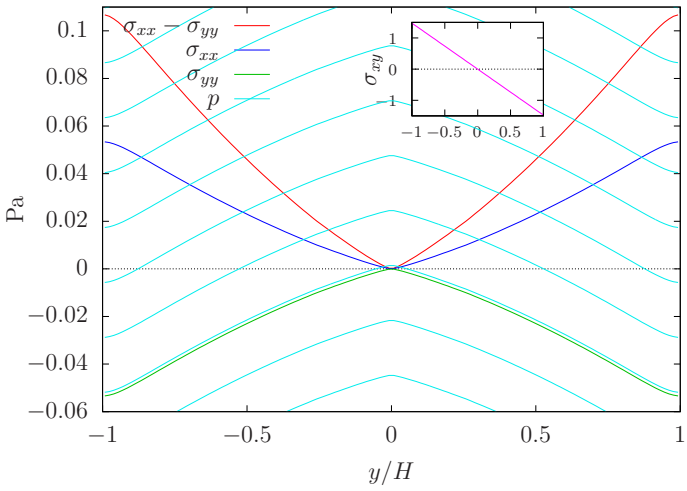

Figure 4.37: Stress tensor elements $\sigma_{\alpha\beta}$ and pressure p for a pressure-driven channel flow of the sMCT model. The pressure gradient is projected in flow direction. The driving gradient in flow direction is constant and gives rise to an offset between the transversal profile at different positions in the channel.

cf. Eq. (3.15). Fig. 4.36 gives the correlator at different channel positions. The dashed line shows the correlator decay if no shear is applied. The smallest velocity gradients are in the center of the channel, and indeed, we find the central correlator, $d = y/H = 1/128$, (red) to only deviate at the very end from the correlator without shear. The next few correlators are still quite unperturbed by shear, but as soon as we leave the plug behind, we find the correlator decay to be clearly accelerated by the flow. Φ cannot decay arbitrarily fast as Γ sets a lower limit. In the high-shear regions, the correlators are already quite close to this limit and therefore aggregate.

The components of the stress tensors are shown in Fig. 4.37. The shear stress profile (inset) decreases linearly in d as we would expect. The slope differs from the non-linear Maxwell model by a factor of 3, as we chose a different pressure $p = 0.15\nu_\sigma = 3\text{Pa}$. Because the normal stresses are non-linear in both models, we cannot compare the results to the nlM model as easily. For the sMCT model, too, the normal stresses arise solely from the Finger tensor, so the principal structure is the same. However, the normal stresses show completely new profiles and nothing similar to the nlM model, where the normal stress difference has a parabolic shape in the plug and takes a constant value otherwise. Here, we do not observe any qualitative differences between the plug and the high-shear regions. Only if we take a close look, we find the slope in the center slightly smaller, otherwise the profile is very much linear. The small decrease at the walls is the same we have already seen in the velocity gradient profile.

The fluid is still quite far away from the glass phase. We have to choose ϵ much closer to zero for the correlators to form a real plateau. Unfortunately, the much larger shear stress differences, i.e. changes in the viscosity, would have slowed down the simulation too much. The non-linear Maxwell model favors the glass limit and tends to exaggerate some effects, so we already find the transition for quite small θ. Nevertheless, because the normal stress difference is balanced by a pressure gradient and the flow is laminar, the velocity profile remains unaffected.

4.4.2 Transient dynamics

We consider the startup and cessation profiles next. Just like before, we apply a sudden pressure difference between both ends of the channel. After reaching a flowing steady state, we switch off the pressure and wait for the flow to stop. We again define a characteristic time

$$t_{\text{on}} = \frac{L^2 \rho}{\pi^2 \eta_{\text{min}}}, \tag{4.15}$$

which removes the quantitative influence of the channel diameter on the dynamics. The flow in a narrow channel develops faster (t_{on} small), which allows us to use the channel diameter to vary the influence of the transient stress on the evolution of the flow profile. For the narrow channel the characteristic time is $t_{\text{on}} = 0.011\text{s}$ and $t_{\text{on}} = 0.081\text{s}$ for the wide channel. Considering that the minimal viscosity has changed by a factor of about 100, these two channels correspond roughly to the narrow and intermediate channel we discussed for the non-linear Maxwell model.

Fig. 4.38 and Fig. 4.39 show the velocity and shear stress profiles of the starting flow for both channels. Indeed, we find the same transient dynamics as before. In the narrow channel, the velocity increases faster than the stress can develop, and an overshoot occurs. At the time when the stress exceeds its steady state value, $t_{\text{on}} \approx 0.69$, the velocity has a maximum and slowly decreases to the steady state value. Only then a plug forms in the velocity profile. In the wide channel, the velocity develops more slowly and gives the stress enough time to adjust. We can see a clear kink in the transients, where the shear-thinning sets in and takes control of the dynamics. The non-linear Maxwell model gives rise to very much the same dynamics, and we can hardly find any differences so far. Even the time scales compare quite well. For the sMCT model, the overshoots in the velocity profile happen at different times throughout the channel. We observed this effect in the non-linear Maxwell model during cessation, but using the full model allows the transients to evolve more freely already in the starting flow.

The normal stress difference, Fig. 4.40, gives rise to no surprises. In the narrow channel, the non-monotonous velocity profile is responsible for an overshoot in the normal stresses at about the same time the overshoot in the shear stress takes place. Because the fluid is still very much in the fluid phase and there is no qualitative change in the normal stresses, no overshoots appear in the wide channel.

There is more to learn from the cessation profiles. Fig. 4.38 and Fig. 4.39 show the velocity and shear stress profiles after the driving pressure has been removed. The principle of the viscoelastic stopping flow is the same as for the non-linear Maxwell model. Velocity and shear stress decay on different time scales. Resident stresses make the fluid move again, and oscillations allow the stress to build up again. As we expect for a shear-thinning fluid, the center velocity decays fastest. For the correlator, things get interesting when the fluid turns around. Fig. 4.43 shows the correlator for different time during the stopping flow. As the shear decreases and accelerates the decay less, all correlators in the channel approach the no-shear limit (dashed line) again (top right). However, after the fluid passes the minimum, the fluid retraces its own flow history backwards. There is a high correlation between the velocity flow before and after the minimum, which shows up as a peak in the now

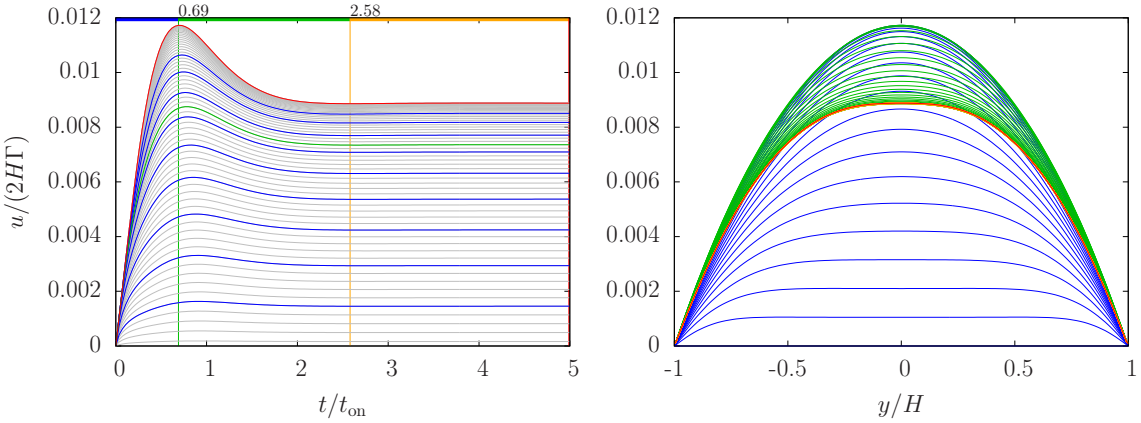

(a) $t_{\mathrm{on}} = 0.011$s. $\Delta t^{\mathrm{blue}} = 0.036 t_{\mathrm{on}}$, doubling with each new color.

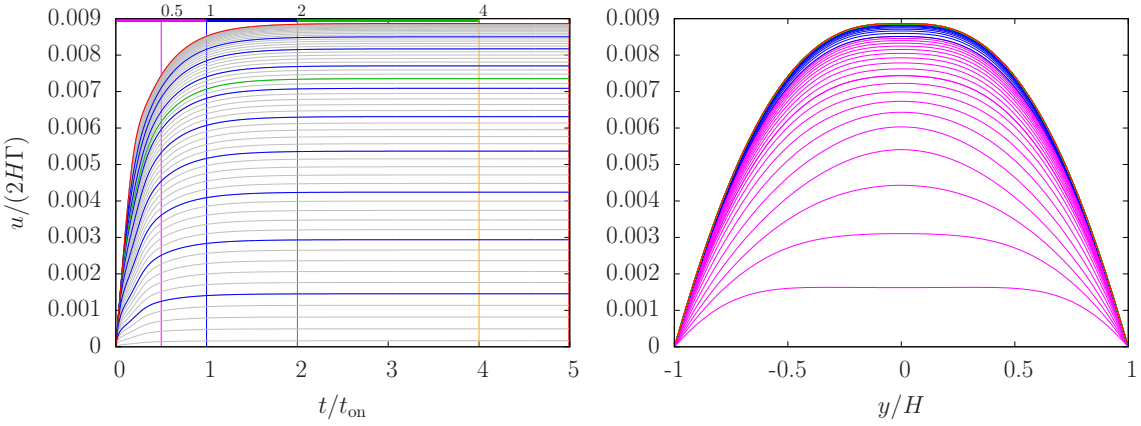

(b) $t_{\mathrm{on}} = 0.081$s. $\Delta t^{\mathrm{magenta}} = 0.05 t_{\mathrm{on}}$, doubling with each new color.

Figure 4.38: Startup flow of the velocity u for two channel diameters. The intermediate profiles (right) are plotted for different times indicated by a horizontal line of the same color at the top (left). Each line of the same color is separated by Δt. Profiles printed with bold lines (right) are taken at times marked by a vertical line (left).

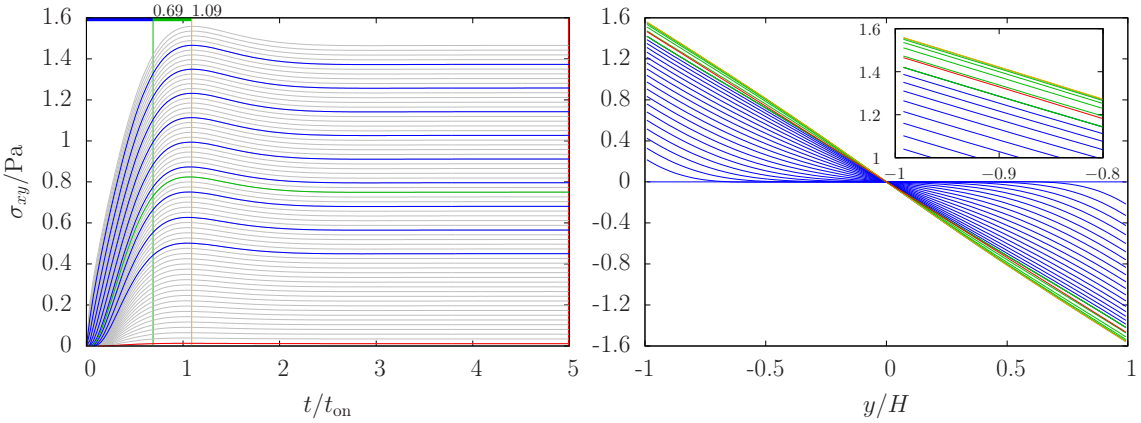

(a) $t_{\mathrm{on}} = 0.011$s. $\Delta t^{\mathrm{blue}} = 0.036 t_{\mathrm{on}}$, doubling with each new color.

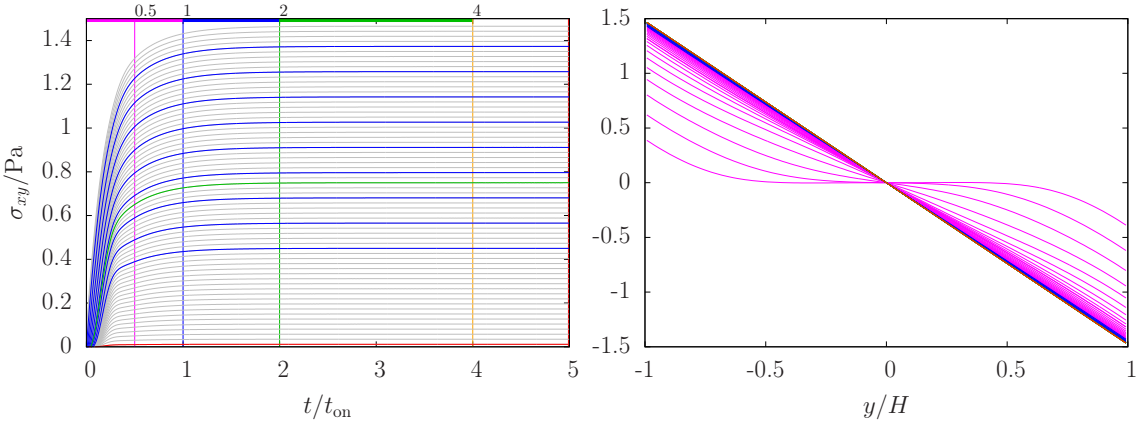

(b) $t_{\mathrm{on}} = 0.081$s. $\Delta t^{\mathrm{magenta}} = 0.05 t_{\mathrm{on}}$, doubling with each new color.

Figure 4.39: Startup flow of the shear stress σ_{xy} for two channel diameters. The intermediate profiles (right) are plotted for different times indicated by a horizontal line of the same color at the top (left). Each line of the same color is separated by Δt. Profiles printed with bold lines (right) are taken at times marked by a vertical line (left).

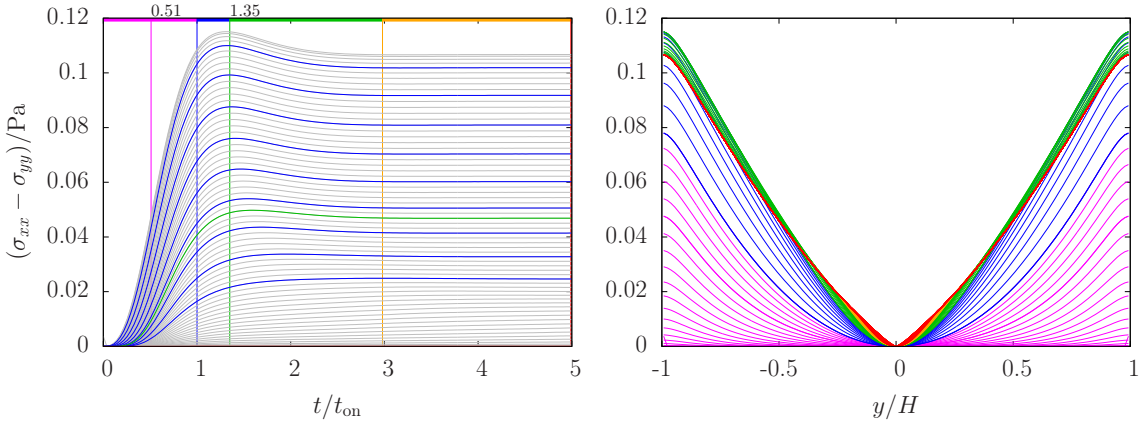

(a) $t_{\mathrm{on}} = 0.011$s. $\Delta t^{\mathrm{magenta}} = 0.036 t_{\mathrm{on}}$, doubling with each new color.

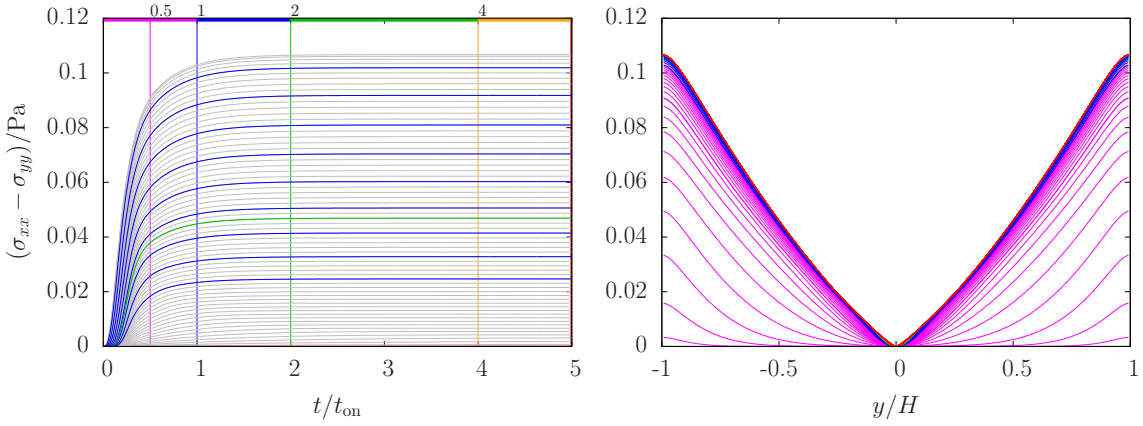

(b) $t_{\mathrm{on}} = 0.081$s. $\Delta t^{\mathrm{magenta}} = 0.05 t_{\mathrm{on}}$, doubling with each new color.

Figure 4.40: Startup flow of the normal stress difference $(\sigma_{xx} - \sigma_{yy})$ for two channel diameters. The intermediate profiles (right) are plotted for different times indicated by a horizontal line of the same color at the top (left). Each line of the same color is separated by Δt. Profiles printed with bold lines (right) are taken at times marked by a vertical line (left).

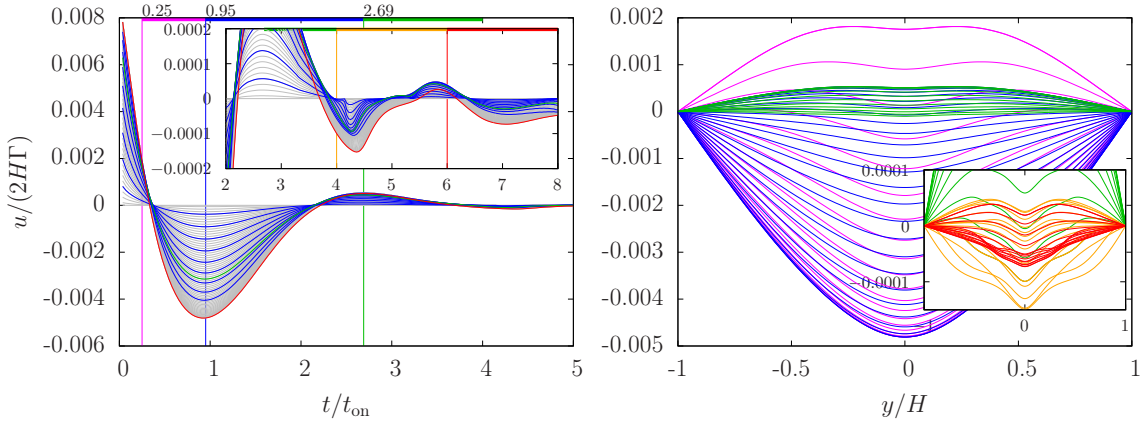

(a) $t_{\mathrm{on}} = 0.011$s. $\Delta t^{\mathrm{magenta}} = 0.036 t_{\mathrm{on}}$, doubling with each new color.

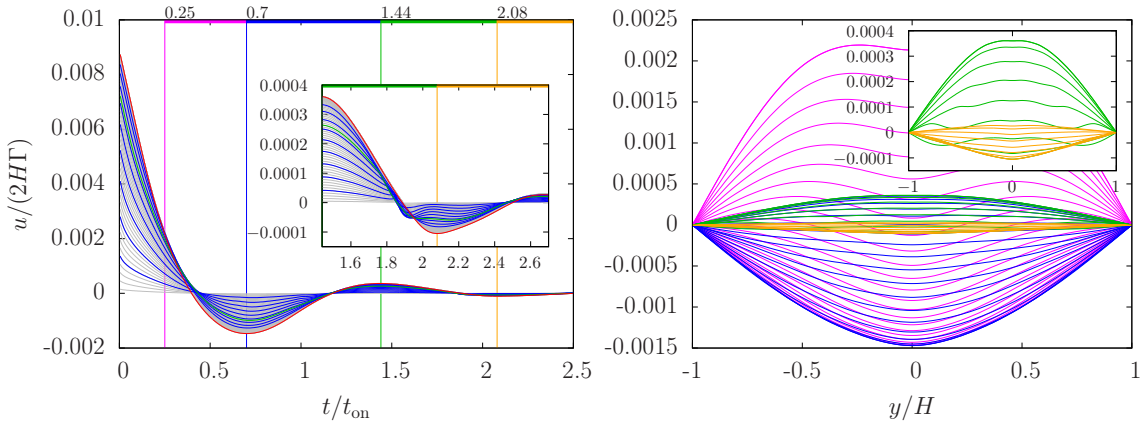

(b) $t_{\mathrm{on}} = 0.081$s. $\Delta t^{\mathrm{magenta}} = 0.02 t_{\mathrm{on}}$, $\Delta t^{\mathrm{blue}} = 0.04 t_{\mathrm{on}}$, $\Delta t^{\mathrm{green,\ orange}} = 0.08 t_{\mathrm{on}}$.

Figure 4.41: Cessation flow of the velocity u for two channel diameters. The intermediate profiles (right) are plotted for different times indicated by a horizontal line of the same color at the top (left). Each line of the same color is separated by Δt. Profiles printed with bold lines (right) are taken at times marked by a vertical line (left).

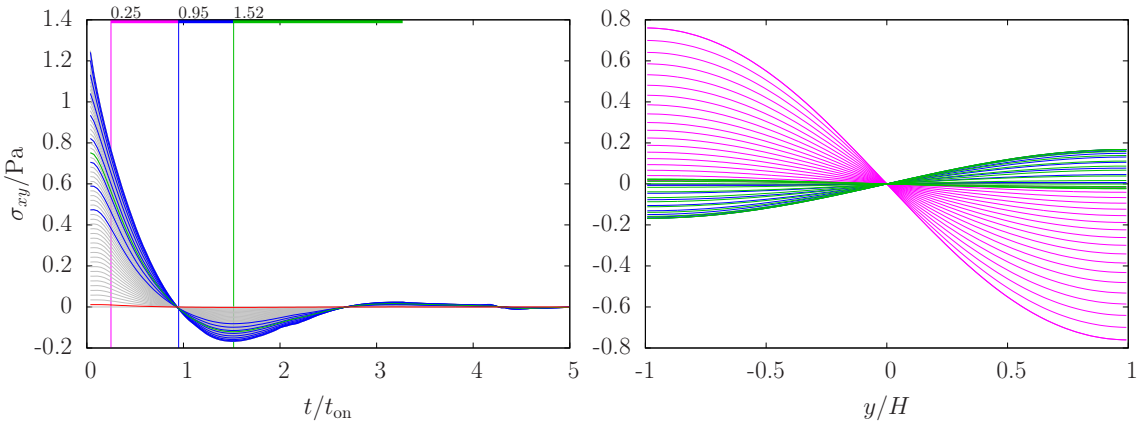

(a) $t_{\mathrm{on}} = 0.011$s. $\Delta t^{\mathrm{magenta}} = 0.036 t_{\mathrm{on}}$, doubling with each new color.

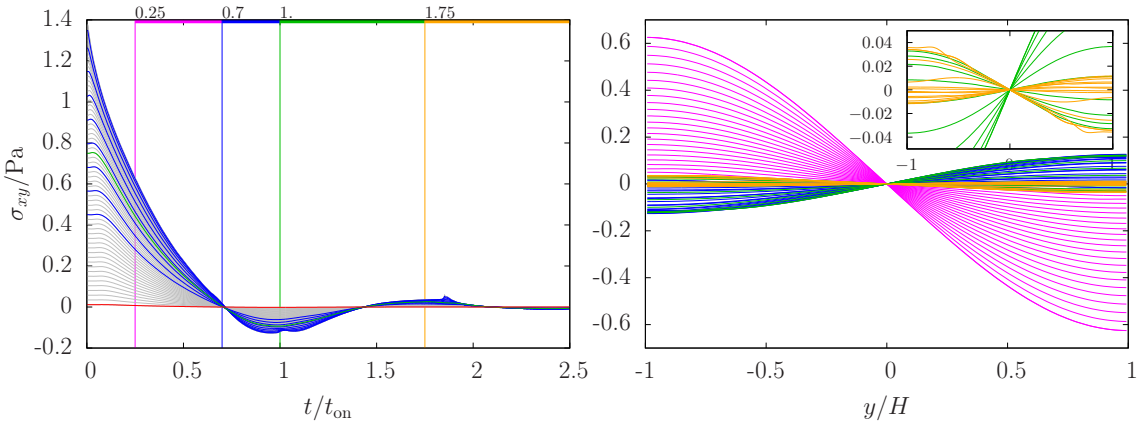

(b) $t_{\mathrm{on}} = 0.081$s. $\Delta t^{\mathrm{magenta}} = 0.02 t_{\mathrm{on}}$, $\Delta t^{\mathrm{blue}} = 0.04 t_{\mathrm{on}}$, $\Delta t^{\mathrm{green,\ orange}} = 0.08 t_{\mathrm{on}}$.

Figure 4.42: Cessation flow of the shear stress σ_{xy} for two channel diameters. The intermediate profiles (right) are plotted for different times indicated by a horizontal line of the same color at the top (left). Each line of the same color is separated by Δt. Profiles printed with bold lines (right) are taken at times marked by a vertical line (left).

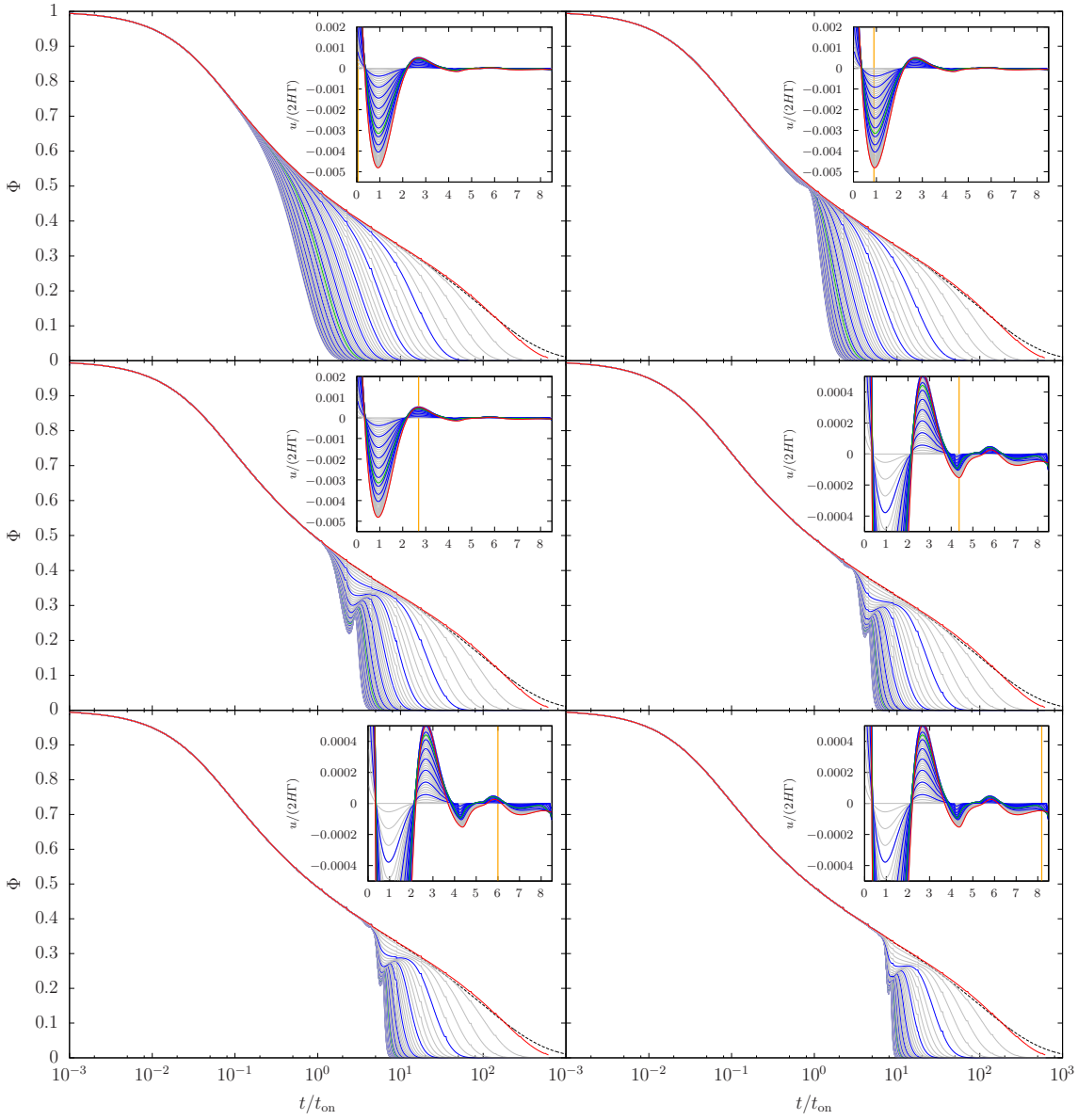

Figure 4.43: Correlator at different channel positions during cessation. The time is indicated by an orange vertical line in the inset showing the velocity profile. The red ($d = -0.008$) and green ($d = -0.508$) lines are the central and half-to-center lines. Every fifth line is colored blue. The dashed line gives the correlator under no shear computed with the single-time algorithm.

non-monotonous correlator (middle left). With each oscillation the process happens anew, but becomes smaller as the flow decays. When the correlator becomes non-monotonous, for the first time the sMCT model is truly different from an exponential decay. This has important consequences on the transients, and the fluid behaves radically different after the first undershoot. Unfortunately, at this point the flow has almost come to a stop and the fluid velocity is very small. At later times (not shown), the numerical solution becomes unstable as the peak in the correlator can no longer be resolved.

The normal stress difference, Fig. 4.45, shows a similar cessation profile as the non-linear Maxwell model, and the oscillations slow down the decay. At some times, the normal stress even increases again, although the sharp kinks in the profile indicate that this may already be an artifact of the correlator discretization. Since the fluid is not close enough to the glass limit, we do not find any local long-lasting normal stress differences in the channel center as we have seen for the non-linear Maxwell model.

Conclusion

We have demonstrated how the schematic MCT constitutive equations can be combined with a modified Lattice Boltzmann scheme to solve a pressure-driven channel flow. We found the steady state velocity profile to reproduce nearly exactly the flow of a non-linear Maxwell fluid. This is even more remarkable if we consider that there exists an analytical solution for the channel flow profile. We can deduce that the laminar flow velocity is primarily defined by the change in viscosity.

At least in the starting flow, the agreement continues. We find the same qualitative behavior as for a non-linear Maxwell fluid. However, the stopping flow profiles exhibits new and unique features. We could trace the non-trivial flows back to the correlator which becomes non-monotonous under oscillations as has been observed before [15]. Fig. 4.44 shows the Fourier transform of a typical correlator we found during cessation and confirms this picture.

The memory kernel of the sMCT model provides one more time dependence one would not easily guess in empirical constitutive equations. In a glass $\epsilon > 0$, stresses relax only partially under sudden cessation [4]. The non-linear Maxwell model always decays to zero and cannot capture these frozen stresses. Using the sMCT model to simulate a fluid closer to the glass transition or a glass should give rise to even richer phenomena than the nlM model. However, because the LB method is a fluid dynamics solver, it struggles with high, yet alone divergent, viscosity changes. Going into the glass phase presents a challenge, but does not make a simulation impossible in principle. One would need to set an upper time limit for the transient flow, and weigh the fast increasing computation time against the needed numerical precision.

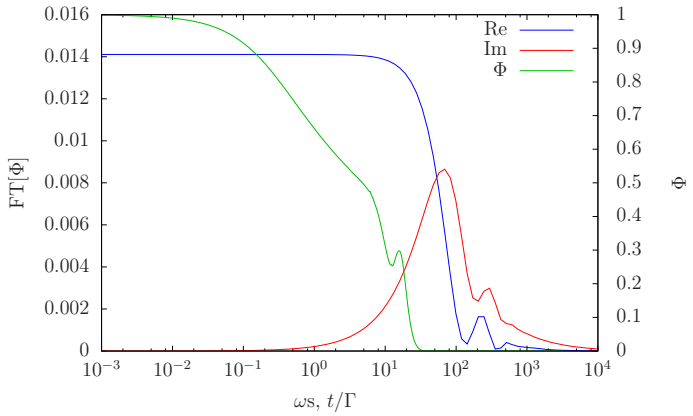

Figure 4.44: Real and Imaginary part of the Fourier transform of a typical non-monotonous correlator Φ taken at $d = -0.25$.

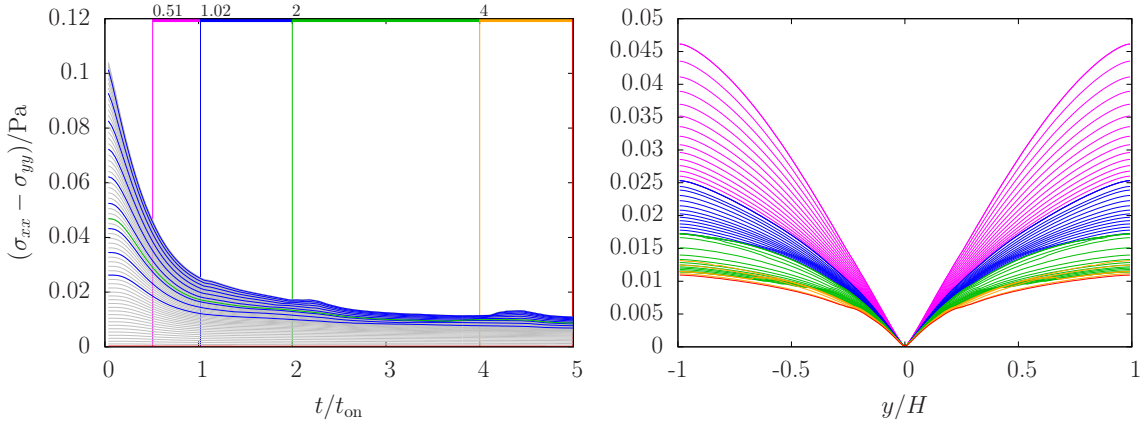

(a) $t_{on} = 0.011$s. $\Delta t^{magenta} = 0.036 t_{on}$, doubling with each new color.

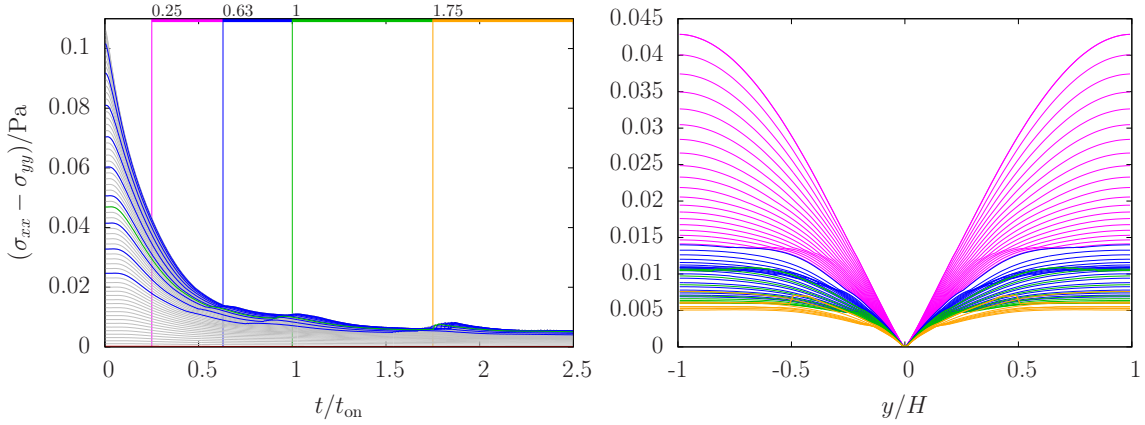

(b) $t_{on} = 0.081$s. $\Delta t^{magenta} = 0.02 t_{on}$, doubling with each new color.

Figure 4.45: Cessation flow of the normal stress difference $(\sigma_{xx} - \sigma_{yy})$ for two channel diameters. The intermediate profiles (right) are plotted for different times indicated by a horizontal line of the same color at the top (left). Each line of the same color is separated by Δt. Profiles printed with bold lines (right) are taken at times marked by a vertical line (left).

5 Outlook

The studies we have made so far are by no means concluding. We have only considered simple flow problems, but the interesting dynamics we already found in this proof of concept are very promising for future studies. There are several possible ways to follow up our research, and some major points come to mind.

The schematic MCT model does not consider shear gradient terms, which affect the Poiseuille flow profile and the yield threshold [19, 70]. It would be interesting to further consider the consequences of a higher pressure in the channel center. MD simulations do not show this increase in pressure [90], but blood cells are known to migrate towards the channel center [10]. Small concentration gradients become important in a yield stress fluid and can lead to shear banding [7]. An expansion of the MCT model to account for these gradient terms, would be an interesting option.

The modified LB method does not advect the non-Newtonain stress contributions. For laminar channel flows, this does not present a problem, but studying more complex geometries, like contractions, or going to unstable flows would require the algorithm to consider the advection term. We already learned how to deal with the trace of the stress tensor and how to advect the pressure via a term $\partial_t \tilde{\rho}$. $(\boldsymbol{u} \cdot \boldsymbol{\partial})\boldsymbol{\sigma}$ has the same units as the time derivative of the stress tensor, and an implementation should work similarly.

Maybe the most obvious next step is to simulate closer to the glass transition, or even in the glass phase, and to try to find a change in physics when the second time dependence of the MCT model becomes relevant. In principle, this is only a problem of finding a fast enough computer, but one should be able to think of some neat tricks to prevent the computational demand increase too much. The total simulation time gives an upper limit of the viscosity, and one would probably try not to sample the whole viscosity range for each lattice node.

6 Conclusion

We propose a new way to study the dynamics of glass-forming colloidal suspensions by successfully combining mode-coupling theory (MCT) with a Lattice Boltzmann (LB) scheme. The mode-coupling theory provides a constitutive equation which is fully determined by the microscopic interactions of the system. We use a schematic MCT model, which incorporates the essential features of the full model, to close the Navier-Stokes (NS) equation. The LB method presents an elegant and computational efficient way to find a solution for the NS equation even for complex flow problems. We propose a modified LB algorithm capable of handling tensorial and integral constitutive equations. Combining a mesoscopic flow solver with microscopic dynamics offers some significant advantages. We are now able to study complex flow problems which would be inaccessible when using microscopic approaches such as Molecular Dynamics simulations.

To test our method, we have studied the pressure-driven Poiseuille flow through a straight channel. Further approximations to the schematic MCT (sMCT) model yield a shear-thinning constitutive equation similar to Maxwell's well-known model of viscoelastic fluids. We have implemented this non-linear Maxwell (nlM) model in its integral formulation and in its differential form (inlM), which assumes a fully developed flow. The inlM model adjusts instantaneously to changes in the flow and is similar to other shear-thinning constitutive equations often used in LB simulations. Under the reasonable constraint of an incompressible flow, the steady state channel flow profile of the non-linear Maxwell model can be solved analytically.

The LB results agree very well with the theoretical predictions. In a channel, the shear-thinning fluid forms a no-shear plug in the center and high-shear regions near the walls. Normal stresses working on the plug are balanced by a pressure gradient. The non-linear Maxwell model shows glass-like dynamics already for moderate large drops in the viscosity. For cessation flows, this makes the inlM fluid show nearly finite stopping times hinting at a yield stress, which exists only in the glass limit.

In the nlM model, the stress takes the flow history into account, and viscoelastic effects enter the transient dynamics. The intriguing interplay between the evolution of the stress and velocity of the fluid presents an interesting field of study. The velocity can vary more rapidly than the stress, and overshoots and oscillations appear in the transient profiles. For the stopping flow, this is especially interesting as resident stresses make the stopped flow start moving again, but in opposite direction. Comparing with the linear Maxwell model, we could visualize the shear-thinning setting in. We have identified two different regimes and a characteristic time scale t_{on} we can vary by changing the channel diameter. For narrow channels (small t_{on}), the starting flow exhibits overshoots in the velocity and stress. In wide channels, the velocity profile develops monotonously again. Increasing the channel diameter restores the scaling with t_{on} on a single master curve, which is the same for the inlM model.

Comparing the results of the non-linear Maxwell model with the dynamics of the schematic

mode-coupling model, we find the nlM model to capture the dynamics of the velocity and shear stress exceptionally well. The steady state profiles are nearly indistinguishable, and we find the same qualitative change for different channel diameters in the starting flow of the sMCT model. The cessation dynamics are more complex. The correlator becomes non-monotonous due to the oscillating flow and affects the stopping flow after the initial undershoot. The normal stress profiles are different from the ones found for the non-linear Maxwell model, but the agreement should improve for simulations closer to the glass transition.

We have shown that the non-linear Maxwell model reproduces the dynamics of the schematic MCT model extremely well. It incorporates most features of the microscopic dynamics known from mode-coupling theory in a relatively simple constitutive equation and presents a good compromise between microscopic details and practicability. We have demonstrated how to use mode-coupling theory, if in a simplified model, to close the Navier-Stokes equation and apply it to flow problems. We have compared our results with theoretical predictions and found them in good agreement. Already in a pressure-driven channel flow, the dynamics are highly non-trivial and promise even more interesting physics for more complex flow geometries.

7 Zusammenfassung

Wir präsentieren eine neue Methode, die Dynamik von glasbildenden kolloidalen Suspensionen zu untersuchen, indem wir erfolgreich die Modenkopplungstheorie (MCT) mit einem Lattice Boltzmann (LB) Algorithmus verbinden. Die Modenkopplungstheorie liefert eine Konstituierendengleichung, die vollständig von den mikroskopischen Wechselwirkungen des Systems bestimmt wird. Wir benutzen ein schematisches MCT Modell, das die wesentlichen Eigenschaften des vollständigen Modells aufweist, um die Navier-Stokes (NS) Gleichung zu schließen. Die LB Methode ist ein eleganter und effizienter Weg, Lösungen der NS Gleichung zu finden, der sich gut auf komplexe Flüsse anwenden lässt. Wir zeigen einen abgewandelten LB Algorithmus, der es erlaubt tensorielle und integrale Konstituierendengleichungen zu integrieren. Die Kombination einer mesoskopischen Flussberechnung mit einer mikroskopischen Dynamik bietet große Vorteile. Wir können so komplexe Flüsse berechnen, die mit mikroskopischen Zugängen wie der Molekulardynamik-Simulation nicht zugänglich wären.

Um unsere Methode zu testen, untersuchen wir den druckgetriebenen Poiseuille Fluss durch einen geraden Kanal. Weitere Näherungen am schematischen MCT (sMCT) Modell liefern eine scherverdünnende Konstituierendengleichung, die ähnlich zu dem bekannten Maxwell Modell für viskoelastische Flüssigkeiten ist. Wir haben dieses nichtlineare Maxwell (nlM) Modell in seiner integralen und in seiner differentiellen Form (inlM), welches einen bereits vollständig ausgeprägten Fluss voraussetzt, integriert. Das inlM Modell ändert sich instantan mit dem Fluss und ähnelt anderen scherverdünnenden Konstituierendengleichungen, die häufig in LB Simulationen eingesetzt werden. Unter der vernünftigen Annahme, dass der Fluss inkompressibel ist, ist der stationäre Fluss für das nichtlineare Maxwell Modell analytisch lösbar.

Die LB Ergebnisse stimmen sehr gut mit den theoretischen Vorhersagen überein. In einem Kanal formt die scherverdünnende Flüssigkeit einen scherfreien Propfen in der Mitte und stark gescherte Regionen an der Wand. Normalspannungen, die auf den Pfropfen wirken, werden durch einen Druckgradienten ausgeglichen. Das nichtlineare Maxwell Modell zeigt schon für mittelgroße Änderungen in der Viskosität glasartige Dynamik. Beim Stoppen des Flusses kommt die inlM Flüssigkeit annährend abrupt zu stehen und deutet eine Fließspannung an, die eigentlich erst im Glas auftritt.

Beim nlM Modell berücksichtigt die Spannung die Vergangenheit des Flusses, und viskoelastische Effekte beeinflussen die nichtstationäre Dynamik. Es ist interessant, das Zusammenspiel von der Entwicklung des Spannungs- und des Geschwindigkeitsprofils zu untersuchen. Die Geschwindigkeit kann sich schneller als die Spannung ändern, und Überschwinger und Oszillationen tauchen in den nichtstationären Profilen auf. Dies ist besonders für den Ausschaltvorgang interessant, weil die verbliebene Spannung den bereits angehaltenen Fluss wieder in Bewegung setzt, aber in die entgegengesetzte Richtung. Beim Vergleich mit dem linearen Maxwell Modell konnten wir das Einsetzen der Scherverdünnung sichtbar machen. Wir haben zwei unterschiedliche Regime und eine charakteristische Zeit

t_{on}, die wir durch Ändern der Kanalweite variieren können, identifiziert. In schmalen Kanälen (kleines t_{on}) kommt es zu Überschwingern in der Geschwindigkeit und in der Spannung beim Einschalten. In breiten Kanälen sind die Profile monoton. Das Vergrößern des Kanalquerschnitts stellt das Skalieren auf eine einzelne Kurve wieder her. Diese Kurve ist die gleiche wie für das inlM Modell.

Der Vergleich des nichtlinearen Maxwell Modells mit dem schematischen Modenkopplungsmodells zeigt eine außergewöhnlich gute Übereinstimmung beider Modelle. Die stationären Profile sind fast ununterscheidbar, und das Einschaltverhalten ändert sich erneut qualitativ mit der Kanalbreite. Der Ausschaltvorgang ist komplexer. Der Korrelator wird nicht-monoton durch die Oszillationen und beeinflusst das Geschwindigkeitsprofil beim Anhalten nach dem ersten Unterschwinger. Die Normalspannungsprofile unterscheiden sich, aber die Übereinstimmung sollte näher am Glasübergang besser werden.

Wir haben gezeigt, dass das nichlineare Maxwell Modell die Dynamik des schematischen MCT Modells extrem gut wiedergibt. Es enthält die meisten Eigenschaften der mikroskopischen Dynamik, die aus der Modenkopplungstheorie bekannt sind, in einer relativ einfachen Konstituierendengleichung und bietet einen guten Kompromiss zwischen mikroskopischen Details und Anwendbarkeit. Wir haben gezeigt, wie die Modenkopplungstheorie, wenn auch in einer vereinfachten Form, die Navier-Stokes Gleichung schließen und auf Flussprobleme angewendet werden kann. Wir haben unsere Ergebnisse mit theoretischen Vorhersagen verglichen und in guter Überinstimmungen gefunden. Bereits für druckgetriebene Kanalströmung ist die Dynami nicht-trivial und verspricht noch interessantere Physik für komplexere Geometrien.

References

[1] E. Aharonov and D. H. Rothman: Non-Newtonian Flow (Through Porous-Media) - a Lattice-Boltzmann Method, Geophysical Research Letters **20**, 679 (1993).

[2] P. Ahlrichs and B. Dünweg: Simulation of a single polymer chain in solution by combining lattice Boltzmann and molecular dynamics, Journal of Chemical Physics **111**, 8225 (1999).

[3] G. Arwatz and A. J. Smits: A viscoelastic model of shear-induced hemolysis in laminar flow, Biorheology **50**, 45 (2013).

[4] M. Ballauff, J. M. Brader, S. U. Egelhaaf, M. Fuchs, J. Horbach, N. Koumakis, M. Krüger, M. Laurati, K. J. Mutch, G. Petekidis, M. Siebenbürger, Th. Voigtmann, and J. Zausch: Residual Stresses in Glasses, Phys. Rev. Lett. **110**, 215701 (2013).

[5] G. K. Batchelor: An introduction to fluid dynamics, Cambridge Univ. Press, Cambridge (1994), ISBN 0521098173.

[6] R. Benzi, S. Succi, and M. Vergassola: The lattice Boltzmann equation: theory and applications, Physics Reports **222**, 145 (1992).

[7] R. Besseling, L. Isa, P. Ballesta, G. Petekidis, M. E. Cates, and W. C. K. Poon: Shear Banding and Flow Concentration Coupling in Colloidal Glasses, Phys. Rev. Lett. **105**, 268301 (2010).

[8] P. L. Bhatnagar, E. P. Gross, and M. Krook: A Model for Collision Processes in Gases. I. Small Amplitude Processes in Charged and Neutral One-Component Systems, Phys. Rev. **94**, 511 (1954).

[9] R. B. Bird, R. C. Armstrong, and O. Hassager: Dynamics of polymeric liquids, Fluid mechanics, volume 1, Wiley, New York (1987).

[10] J. J. Bishop, A. S. Popel, M. Intaglietta, and P. C. Johnson: Rheological effects of red blood cell aggregation in the venous network: A review of recent studies, Biorheology **38**, 263 (2001).

[11] T. Borg and E. J. Pääkkönen: Linear viscoelastic models: Part III. Start-up and transient flow effects from the molecular weight distribution, Journal of Non-Newtonian Fluid Mechanics **159**, 17 (2009).

[12] J. M. Brader: Nonlinear rheology of colloidal dispersions, Journal of Physics-Condensed Matter **22**, 363101 (2010).

[13] J. M. Brader, M. E. Cates, and M. Fuchs: First-Principles Constitutive Equation for Suspension Rheology, Phys. Rev. Lett. **101**, 138301 (2008).

[14] J. M. Brader, M. E. Cates, and M. Fuchs: First-principles constitutive equation for suspension rheology, Phys. Rev. E **86**, 021403 (2012).

[15] J. M. Brader, M. Siebenbürger, M. Ballauff, K. Reinheimer, M. Wilhelm, S. J. Frey, F. Weysser, and M. Fuchs: Nonlinear response of dense colloidal suspensions under oscillatory shear: Mode-coupling theory and Fourier transform rheology experiments, Phys. Rev. E **82**, 061401 (2010).

[16] J. M. Brader, Th. Voigtmann, M. E. Cates, and M. Fuchs: Dense Colloidal Suspensions under Time-Dependent Shear, Phys. Rev. Lett. **98**, 058301 (2007).

[17] J. M. Brader, Th. Voigtmann, M. Fuchs, R. G. Larson, and M. E. Cates: Glass rheology: From mode-coupling theory to a dynamical yield criterion, Proc. Natl. Acad. Sci. U. S. A. **106**, 15186 (2009).

[18] M. E. Cates, O. Henrich, D. Marenduzzo, and K. Stratford: Lattice Boltzmann simulations of liquid crystalline fluids: active gels and blue phases, Soft Matter **5**, 3791 (2009).

[19] P. Chaudhuri, V. Mansard, A. Colin, and L. Bocquet: Dynamical Flow Arrest in Confined Gravity Driven Flows of Soft Jammed Particles, Phys. Rev. Lett. **109**, 036001 (2012).

[20] H. Chen and C. Teixeira: H-theorem and origins of instability in thermal lattice Boltzmann models, Computer Physics Communications **129**, 21 (2000).

[21] S. Chen, H. Chen, D. Martnez, and W. Matthaeus: Lattice Boltzmann model for simulation of magnetohydrodynamics, Phys. Rev. Lett. **67**, 3776 (1991).

[22] S. Chen and G. D. Doolen: Lattice Boltzmann Method for Fluid Flows, Annual Review of Fluid Mechanics **30**, 329 (1998).

[23] C. Denniston, E. Orlandini, and J. M. Yeomans: Lattice Boltzmann simulations of liquid crystal hydrodynamics, Phys. Rev. E **63**, 056702 (2001).

[24] J. J. Derksen: Drag on random assemblies of spheres in shear-thinning and thixotropic liquids, Physics of Fluids **21**, 083302 (2009).

[25] J. J. Derksen and Prashant: Simulations of complex flow of thixotropic liquids, Journal of Non-Newtonian Fluid Mechanics **160**, 65 (2009).

[26] M. Doi and S. F. Edwards: Dynamics of concentrated polymer systems. Part 1.-Brownian motion in the equilibrium state, J. Chem. Soc., Faraday Trans. 2 **74**, 1789 (1978).

[27] M. Doi and S. F. Edwards: Dynamics of concentrated polymer systems. Part 2.-Molecular motion under flow, J. Chem. Soc., Faraday Trans. 2 **74**, 1802 (1978).

[28] M. Doi and S. F. Edwards: Dynamics of concentrated polymer systems. Part 3.-The constitutive equation, J. Chem. Soc., Faraday Trans. 2 **74**, 1818 (1978).

[29] M. Doi and S. F. Edwards: Dynamics of concentrated polymer systems. Part 4.-Rheological properties, J. Chem. Soc., Faraday Trans. 2 **75**, 38 (1979).

[30] E. S. F. Doi M.: The Theory of Polymer Dynamics, Oxford University Press, Oxford (1986).

[31] B. Dünweg and A. J. Ladd: Lattice Boltzmann Simulations of Soft Matter Systems, in C. Holm and K. Kremer (Editors), Advanced Computer Simulation Approaches

for Soft Matter Sciences III, volume 221 of *Advances in Polymer Science*, pp. 89–166, Springer Berlin Heidelberg (2009), ISBN 978-3-540-87705-9.

[32] M. P. Escudier and F. Presti: Pipe flow of a thixotropic liquid, J. Non-Newtonian Fluid Mech. **62**, 291 (1996).

[33] F. Frahsa, A. K. Bhattacharjee, J. Horbach, M. Fuchs, and Th. Voigtmann: On the Bauschinger effect in supercooled melts under shear: Results from mode coupling theory and molecular dynamics simulations, The Journal of Chemical Physics **138**, 12A513 (2013).

[34] U. Frisch, B. Hasslacher, and Y. Pomeau: Lattice-Gas Automata for the Navier-Stokes Equation, Phys. Rev. Lett. **56**, 1505 (1986).

[35] M. Fuchs: Nonlinear Rheological Properties of Dense Colloidal Dispersions Close to a Glass Transition Under Steady Shear, in M. Cloitre (Editor), High Solid Dispersions, volume 236 of *Advances in Polymer Science*, pp. 55–115, Springer Berlin Heidelberg (2010), ISBN 978-3-642-16381-4.

[36] M. Fuchs and M. E. Cates: Theory of Nonlinear Rheology and Yielding of Dense Colloidal Suspensions, Phys. Rev. Lett. **89**, 248304 (2002).

[37] M. Fuchs and M. E. Cates: Schematic models for dynamic yielding of sheared colloidal glasses, Faraday discussions **123**, 267 (2003).

[38] M. Fuchs and M. E. Cates: A mode coupling theory for Brownian particles in homogeneous steady shear flow, Journal of Rheology **53**, 957 (2009).

[39] S. Gabbanelli, G. Drazer, and J. Koplik: Lattice Boltzmann method for non-Newtonian (power-law) fluids, Phys. Rev. E **72**, 046312 (2005).

[40] W. Götze: Complex Dynamics of Glass-Forming Liquids: A Mode-Coupling Theory, Oxford University Press (2009).

[41] O. Gräser and A. Grimm: Adaptive generalized periodic boundary conditions for lattice Boltzmann simulations of pressure-driven flows through confined repetitive geometries, Phys. Rev. E **82**, 016702 (2010).

[42] G. S. Grest and K. Kremer: Molecular dynamics simulation for polymers in the presence of a heat bath, Physical Review A **33**, 3628 (1986).

[43] Z. Guo, B. Shi, and C. Zheng: A coupled lattice BGK model for the Boussinesq equations, International Journal for Numerical Methods in Fluids **39**, 325 (2002).

[44] Z. Guo, C. Zheng, and B. Shi: Discrete lattice effects on the forcing term in the lattice Boltzmann method, Phys. Rev. E **65**, 046308 (2002).

[45] I. Halliday, L. A. Hammond, C. M. Care, K. Good, and A. Stevens: Lattice Boltzmann equation hydrodynamics, Phys. Rev. E **64**, 011208 (2001).

[46] X. He, Q. Zou, L.-S. Luo, and M. Dembo: Analytic solutions of simple flows and analysis of nonslip boundary conditions for the lattice Boltzmann BGK model, Journal of Statistical Physics **87**, 115 (1997).

[47] F. J. Higuera, S. Succi, and R. Benzi: Lattice Gas Dynamics with Enhanced Collisions, EPL (Europhysics Letters) **9**, 345 (1989).

[48] C.-F. Ho, C. Chang, K.-H. Lin, and C.-A. Lin: Consistent Boundary Conditions for 2D and 3D Lattice Boltzmann Simulations, Computer Modelling in Engineering & Sciences **44**, 137 (2009).

[49] R. R. Huilgol: Variational inequalities in the flows of yield stress fluids including inertia: Theory and applications, Physics of Fluids **14**, 1269 (2002).

[50] T. Inamuro: A lattice kinetic scheme for incompressible viscous flows with heat transfer, Phil. Trans. R. Soc. Lond. A **360**, 477 (2002).

[51] I. Ispolatov and M. Grant: Lattice Boltzmann method for viscoelastic fluids, Phys. Rev. E **65**, 056704 (2002).

[52] M. Junk and Z. Yang: One-point boundary condition for the lattice Boltzmann method, Phys. Rev. E **72**, 066701 (2005).

[53] M. Junk and Z. Yang: Convergence of lattice Boltzmann methods for Navier-Stokes flows in periodic and bounded domains, Numerische Mathematik **112**, 65 (2009).

[54] A. Kaye: A Bouncing Liquid Stream, Nature **197**, 1001 (1963).

[55] D. Kehrwald: Lattice Boltzmann Simulation of Shear-Thinning Fluids, Journal of Statistical Physics **121**, 223 (2005).

[56] S. H. Kim and H. Pitsch: A generalized periodic boundary condition for lattice Boltzmann method simulation of a pressure driven flow in a periodic geometry, Physics of Fluids **19**, 108101 (2007).

[57] U. A. Kleßinger, B. K. Wunderlich, and A. R. Bausch: Transient flow behavior of complex fluids in microfluidic channels, Microfluid Nanofluid **15**, 533 (2013).

[58] J. M. V. A. Koelman: A Simple Lattice Boltzmann Scheme for Navier-Stokes Fluid Flow, EPL (Europhysics Letters) **15**, 603 (1991).

[59] T. Koga, F. Tanaka, I. Kaneda, and F. M. Winnik: Stress Buildup under Start-Up Shear Flows in Self-Assembled Transient Networks of Telechelic Associating Polymers, Langmuir **25**, 8626 (2009), pMID: 19438184.

[60] M. Krüger, F. Weysser, and Th. Voigtmann: From equilibrium to steady-state dynamics after switch-on of shear, Phys. Rev. E **81**, 061506 (2010).

[61] T. Krüger, M. Gross, D. Raabe, and F. Varnik: Crossover from tumbling to tank-treadinglike motion in dense simulated suspensions of red blood cells, Soft Matter **9**.

[62] T. Krüger, F. Varnik, and D. Raabe: Shear stress in lattice Boltzmann simulations, Phys. Rev. E **79**, 046704 (2009).

[63] T. Krüger, F. Varnik, and D. Raabe: Second-order convergence of the deviatoric stress tensor in the standard Bhatnagar-Gross-Krook lattice Boltzmann method, Phys. Rev. E **82**, 025701 (2010).

[64] A. J. C. Ladd: Numerical simulations of particulate suspensions via a discretized Boltzmann equation. Part 1. Theoretical foundation, Journal of Fluid Mechanics **271**, 285 (1994).

[65] A. J. C. Ladd: Numerical simulations of particulate suspensions via a discretized Boltzmann equation. Part 2. Numerical results, Journal of Fluid Mechanics **271**, 311 (1994).

[66] R. G. Larson: The Structure and Rheology of Complex Fluids, Oxford University Press, Inc., New York (1999).

[67] J. Latt: Choice of units in lattice Boltzmann simulations (2008), <http://wiki.palabos.org/_media/howtos:lbunits.pdf>, Jan. 2013.

[68] J. Latt, B. Chopard, O. Malaspinas, M. Deville, and A. Michler: Straight velocity boundaries in the lattice Boltzmann method, Phys. Rev. E **77**, 056703 (2008).

[69] H. M. Laun: Description of the non-linear shear behaviour of a low density polyethylene melt by means of an experimentally determined strain dependent memory function, Rheologica Acta **17**, 1 (1978).

[70] V. Mansard, A. Colin, P. Chaudhuri, and L. Bocquet: A molecular dynamics study of non-local effects in the flow of soft jammed particles, Soft Matter **9**, 7849 (2013).

[71] D. Marenduzzo, E. Orlandini, and J. M. Yeomans: Permeative Flows in Cholesteric Liquid Crystals, Phys. Rev. Lett. **92**, 188301 (2004).

[72] D. Marenduzzo, E. Orlandini, and J. M. Yeomans: Hydrodynamics and Rheology of Active Liquid Crystals: A Numerical Investigation, Phys. Rev. Lett. **98**, 118102 (2007).

[73] G. R. McNamara and G. Zanetti: Use of the Boltzmann Equation to Simulate Lattice-Gas Automata, Phys. Rev. Lett. **61**, 2332 (1988).

[74] L. Muravleva, E. Muravleva, G. C. Georgiou, and E. Mitsoulis: Numerical simulations of cessation flows of a Bingham plastic with the augmented Lagrangian method, Journal of Non-Newtonian Fluid Mechanics **165**, 544 (2010).

[75] J. G. Oldroyd: On the Formulation of Rheological Equations of State, Proceedings of the Royal Society of London. Series A. Mathematical and Physical Sciences **200**, 523 (1950).

[76] J. Onishi, Y. Chen, and H. Ohashi: A Lattice Boltzmann model for polymeric liquids, Progress in Computational Fluid Dynamics **5**, 75 (2005).

[77] J. Onishi, Y. Chen, and H. Ohashi: Dynamic simulation of multi-component viscoelastic fluids using the lattice Boltzmann method, Physica A: Statistical Mechanics and its Applications **362**, 84 (2006).

[78] T. N. Phillips and G. W. Roberts: Lattice Boltzmann models for non-Newtonian flows, IMA Journal of Applied Mathematics **76**, 790 (2011).

[79] Y.-H. Qian and Y.-F. Deng: A Lattice BGK Model for Viscoelastic Media, Phys. Rev. Lett. **79**, 2742 (1997).

[80] Y. H. Qian, D. D'Humières, and P. Lallemand: Lattice BGK Models for Navier-Stokes Equation, EPL (Europhysics Letters) **17**, 479 (1992).

[81] R. P. Rand: Mechanical Properties of the Red Cell Membrane II. Viscoelastic Breakdown of the Membrane, Biophys J. **4**, 303 (1964).

[82] W. Reinke, P. Gaehtgens, and P. C. Johnson: Blood viscosity in small tubes: effect of shear rate, aggregation, and sedimentation, Am. J. Physiol. **253**, H540 (1987).

[83] M. Ring: A generalized Maxwell model for the non-linear rheology of supercooled melts, Bachelor thesis, Universität Konstanz (2011).

[84] M. Rudman, H. M. Blackburn, L. J. W. Graham, and L. Pullum: Turbulent pipe flow of shear-thinning fluids, J. Non-Newtonian Fluid Mech. **118**, 33 (2004).

[85] M. Siebenbürger, M. Ballauff, and Th. Voigtmann: Creep in Colloidal Glasses, Phys. Rev. Lett. **108**, 255701 (2012).

[86] K. Stratford, R. Adhikari, I. Pagonabarraga, J.-C. Desplat, and M. E. Cates: Colloidal Jamming at Interfaces: A Route to Fluid-Bicontinuous Gels, Science **309**, 2198 (2005).

[87] S. Succi: The Lattice Boltzmann Equation for fluid dynamics and beyond, Clarendon Press, Oxford (2009), ISBN 9780198503989.

[88] G. J. Tangelder, D. W. Slaaf, A. M. Muijtjens, T. Arts, M. G. Egbrink, and R. S. Reneman: Velocity profiles of blood platelets and red blood cells flowing in arterioles of the rabbit mesentery., Circulation Research **59**, 505 (1986).

[89] F. Varnik, J. Baschnagel, and K. Binder: Reduction of the glass transition temperature in polymer films: A molecular-dynamics study, Phys. Rev. E **65**, 021507 (2002).

[90] F. Varnik and D. Raabe: Profile blunting and flow blockage in a yield-stress fluid: A molecular dynamics study, Phys. Rev. E **77**, 011504 (2008).

[91] R. Verberg and A. J. C. Ladd: Lattice-Boltzmann Model with Sub-Grid-Scale Boundary Conditions, Phys. Rev. Lett. **84**, 2148 (2000).

[92] A. Vikhansky: Lattice-Boltzmann method for yield-stress liquids, Journal of Non-Newtonian Fluid Mechanics **155**, 95 (2008).

[93] A. Vikhansky: Construction of Lattice-Boltzmann Schemes for non-Newtonian and Two-Phase Flows, The Canadian Journal of Chemical Engineering **90**, 1081 (2012).

[94] Th. Voigtmann: Idealized Glass Transitions under Pressure: Dynamics versus Thermodynamics, Phys. Rev. Lett. **101**, 095701 (2008).

[95] Th. Voigtmann: Fließen, Scheren, Schmelzen, Physik Journal **12**, 29 (2013).

[96] Th. Voigtmann: Slow dynamics in external forces: Creep and microrheology, AIP Conference Proceedings **1518**, 94 (2013).

[97] Th. Voigtmann, J. M. Brader, M. Fuchs, and M. E. Cates: Schematic mode coupling theory of glass rheology: single and double step strains, Soft Matter **8**, 4244 (2012).

[98] Th. Voigtmann and W. C. K. Poon: Glasses under high pressure: a link to colloidal science?, Journal of Physics: Condensed Matter **18**, L465 (2006).

[99] M. Wagner: Analysis of stress-growth data for simple extension of a low-density branched polyethylene melt, Rheologica Acta **15**, 133 (1976).

[100] C.-H. Wang and J.-R. Ho: A lattice Boltzmann approach for the non-Newtonian effect in the blood flow, Comput. Math. Appl. **62**, 75 (2011).

[101] N. Waters and M. King: Unsteady flow of an elastico-viscous liquid, Rheologica Acta **9**, 345 (1970).

[102] N. Waters and M. J. King: The unsteady flow of an elastico-viscous liquid in a straight pipe of a circular cross section, J. Phys. D: Appl. Phys. **4**, 204 (1971).

[103] F. Weysser, A. M. Puertas, M. Fuchs, and Th. Voigtmann: Structural relaxation of polydisperse hard spheres: Comparison of the mode-coupling theory to a Langevin dynamics simulation, Phys. Rev. E **82**, 011504 (2010).

[104] Y. Yan and J. Koplik: Flow of power-law fluids in self-affine fracture channels, Phys. Rev. E **77**, 036315 (2008).

[105] W.-A. Yong and L.-S. Luo: Nonexistence of H Theorem for Some Lattice Boltzmann Models, Journal of Statistical Physics **121**, 91 (2005).

[106] A. Yoshino, Y. Hotta, T. Hirozane, and M. Endo: A numerical method for incompressible non-Newtonian fluid flows based on the lattice Boltzmann method, Journal of Non-Newtonian Fluid Mechanics **147**, 69 (2007).

[107] J. Zausch, J. Horbach, M. Laurati, S. U. Egelhaaf, J. M. Brader, Th. Voigtmann, and M. Fuchs: From equilibrium to steady state: the transient dynamics of colloidal liquids under shear, Journal of Physics: Condensed Matter **20**, 404210 (2008).

[108] J. Zhang and D. Y. Kwok: Pressure boundary condition of the lattice Boltzmann method for fully developed periodic flows, Phys. Rev. E **73**, 047702 (2006).

[109] Q. Zou and X. He: On pressure and velocity boundary conditions for the lattice Boltzmann BGK model, Physics of Fluids **9**, 1591 (1997).